Dissertation

submitted to the

Combined Faculties of the Natural Sciences and Mathematics

of the Ruperto-Carola-University of Heidelberg, Germany

for the degree of

Doctor of Natural Sciences

Put forward by

M. Sc. Lars Müller

born in Heidelberg, Germany

Oral examination: 07.02.2018

ON THE CORRELATION BETWEEN STRUCTURAL ORDER AND MOLECULAR DOPING IN SEMICONDUCTING POLYMERS

Referees: Prof. Dr. Wolfgang Kowalsky
Prof. Dr. Albrecht Winnacker

On the Correlation Between Structural Order and Molecular Doping in Semiconducting Polymers - In contrast to the improved understanding of pristine organic semiconductors that has been developed over the last decades, fundamental questions about the complex interplay between molecular doping and structural order in semiconducting polymers are still to be answered. In the present work, new insights on this interplay were unveiled using electron diffraction, spectroscopic methods, and electrical characterization. The doped polymer P3HT was explored in three states: in the solution before film formation, in the static thin film, and in a dynamic non-equilibrium state. Mechanisms related to the charging upon doping were found to govern the formation of order in the polymer P3HT already in the solution state. In doped solid films, the controversially discussed change of polymer crystal lattice spacing upon doping was examined, and a model explaining the changes based on the doping-induced charges was developed. In non-equilibrium conditions, the semi-crystalline morphology of the polymer P3HT was found to be an important prerequisite for the diffusion of dopants. Furthermore, an electric-field-controlled drift of molecular dopants was demonstrated and analyzed in detail for the first time. Proof of concept memory and memristive devices illustrate potential applications of this controlled dopant drift.

Über den Zusammenhang struktureller Ordnung und molekularer Dotierung in halbleitenden Polymeren - Während die Strukturbildung in reinen organischen Halbleitern in der Vergangenheit Gegenstand intensiver Forschung war, gibt es bei dotierten Polymeren noch keinen Konsens über die Ausbildung struktureller Ordnung sowie deren Auswirkung auf die Dotiereffizienz. In dieser Arbeit konnte mittels Elektronendiffraktion, spektroskopischen Methoden und elektrischer Charakterisierung gezeigt werden, dass eine Interaktion des Polymers P3HT mit Dotanten im Lösungsmittel die spätere Strukturbildung dominiert. Weiterhin klärte ein Vergleich verschieden großer Dotanten sowie eine Variation des Dotierprozesses die Einlagerung und räumliche Position der Dotanten in kristallinem P3HT auf. Ein Modell wurde entwickelt, welches eine in dieser Arbeit gemessene und in der Literatur kontrovers diskutierte Änderung der Kristallebenenabstände durch die von der Dotierung induzierte Ladung des Polymers erklären kann. Über die Untersuchung der statischen Eigenschaften hinaus wurde die semikristalline Morphologie von Polymeren als wichtige Voraussetzung für die Diffusion molekularer Dotanten identifiziert. Zusätzlich zur Diffusion wurde erstmalig ein Drift geladener Dotanten in einem elektrischen Feld nachgewiesen und charakterisiert. Zudem zeigt diese Arbeit, dass ein solcher Drift potenziell in Speicherelementen und memristiven Bauteilen Anwendung finden kann.

CONTENTS

ACRONYMS

TEM	transmission electron microscopy
ED	electron diffraction
BFTEM	bright-field TEM
HOMO	highest occupied molecular orbital
LUMO	lowest unoccupied molecular orbital
CF	chloroform
(D)CB	(di)chlorobenzene
DFT	density functional theory
ICT	integer charge transfer
CPX	charge transfer complex
DOS	density of states
OFET	organic field-effect transistor
OLED	organic light-emitting diode
OPVC	organic photovoltaic cell
EA	electron affinity
IE	ionization energy
IV	current-voltage
UV-Vis	ultraviolet - visible (spectroscopy)
(FT) IR	(Fourier transform) infrared (spectroscopy)

1

INTRODUCTION

We believe the polyacetylene halides may be the forerunners of a new class of organic polymers with electrical properties which may be systematically and controllably varied over a wide range by chemical doping.

Hideki Shirakawa
Alan G. MacDiarmid
Alan J. Heeger
J.C.S. Chem. Comm., 1977

With this quote, Shirakawa, MacDiarmid, and Heeger concluded their article on the discovery that the polymer polyacetylene can be doped with halogens in the late 1970s [1]. The prediction quoted above came true as this discovery and related work initiated research activities that led to the emergence of the field of organic electronics [2]. For their early work, the Nobel Prize for Chemistry 2000 was awarded to the three authors "for the discovery and development of conductive polymers" [3]. Based on these findings, the first generation of dopants for semiconducting polymers comprised species that form monoatomic ions, for example halogens such as iodine or electropositive metals, for example strontium or lithium [1, 4, 5]. However, the strong tendency to diffuse that these dopants show [6] does not allow for a usage comparable to doped inorganic semiconductors, where stable p-n-junctions provide the fundamental basis for light emitting diodes or solar cells [7]. As a consequence, the first organic photovoltaic cells (OPVCs) and organic light-emitting diodes (OLEDs) utilized two different materials that imitate the p- and n-doped inorganic counterpart [8, 9]. Such devices convert photons to charge carriers or vice versa in the direct vicinity (tens of nanometers) of the interface between the two materials, which was realized as a planar heterojunction in the beginning. In the case of OPVCs, this planar interface developed to more complex interdigitated bulk heterojunctions over time [10]. Despite these developments, the complex alignment of energy levels at interfaces, the low conductivity of transport layers, and the need for a certain thickness of transport layers to optimize absorption or outcoupling of light in OPVCs and OLEDs limited device performance. Therefore, molecular dopants that can be larger in size in combination with small molecule host materials were developed. These allow for p-i-n structured devices in which charge transport, injection, or extraction layers are doped. This principle is now successfully applied in OPVCs [11, 12], OLEDs [13, 14], and organic field-effect transistors (OFETs) [15]. Furthermore, the field of

organic thermoelectrics makes use of molecular dopants which allow for an increase of the electric conductivity without changing the thermal conductivity strongly at the same time [16, 17].

The objective of the present work is to shed light on some of the presently unsolved questions regarding the doping of organic semiconductors: First, what are the mechanisms leading to structural order in blends of host and dopant and what influence does the solvent have in particular? Second, what are the morphological characteristics of doped films—for example, how do the observed changes in lattice spacing correlate to an intercalation of dopants in crystallites of P3HT? Third, which morphological and molecular parameters dominate the diffusion of dopants in a host matrix and can there be a drift of charged dopant molecules in an externally applied electric field? The following gives a short introduction to the state of the art in molecular doping and motivates the research questions this thesis focuses on.

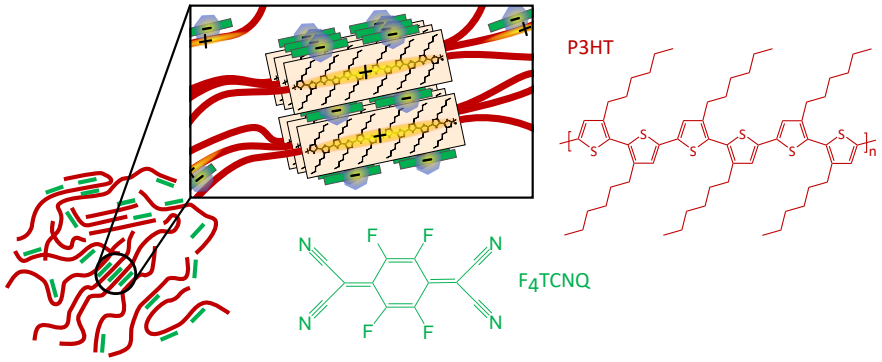

Figure 1.1: Chemical structures of the polymer P3HT and the molecular p-type dopant F_4TCNQ, together with a schematic of the investigated blend microstructure.

While high-performance devices such as commercially available OLEDs are processed by thermal evaporation of small molecules in vacuum conditions, the long-term goal of printed organic electronics requires a basic understanding of film formation from the solution state. This starts with understanding the interplay between solvent and organic materials to gain full control over the formation of structural order and intermixing effects upon drying. Finally, an exact understanding of the morphology-related properties of the resulting (doped) organic thin films is key. Such structure-property relationships and the relevant parameters that allow for a precise control of the structure were established in the past for many pristine materials such as the thoroughly investigated polymer P3HT [18]. When combined with molecular dopants though, the charge transfer can significantly alter the formation of structural order due to changed interactions with solvents and surrounding material. One prominent

host:dopant combination used widely in literature is P3HT:F_4TCNQ, for which the microstructure to be investigated is schematically depicted in Figure 1.1. The present work elucidates previously noticed discrepancies between existing studies [2] by a structural and spectroscopic study of solutions and thin films of doped P3HT. A detailed comparison of thin films processed from two solvents that differ in boiling point and polarity in addition to optical spectroscopy on the still dissolved host-dopant blend uncovers that in case of doped P3HT, the formation of structural order upon drying is dominated by the solvent polarity. This is in contrast to pristine P3HT, where the boiling point is decisive. Hence, new processing guidelines are needed for the preparation of thin films from blend host-dopant solutions.

Although doped transport and injection layers are already a part of functioning devices, the fundamental processes of doping organic semiconductors are not fully understood yet. One example is the still missing unifying description of doped organic semiconductors comprising small molecules and polymers [2]. Whereas doping of polymers usually leads to full transfer of a charge between dopant and polymer (integer charge transfer, ICT), doping of small molecules often leads to the formation of charge transfer complexes (termed CTC or CPX) [2]. A unifying explanation of doping could allow to predict the charge transfer and doping efficiency based on the molecular structure of dopant and host, which is not possible to date [2, 19]. In addition, a clear understanding of how the structural order of semicrystalline polymers is connected to the doping efficiency is not established and the roles of structure, spatial position and orientation of the dopant are still subjects of investigation. Especially the question if molecular dopants can reside in crystallites of P3HT and their spatial position in the crystalline structure is controversially discussed [20–23]. The present work contributes to this debate with the comparison of structure-revealing electron diffraction measurements on P3HT doped with differently sized dopants. From the measurements shown here, an intercalation of dopants in the π-π stacking of P3HT crystallites is found to be unlikely.

A recent development that circumvents the difficulties arising from the complex interplay of host, dopant, and solvent upon film formation is a sequential doping technique which allows for a solution-processed doping of already formed thin films of polymers [24, 25]. Using this technique, it is possible to analyze the influence of the host morphology on doping efficiency and charge transport of doped polymers [22, 23]. As this technique relies on the ability of the dopant to diffuse into the polymer, knowledge about the diffusion behavior and its dependence on the structural order is needed. However, few studies have yet been conducted that measure diffusion constants of neutral and ionized dopants and explore the complex interplay with chemical structure of host and dopant [19, 26–28]. The present work

provides insight on the influence of structural order in the host matrix on the diffusion of dopants. For this purpose, and to determine the general impact of doping on the structural order, the semi-crystalline polymer P3HT and a fully amorphous version of it were sequentially doped with different techniques and dopants. The semi-crystalline morphology is found facilitate diffusion. In addition to diffusion, an electric-field-induced drift of charged molecular dopants was observed and characterized in this work for the first time. Such a drift can be cause to severe device degradation since the electrical properties change significantly upon de-doping of contact regions. On the other hand, the present work demonstrates that a controlled drift of dopants can be utilized in memory and memristive devices, for which proof-of-principle studies are presented. To succeed in achieving stable and high-performance polymer-based devices, a detailed study of the dynamic processes is essential. Further optimization of the chemical structures and thin film morphology is necessary in order to control or inhibit the diffusion and drift of molecular dopants. This work constitutes one step towards this goal, providing the analysis of chemically modified n-type dopants that were specifically synthesized by the research group of Prof. Bunz at the Institute for Organic Chemistry to be immobilized in a host matrix. An azide group is intended to chemically bind the dopant to the host matrix upon thermal or optical activation [29, 30].

One analytic method used in this thesis is transmission electron microscopy (TEM) with a focus on electron diffraction. With high-resolution TEM, imaging of ordered polymer domains is possible [31], and electron diffraction reveals detailed information about the crystalline content, especially the lattice spacings of crystalline domains. In addition to this powerful technique that characterizes the structural order in doped thin films, optical spectroscopy in the UV-Vis spectral range in combination with theoretical models to correlate the observed absorption features with structural and electronic properties [32, 33] was employed in this work. Electrical measurements accompany the analyses to determine the conductivity upon doping, and chronoamperometry was used to investigate the dopant drift. Collaborations and joint measurements with colleagues are presented in this thesis where they contribute essential insights.

1.1 OUTLINE

This thesis is structured as follows: Chapter 2 introduces the relevant theoretical background of charge transport and doping in organic semiconductors together with the theory behind electron diffraction, ionic-electronic diffusion and drift, as well as memristive systems. The experimental techniques used in this thesis are introduced in Chapter 3, and relevant measurement parameters and conditions are provided. Chapter 4 summarizes the relevant characteristics of the used materials and gives a description of sample layouts and preparation for the various measurement techniques. The results and corresponding discussions are split in two parts: Part I comprises Chapter 5 to Chapter 8 and focuses on the fundamental changes in structural order and related effects that occur upon doping. Chapter 5 introduces the structural features, characteristic optical spectra, and conductivity measurements of pristine and doped organic semiconductors used throughout this thesis. The influence of solvent on the formation of structural order and related parameters in P3HT doped from blend solutions is discussed in Chapter 6. Going from blend to sequential doping, Chapter 7 gives an overview on how sequential doping influences the ordered domains of P3HT and the corresponding electronic properties. The impact of doping on the π-π stacking in P3HT crystallites and the resulting implications are discussed in Chapter 8 on basis of electron diffraction measurements and corresponding density functional theory calculations. Part II of the results and discussions focuses on the dynamic processes of diffusion and drift of molecular dopants in organic semiconductors. After a short literature review in Chapter 9, Chapter 10 discusses the dependence of dopant diffusion on the structural order of P3HT. The electric-field-induced drift of dopant molecules is then shown and characterized in detail in Chapter 11. This chapter additionally presents proof of principle memory and memristive devices based on a dopant drift. Finally, Chapter 12 concludes on the results of this thesis and gives a short outlook of expected future developments.

2 THEORY

This chapter summarizes the basic theoretical concepts needed for an understanding of the measurements that are discussed throughout this thesis. After a short general introduction to organic semiconductors, a framework to describe charge transport in intrinsic and doped organic semiconductors is presented. Prevalent doping models and the physics of optical transitions between molecular states are discussed to facilitate the understanding of UV-Vis and infrared spectra of doped and undoped organic semiconductors. Finally, the theoretic background of electron diffraction is shortly introduced, followed by the description of ionic-electronic drift and diffusion and an introduction to the concepts of the memristor and memristive systems.

2.1 ORGANIC SEMICONDUCTORS

The class of organic semiconductors comprises carbon-based materials that reveal properties comparable to inorganic semiconductors such as a band gap of a few electronvolt (eV) [34]. In contrast to the crystalline lattice of single atoms that gives rise to the formation of bands such as the valence and conduction band in inorganic semiconductors, single molecules or sections of polymers that are separated by kinks or twists in the backbone make up the basic units of organic semiconductors [35]. These basic units are—in a majority of organic semiconducting materials—not part of one single crystal and hence, the classical description of band formation is limited [34]. In addition, the bonds between the single units are not covalent, but of the significantly weaker van der Waals type. In contrast to inorganic semiconductors, this class of materials requires consideration of the properties of the basic units rather than a collective description. The conjugation which is the overlap of p-orbitals of adjacent atoms, usually carbon, enables a delocalization of electrons in a molecule or along a polymer, which gives rise to the charge transport properties of such materials. The atomic orbitals of the single atoms in a molecule combine and form new orbitals with a splitting in energy that defines a highest occupied and lowest unoccupied molecular orbital named HOMO and LUMO, respectively [34].

When the view is expanded from single molecules or units to the entirety of many units in a solid, the disorder in molecular alignment and hence energetic surrounding determines the electronic properties of the system [35]. The molecular orbitals in different surroundings vary in energetic position and sum up to a density of states that

is broad and—due to the stochastic distribution—usually described with a Gaussian. The sum of energetic positions of all HOMO and LUMO values of the single molecules then defines what is usually compared to the valence and conduction bands in inorganic semiconductors [34].

2.2 CHARGE TRANSPORT

The following introduces the fundamental mechanisms that determine the charge transport in organic solids to provide a basis for doping-induced effects. Charge transport in organic solids can be governed by several contributions, leading to descriptions that range from disorder-based models to band transport, depending on the material's structural order [35–37]. The one-electron Hamiltonian for low charge carrier densities and negligible electron correlation and coulomb interaction effects is generally given by [36]:

$$H = H_{el} + H_{vib} + H_{et} + H_{dd} + H_{sd} \,. \tag{2.1}$$

Here, H_{el} describes the electronic, H_{vib} the vibrational, H_{et} the electron transfer, H_{dd} the dynamic disorder, and H_{sd} the static disorder term. A description of the single contributions and an assignment which contributions dominate in which case are given in the following, based on references [37] and [35].

The total energy of the system without intermolecular interactions is described by H_{el} and H_{vib}. Here, the molecules and the lattice can be electronically and vibrationally excited. H_{et} governs the transfer of an electron from one site to another and H_{dd} introduces polaronic effects, meaning interactions of the electronic excitation with the lattice. The polaronic effects include a site-energy reduction due to the interaction with lattice vibrations and a change of probability of transitions between two sites. Vibrations can occur between molecules (inter) and within one molecule (intra). H_{sd} governs changes in site energy (often termed diagonal) and transition probabilities due to static structural variations (off-diagonal), i.e. static variations of inter- and intra-molecular distances as well as orientations. The three limiting cases are pure band transport, polaronic transport, and disorder-based transport:

- Band transport: The interaction between neighboring molecules dominates the system, leading to a delocalization of the charge carriers and band transport. However, band transport in organic semiconductors can only be observed for a charge carrier mobility around $10\,\mathrm{cm^2\,V^{-1}\,s^{-1}}$ and higher [37], which is not given for the materials studied in this thesis.

- Polaronic transport: The reduction of the site energy emerging from a coupling of electronic excitations to inter- or intramolecular vibrations has to be overcome by thermal activation.

Charge transport between two sites takes place as a phonon-assisted hopping process and the term H_{dd} dominates the system.

- Disorder-based transport: It takes place when the density of states is broad due to large variations in site energy and transition probability amplitude. In this case, thermal activation is required to allow for a hopping transport between the distinct sites.

For the materials investigated in this thesis, disorder-based charge transport dominates the system. Polaronic transport possibly adds, depending on the conditions given by material and processing.

A description of disorder-based transport can be given with the Gaussian disorder model (GDM) that describes hopping between distinct sites. The dependence of the charge carrier mobility on temperature and electric field can be described with a model that takes into account energetic (diagonal) disorder as well as positional (off-diagonal) disorder:

$$\mu(\hat{\sigma}, F) = \mu_0 \exp\left[-\frac{4\hat{\sigma}^2}{9}\right] \exp\left[C(\hat{\sigma}^2 - \Sigma^2)\sqrt{F}\right] \quad \text{for} \quad \Sigma \geqslant 1.5\,, \tag{2.2a}$$

$$\mu(\hat{\sigma}, F) = \mu_0 \exp\left[-\frac{4\hat{\sigma}^2}{9}\right] \exp\left[C(\hat{\sigma}^2 - 2.25)\sqrt{F}\right] \quad \text{for} \quad \Sigma \leqslant 1.5\,. \tag{2.2b}$$

Here, Σ is the positional disorder parameter, σ an energetic disorder parameter, $\hat{\sigma} = \sigma/kT$, and C a constant that depends on the site separation. This model predicts a Poole Frenkel-like field dependence of $\ln \mu \propto \sqrt{F}$ and a temperature-dependence of $\ln \mu \propto 1/T^2$.

This description disregards polaronic effects such as readjustments of bond lengths when an electron is removed or added. To include this, Fishchuk *et al.* developed an analytical theory based on the effective medium approach (EMA) [38]:

$$\mu = \mu_0 \exp\left(-\frac{E_a}{kT} - \frac{\hat{\sigma}}{8q^2}\right) \exp\left(\frac{\hat{\sigma}^{1.5}}{2\sqrt{2}q^2}\sqrt{\frac{eaF}{\sigma}}\right) \exp\left(\frac{eaF}{4q^2kT}\right)\,. \tag{2.3}$$

Here, a is the lattice constant, $q = \sqrt{1 - \sigma^2/8eakT}$, and E_a is defined as half of the polaron binding energy. The equations presented above were successfully applied to organic semiconducting polymers, whereas it depends on the material system if polaron or disorder effects dominate [37].

Figure 2.1a describes the electron transport in the LUMO level for low charge carrier concentrations. Electrons that are generated or injected relax in energy so that the occupational density of states (ODOS) is shifted to lower energy by σ^2/k_BT compared to the initial

DOS [39]. For a low charge carrier density, the Fermi level is far from the Transport energy (E_T) that allows for optimum hopping transport [40]. Hence, the hopping transport requires large activation and is greatly enhanced by increased temperature, large electric fields, or photo-generation of high-energy charges.

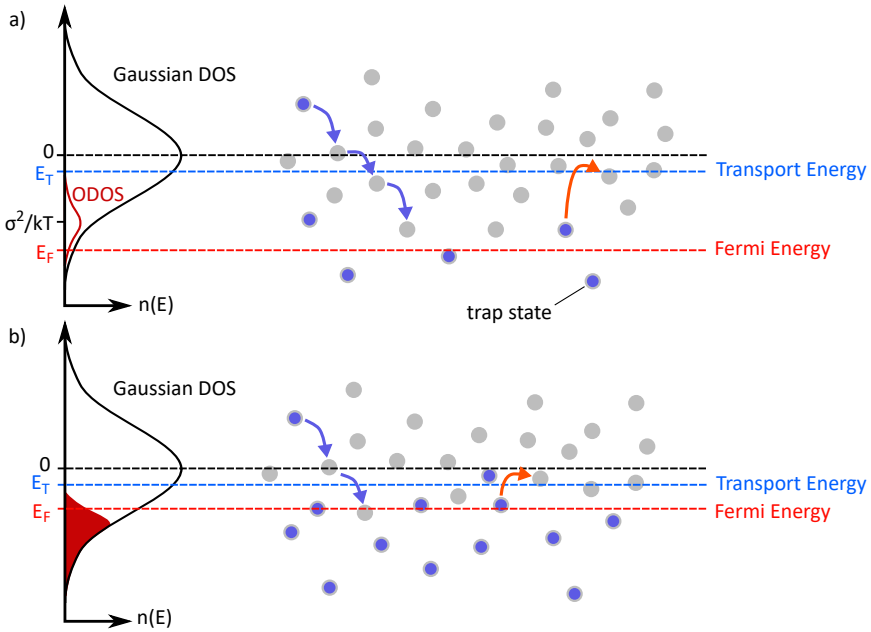

Figure 2.1: Schematic that illustrates charge transport in the case of a low (a) and high (b) charge carrier density. The black line shows the center of the Gaussian DOS representing the LUMO. Gray empty and blue filled circles show available empty and occupied states, respectively. The blue arrows illustrate thermal relaxation of generated or injected charge carriers. a) Charge transport requires thermally activated transitions of charge carriers from the occupational DOS (ODOS) to the transport energy E_T in the low carrier limit (red arrow). b) In the presence of space charges, Fermi-Dirac statistics governs the DOS occupation. Activation from the Fermi level E_F to E_T is required for charge transport. A broadening of the DOS due to counter-charges (dopants) is neglected here [35].

2.3 DOPING OF ORGANIC SEMICONDUCTORS

To provide a basis for the electrical measurements shown in this thesis, the changes in charge transport upon doping are discussed in the following. Furthermore, the peculiarities of molecular doping of organic semiconductors are introduced, together with prevalent models that describe the doping process.

2.3.1 *Charge Transport Upon Doping*

The charge carrier density can be strongly increased by doping or high induced currents as for example in the channel of an organic field-effect transistor (OFET) due to the gate bias. In the case of doping, the distribution of the internal electric field can be distorted by trapped space charges and the DOS is additionally modified by ionized dopant molecules [37]. In an OFET or situation where a space charge limited current (SCLC) exists, tail states are occupied by the large currents flowing. Hence, the interactions between single charges are no longer negligible. In this case, where the DOS is filled beyond the quasi-equilibrium which lies energetically below the center of the DOS by σ^2/k_BT, the carrier statistics change from Boltzmann-like to Fermi-Dirac-like [37]. Since charge carriers no longer start from a temperature-dependent occupational DOS, the charge carrier mobility changes from $\ln\mu \propto T^{-2}$ to an Arrhenius-like dependence of $\ln\mu \propto T^{-1}$ for increasing concentrations [35]. Figure 2.1b schematically depicts the situation for a high charge carrier concentration. In this case, the activation energy to reach the transport level is strongly decreased, which leads to an increase in charge carrier mobility [37]. Experimentally, the prediction that μ depends on the charge carrier density n was confirmed by measurement of a charge carrier mobility in FETs that can be up to three orders of magnitude higher compared to a diode [41]. In the case of doped organic semiconductors, the the ionized and oppositely charged dopants lead to an additional broadening of the DOS [37, 42] and can act as traps themselves [43]. Generally, the observed conductivity

$$\sigma = ne\mu \tag{2.4}$$

depends on the interplay between the number of free charge carriers generated by doping which increase the total charge carrier density n and the charge carrier mobility μ, which can strongly depend on the structural order of the organic semiconductor, as discussed in this thesis.

2.3.2 *General Considerations*

Doping of inorganic semiconductors is achieved by replacing atoms of the semiconductor with atoms that possess one valence electron more (n-doping) or less (p-doping) than the host in a crystal lattice. In contrast, doping of organic (usually disordered) semiconductors is realized by addition of entire molecules that act as p- or n-type dopants. For the case of doping inorganic semiconductors, the bind-

ing energy E_B of a hole to the dopant site can be estimated analogue to the binding energy of an electron in the hydrogen atom

$$E_B = -\frac{1}{2}\frac{m_h^* e^4}{(4\pi\epsilon_0\epsilon_r)^2\hbar^2}, \tag{2.5}$$

where m_h^* is the effective mass of the hole, ϵ_0 the vacuum permittivity, and ϵ_r the dielectric constant. Calculation of E_B for silicon with $m_h^* = 0.3m_e$ and $\epsilon_{r,Si} = 11.7$ [44] yields roughly 30 meV binding energy, which is comparable to k_BT at room temperature. For organic semiconductors, the Coulomb interaction energy

$$E_{Coulomb} = \frac{e^2}{4\pi\epsilon_0\epsilon_r a} \tag{2.6}$$

with the distance between dopant and host molecule a can be used to approximate the binding energy that has to be overcome by a charge carrier. a is typically on the order of 5 Å to 10 Å in organic semiconductors [22] and the dielectric constant of $\epsilon_r = 3-4$ is significantly smaller compared to the inorganic counterpart [34]. This leads to binding energies of hundreds of meV inducing a strong localization of charge carriers and low doping efficiencies whereas in the case of inorganic semiconductors, each dopant introduced is assumed to contribute one free charge carrier. To understand why doping can still be observed in OSC's, a closer look at the energetic landscape the doped molecules are embedded in [45] and the energetic readjustment of electronic orbitals [46] is taken in the next sections. Because of the low doping efficiency, dopant concentrations of 10^{-2} mol % to 10^{-1} mol % are common for organic semiconductors [2] compared to 10^{-6} mol % to 10^{-3} mol % in the inorganic case [44].

2.3.3 *Doping Models*

In the following, the two prevalent doping models *Integer Charge Transfer* (ICT) and *Charge Transfer Complex Formation* (CPX or CTC) are discussed on the example of p-type doping.

2.3.3.1 *Integer Charge Transfer*

To generate one additional hole on the host in case of p-doping, a dopant molecule must receive one electron from the organic host. To allow for this process, the electron affinity (EA) of the dopant has to be lower in energy (corresponding to a higher binding energy) than the ionization energy (IE) of the host, which is depicted in Figure 2.2a. In this case, the integer charge transfer between host and dopant leads to one additional hole in the host's HOMO which potentially can contribute to charge transport. However, Coulombic interaction can still bind the hole to the dopant, turning the pure integer charge transfer into a necessary but not sufficient prerequisite for a high doping

efficiency. Whereas the energy levels of the neutral host and dopant molecules determine if charge transfer happens, they do not remain constant upon charge transfer. Due to on-site Coulombic interaction, the occupied and unoccupied HOMO sublevels of the cation split in energy with a splitting termed Hubbard U. The reorganization energy determined as the difference of frontier molecular orbital in the neutral and the charged state is usually called reorganization energy λ. Figure 2.2b schematically illustrates how these readjusted energy levels of charged dopant and host molecules are arranged energetically within the surrounding undoped molecules [46]. The right side of Figure 2.2b shows the DOS of neutral and newly introduced occupied and unoccupied states. Although the situation here is depicted for separate molecules, polymers as host usually behave comparably due to twists or kinks in the polymer backbone which reduce the conjugation length to a few repeat units. Therefore, polymers can be described as a sequence of weakly coupled sub-units comparable to small molecules [37]. However, this description breaks down for highly ordered polymers or polymers with a planar and torsion-free backbone that even may possess a near-amorphous microstructure [37, 47].

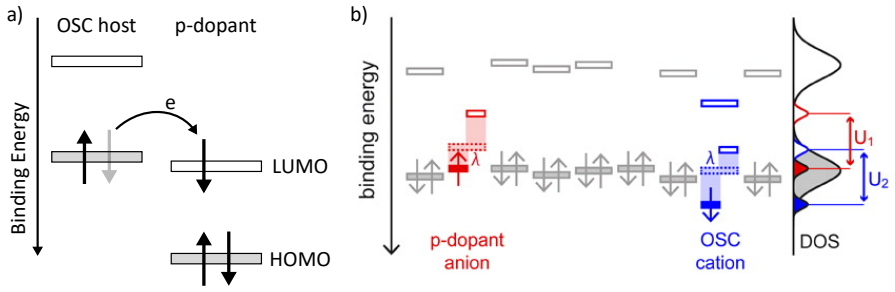

Figure 2.2: a) Schematic of ICT p-doping where the electron affinity of the dopant is lower in energy compared to the ionization energy of the host. b) Energy levels of neutral and p-doped OSC, and dopant anion together with the corresponding DOS in the integer charge transfer scheme. λ and U are the reorganization energy and Hubbard, respectively. (b) is reprinted from [46].

2.3.3.2 *Charge Transfer Complex Formation*

Besides the integer charge transfer, a process termed ground state charge transfer complex (CPX or CTC) formation is known. This process takes place if the overlap of electronic orbitals of dopant and host favors the formation of supramolecular hybrid orbitals instead of a complete charge transfer from host to dopant molecule. These orbitals form as symmetric and antisymmetric linear combinations of the doubly occupied HOMO of the host and the empty LUMO of the dopant [2]. The new doubly occupied bonding and empty antibonding orbitals of the CPX are illustrated in Figure 2.3a. The charge

transfer δ is defined by the share of the CPX-orbitals located on the host molecule and can be a non-integer value in case of CPX formation. In a Hückel-type model, the energetic position of the HOMO (H) and LUMO (L) of the CPX are given as

$$E_{CPX,H/L} = \frac{H_{OSC} + L_{dop}}{2} \pm \sqrt{(H_{OSC} - L_{dop})^2 + 4\beta^2}\,. \tag{2.7}$$

Here, H_{OSC} and L_{dop} are the HOMO of the organic semiconductor host and LUMO of the dopant molecule, respectively, and β is the resonance integral [46]. CPX formation does not require L_{dop} to be lower in energy than H_{OSC}. Figure 2.3b shows the energetic position of the CPX in the environment of a solid film. The charge transfer complex forms in the neutral state, which leads to one occupied level below and one empty level above the HOMO of the OSC. If L_{CPX} is accessible for electrons in the HOMO of the OSC *via* thermal activation, the neutral CPX itself can act as dopant and an electron can be transferred from H_{OSC} to L_{CPX}.

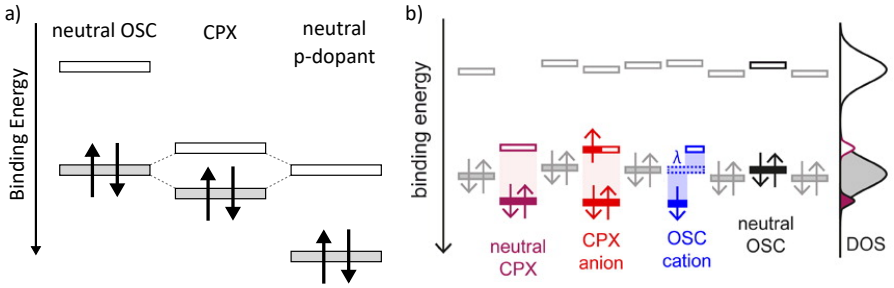

Figure 2.3: a) Schematic of charge transfer complex (CPX) formation. b) Energy levels of neutral host, neutral CPX, doped host, and CPX anion together with the corresponding DOS (only contribution of neutral CPX shown) with the reorganization energy λ. (b) is adapted from [46].

ICT Versus CPX Formation

Doping *via* integer charge transfer is usually desirable since it directly yields spatially separated charge carriers and molecular orbitals on host and dopant. However, CPX formation can occur for energetic configurations of $L_{dop} \geqslant H_{OSC}$ which are usually not accessible for ICT. But, to actually dope the OSC, L_{CPX} has to be comparable in energy to H_{OSC}. The design of an efficient dopant therefore strives to lower L_{CPX} in case of CPX formation or to reduce L_{dop} in the first place to ensure ICT. However, to achieve ICT, the intermolecular resonance integral β has to be low, which could be reached by sterically shielding the orbitals of host and dopant with chemical side groups [48]. For the organic semiconducting polymer P3HT investigated in this thesis, ICT occurs with the dopants F_4TCNQ and Mo(tfd-CO_2Me)$_3$. However, the small molecule 4T composed of four thiophene units

which also make up the functional backbone of P3HT was shown to form charge transfer complexes with F_4TCNQ and nominal charge transfer of $\delta = 0.25$ [49]. This highlights, that detailed knowledge about the specific material system in terms of energy levels and electronic orbitals as well as spatial alignment and orientation of dopant and host are necessary to predict, if ICT or CPX formation occurs.

2.4 TRANSITIONS BETWEEN MOLECULAR STATES

To understand the spectral signature of molecular transitions and what can be learned from it, an introduction based on reference [35] is given in the following. The wavefunction of a molecular state Ψ_{total} can be approximated by the product of the (many-electron) electronic wavefunction Ψ_{el}, the spin wavefunction Ψ_{spin}, and the vibrational wavefunction Ψ_{vib}:

$$\Psi_{total} = \Psi_{el}\Psi_{spin}\Psi_{vib}\,. \tag{2.8}$$

In this picture, Ψ_{el} depends on the positions of the electrons as well as of the nuclei. Ψ_{spin} is a combination of the individual electron spins, and Ψ_{vib} depends on the positions of the atomic nuclei. This approach to separate the overall wavefunction into a product of electronic and nuclear wavefunctions (Born-Oppenheimer approximation) is legitimate as long as there are no significant interactions between the single contributions. In the case of optical excitation, this is given since the nuclei move slow compared to electrons. An optical excitation of a molecule described as a system of coupled oscillators in this picture can be illustrated with potential energy curves that represent the molecule in certain molecular configuration coordinates Q_i. Each potential represents one electronic state of the system, for example the ground state S_0 or the first electronically excited state S_1. In each electronic state, vibronic excitation is possible, which gives rise to distinct vibronic states within the potential curve. The form of such a potential can be described analogue to a Morse potential for a diatomic molecule with a minimum that is reached for a certain configuration coordinate and an exponential increase towards closer nuclei distances. In vicinity of the equilibrium, a harmonic oscillator potential can be used to approximate the potential shape. Figure 2.4a schematically illustrates the described situation and further processes that are discussed in the following.

For the case of light absorption and the assumption that the energy of the molecule is changed only a little when excited, the dipole operator $e\hat{\mathbf{r}}$ can be used as perturbing Hamiltonian that excites the molecule. With this approach, it is possible to derive, how the transition k_{if} between initial and final state depends on the perturbation:

$$k_{if} = \frac{2\pi}{\hbar}\left|\left\langle \Psi_{el,f}\Psi_{spin,f}\Psi_{vib,f}\right|\, e\hat{\mathbf{r}}\,\left|\Psi_{el,i}\Psi_{spin,i}\Psi_{vib,i}\right\rangle\right|^2 \rho\,, \tag{2.9}$$

where the molecular wavefunction Ψ_{total} is already divided into its constituents, and ρ gives the density of the final states. Since the incident electromagnetic wave oscillates too fast to affect the heavy nuclei and the change in magnetic field induced by the electromagnetic wave is too small to have an effect on the spins, the dipole operator $e\hat{\mathbf{r}}$ solely acts on Ψ_{el} [35]. This leads to the following expression:

$$k_{if} = \frac{2\pi}{\hbar}\rho \left| \left\langle \Psi_{el,f} \right| e\hat{\mathbf{r}} \left| \Psi_{el,i} \right\rangle \right|^2 \left| \left\langle \Psi_{spin,f} | \Psi_{spin,i} \right\rangle \right|^2 \left| \left\langle \Psi_{vib,f} | \Psi_{vib,i} \right\rangle \right|^2 . \quad (2.10)$$

In the following, the electronic, vibronic, and spin contributions to the rate and intensity of an optical transition are briefly discussed.

2.4.1 *Electronic Factor*

If the electronic contribution $\left| \left\langle \Psi_{el,f} \right| e\hat{\mathbf{r}} \left| \Psi_{el,i} \right\rangle \right|^2$ is different from zero, the transition is dipole-allowed (otherwise dipole-forbidden). The value of this contribution scales with the overlap of initial and final state wavefunctions, which means that rates for orbitals localized on the same part of the molecule such as π-π^*-transitions are higher than rates of for example charge-transfer transitions that are located on different positions. In addition to the orbital overlap, the rate increases with spatially more extended orbitals. This was for example shown on the absorption of conjugated oligomers, which increases with increasing oligomer length [35, 50]. With this knowledge, the strength of an absorption signal can be used to determine its nature [35].

2.4.2 *Vibronic Factor*

Whereas the electronic factor determines the absorption intensity, the vibronic factor $\left| \left\langle \Psi_{vib,f} | \Psi_{vib,i} \right\rangle \right|^2$, also known as the Franck-Condon factor, controls the spectral shape of the absorption. With an excitation energy around 100 meV and higher, the molecules are usually in their vibronic ground state at room temperature. The electronically excited state S_1 has a molecular configuration coordinate that is shifted by ΔQ_i compared to S_0. At the same time, the heavy nuclei are too slow to adapt on a time scale of the electronic excitation upon absorption of an incident electromagnetic wave. Therefore, the transition probability I_{0-m} of a transition from the vibronic ground state in S_0 to any vibronic state m in S_1 is usually not maximum for $m = 0$. Figure 2.4a illustrates this process with vertical lines representing the excitation. For a treatment of the oscillation in the potential depicted in Figure 2.4a as harmonic oscillator with reduced mass M, force constant $k = M\omega^2$, and angular frequency ω_m, the Frank-Condon factor is related to ΔQ_i by:

$$I_{0-m} = \left| \left\langle \Psi_{vib,f} | \Psi_{vib,i} \right\rangle \right|^2 = \frac{S^m}{m!} e^{-S} , \quad (2.11)$$

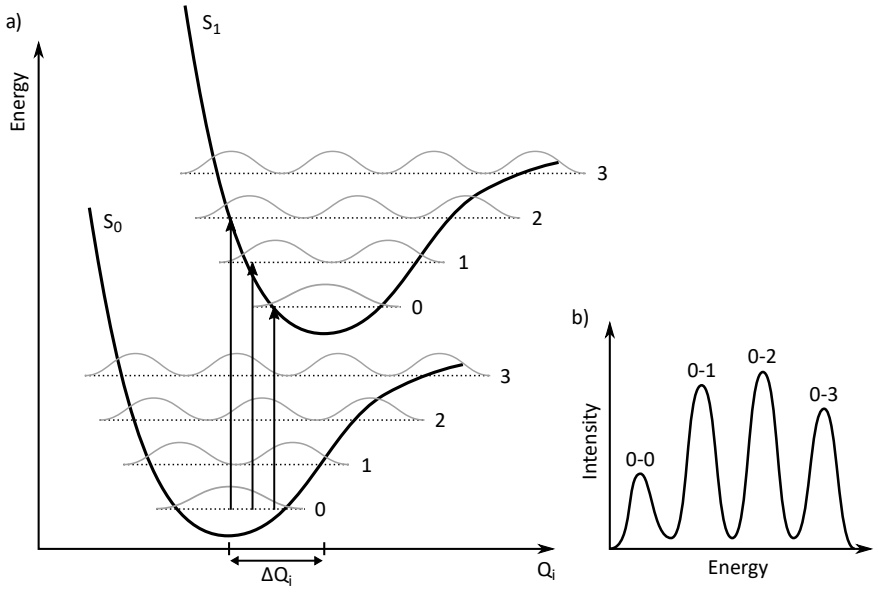

Figure 2.4: Illustration of the Franck-Condon principle with simplified potential curves for the electronic ground and excited states S_0 and S_1 that are shifted in molecular configuration coordinates by ΔQ_i. Optical excitations from S_0 to S_1 are represented by vertical arrows, illustrating the overlap of the vibrational wavefunctions in each potential that determines the shape of absorption (b) and emission spectra.

$$\text{where} \quad S = \frac{1}{2} k \frac{\Delta Q_i^2}{\hbar \omega_m} = \frac{1}{2} M \omega_m \frac{\Delta Q_i^2}{\hbar} \tag{2.12}$$

is the Huang-Rhys parameter. Equation 2.11 determines the absorption (and emission) spectrum of a certain molecule. For molecules with rigid bonds that do not change much upon excitation, the 0-0 transition dominates, whereas molecules with greater change in conformational coordinates reveal absorption spectra where for example the 0-2 transition dominates, as depicted in Figure 2.4b. Whereas the transitions can be observed as distinct lines in the gas phase, spectra from solution or solid films reveal line broadening due to variations in the surroundings of the molecules. This can be accounted for with introduction of a lineshape function Γ, usually a Gaussian or Lorentzian. Together with the influence of the photon-density-of-states in the surrounding medium, which is introduced with a factor of $[n(\hbar\omega) \cdot \hbar\omega]$, the normalized absorption spectrum can be described as:

$$I_{Abs} = [n(\hbar\omega) \cdot \hbar\omega] \cdot \sum_m \frac{S^m}{m!} e^{-S} \cdot \Gamma \cdot \delta(\hbar\omega - (\hbar\omega_0 + m\hbar\omega_m)) \,. \tag{2.13}$$

Here, $n(\hbar\omega)$ is the refractive index at the given energy $\hbar\omega$, m gives the vibrational level with energy $\hbar\omega_m$, $\hbar\omega_0$ is the 0-0 transitional

energy, and δ the Delta-function that defines the energetic position of the 0-m transition. The formalism introduced above was extended by Spano and coworkers, who considered the coupling of electronic states to molecular vibrations and explain how the Franck-Condon progression of a single molecule or polymer is changed when embedded in an aggregate [32, 33, 51]. Together with a Frank-Condon fit of optical absorption spectra, this allows for a calculation of the free exciton bandwidth, which is directly related to the intrachain order and conjugation length of a polymer. In Section 5.1.2, this theory is utilized to assess the structural order of differently processed P3HT thin films.

2.4.3 *Spin Factor*

The integral $\langle \Psi_{spin,f} | \Psi_{spin,i} \rangle$ which represents the spin component of Equation 2.10 is 1 if the spins of initial and final state are equal and 0 if the spins differ. Hence, transitions between singlet and singlet (fluorescence) or between triplet and triplet are generally spin-allowed, whereas transitions between triplet and singlet states (phosphorescence) are spin-forbidden. However, phosphorescence is observed when spin-orbit coupling perturbs the wavefunctions so that a change in spin angular momentum can be counterbalanced by an opposite change in orbit angular momentum. Prominent examples for this process are molecules that include heavy atoms for the use in phosphorescent OLEDs.

2.4.4 *Transitions of Charged Molecules*

Before discussing the transitions between charged molecules, the terminology is clarified in the following. The molecular structure of organic semiconductors leads to a different usage of the term polaron compared to inorganic semiconductors, which is important to be aware of. The initial definition of a polaron is based on a crystal in which a charge or charged site distorts the crystal lattice by changing the distance to neighboring units due to the different polarization. The charge with the surrounding lattice distortion is correctly termed polaron. While this definition holds true for molecular crystals, charged molecules in an amorphous solid need an adapted description. In addition to the inter-molecular (outer) reorganization energy that dominates in the classical polaron definition, there is a significant intra-molecular (inner) reorganization energy for organic molecules or polymers. A doped and hence charged and excited molecule usually has a different molecular geometry compared to its neutral state. The transition energy between both is termed inner reorganization energy. The overall reorganization energy is then given by $\lambda = \lambda_{inner} + \lambda_{outer}$. In (partly amorphous) organic semiconductors,

λ_{inner} is large compared to λ_{outer} [35]. However, the term polaron is still used in the context of amorphous molecules or polymers, but now refers to the combination of charge and the connected distortion which is mainly intra-molecular.

Charging of molecules can be described analogue to the above introduced picture. Adding (n-doping) or removing (p-doping) an electron leads to reorganization of the molecule with a shift of the conformational coordinates ΔQ_i and a corresponding change in electronic orbitals and respective energy levels. Whereas the electronic excitation of a molecule preserves the overall neutrality, the charging does not. This leads to an interaction energy and hence polarization of the surrounding that scales with r^{-4} compared to the r^{-6} dependence in the case of an excited state [35]. A charged molecule hence impacts its surrounding in a larger radius.

Figure 2.5a illustrates the HOMO and LUMO energetic positions of the neutral molecule or polymer. S1 depicts the optical excitation of an electron from the HOMO to the LUMO. Figure 2.5b shows the situation for a positively charged system that originates from the Su-Schrieffer-Heeger (SSH) model for conjugated polymers which was developed to explain effects like the optical band gap of polyacetylene [34, 35]. This band gap originates from the dimerization of carbon bonds in a polymer chain (Peierls' distortion) that is energetically favorable compared to equidistant carbon bonds. A lattice mismatch where the two senses of bond alternations meet carries a spin that originates from the unpaired electron which does not participate in bonding. It is called soliton and has an energy in the middle of the band gap. As most other polymers do not have a degenerate ground state, the SSH model was extended and instead of one state, two states in the band gap appear. The spatial distortion that accompanies the mid-gap states led to the terminology polaron. Whereas this model was developed for ordered polymers, it is widely applied also for solids of amorphous small molecules. Figure 2.5b depicts the situation of a positively charged system where the two states in the band gap lead to observable absorptions P1 and P2. For the polymer P3HT that is mainly investigated in this thesis, P1 is observed in the infrared range around 0.5 eV and P2 at energies around 1.5 eV. Figure 2.5c illustrates the model of a polaron that is delocalized not only along the molecule or polymer backbone (intra-molecular), but also across molecules or polymer chains, usually in the direction of π-π stacking. In this case, the term 2D polaron is used and absorptions DP1 and DP2 are observed for lower and higher energies than P1 and P2, respectively [54].

Although often used, the underlying SSH model has significant shortcomings when applied to disordered organic semiconductors.

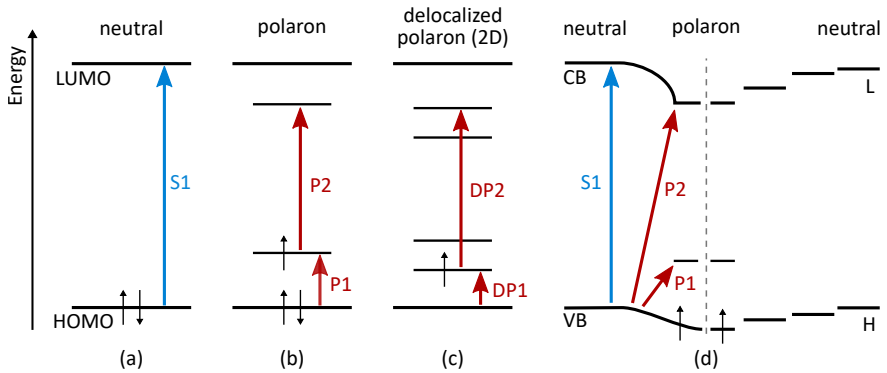

Figure 2.5: a) Scheme of an optical transition S1 in a neutral molecule or polymer. b) Traditional energy level schematic of a positively charged molecule with two polaron levels in the bandgap that give rise to absorptions P1 and P2. c) As in (b), but the polaron is delocalized inter- and intra-molecular. d) Recently proposed scheme for polarons on polymers (left) [52] and small molecules (right) [53] that includes electronic interactions with the surrounding.

One main assumption of this model is that electronic interactions such as the Coulomb interaction of π-electrons are small. For organic semiconductors with a dielectric constant between 3 and 4, this is not given. Recent studies by Winkler *et al.* and Heimel include the electronic interactions and propose the energy-level assignment shown in Figure 2.5d [52, 53]. The left side illustrates the energetic situation for a polymer where CB and VB are the conduction and valence band, respectively. On the right side, a system composed of small molecules is depicted with analogue LUMO (L) and HOMO (H) in the neutral state. The discrete levels depict the charged molecule in the center with the newly established level in the bandgap that gives rise to P1 and the energetically shifted LUMO level that gives rise to P2. The neighboring molecules are affected by the charge which is indicated by a shift in energetic position that decreases for increasing distance to the charged molecule. This new model is currently under discussion in the community and an extension to describe also 2D polarons is yet missing, which leads to a mixed usage of both models in current literature [55, 56].

2.5 THEORETIC BACKGROUND OF ELECTRON DIFFRACTION

In the transmission electron microscope (TEM), different types of interactions between the incident electrons and the specimen can occur, with elastic and inelastic scattering as prominent examples. Elastic scattering occurs usually to low angles from 1° to 10°. For thin and crystalline specimens, elastic scattering is coherent in most cases, whereas coherence can be lost for high scattering angles [57]. Inelas-

tic scattering mostly occurs to low angles $< 1°$ and is usually incoherent. Inelastic scattered electrons lost energy due to interactions with the atoms in the specimen, e.g. *via* plasmonic or electronic excitation. The following theoretical description focuses on elastic scattering which dominates the formation of the investigated diffraction patterns recorded in the TEM.

As displayed in Figure 2.6a, a wavefront normal defined by incident electrons is named $\mathbf{k}_0$, the diffracted wavefront normal is $\mathbf{k}_1$, and the difference or scattering vector is defined as $\mathbf{q}$. Furthermore, $|\mathbf{k}_0| = |\mathbf{k}_1| = 2\pi/\lambda$ since elastically scattered electrons do not lose energy. Geometric considerations yield $|\mathbf{q}| = 2|\mathbf{k}_0|\sin(\Theta/2)$, where Θ is defined as the angle between scattered and incident electron beam. To account for the phase difference between scattered waves, the structure factor $\mathbf{F}(\Theta)$ can be introduced:

$$\mathbf{F}(\Theta) = \sum_j f_j(\Theta)\exp(-i\mathbf{q}\cdot\mathbf{r}_j)\,. \tag{2.14}$$

Here, f_j is the scattering factor and $\mathbf{r}_j$ the coordinate of atom j. The phase factor is given by $\mathbf{q}\cdot\mathbf{r}_j$ and the sum is derived for all atoms in one unit cell [58]. An alternative expression of $\mathbf{F}(\Theta)$ illustrates that the structure factor is closely related to the Fourier transform of the lattice potential:

$$\mathbf{F}(\Theta) \propto \int V(r)\exp(-\mathbf{q}\cdot\mathbf{r})\,d\tau\,. \tag{2.15}$$

The integral is carried out over all volume elements within the unit cell and $V(r)$ is the scattering potential [58]. $|\mathbf{F}(\Theta)|^2$ gives the intensity for a wave scattered with the angle Θ relative to the incident beam. It is maximum where the scattered waves are in phase, which can be visualized analogue to classical optics with Bragg's law. Figure 2.6b shows a schematic where atoms are arranged in the planes P_1 and P_2 and incident electrons are scattered elastically from three exemplary points A, B, C on these planes. The condition for a constructive interference is that the path difference due to scattering at two different points equals $n\lambda$, where n is an integer and $\lambda = 2\pi/|k_0|$ the wavelength of incident electrons [57]. With the incident angle $\Theta/2$ and the inter-plane distance d, Bragg's law can be derived to

$$2d\sin\left(\frac{\Theta}{2}\right) = n\lambda\,. \tag{2.16}$$

It defines the conditions for which diffracted electron wavefronts interfere constructively, which can be detected in the experiment. The incident angle $\Theta/2 = \Theta_B$ that fulfills Equation 2.16 is termed Bragg angle.

An alternative approach can be given with the Laue equations. In this description, the vectors $\mathbf{a}$, $\mathbf{b}$, and $\mathbf{c}$ are the unit-cell translations

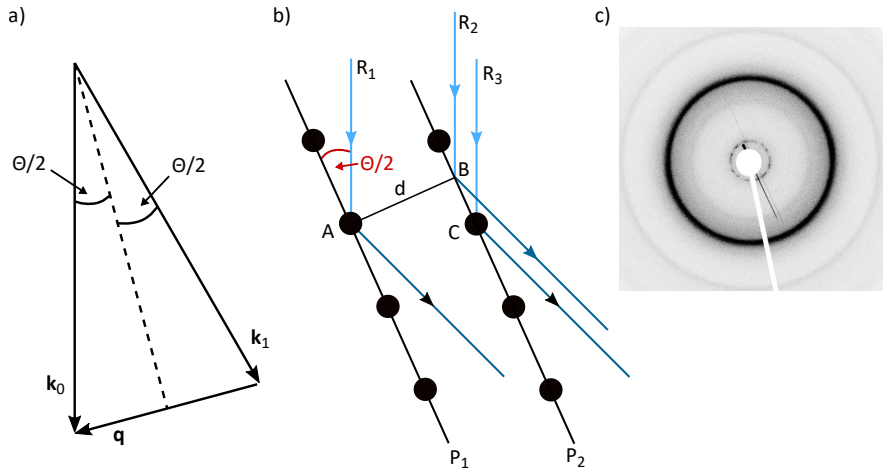

Figure 2.6: a) Illustration of the incoming wavefront normal $\mathbf{k}_0$, the diffracted wave normal $\mathbf{k}_1$, scattered by the angle Θ, and the scattering vector $\mathbf{q}$. b) Incident electrons scatter from points A, B, and C on the two planes P_1 and P_2. The path difference for scattering from A and B equals the path difference for scattering from points A and C and is $2d\sin(\Theta/2)$. c) False-color electron diffraction pattern of a polymer composed of randomly oriented small crystallites, showing Debye-Scherrer rings.

of the lattice in real space. The scattering vector $\mathbf{q}$ then must satisfy the Laue equations to yield constructive interference:

$$\mathbf{q} \cdot \mathbf{a} = h \tag{2.17a}$$

$$\mathbf{q} \cdot \mathbf{b} = k \tag{2.17b}$$

$$\mathbf{q} \cdot \mathbf{c} = l\,. \tag{2.17c}$$

Here, (hkl) are called Miller indices and must be integer numbers. They, together with the reciprocal unit-cell translational vectors $\mathbf{a}^*$, $\mathbf{b}^*$, and $\mathbf{c}^*$ define the reciprocal lattice where

$$\mathbf{g} = h\mathbf{a}^* + k\mathbf{b}^* + l\mathbf{c}^* \tag{2.18}$$

is the reciprocal lattice vector. Bragg's law and the Laue conditions are equivalent and both approaches can be transformed into each other mathematically [44, 57].

2.5.1 *Diffraction of Polycrystalline Materials*

For wavefronts of electrons scattered from one single crystal, discrete spots at positions in reciprocal space where constructive interference occurs show up in the recorded diffraction pattern. The distance from the center and the position in reciprocal space which is imaged by a diffraction measurement correspond to stacking distances and orientation of the crystal [57, 59]. Many crystallites with random orientations that are distributed within the illuminated volume of the sample

cause diffraction spots distributed randomly in azimuth angle (horizontal angle, in the plane of detection). For a number of crystallites large enough or the size of the crystallites small enough, the entirety of diffraction spots forms Debye-Scherrer rings, exemplary shown in Figure 2.6c for the semi-crystalline polymer P3HT. Each combination of hkl with non-zero structure amplitude F forms one ring [59]. The integrated intensity of a total ring with Miller indices hkl can be expressed as

$$I_{hkl} = j_s \frac{2\pi^2 m^2 e^2}{h^4} KNV_e p_{hkl} |V_g|^2 \exp(-2M_g) \lambda^2 d_{hkl}\,, \qquad (2.19)$$

where j_s is the electron current density in the specimen plane, K the number of crystallites with an average of N unit cells, each of volume V_e. p_{hkl} is the multiplicity of planes with the specific hkl values. V_g gives the so-called lattice potential that is decreased by the Debye-Waller factor $\exp(-2M_g)$ due to thermal vibrations of the nuclei and hence the lattice [59]. Equation 2.19 shows that the intensity of the Debye-Scherrer rings depends on the absolute number of unit cells ($K \cdot N$) the electron beam passes through, but not on the dimensions and shape of the single crystals. However, this only applies to randomly oriented crystals and the ring intensities can change if a preferential orientation (texture) is apparent. Additionally, the so-called shape effect that describes the peculiarities of diffraction from small volumes leads to a broadening of the diffraction spots of each crystallite and hence to a broadening of the observed rings [60].

2.6 IONIC-ELECTRONIC DRIFT AND DIFFUSION

In Part II of the results and discussion of this thesis, the diffusion and drift of dopant molecules is investigated. The following provides the theoretic background that describes the motion of (charged) dopant molecules as ions in addition to the electronic currents of electrons and holes. In this basic consideration, the charged host molecules or parts of a polymer chain are assumed to be spatially stable.

The Poisson equation links the distribution of electrostatic potential $\phi(x)$ to the local charge density with

$$\epsilon_0 \epsilon_r \Delta\phi(x) = -ep(x) + en(x) + ef_i(x)N_i(x)\,. \qquad (2.20)$$

Here, $p(x)$ and $n(x)$ are hole and electron densities, $f_i(x)$ an ionization factor, and $N_i(x)$ the ion (dopant) concentration [61]. The charge q on the dopant in the case of p-type doping is negative and hence $-e$. An electric field can be generated by internal charge density variation and an external potential. Such an electric field E in the simplest case leads to a drift of ions according to $v_i = \mu_i E$ with the drift velocity v_i

and the drift mobility μ_i. The ion drift current density is then given by

$$\mathbf{J}_{\text{drift}} = -eN_i\mu_i\mathbf{E} = qN_i\boldsymbol{\nu}_i\,. \tag{2.21}$$

In addition to the drift current described in Equation 2.21, a contribution of ion diffusion adds to the total ion current density. According to Fick's first law, the diffusion current density depends on the diffusion constant D_i and the gradient of the ion concentration [7]. Both contributions add up to the total ion current density

$$\mathbf{J}_{\text{ion}}(x) = eD_i\nabla N_i(x) + eN_i(x)\mu_i\nabla\phi(x)\,. \tag{2.22}$$

The diffusion constant D_i and ion mobility μ_i are coupled *via* the Nernst-Einstein equation [7]. A short discussion if this equation holds true in the system investigated here is given in Section 11.1.3. Analogue considerations hold for the currents of electrons (n) and holes (p)

$$\mathbf{J}_{n,p}(x) = \mp eD_{n,p}\nabla N_{n,p}(x) \pm eN_{n,p}(x)\mu_{n,p}\nabla\phi(x)\,. \tag{2.23}$$

The ion flux as well as electron and hole flux are furthermore characterized by the continuity equation [7]

$$\frac{\partial N_i(x)}{\partial t} = \frac{1}{e}\nabla\cdot\mathbf{J}_i(x) \tag{2.24a}$$

$$\frac{\partial p(x)}{\partial t} = -\frac{1}{e}\nabla\cdot\mathbf{J}_p(x) \tag{2.24b}$$

$$\frac{\partial n(x)}{\partial t} = \frac{1}{e}\nabla\cdot\mathbf{J}_n(x)\,. \tag{2.24c}$$

In these equations, it is assumed that all dopant molecules are ionized and independent of the counter-charge they generate. One possible extension would be the addition of generation and recombination rates to introduce a doping efficiency below 100 % that could change with conditions such as the electric field or temperature. This addition would then be necessary for the continuity equation of ions and holes since one ionized dopant ideally corresponds to one free charge carrier, which is a hole in case of p-doping.

2.7 THE MEMRISTOR & MEMRISTIVE SYSTEM

The following gives a brief introduction to the concept of the ideal memristor proposed theoretically by Chua in 1971 and extends the description to memristive systems in general.

2.7.1 *The Ideal Memristor*

The four circuit parameters relevant for electronic theory and application are charge Q, current I, voltage V, and magnetic flux Φ. Two relations link the charge to the current and the flux to the voltage:

$$\begin{aligned} \frac{dQ}{dt} &= I \\ \frac{d\Phi}{dt} &= V\,. \end{aligned} \tag{2.25}$$

Furthermore, charge, voltage, current, and flux are known to be related *via* the following equations:

$$\begin{aligned} \frac{dV}{dI} &= R \\ \frac{dQ}{dV} &= C \\ \frac{d\Phi}{dI} &= L\,. \end{aligned} \tag{2.26}$$

Here, R is the resistance, C the capacitance, and L the inductance. However, a possible connection between flux Φ and charge Q was not discussed until Chua in 1971 proposed the following relation:

$$\frac{d\Phi}{dQ} = M\,. \tag{2.27}$$

M is defined as memristance, which is the characteristic property of a theoretically proposed device called memristor [62]. It is displayed in Figure 2.7a as fourth fundamental circuit element, since its properties cannot be reproduced by a combination of resistors, capacitors, and inductors. A memristor is a nonlinear element and behaves like a resistor which changes the resistance with the charge flowing through it. Due to the ability to keep the resistance it had due to the charge flow history, Chua gave it a name that combines memory and resistor: the memristor. Having been proposed already in 1971, a team from the Hewlett-Packard Labs described the practical realization of a device that behaves like a memristor in 2008 [63]. From that point on, memristors gained attention and more and more devices were published as memristors. However, the claim that the perfect memristor was realized and the question if a practical realization in the strict description of 1971 is possible at all is under debate [64]. Due to this inconsistency in literature, the term *ideal memristor* is used for the device originally proposed in 1971, whereas *memristor* and *memristive device* is used for the extended description of memristive devices that Chua gave in 1976 [65].

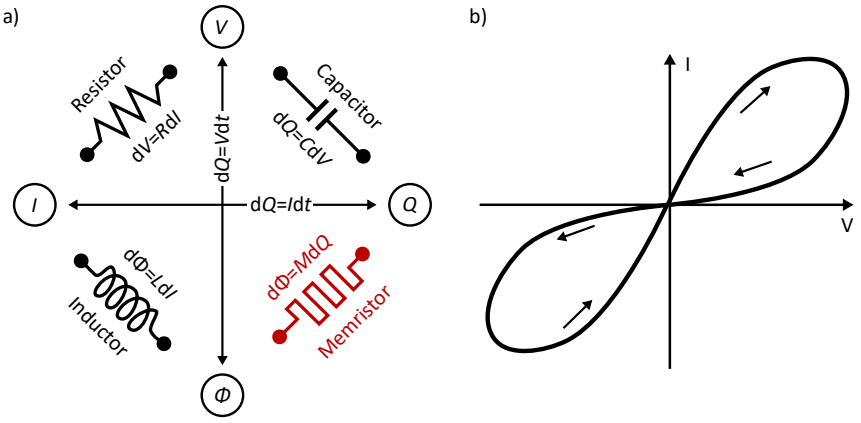

Figure 2.7: a) Connections between the four circuit parameters voltage V, charge Q, magnetic flux Φ, and current I, linked by the fundamental curcuit elements resistor, capacitor, inductor, and memristor. Resistors and memristors are part of the broader class of memristive systems. b) A current-voltage curve with large hysteresis and zero current at zero voltage is characteristic for a voltage-controlled memristive system.

2.7.2 *Memristive Systems*

The ideal memristor is part of the broader class of memristive systems, which are generally defined by

$$\begin{aligned} \dot{x} &= f(x, u, t) \\ y &= g(x, u, t) \cdot u \,. \end{aligned} \tag{2.28}$$

In these equations, u denotes the input, y the output, and x the state of the system [65]. The multiplication of the scalar function g with the input is what defines the special property of memristive systems: The output y at zero input is always zero, regardless of the state x. The case that is investigated in this thesis can be identified as a voltage-controlled memristive one-port device [65]:

$$\begin{aligned} \dot{x} &= f(x, V, t) \\ I &= G(x, V, t) \cdot V \,. \end{aligned} \tag{2.29}$$

Here, V and I are the voltage and current, respectively, and G denotes the conductance. The second part of Equation 2.29 defines that in such systems, the input-output Lissajous figure (in this case, the I-V curve for a sweep between two boundaries) always passes through the origin as depicted in Figure 2.7b. Another property of the system is a dependence on the excitation frequency ω. The higher ω, the narrower the Lissajous figure gets, until it approaches a straight line through the origin [65]. Hence, the hysteretic effect decreases with a frequency increase until the properties resemble that of a solely resistive system. Systems like temperature-dependent resistors or the

Hodgkin-Huxley circuit model of the nerve axon membrane can be described as current- or voltage-controlled memristive systems with this approach [65].

3

EXPERIMENTAL TECHNIQUES

This chapter provides an introduction to the experimental techniques used throughout this thesis and introduces the main modes of operation that are relevant for shown measurements. In addition, relevant measurement parameters are listed and explained. The TEM and spatially resolved IR spectroscopy measurements were performed at Heidelberg University, while all other measurements were carried out at the InnovationLab in Heidelberg. The InnovationLab is a joint platform with competences ranging from fundamental research to simulations, device physics, and application-driven development in the context of organic and hybrid printed electronics.

3.1 TRANSMISSION ELECTRON MICROSCOPY

The transmission electron microscope (TEM) used for all measurements presented in this thesis is a *Carl Zeiss Libra 200 MC Cryo DMU (Kronos)*. It is equipped with a field-emission gun, in which electrons are extracted by an applied voltage, marked as *Source* in Figure 3.1a. In this TEM, the extracted electrons can be accelerated with 60 kV or 200 kV acceleration voltage, whereas all measurements within this thesis were performed in the 60 kV mode. Between source and condenser system, the TEM is equipped with a monochromator that allows for a narrowing of the energy and hence wavelength bandwidth of electrons, thus creating a more coherent beam [57]. This is especially useful for high-resolution electron energy loss spectroscopy (EELS) and electron spectroscopic imaging (ESI). In the condenser system, electromagnetic lenses focus the beam to the front focal plane of the objective (specimen position) in case of imaging and the back focal plane of the objective in case of diffraction [66]. After interaction with the specimen and passing objective lenses, the electron beam enters further electron-optical systems, summarized as *Final Imaging System* in Figure 3.1a. The TEM used for measurements within this thesis is equipped with a C_s corrector that corrects for spherical aberration and an ω energy filter which allows for an energy resolution down to $70-90$ meV at 60 kV acceleration voltage. The image or diffraction pattern can finally be recorded with a camera (TemCam F416, TVIPS GmbH, Germany). The whole beam path from source to camera is kept under vacuum to exclude any interaction of the electron beam with particles or atoms in the beam path excluding the specimen. For the measurements presented in Chapter 6, a two-axis tilt sample holder was used that could also be used for electron tomography. For

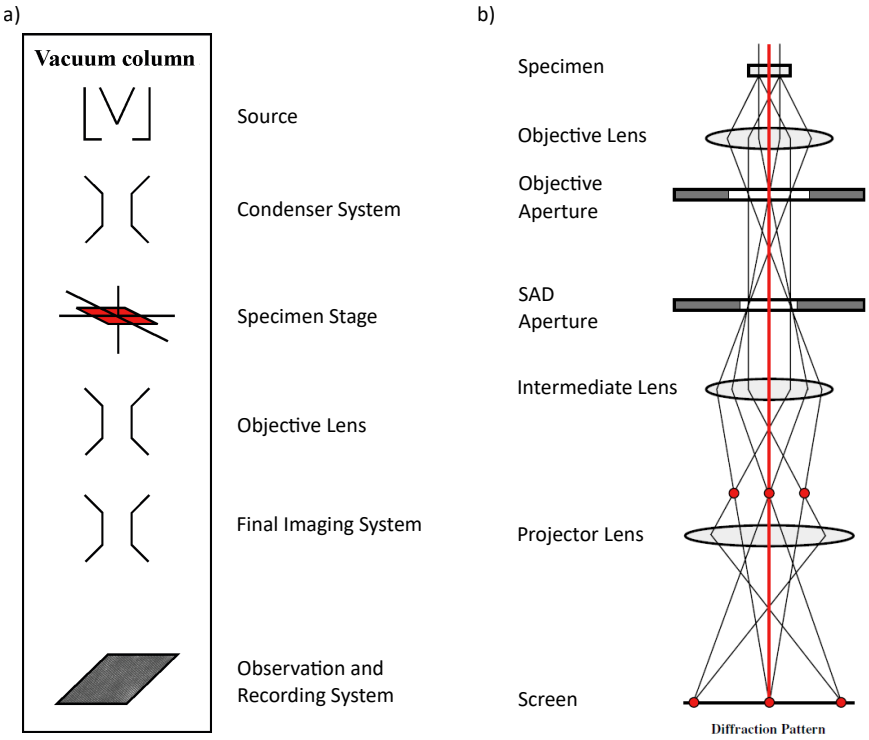

Figure 3.1: a) The basic setup of a transmission electron microscope. b) Beam path illustrated for the case of diffraction. To obtain a diffraction pattern on the screen or camera, the imaging system must be focused on the back focal plane of the objective, which corresponds to the first image plane for the electron diffraction pattern. SAD: selected area diffraction. (a,b) are reprinted with permission from [66], Copyright 2008 by John Wiley Sons, Inc.

these measurements, a dose of ~ 670 electrons per nm^{-2} was applied. For all other measurements, a cryo sample holder in which the sample is cooled with liquid nitrogen to minimize beam-induced damage in the specimen was used and a dose of up to ~ 1800 electrons per nm^{-2} was applied. All TEM images and electron diffraction patterns shown in this thesis were measured directly after sample preparation in a glovebox at the InnovationLab and transport to the TEM which is located at Heidelberg University.

3.1.1 *Electron Diffraction*

Figure 3.1b shows the electron beam path for the case of diffraction. After passing the sample, the electron beam is focused to the back focal plane of the objective (diffraction plane) at which the selected area diffraction (SAD) aperture is located. It can be used to select specific parts of the image that are particularly interesting for diffraction measurements. Depending on the TEM, several electron-

optical components like lenses or stigmators follow until the screen or camera is reached where the diffraction pattern is displayed or recorded [66]. One important measurement parameter is the camera length (CL) which defines the magnification of the diffraction pattern on the screen or camera. It is adjusted with electromagnetic lenses. Calibration of the TEM for electron diffraction for the measurements presented in this thesis was done with polycrystalline gold for which the (111)-orientation shows a spacing of 2.35 Å. Due to inelastic scattering, a halo can occur around single diffraction spots [58]. Filtering the electrons that lost energy due to the inelastic scattering hence leads to sharper Bragg spots and less background between the single spots. This procedure is called zero-loss (ZL) filtering, since only elastically scattered electrons or electrons that did not interact with the specimen at all arrive at the camera [58]. Electron diffraction patterns presented in this thesis were measured with exposure times between 500 ms and 1000 ms. Diffraction patterns with varying exposure times were compared to exclude artifacts from beam damage. Diffraction patterns were evaluated with the Fiji distribution of

	CA [µm]	CL [mm]	Illu	MC [µm]	ZL	Mag
P3HT & P3HTrra	15	225	8	no	yes	89×10^3
P3HT:Mo	15	225	8	no	yes	89×10^3
P3HT:F4	37.5	288	13	2	yes	89×10^3

Table 3.1: Measurement parameters for electron diffraction measurements. CA: condenser aperture, CL: camera length, Illu: level of illumination, MC: monochromator aperture, ZL: zero-loss filtered, Mag: magnification. P3HT:Mo and P3HT:F4 represent the measurements on doped thin films of P3HT:Mo(tfd-CO_2Me)$_3$ and P3HT:F_4TCNQ, respectively.

ImageJ [67]. To increase the signal-to-noise ratio, radial integration over parts of the spectrum was performed, whereas deviations from the ideal perfectly round diffraction patterns were considered in calibration as well as the evaluation of peak positions. Table 3.1 lists the relevant measurement parameters for diffraction profiles shown in Chapter 5 (P3HT & P3HTrra), Chapter 7 (P3HT:Mo(tfd-CO_2Me)$_3$), and Chapter 6 (P3HT:F_4TCNQ).

3.1.2 *Bright-Field Mode*

If the transmission electron microscope is operated in the imaging mode, the objective aperture and a beam tilt can be utilized to obtain different kinds of contrast. If the objective aperture is small enough to limit the angle of acceptance α to smaller values than the Bragg

angle Θ for all scattered electrons, a *bright-field shadow projection* is obtained, imaging only the intensity variations of the electron beam current transmitted by the specimen [66]. A *dark field* image can be obtained by tilting the beam in a Bragg angle so that not the directly transmitted beam is imaged but specific coherently scattered electrons. For an aperture that allows for acceptance angles $\alpha > 2\Theta$, interference patterns resulting from electron path length differences add to the bright-field image. This phase contrast depends on several factors such as the (chromatic and spherical) aberration coefficient of the microscope, the focus, and more [66].

To understand the phase contrast that dominates image formation for carbon-based organic materials, the specimen or object investigated can be described as a number of point sources. $f(r)$ (in radial coordinates) describes the electron wave distribution in the object plane with $g(r)$ representing the phase and amplitude of $f(r)$ in the image plane at the end of the beam path. $g(r)$ can be described as the convolution of $f(r)$ with a point-spread function $h(r)$:

$$g(r) = \int f(r')h(r-r')\,dr' = f(r) \times h(r-r')\,. \tag{3.1}$$

$h(r)$ defines how the electron wave distribution function $f(r)$ is altered between each object point and any image point. This describes the contribution of the microscope column the electron beam passes before it is recorded in the image plane. In reciprocal space, g(r) is given by a Fourier transform

$$g(r) = \sum (G(\mathbf{u}) \exp(2\pi i \mathbf{u}\cdot\mathbf{r}) \text{ with } G(\mathbf{u}) = H(\mathbf{u})F(\mathbf{u})\,. \tag{3.2}$$

$F(\mathbf{u})$ and $H(\mathbf{u})$ are defined as the Fourier transform of $f(r)$ and $h(r)$, respectively. $H(\mathbf{u})$ is termed contrast transfer function (CTF) and describes the properties of the electron microscope that define the phase shift of an electron wave propagating through the microscope column. It can be written as a product of the contribution of apertures $A(\mathbf{u})$, the attenuation $E(\mathbf{u})$, and the aberration of lenses $B(\mathbf{u})$:

$$H(\mathbf{u}) = A(\mathbf{u})E(\mathbf{u})B(\mathbf{u})\,. \tag{3.3}$$

The aberration function $B(\mathbf{u})$ contains the underfocus of the objective lens, the wavelength, and the spherical aberration coefficient of the objective lens C_s. The objective aperture can hence be used to reduce the error in C_s by limiting the acceptance angle α.

3.2 UV-VIS SPECTROSCOPY

Optical absorption spectroscopy in the visible and ultraviolet (UV) spectral range was performed with the *AvaSpec-ULS3648* spectrometer. With a halogen light source (*AvaLight-DH-S-BAL*) for the visible and a deuterium lamp that emits in the UV, a wavelength range

from 200 nm to 1100 nm is covered. The spectra presented in this thesis for thin films and solutions were measured in the transmission mode. Since the measurement setup is located outside the glovebox, all samples were transferred to ambient conditions directly before the measurements.

The attenuation of light in an absorbing substance can be described with the Lambert-Beer law as

$$E_\lambda = \lg\left(\frac{I_0}{I_1}\right) = \epsilon_\lambda \cdot c \cdot z\,, \tag{3.4}$$

where E_λ is the molar attenuation coefficient, ϵ_λ the extinction coefficient at a wavelength λ, c is the molar concentration, and z the penetration depth [34]. An alternative formulation describes the intensity I at a certain penetration depth z as

$$I(z) = I_0 \cdot e^{(-\alpha z)} = I_0 \cdot \exp\left(-2n''\frac{\omega}{c}z\right), \tag{3.5}$$

where $\alpha = 2n''\omega/c$ is the absorption coefficient, n'' the extinction coefficient, ω the angular frequency of the probing light, c the speed of light, and I_0 the initial intensity.

Effects that introduce errors to the measurements are reflections and scattering to angles larger than the collection angle. These light beams are not detected. For strongly scattering and reflecting samples, an integrating sphere that allows for the detection of all contributions is hence desired. The measurements presented in this thesis were performed without such a sphere. However, the samples investigated did not strongly reflect or scatter which minimizes the error.

3.3 INFRARED SPECTROSCOPY

With the energy of photons in the mid-IR range, bonds in organic molecules can be excited. Such vibrations represent fingerprints of the molecules and their dielectric background and can hence be used to identify molecular species. In addition to molecular vibrations, states in the bandgap of charged polymers can be electronically excited in this spectral region. Since the infrared (IR) spectroscopy measurements presented in this thesis were performed together with or by members of the group of Professor Pucci from the Kirchhoff-Institute for Physics, the following gives only a brief introduction to the measurement principles and setup that was used. A detailed description can be found in [68].

All IR spectra in this thesis except of the spatially resolved ones were measured with the *Vertex 80v* Fourier transform infrared (FTIR) spectrometer from Bruker which can record spectra at wavelengths between 2.5 µm to 5 µm corresponding to 200 cm^{-1} to 4000 cm^{-1}. This spectrometer has a sample chamber into which samples are transferred from ambient conditions and measured at a pressure of 4 mbar.

Alternatively, samples can be measured in a UHV chamber which is connected to the spectrometer. This was necessary only for the measurements shown in Chapter 7 (Figure 7.2). The measurement setup is based on a Michelson interferometer, which uses a beam splitter and a movable mirror to induce a path length difference Δx between transmitted and reflected beam that leads to interference of both beams. Figure 3.2 illustrates the beam path in the spectrometer. In the following, a short derivation illustrates how the interferogram $I(\Delta x)$ is linked to the spectral intensity $I(\tilde{\nu})$.

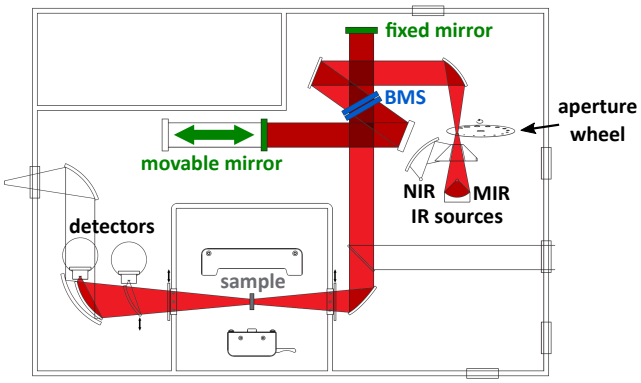

Figure 3.2: Beam path in the *Vertex 80v* spectrometer. The beam splitter and mirror system represent the Michelson interferometer. Adapted from [68].

The measured intensity is defined by $I(\Delta x) = |E(\Delta x, t)|^2$ with the amplitude of the electromagnetic wave $E(\Delta x, t)$, which is a combination of the direct beam E_1 and the beam that has a variable path length E_2:

$$E(\Delta x, t) = E_1 + E_2 = \frac{E_0}{2}\left(e^{i(2\pi\tilde{\nu}x-\omega t)} + e^{i(2\pi\tilde{\nu}(x+\Delta x)-\omega t)}\right) . \quad (3.6)$$

Here, E_0 is the field strength of the initial beam, $\tilde{\nu} = \lambda^{-1}$, and ω is the angular frequency of the light. The intensity can then be derived to

$$I(\Delta x) = \frac{E_0^2}{4}\left(1 + \cos\left(2\pi\tilde{\nu}\Delta x\right)\right) \quad (3.7)$$

To obtain the intensity for the whole spectrum, integration over all wavenumbers $\tilde{\nu}$ is performed:

$$\begin{aligned} I(\Delta x, \tilde{\nu}) &= \int_0^\infty I(\tilde{\nu})\left(1 + \cos\left(2\pi\tilde{\nu}\Delta x\right)\right) d\tilde{\nu} \\ &= C + \int_{-\infty}^{\infty} I(\tilde{\nu}) \cos\left(2\pi\tilde{\nu}\Delta x\right) d\tilde{\nu} . \end{aligned} \quad (3.8)$$

In this equation, C denotes a constant and the integral gives the Fourier transform of the spectral intensity $I(\tilde{\nu})$, which yields the desired spectrum:

$$I(\tilde{\nu}) = \frac{1}{2\pi} \int_{-\infty}^{\infty} I(\Delta x) \cos(2\pi\tilde{\nu}\Delta x)\, d\Delta x \ . \tag{3.9}$$

To eliminate influences of the setup and to distinguish between the material that is investigated and the substrate, the recorded spectrum is divided by a reference spectrum of a bare substrate. For the measurements in this thesis except the ones for spatially resolved IR spectroscopy (see next section), silicon was used as substrate and the spectra were measured in transmission.

Spatially Resolved IR Spectroscopy

In a spectrometer like the one described above, the beam spot diameter is on the order of millimeters. For infrared spectroscopy where a spatial resolution down to micrometers is desired, a setup combined of a spectrometer and an infrared microscope can be used. The spatially resolved IR spectra shown in Section 11.1 were recorded with the *Hyperion 100* IR microscope coupled to the *Tensor 27* FTIR spectrometer from Bruker. A custom-made sample holder (described in [69]) allows to bias the electrodes and measure the current flow between them before and after the spectroscopic measurement, which is spatially confined to a small spot in between the electrodes (see Section 4.3.3 for a description of the substrate layout). Optical and IR measurements in this setup are performed in transmission, which requests for transparency in the visible as well as the infrared spectral range. Calcium fluoride (CaF_2) was used for the measurements shown in this thesis. Apertures between 8.3 µm and 104 µm can be chosen to define the spatial resolution. Since a better spatial resolution implies less signal, a trade-off between integration time and spatial resolution has to be found. The measurements in this thesis were performed with an aperture of 21 µm, 250 scans for each spectrum, and a spectral resolution of $4\,cm^{-1}$. During the measurement, the sample compartment is constantly flushed with dry air to ensure stable measurement conditions and no influence of water or residual gases.

3.4 METHODS TO DETERMINE THE CONDUCTIVITY

In the following, the methods two-terminal and four-terminal sensing are introduced. All measurements were performed directly after production of the thin films or devices in an inert N_2 atmosphere and at room temperature.

3.4.1 *Two-Terminal Sensing*

To analyze the current-voltage correlation of a specific material, a device layout comparable to Figure 3.3a with a thin film between two electrodes (in lateral or vertical direction) is usually chosen. The current between the two electrodes depends on the contact resistance R_C which is defined by energy level alignment of electrode and organic semiconductor and the resistance of the organic semiconductor thin film R_{OS}. To obtain meaningful data, $R_C \ll R_{OS}$ must be fulfilled. The conductivity of the organic thin film is then given by

$$\sigma = \frac{1}{\rho} = \frac{d}{A} \cdot \frac{1}{R_{OS}} = \frac{d}{A} \cdot \frac{I}{V}, \tag{3.10}$$

where d is the distance between the electrodes, A the cross-section area, and I the measured current at voltage V. This evaluation only

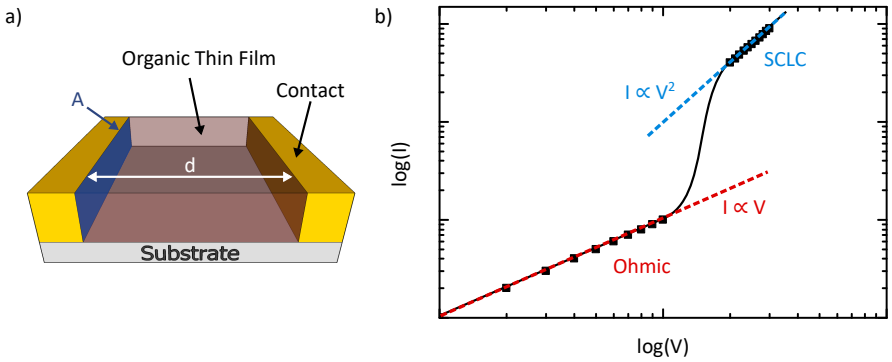

Figure 3.3: a) Schematic illustration of a two-electrode device for current-voltage measurements. b) Current-voltage curve in a double-logarithmic plot with ohmic and SCLC regime.

yields the intrinsic conductivity of the material if the charge transport is in the ohmic regime, where $I \propto V$. For higher voltages, charge injection leads to trap-filling and finally a space-charge-limited current (SCLC), where $I \propto V^2$. Figure 3.3b illustrates the different current regimes. The IV-measurements presented in this thesis are measured with a *Keithley 2636A Sourcemeter*. In cases where $R_C \geqslant R_{OS}$, a four-terminal sensing allows for a measurement of the thin film conductivity, as described in the following.

3.4.2 *Four-Terminal Sensing*

In the thin films investigated in this thesis with thicknesses between 20 nm and 100 nm, the charge transport occurs mostly in lateral direction. Hence, the sheet resistance R_{sheet} is the relevant variable [70] and is defined as:

$$R_{sheet} = \frac{\rho}{t} = \frac{1}{\sigma t} = \frac{1}{q(n\mu_n(n) + p\mu_p(p))t}. \tag{3.11}$$

In this equation, ρ is the electrical resistivity, which is the reciprocal of the electrical conductivity σ. t defines the film thickness, q the charge, and n and p the electron and hole density, respectively. The electron and hole mobility $\mu_n(n)$ and $\mu_p(p)$ can depend on the densities. For the doped layers investigated in this thesis, the p- or n-term is expected to dominate for p- and n-doping, respectively. R_{sheet} is given in units of $\Omega\,\square^{-1}$ to differentiate from the bulk resistance.

One way to measure the sheet resistance is four-terminal sensing. For this technique, four contacts are necessary. A defined current flow is set between two electrodes, whereas the voltage drop over the remaining two electrodes is measured. In this way, the contact resistance is eliminated in the voltage measurement. Since contact resistance can be comparable in magnitude to the resistance of the thin film, this method is superior to two-electrode methods where large errors can be obtained. In principle, the four electrodes can be at random positions with the *van der Pauw* method [71]. The geometry that is used within this thesis is a linear configuration of the electrodes with constant defined distances d between the probes, as shown in Figure 3.4. In this configuration, the sheet resistance is given as

$$R_{sheet} = \frac{\pi}{\ln(2)} \cdot \frac{V}{I}, \tag{3.12}$$

where I is the set current and V the measured voltage. With the sheet resistance and the film thickness, the conductivity can be calculated using Equation 3.11. A *Keithley 2400 Sourcemeter* was used for the four-terminal sensing measurements.

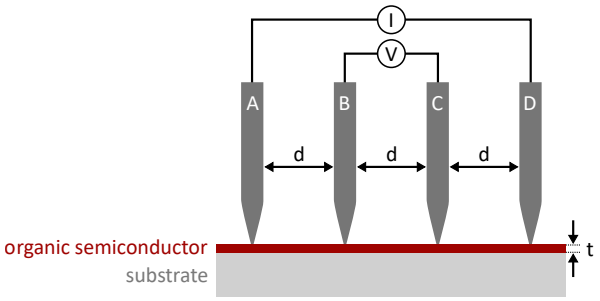

Figure 3.4: Schematic illustration of a four-terminal sensing setup with linearly aligned electrodes in fixed equal distances d and a thin film of thickness t on a not conductive substrate. A defined current flows between electrodes A and D, whereas the voltage is measured between electrodes B and C.

3.5 SCANNING KELVIN PROBE MICROSCOPY

Since the scanning kelvin probe microscopy (SKPM) measurement shown in this thesis was not performed by the author of this thesis,

only a short introduction is given, together with the measurement parameters that were used for the shown measurement. SKPM is a variant of atomic force microscopy (AFM) in which the work function difference of the scanning tip and the sample surface is measured. With knowledge of the work function of the scanning tip, the work function of the surface can be extracted. Furthermore, this method allows for a measurement of the lateral distribution of the surface potential which corresponds to the potential drop induced by an externally applied electric field in the thin-film two-electrode geometry displayed in Figure 3.3a. Details about the measurement principle and setup are given in reference [72]. The measurements shown here were performed in the amplitude-modulated single-pass mode of an ambient atomic force microscope (AFM) from DME (Semilab). A Pt-Ir coated Si-cantilever with a spring constant of $k = 42\,N\,m^{-1}$ and a resonance frequency of 236.5 kHz was mechanically excited with a −30 % offset. The Kelvin probe signal was measured with a frequency offset of 20 kHz at the same resonance. The measurements were carried out in ambient conditions at room temperature.

4

MATERIALS & DEVICE PREPARATION

This chapter provides detailed information about the organic semiconductors and molecular dopants that are used within this thesis. Furthermore, the processing and doping techniques are introduced and details about sample preparation and electrode layouts are given.

4.1 MATERIALS

The following summarizes relevant characteristics of host and dopant materials, such as the energetic positions of HOMO and LUMO levels and the chemical structures.

4.1.1 *Host Materials*

P3HT Poly(3-hexylthiophene-2,5-diyl) is a semi-crystalline polymer with a backbone of linked thiophene units and hexyl side chains attached to it. In this work, three different types of P3HT with varying regioregularity are used as summarized in Table 4.1. The position between the sulfur atom and the alkyl chain is called head, and perfectly regioregular P3HT exhibits only head-tail coupling. The percentage of thiophene units that shows this coupling defines the regioregularity, which determines the degree of structural order that can be formed in thin solid films [18]. Figure 4.1a and b display the chemical structure of perfectly regioregular P3HT with only head-tail coupling and regiorandom P3HT where the coupling is random. The HOMO and LUMO energy levels for regioregular P3HT are positioned at 4.65 eV and 2.13 eV, respectively [73]. For regiorandom P3HT (P3HTrra), a lower-lying LUMO at 5.25 eV was found. The shift compared to regioregular P3HT could possibly be induced by the increased backbone twist [74]. P3HT absorbs in the visible range between 400 nm and 600 nm and is employed in organic photovoltaics (OPV) [18], organic field-effect transistors (OFETs) [75], and thermoelectrics [17]. P3HT was purchased from Merck KGaA (lisicon SP001), P3HTrra from Rieke Metals, and P3HTrr was obtained from BASF SE.

Spiro-MeOTAD N2,N2,N2′,N2′,N7,N7,N7′,N7′-octakis(4-methoxyphenyl)-9,9′-spirobi[9H-fluorene]-2,2′,7,7′-tetramine is a small molecule that forms amorphous thin films [76]. It is used as hole transport material in OLEDs and organic as well as perovskite solar cells [77, 78] and has a LUMO energy of 5.21 eV [79]. Figure 4.1c displays the

	M_w [g mol^{-1}]	Regioregularity [%]	Polydispersity
P3HT	24 320	93.7	2.10
P3HTrr	26 623	96.7	1.75
P3HTrra	57 000	-	2.9

Table 4.1: Characteristic parameters molecular weight M_w, regioregularity, and polydispersity (PD) of the used P3HT.

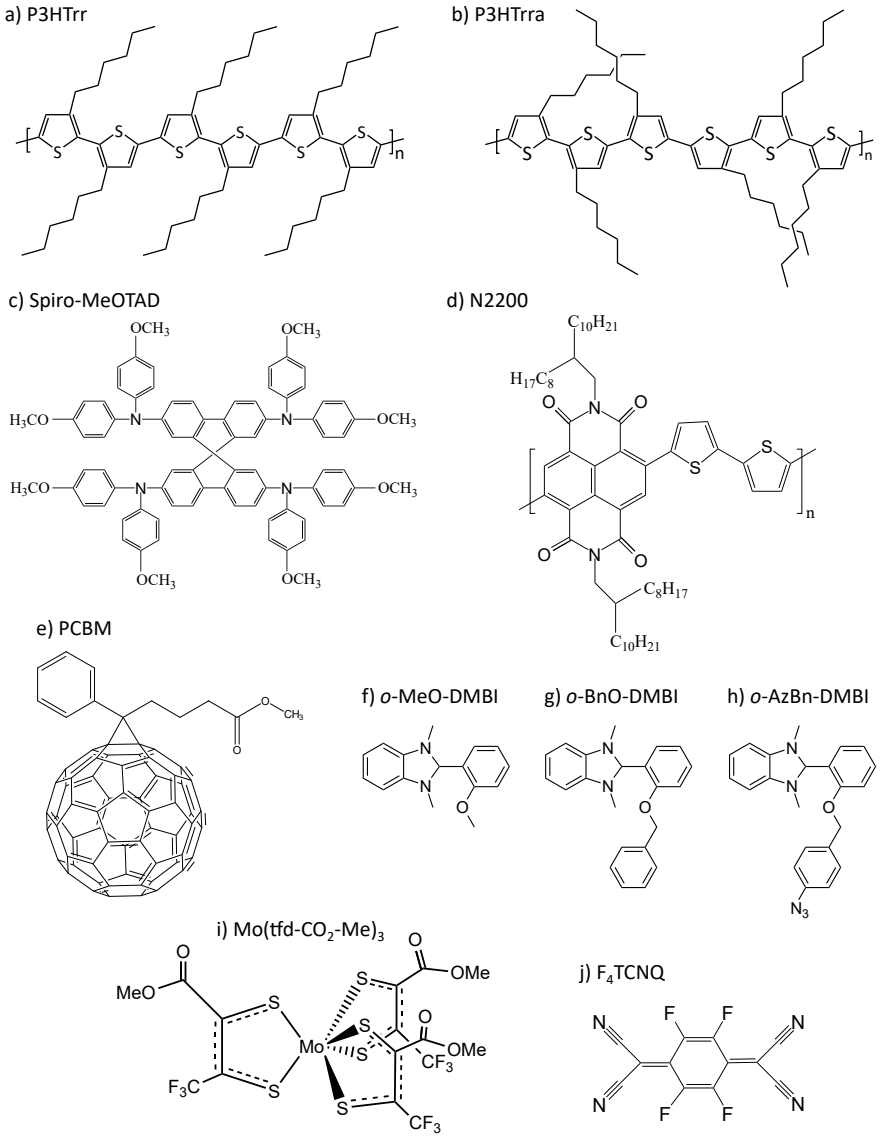

Figure 4.1: Molecular structures of regioregular P3HT (a), regiorandom P3HT (b), Spiro-MeOTAD (c), N2200 (d), PCBM (e), *o*-MeO-DMBI (f), *o*-BnO-DMBI (g), *o*-AzBnO-DMBI (h), Mo(tfd-CO_2Me)$_3$ (i), and F_4TCNQ (j).

molecular structure. Spiro-MeOTAD was purchased from Luminescence Technology Corp. (Lumtec).

N2200 poly([N,N′-bis(2-octyldodecyl)-1,4,5,8-naphthalenedicarboximide-2,6-diyl]-alt-5,5′-(2,2′-bithiophene)), also named P(NDI2OD-T2) is a semi-crystalline electron-transporting polymer. It is used in n-channel transistors due to a high charge carrier mobility, stability at ambient conditions, and good solubility that allows for printing [80]. LUMO and HOMO values are 3.91 eV and 5.36 eV, respectively [81]. Figure 4.1d shows the chemical structure. N2200 was purchased from Polyera Corporation with a molecular weight of 31.8 $kg\,mol^{-1}$ and a polydispersity of 2.3.

PCBM Phenyl-C_{61}-butyric acid methyl ester is a solution processable fullerene derivative which is often used as electron acceptor material in organic photovoltaics [18]. Due to the three-dimensional symmetry, the charge transport is isotropic which eases processing. The LUMO and HOMO values are 4.3 eV and 6.1 eV [82] and the molecular structure is displayed in Figure 4.1e. PCBM was purchased from American Dye Source, Inc.

4.1.2 *P-Dopants*

F_4TCNQ 2,3,5,6- tetrafluoro-7,7,8,8- tetracyanoquinodimethan is a commonly used p-type dopant with low-lying LUMO level of 5.24 eV [83]. It can be thermally evaporated and solution-processed. However, the solubility in common solvents like chlorobenzene is limited to $\approx 0.5\,g\,L^{-1}$, but a better solubility in acetonitrile and dichloromethane that do not dissolve P3HT allow for a sequential processing of F_4TCNQ on top of P3HT [24, 25]. F_4TCNQ was purchased from Sigma-Aldrich and the chemical structure is displayed in Figure 4.1j.

Mo(tfd-CO_2Me)$_3$ Molybdenum tris[1-(methoxycarbonyl)-2-(trifluoromethyl)- ethane-1,2-dithiolene] is a derivative of the usually thermally evaporated dopant Mo(tfd)$_3$ and is well soluble in solvents like chlorobenzene or chloroform [84]. Furthermore, it can still be thermally evaporated, allowing for a comparison of differently doped thin films. The LUMO of Mo(tfd-CO_2Me)$_3$ is positioned at 5.0 eV [84] and the chemical structure is shown in Figure 4.1i. The Mo(tfd-CO_2Me)$_3$ used in this thesis was synthesized by Yadong Zhang.[1]

1 Yadong Zhang is part of the group of Prof. S. Marder at the Center for Organic Photonics and Electronics and the School of Chemistry and Biochemistry at the Georgia Institute of Technology, USA.

4.1.3 *N-Dopants*

***o*-MeO-DMBI** 2-(2-methoxyphenyl)-1,3-dimethyl-2,3-dihydro- 1H-benzoimidazole is a small molecule that—after hydrogen transfer—is a radical, which is soluble in chloroform and dichloromethane and was shown to efficiently dope for example PCBM [85, 86]. Due to the hydrogen-transfer, the SOMO (singly occupied molecular orbital) energy is relevant and was determined to be 2.53 eV [86]. The chemical structure is shown in Figure 4.1f. All three n-type dopants used in this thesis were synthesized by Simon Benneckendorf.[2]

***o*-BnO-DMBI** 2-(2-(benzyloxy)phenyl)-1,3-dimethyl-2,3-dihydro-1H-benzoimidazole is a chemically modified version of *o*-MeO-DMBI with one benzene ring attached to the oxygen. This modification is intended to not alter the doping properties but to provide a reference that allows for a comparison of *o*-MeO-DMBI to *o*-AzBnO-DMBI. Figure 4.1g displays the chemical structure.

***o*-AzBnO-DMBI** 2-(2-((4-azidobenzyl)oxy)phenyl)-1,3-dimethyl-2,3-dihydro-1H-benzoimidazol is a chemically modified version of *o*-BnO-DMBI, where an azide group (N_3) is attached to the additionally introduced benzene ring. This azide is intended to react with the surrounding host matrix *via* insertion to a C-H-bond to spatially immobilize the dopant molecule [29, 30, 87]. Activation of the azide group can be initiated *via* thermal annealing above 119 °C or by irradiation with UV light at a wavelength of 250 nm.[3] The molecular structure is shown in Figure 4.1h.

4.2 PROCESSING TECHNIQUES

In the following, the processing and doping techniques used for sample-preparation in this thesis are explained and used parameters are given. Unless otherwise noted, all samples are produced under inert N_2 atmosphere with O_2 and H_2O concentration below 15 ppm and 25 ppm, respectively.

4.2.1 *Spin Coating and Drop Casting*

The thin films characterized in this thesis were produced with the spin coating technique, in which a certain amount of material, dissolved in a solvent of choice, is given on the substrate, which then rotates for a defined time with a certain speed and acceleration. This

2 Simon Benneckendorf is part of the group of Prof. Bunz at the Institute of Organic Chemistry (OCI) at Heidelberg University.

3 Concluded from thermogravimetric analysis and UV-Vis absorption spectroscopy carried out by Simon Benneckendorf.

technique can yield well-defined thin films down to a few nanometers in thickness, whereas the parameters velocity, acceleration, and duration depend on the material, solvent, and final film thickness that is aimed at. Typical spin coating parameters to get films of 50 nm thickness for P3HT dissolved in chlorobenzene at 13.6 g L^{-1} are 1200 rpm, 600 rpm s^{-1}, and 30 s for velocity, acceleration, and duration, respectively. The films of around 3 µm to 4 µm thickness for the memristive devices shown in Section 11.5 are produced with a drop casting technique, in which a defined amount of dissolved material is given onto the substrate where the solvent evaporates and a solid film forms. To minimize unwanted drying effects, the sample is placed on a spin coater which rotates at 50 rpm while drying.

4.2.2 *Blend Doping*

Doping from blend solutions of host and dopants is the standard technique to obtain solution-processed doped thin films. Host and dopant are first dissolved separately in the same solvent. For the p-doped materials in this thesis, chlorobenzene or chloroform was used in which the materials were stirred at 50 °C for several hours on a hotplate until the materials are perfectly dissolved. Then, both solutions are mixed with defined amounts to yield the desired doping ratio. The blend solutions for this work were stirred again for 3 h prior to spin coating. Note that the stirring time and temperature can influence the dopant-host interaction in solution [88, 89].

4.2.3 *Sequential Doping*

In this thesis, two sequential doping techniques are used: a sequential doping from solution and sequential doping by thermal evaporation of the dopant in vacuum. Both methods are introduced in the following.

4.2.3.1 *Sequential Doping from Solution*

In this technique, a thin film of the host material is produced first. In a second step, the dopant, dissolved in an orthogonal solvent which does not dissolve the host film is spin cast onto the host. For a sequential doping of P3HT, for example acetonitrile or dichloromethane can be used. Recent literature suggests that the solvent swells the amorphous parts of P3HT, but not the crystallites [22]. However, the necessity for a swelling is questioned in Chapter 7 of this thesis where it is shown that evaporated dopants can also diffuse into P3HT and comparably dope it without any solvent present. Prior to the sequential deposition, the dopants are dissolved in a concentration of 1 g L^{-1} in acetonitrile and stirred for a few minutes. It is then given onto

the P3HT thin film where it resides for 5 s before spin coating with 1000 rpm and 1000 rpm s^{-1} for 30 s.

4.2.3.2 *Sequential Doping by Thermal Evaporation*

If the dopants are thermally stable, sublimation at elevated temperatures in vacuum can be used to sequentially dope a thin film if the dopant diffuses into the host film. This is given for Mo(tfd-CO_2Me)$_3$ and F_4TCNQ used in this thesis. Mo(tfd-CO_2Me)$_3$ can be evaporated at around 130 °C under vacuum conditions. The thermal evaporation of Mo(tfd-CO_2Me)$_3$ shown in Chapter 7 was performed by Patrick Reiser[4] and Jakob Bernhardt[5]. Due to the low evaporation temperature of around 100 °C of F_4TCNQ in vacuum, it was not thermally evaporated in vacuum conditions. Instead, a vapor doping at ambient conditions as described in [23] was done for measurements shown in Figure A.6.

4.3 SAMPLE PREPARATION

The various measurement techniques require specific sample materials, electrode geometries in case of electrical measurements, or even holey samples in case of transmission electron microscopy. The different requirements and samples are described in the following.

4.3.1 *Samples for TEM Measurements*

To exclude interactions of the transmitted electrons with anything but the the thin film investigated in a transmission electron microscope, it must be free-standing. To achieve this, a carrier film of Poly (3,4-ethylenedioxythiophene) -poly(styrenesulfonate) (PEDOT:PSS) (Heraeus Clevios) which is soluble in water is spin cast onto borosilicate glass substrates. After filtering with a 0.45 µm PTFE filter, PEDOT:PSS is spin coated in a two-step sequence: 1000 rpm and 4300 rpm s^{-1} for 10 s, followed by 4300 rpm and 4300 rpm s^{-1} for 30 s. To get rid of water residues, the PeDOT:PSS thin film is thermally annealed on a hotplate at 130 °C for 30 min and transferred into a glovebox. The organic thin film of interest is then spin coated onto the PEDOT:PSS. After processing, the organic thin film is floated on deionized water, which dissolves the underlying PEDOT:PSS. The film is then skimmed with a copper grid (200 mesh) which is coated with a holey carbon film (QUANTIFOIL 3.5/1). Prior to the skimming, the grids are treated with argon plasma for 10 s to make them hydrophilic. The copper

4 Materials Science Department, Surface Science Division, TU Darmstadt
5 Kirchhoff Institute for Physics, Heidelberg University

grid and an electron microscopy image of the holey carbon film are shown in Figure 4.2e and f.[6]

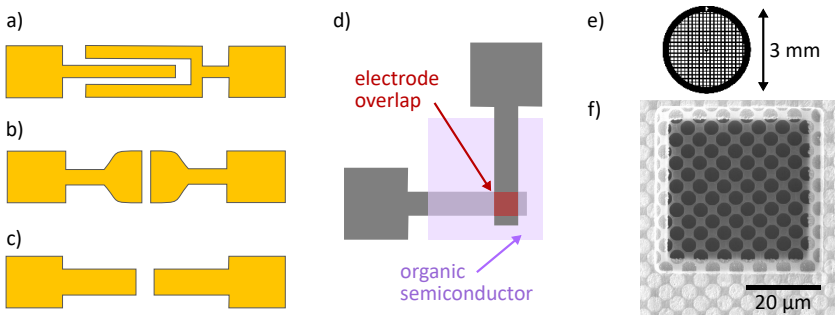

Figure 4.2: a, b) Electrode structures for IV-measurements with varying channel lengths between 10 µm and 240 µm. c) Electrode structure for spatially resolved IR spectroscopy measurements. The channel length is 140 µm. d) Electrode structure for vertical memristive devices. The electrode overlap defines the active area and is 1 mm^2. e, f) TEM copper grid and electron microscope image of holey carbon film on the grid.

4.3.2 *Samples for IV-Measurements*

Current-voltage measurements were conducted with two-electrode structures shown in Figure 4.2a and b. For p- and n-doping, gold and silver was used as electrode material, respectively, to minimize barriers due to an energy-level mismatch. The electrodes were thermally evaporated to thickness of 60 nm. As substrate, borosilicate glass (Borofloat 33, Schott) with a roughness of < 2 nm was used. Four-point probe measurements were conducted on thin films that were spin coated onto bare borosilicate glass substrates of size 2.5 cm $\times$ 2.5 cm.

4.3.3 *Samples for IR Spectroscopy*

Thin films for IR spectroscopy were spin coated onto intrinsic silicon of 1 mm thickness since silicon is transparent in the IR spectral range of interest. For spatially resolved IR spectroscopy, CaF_2 was used as substrate material to allow for simultaneous optical microscopy and IR spectroscopy in transmission mode. Since an electric field must be applied to observe electric-field-induced drift of dopants (see Chapter 11), gold electrodes of 60 nm thickness displayed in Figure 4.2c were thermally evaporated onto the CaF_2 substrate. Spatially resolved IR spectra were recorded in the channel of the electrodes.

6 Images from http://www.quantifoil.com, accessed on 11/15/2017.

4.3.4 *Samples & Solutions for UV-Vis spectroscopy*

Thin films for UV-Vis measurements were spin coated onto bare borosilicate glass substrates and measured under ambient conditions in transmission mode. UV-Vis spectra of solutions were measured in transmission through a glass cuvette. The solutions were prepared similar to solutions for spin coating, but diluted to $0.012\,\mathrm{mg\,mL^{-1}}$ directly before the measurement. The temperature of the blend solutions was $\sim 50\,^{\circ}\mathrm{C}$ to ensure comparability to solutions for spin coating.

4.3.5 *Memristive Devices*

Memristive devices were fabricated in a crossbar architecture on borosilicate glass substrates. Through a shadow mask, a bottom electrode of 100 nm silver was thermally evaporated in a vacuum chamber. The electrode structure is shown in Figure 4.2d. Without contact to ambient atmosphere, the substrate with bottom electrode was then transferred to a glovebox with inert N_2 atmosphere. There, the doped P3HT layer was drop cast as described in Section 4.2.1. Subsequently, the sample was transferred back to the vacuum chamber, where an injection layer of 5 nm MoO_3 was thermally evaporated, followed by 100 nm silver. After transfer back to the glovebox, the devices were measured in the glovebox as well.

Results & Discussion

Part I

STRUCTURAL ORDER IN DOPED SEMICONDUCTING POLYMERS

Part I of the results and discussion starts with an introduction of the structural order of the polymer P3HT to provide the basis for an evaluation of doping-related effects. In Chapter 5, properties ranging from optical absorption to electrical conductivity are analyzed for pristine as well as p- and n-doped organic semiconductors to introduce the dopants that are used in this thesis. After these preliminary studies, the influence of processing in terms of the used solvent is analyzed in detail in Chapter 6, illustrating the necessity to reevaluate existing processing guidelines when working with doped instead of pristine polymers. Chapter 7 expands the view to sequential doping techniques, which circumvent the problems that arise from the insights gained in Chapter 6. A detailed analysis of how the crystalline packing is affected by doping a polymer such as P3HT is given in Chapter 8 on the basis of electron diffraction measurements. DFT calculations are presented that allow to approach the underlying mechanism of changes in crystalline spacing upon doping.

5 INTRODUCTORY STUDIES

This chapter evaluates the fundamental properties of the organic semiconductors used throughout this thesis to provide the basis for a discussion of doping-related effects. First, the structural properties of the pristine materials as well as doping-related spectral signatures in the infrared (IR) and ultraviolet-visible (UV-Vis) spectral range are introduced. Then, an evaluation of the doping efficiency based on conductivity measurements is presented.

5.1 STRUCTURAL ORDER OF THE PRISTINE POLYMER P3HT

To understand the influence of dopants on organic semiconducting polymers, it is necessary to understand the basic structural properties of the undoped materials. Most investigations presented in this work are conducted with the polymer P3HT. This material is widely used as benchmark system for structural investigations as well as applications ranging from transistors to photovoltaics and thermoelectrics [18, 90–92]. Thus, this material provides a suitable starting point for further investigations. In the following, electron diffraction measurements and Franck-Condon fits to UV-Vis spectra of pure P3HT provide a basis for the investigation of doped P3HT thin films.

5.1.1 *Electron Diffraction*

To access the structure on the nanoscale, (cryo-) transmission electron microscopy (TEM) is used in this thesis. With this technique, an impression of the overall morphology can be obtained in the bright-field-mode (BF). Furthermore, electron diffraction can be used to extract detailed information on crystallinity and stacking distances in crystallites. All bright-field as well as electron diffraction measurements shown here were recorded with the microdose focusing mode to reduce beam damage. Additionally, the samples were cooled with liquid nitrogen to obtain the highest possible stability in the electron beam. Figure 5.1a shows an exemplary BF-TEM image of regioregular P3HT and a Fourier transform (FFT). The main contrast in the overview image is due to thickness variations, but a closer look reveals distinct phases of unstructured and structured appearance. The inset shows a zoom, in which ordered domains are resolved that resemble the appearance of crystalline domains of P3HT observed with high resolution TEM before [93]. The line profile across the crystalline lamellae in Figure 5.1b reveals a constant spacing of 16 Å, fitting to the

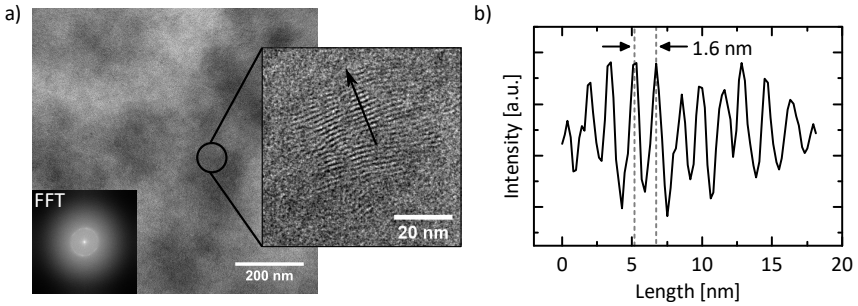

Figure 5.1: a) Bright-field TEM image of P3HT with a zoom-in to visualize the nano-structure. The inlay displays the FFT of the shown image. b) Line scan of the black arrow shown in (a).

(100)-orientation that is expected for crystallites of P3HT [94, 95]. This spacing of 16 Å is also confirmed by the bright circle in the FFT which illustrates the occurrence of this spacing in all (in-plane) directions of the measured thin film. The BF-TEM image hence allows for the assumption that regioregular P3HT is neither completely amorphous nor made of one single crystal, since several ordered but differently oriented and spatially separated domains are visible throughout the thin film.

To confirm this assumption and to assess the details of crystallinity, electron diffraction measurements were performed on P3HT with different degrees of regioregularity. The regioregularity is defined by the orientation of neighboring thiophene units and thus regulates the molecular packing which directly correlates to the structural order in a P3HT thin film. A higher regioregularity leads to better ordered thin films. The molecular structure and the properties of the three different types of P3HT used in this thesis—regiorandom P3HT (P3HTrra), regioregular P3HT (P3HT), and highly regioregular P3HT (P3HTrr)—are described in Section 4.1.1. Figure 5.2a displays the structure of a P3HT crystal as it is usually depicted in literature [96] and an exemplary diffraction pattern of a thin film of P3HT. Details on the formation of such a diffraction pattern are given in Section 2.5.1. Figure 5.2b shows a radial profile, integrated over a certain part of the diffraction pattern as indicated in Figure 5.2a. Here, two main peaks are visible. The first at $0.595\,\mathrm{nm}^{-1}$ (1.68 nm) corresponds to the stacking in (100)-direction, also referred to as lamellar stacking. The peak at $2.63\,\mathrm{nm}^{-1}$ (0.38 nm) can be assigned to stacking in the (010)-direction, which describes the direction in which the delocalized π-orbitals of neighboring P3HT chains face each other in P3HT crystallites. The measured values fit well to measurements reported in literature for regioregular P3HT [96–98]. The observation of speckles in the inner ring ((100)-direction) and a continuous intensity in the outer ring corresponding to the (010)-orientation indicates a preferred edge-on orientation (lamellar stacking vertical to substrate) of P3HT crystallites on the substrate which is in line with literature [18]. Recent studies

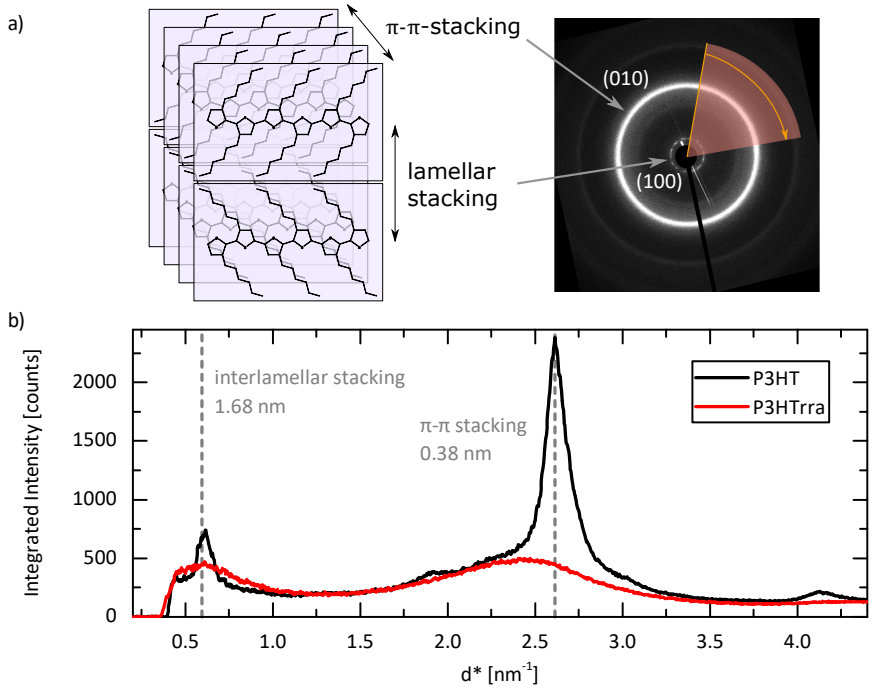

Figure 5.2: a) Schematic drawing of a P3HT crystallite and an electron diffraction pattern with the rings corresponding to the (010)- and (100)-orientation of P3HT. The shaded area indicates that diffraction profiles are usually radially integrated over a certain part of the pattern. b) Radial profiles of electron diffraction patterns of thin films made of P3HT and regiorandom P3HT.

determined the crystalline content of regioregular P3HT to be in the range of 45 % to 70 %, whereas it strongly depends on the molecular weight, regioregularity, and also the measurement technique [99]. The non-crystalline rest is mostly believed to be amorphous, containing chain folds and ends as well as tie molecules that bridge between single crystallites [31]. However, Shen, Hu, and Russell provide evidence for the existence of an ordered amorphous component which would add to the commonly described amorphous and crystalline content of the film [99]. For comparison, Figure 5.2b also shows the radial profile of an electron diffraction pattern of regiorandom P3HT, which lacks long-range order and possesses an amorphous structure in addition to a possible local short-range order [99].

5.1.2 *Franck-Condon-Fits to UV-Vis Absorption Spectra*

The previous section illustrates the power of electron microscopy to analyze the nanostructure of thin polymer films. However, it is furthermore illustrative to take a closer look at UV-Vis absorption spectra. Before discussing how the UV-Vis absorption spectrum changes upon doping in Section 5.2.1, the spectral signatures of differently ordered P3HT thin films shall be discussed here. Figure 5.3a dis-

plays the UV-Vis absorption spectra of P3HT dissolved in chlorobenzene and of already dried thin films of regioregular and regiorandom P3HT.

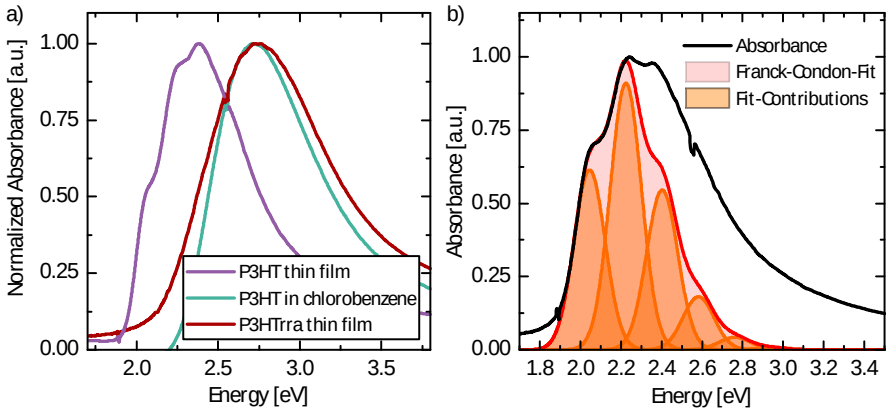

Figure 5.3: a) UV-Vis absorption spectra for dissolved, regiorandom (RRa), and regioregular P3HT. b) Franck-Condon fit to the absorption spectrum of a P3HT thin film.

The absorption of the dissolved and hence not aggregated regioregular and the already dried thin film of regiorandom P3HT peak at almost identical energies and do not differ significantly in shape. This fits to the electron diffraction data of regiorandom P3HT and to findings from literature, emphasizing the amorphous structure of P3HTrra [100, 101]. The broad, less well resolved shape of the spectrum of P3HTrra compared to the one of P3HT can be explained by a wider distribution of conjugation lengths leading to inhomogeneous broadening of the transitions [100]. This leads to similar spectra of dissolved P3HT and thin films of P3HTrra. In contrast, the spectrum of the regioregular P3HT thin film shows several distinct peaks and shoulders at lower energy. As it is extensively discussed in literature, UV-Vis spectra of P3HT are composed of two contributions: At low energies, domains of ordered P3HT which form weakly interacting H-aggregate states contribute well defined peaks and shoulders [33, 51]. Disordered polymer chains (comparable to the dissolved and regiorandom P3HT) add a broad absorption peak at higher energies [32, 33, 100, 102]. To describe the low energy part, the Franck-Condon principle is used. The distinct peaks and shoulders originate from vibronic transitions. The absorption of a photon excites the molecule from the electronic (S_0) and vibronic ground state to an electronic (S_1) and vibronic excited state. The difference of molecular coordinates between vibronic ground and excited states determines the probability for a certain transition. Hence, there is a difference in transition probabilities between well ordered and hence more planar [103, 104] chain segments and amorphous chains. Expressed in a more quantitative way, the free exciton bandwidth of aggregates W together with E_P, the energy of the main intramolecular vibration that couples to the

electronic transition, connects the ratio of intensities of 0-0 and 0-1 vibrational absorptions with the nearest-neighbor interchain Coulombic coupling [51]:

$$\frac{A_{0-0}}{A_{0-1}} \approx \left(\frac{1 - 0.24\frac{W}{E_P}}{1 + 0.073\frac{W}{E_P}} \right)^2 . \tag{5.1}$$

When assuming that the interchain order in the thin films is similar, the value of W is inversely related to the intrachain order and conjugation length of the P3HT chains [105–107]. This means that an increase of conjugation length which is directly related to the structural order in such films leads to a decrease in free exciton bandwidth W. To obtain W, E_P can be set to the energy of the C=C symmetric stretch vibration at 0.18 eV [107, 108]. The ratio A_{0-0}/A_{0-1} is defined by the measured UV-Vis absorption spectra, which can be fitted with a Franck-Condon model. Figure 5.3b shows such a fit for a regioregular P3HT thin film. The following function was used to fit the absorption spectrum in a range from 1.8 eV to 2.25 eV:

$$\begin{aligned} A = & k \cdot \sum_{m=0} \left(\frac{S^m}{m!}\right) \cdot \left(1 - \frac{We^{-S}}{2E_P} \sum_{n \neq m} \frac{S^n}{n!(n-m)} \right)^2 \\ & \cdot \exp\left\{ \left(\frac{(E - E_{0\text{-}0} - mE_P - \frac{1}{2}WS^m e^{-S})^2}{2\sigma^2} \right) \right\}. \end{aligned} \tag{5.2}$$

In this equation, k denotes a constant with fitted amplitude, m is the vibrational level and n depicts the vibrational quantum number. The last exponential describes a gaussian lineshape with the same width for all vibronic transitions. The fit range was restricted to below 2.25 eV since amorphous P3HT absorbs at higher energies. S is the Huang-Rhys factor that describes the electron-phonon coupling which can be set to $S \approx 1$ in non-interacting and planar polythiophene chains [33]. In the weak coupling regime, S should not change upon changes in aggregation [33]. To be able to analyze the influence of order on charge transport properties, UV-Vis absorption spectra and conductivity values of differently prepared P3HT films were measured. Since the solvent that is used to dissolve and spin coat the P3HT is known to affect the order in the resulting thin film [33, 107, 109], the P3HT used herein was spin coated from chloroform (CF), chlorobenzene (CB), and dichlorobenzene (DCB). The drying time of spin coated thin films is directly related to the amount of order that can form in thin P3HT films. Therefore, the solvents were chosen to show large differences in boiling point which determines the drying time: $T_b(CF) = 61\,°C, T_b(CB) = 131\,°C, T_b(DCB) = 174\,°C$. In addition, P3HT with an even higher regioregularity of 96.7 % (P3HTrr) in contrast to 93.7 % (P3HT) was used for comparison. This P3HTrr is expected to reach higher amounts of structural order, since the regioregularity is the main limiter for the alignment of chains [110].

Figure A.1 and Table A.1 in the appendix show Franck-Condon fits to all spectra, including residuals and fit-parameters. According to Equation 5.2, the free exciton bandwidth W was directly extracted from the fit for each spectrum. Values of around 50 meV for highly regioregular and hence ordered thin films and 150 meV for comparably low crystallinity fit to existing literature [22, 33]. Note that differences in molecular weight, regioregularity, and processing render a detailed comparison of values to literature difficult, even if the same solvent was used.

5.1.3 *Correlation of Structural Order with Conductivity*

In Figure 5.4, the free exciton bandwidth W is plotted together with the conductivity for each P3HT thin film. To exclude any influence of contact resistance, the four-point probe technique was used. When increasing the boiling point from 61 °C (CF) to 131 °C (CB) and 174 °C (DCB), the conductivity of P3HT as well as of P3HTrr increases significantly. Simultaneously, $1/W$ follows the same trend with a different change in absolute value, implying a non-linear relationship. An ex-

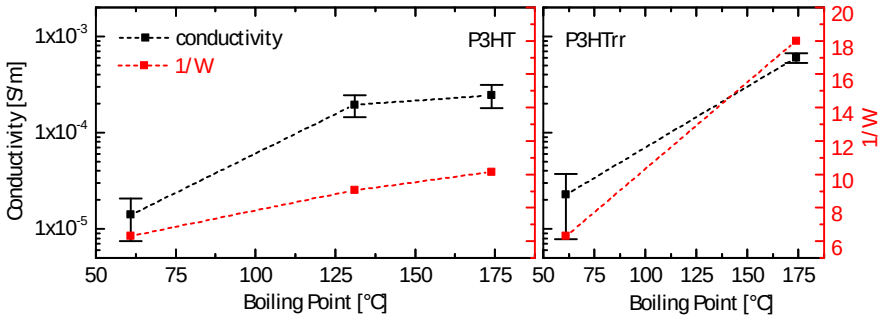

Figure 5.4: Conductivity and inverse exciton bandwidth W^{-1} for thin films of P3HT (left) & P3HTrr (right) spin cast from solvents with boiling points of 61 °C (chloroform), 131 °C (chlorobenzene), and 174 °C (dichlorobenzene). The relation between conductivity and W^{-1} is non-linear (different scales on axes).

planation for the observed behavior is based on the boiling point that can allow the chains in the still wet film to align over time if the drying time is long enough. For chloroform as a solvent, the time until most of the solvent left the film is too short to reach the equilibrium state in which the chains are allowed to develop ordered domains. This is observed for both P3HT and P3HTrr. When increasing the boiling point of the solvent, the chains can form more ordered structures. However, a saturation seems to set in for boiling points higher than that of chlorobenzene, since the conductivity and inverse free exciton bandwidth for P3HT do not increase strongly from chlorobenzene to dichlorobenzene. The comparison of P3HT with P3HTrr both from dichlorobenzene confirms that the higher regioregularity of P3HTrr

allows for a higher maximum amount of order in case the drying conditions allow polymer chains in the film to equilibrate.

5.1.4 *Discussion*

The results presented above are important for the interpretation of the subsequently shown effects of dopants. It is necessary to keep in mind that the conductivity—a frequently used quantity to evaluate the doping efficiency [24, 27, 97, 111]—is determined by two main factors:

$$\sigma = q \cdot n \cdot \mu. \tag{5.3}$$

Here, n denotes the charge carrier concentration, μ the charge carrier mobility, and q the charge. The doping efficiency is usually defined as the ratio of generated free charge carriers that can contribute to a current to the total number of introduced dopant molecules. The following chapters show that there are several possible states between a not-transferred charge and a completely free charge. As seen above, the conductivity of P3HT without any dopant can vary drastically, depending on the processing conditions. Since all films were produced under similar conditions, n is not expected to change. What is known to be heavily dependent on the structural order is the mobility μ [102, 104, 112]. Hence, the observed differences in conductivity are mostly driven by changes in mobility. As it becomes evident in Chapter 6, this consideration is crucial to be able to discriminate between a real difference in doping efficiency and a morphology-driven change in conductivity upon doping.

5.2 P-TYPE DOPANTS FOR SEMICONDUCTING POLYMERS: F_4TCNQ & MO(TFD-CO_2ME)$_3$

The basic effects upon doping P3HT in terms of spectroscopic changes and conductivity are discussed in the following to provide a basis for the subsequent chapters. Unless otherwise stated, doping concentrations are set to 10:1, meaning one dopant molecule per ten thiophene units of the P3HT host polymer. Doping is achieved using blend doping, where dopant and host material are separately dissolved using the same solvent first. Subsequently, both solutions are mixed prior to spin coating the blend (see Section 4.2 for experimental details). Chlorobenzene was used as solvent for the measurements shown in the following.

5.2.1 *Charge Transfer to the P3HT: UV-Vis & Infrared Spectroscopy*

The UV-Vis and IR spectra shown in the following introduce the effects that occur upon doping to provide a basis for the fits and

analyses in following sections and chapters. Figure 5.5 displays the UV-Vis absorption spectra of P3HT doped with F_4TCNQ and Mo(tfd-CO_2Me)$_3$, together with spectra of the pristine materials. The single spectra are scaled to visualize the main contributions and are not used to fit the spectra in this case. The spectrum of charged F_4TCNQ (labeled as *F_4TCNQ anion*) was extracted from literature [88, 113]. In the case of F_4TCNQ-doped P3HT, the spectrum reveals contributions from pure P3HT and charged F_4TCNQ. Although a minor contribution of neutral F_4TCNQ can not be excluded from the UV-Vis spectrum, IR-spectra shown in the following are able to rule out detectable amounts of uncharged F_4TCNQ in the films at the given dopant concentration. When combining the mentioned components, a further contribution between ~ 1.25 eV and ~ 1.9 eV is needed to match the spectrum of the doped P3HT. This contribution is generated by the P2 polaron absorption of charged P3HT (see chapter Section 2.4.4 for theoretic background). A similar picture is given by P3HT doped with Mo(tfd-CO_2Me)$_3$: A broad spectral feature below the bandgap shows up that is assigned to the P2 polaron absorption of charged P3HT. The

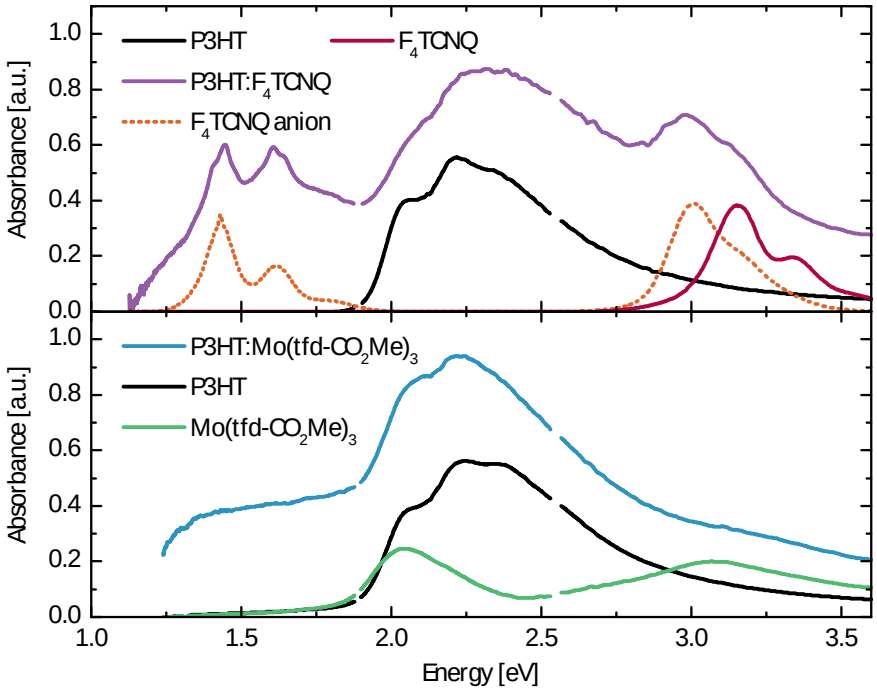

Figure 5.5: UV-Vis absorption spectra of P3HT:F_4TCNQ (top) and P3HT:Mo(tfd-CO_2Me)$_3$ (bottom) with spectra of pristine P3HT, F_4TCNQ, charged F_4TCNQ (F_4TCNQ anion), and pristine Mo(tfd-CO_2Me)$_3$.

intensity of this P2 polaron absorption was previously used to determine the doping efficiency for a fixed doping concentration [113, 114] and as indicator for the doping concentration in case of a sequential doping technique [25]. However, the cross section of this absorption

might additionally depend on the structural order, rendering a calculation of accurate doping efficiency questionable [22]. Additionally, the numbers of how many dopant molecules are ionized in the first place strongly vary: Whereas IR spectroscopy does not detect any neutral F_4TCNQ for doping concentrations investigated (discussed in the following), estimations from F_4TCNQ anion absorption in the visible spectral range yield values ranging from 20 % to 63 %, strongly depending on the processing conditions such as deposition temperature [88, 113, 115].

As described and explained in Section 2.4.4, the P2 polaron absorption feature in the visible spectral region is accompanied by additional polaronic absorptions P1 and DP1 in the infrared spectral region. Figure 5.6a shows infrared spectra complementary to the UV-Vis spectra discussed above for P3HT:F_4TCNQ as well as P3HT:Mo(tfd-CO_2Me)$_3$, measured by Vipilan Sivanesan[1]. The spectrum of pristine P3HT shows narrow absorption lines around 1500 cm^{-1} and 3000 cm^{-1} that mainly originate from stretching modes of the thiophene rings in the backbone and CH_2 as well as CH_3 groups of the hexyl side chain [116, 117]. Upon doping, a broad electronic excitation that (in these examples) peaks between 3000 cm^{-1} and 5000 cm^{-1} becomes visible. It can be assigned to the lowest optical transition P1 of polarons. In the notation of previous studies, the spectral shape and peak position of the P1 polaron absorption can be assigned to mostly one-dinemsional (1D) polarons. 1D in this case describes dominating intrachain delocalization. 2D polarons exhibit a stronger absorption DP1 between 500 cm^{-1} and 1500 cm^{-1} [54, 118] in addition to a strongly red-shifted P1 absorption which was previously associated with stronger interchain coupling compared to the 1D case that is dominant here [54]. Superimposing the DP1 polaron peak, strong absorption lines of vibrations that are not IR-active in the neutral state are visible for doped P3HT. These IR-active vibrations (IRAV) are visible below 1500 cm^{-1}. The features described above were observed before and can be assigned to successful doping of P3HT [49, 54, 88, 113, 116]. A comparison of F_4TCNQ-doped and Mo(tfd-CO_2Me)$_3$-doped P3HT reveals a different shape and position of the polaron absorption. As it is discussed in Chapter 6 in detail, this difference is only indirectly related to the different dopants. Instead, the morphology of the doped P3HT thin film that is formed due to the presence of the dopants plays a major role.

Figure 5.6b and c focus on the spectral region where absorptions of the dopant molecules are located. F_4TCNQ in the neutral state shows a C≡N-stretching peak at 2228 cm^{-1} with a smaller contribution at 2214 cm^{-1} [119]. In the mixture P3HT:F_4TCNQ, the two absorptions are red-shifted to 2194 cm^{-1} and 2169 cm^{-1}, respectively. It was shown

1 Group of Prof. Pucci, Kirchhoff-Institute for Physics, Heidelberg University

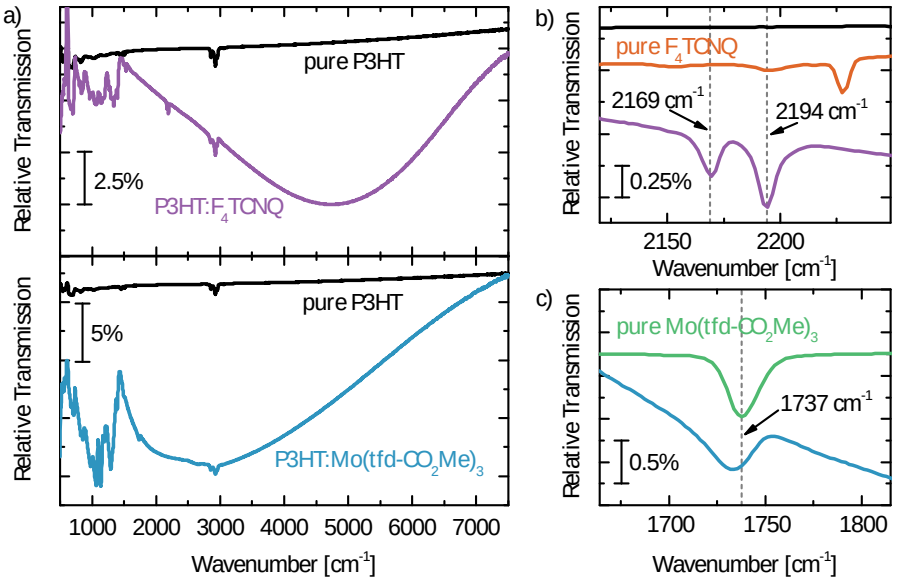

Figure 5.6: Relative transmittance at normal incidence of P3HT (black), F_4TCNQ (orange), Mo(tfd-CO_2Me)$_3$ (green), P3HT:F_4TCNQ (purple), and P3HT:Mo(tfd-CO_2Me)$_3$ (blue) for doping concentrations of 10:1 spin cast from blend solutions in chlorobenzene. The broad absorption band in (a) is caused by the P1 polaron absorption of positively charged P3HT. (b) displays the spectral region of the C≡N stretching vibration of F_4TCNQ (top) and (c) the C=O stretching vibration of Mo(tfd-CO_2Me)$_3$ (bottom).

that this shift increases linearly with an increasing share of the charge located on the F_4TCNQ molecule [120–123]. Additionally, these discrete vibrations interfere with the broad electronic excitation P1 of the polaron, resulting in an asymmetric Fano-type line shape. This effect was previously observed by Österbacka *et al.* for the intramolecular interference of P3HT IRAV modes with the polaron excitation [54]. Depending on the polaron peak position and hence the interference strength, this asymmetric Fano-type line shape must be fitted to reliably extract the position of the C≡N-stretching peak. This holds true as well for the C=O-strechting vibration at 1737 cm^{-1} of Mo(tfd-CO_2Me)$_3$, where a determination of the exact peak position in the doped case is only possible with a fit. This fit reveals no shift of the C=O-stretching peak upon doping within the measurement accuracy [69, 124]. Since the detailed evaluation of the Fano-fitting for P3HT:F_4TCNQ and P3HT:Mo(tfd-CO_2Me)$_3$ was not performed by the author of this thesis, the interested reader is referred to [89] and the thesis of Sivanesan [69]. Figure 5.6 b additionally shows that in the case of F_4TCNQ-doped P3HT, no signature of the C≡N-stretching vibration at 2228 cm^{-1} is visible any more. This reveals that all F_4TCNQ molecules within the detection limit underwent charge transfer.[2] Note

2 Neutral F_4TCNQ can be detected reliably down to a molecular concentration of one neutral F_4TCNQ molecule per 100 thiophene repeating units of P3HT for the

Host:Dopant	Solvent	Conductivity [$S\,m^{-1}$]
P3HT	chlorobenzene	$(2.3 \pm 0.6) \times 10^{-4}$
P3HT:F_4TCNQ	chlorobenzene	0.3 ± 0.1
P3HT:Mo(tfd-CO_2Me)$_3$	chlorobenzene	49.3 ± 9.7

Table 5.1: Thin film conductivity for pristine and doped P3HT at doping ratios of 10:1 and spin coating from blend solutions. The solvent that was used is given for comparison.

that a successful integer charge transfer does not necessarily lead to a free charge that can contribute to charge transport. The underlying mechanisms of charge separation and the connected doping efficiency are still being part of the ongoing discourse. Chapter 6 discusses this in more detail.

5.2.2 *Doping Efficiency*

To prove that both dopants generate additional charges that contribute to the electrical conductivity, Table 5.2 summarizes the thin film conductivity for P3HT:F_4TCNQ and P3HT:Mo(tfd-CO_2Me)$_3$ with a dopant concentration of 10:1. For comparison, both films were prepared from blend solutions under identical conditions. Chlorobenzene was used as solvent and spin coating was performed from solutions at 50 °C onto borosilicate glass substrates. The conductivity of doped P3HT was measured using the four-point probe technique which eliminates the influence of contact resistance. Current-voltage characteristics were used to extract the conductivity of undoped P3HT (see Section 4.3 the details on the electrode layout). It can be seen that P3HT:Mo(tfd-CO_2Me)$_3$ reaches a higher absolute conductivity of $49\,S\,m^{-1}$ compared to $0.3\,S\,m^{-1}$ for P3HT:F_4TCNQ.

These values imply a better doping efficiency of Mo(tfd-CO_2Me)$_3$ at first sight. However, as it is shown in the next chapter, interactions of the solvent with dopant and host can strongly influence the formation of structural order in thin films. Whereas F_4TCNQ dissolves in chlorobenzene only to a limited amount [27], Mo(tfd-CO_2Me)$_3$ was specifically designed to suit solution processing [84]. As it is reported in the next chapter, this could lead to an overall higher amount of order in thin films of P3HT:Mo(tfd-CO_2Me)$_3$ compared to P3HT:F_4TCNQ. This in turn would enhance the charge carrier mobility in P3HT:Mo(tfd-CO_2Me)$_3$-films and further increase the conductivity without the necessity for a higher doping efficiency. Additionally, the structural order itself impacts the charge carrier separation and hence the doping efficiency [20, 21], although the increase

measurement conditions chosen for this experiment. A higher film thickness or a longer integration time could further improve the detection.

of mobility upon increasing structural order might dominate changes in conductivity, as indicated recently [22, 23]. This sheds light on the complex interplay of film formation, structural order, and doping efficiency, which is picked up as central theme in Chapter 6.

Concluding, both dopants strongly increase the electrical conductivity of P3HT. A detailed comparison of doping efficiency however is beyond the scope of this thesis. The frequently used approach in literature is based on careful analysis of optical absorbance spectra, where the intensity of the P3HT polaron an F4TNCQ anion peaks are used as indicators for successful charge transfer [21, 88, 113, 114]. However, a charge transfer per se does not necessarily lead to a free charge that can contribute to charge transport [113] and absorption cross sections might change with the structural order [22].

5.3 DMBI-DERIVATIVES AS N-TYPE DOPANTS FOR ORGANIC SEMICONDUCTORS

To face the problem of dopant diffusion and drift that is discussed in detail in Chapter 10 and Chapter 11, DMBI-derivatives that contain specific functional groups were synthesized by Simon Benneckendorf.[3] A description of the chemical composition and functionalization is given in Chapter 4. Since the characterization of these materials regarding a diffusion and drift is conducted in Chapter 11, the following focuses on the doping effect of the different dopants in a small molecule and a polymer host material.

5.3.1 *Doping Effect of DMBI-Derivatives: Conductivity*

Table 5.2 summarizes the results of the conductivity measurements, with N2200 and PCBM as host materials. PCBM is a soluble C_{60}-derivative and hence a small molecule. It is widely used in organic photovoltaics [125, 126] and gained attention recently as hole transport material for perovskite solar cells—in a pristine and doped form [127]. N2200 is a semi-crystalline polymer that is mostly used in transistor applications [80]. The dopants are based on the literature-known n-dopant *o*-MeO-DMBI [86, 128, 129]. *o*-BnO-DMBI extends the molecule by an additional benzene ring attached to the oxygen as a reference to *o*-AzBnO-DMBI, which contains an azide group (N_3) attached to the benzene unit. This azide unit is intended to react with surrounding organic molecules upon external stimulus to immobilize the dopant atom. Chapter 4 shows the chemical structures as well as a discussion of the doping mechanism whereas Section 11.4 focuses on experiments to test the immobilization.

Table 5.2 reveals that pristine dopants as well as pristine N2200 and PCBM are poor conductors with conductivities around $10^{-6}\,\mathrm{S\,cm^{-1}}$.

3 Group of Prof. Bunz, Institute of Organic Chemistry (OCI), Heidelberg University.

Host:Dopant	Conductivity [$S\,m^{-1}$]
o-BnO-DMBI	$< 5 \times 10^{-6}$
o-MeO-DMBI	$< 5 \times 10^{-6}$
N2200	$(6.6 \pm 7.8) \times 10^{-6}$
N2200:*o*-BnO-DMBI	$(2.2 \pm 2.4) \times 10^{-1}$
N2200:*o*-MeO-DMBI	$(4.9 \pm 1.4) \times 10^{-2}$
N2200:*o*-AzBnO-DMBI	$(4.5 \pm 1.6) \times 10^{-2}$
N2200:*o*-AzBnO-DMBI (therm. activated)	$(7.7 \pm 2.8) \times 10^{-2}$
PCBM	$< 5 \times 10^{-6}$
PCBM:*o*-BnO-DMBI	$(3.96 \pm 1.24) \times 10^{-3}$
PCBM:*o*-MeO-DMBI	$(4.19 \pm 0.22) \times 10^{-3}$

Table 5.2: Thin film conductivity of PCBM and N2200 doped with various DMBI-derivatives. Thin films were spin coated from blend solutions in chloroform and doping ratios of 10:1. Thermal activation where indicated was performed at 130 °C for 10 min in nitrogen atmosphere.

All values for doped materials are extracted from current-voltage characteristics, the layers are processed from blend solutions with chloroform and a doping ratio of 10:1. For PCBM, both *o*-MeO-DMBI and *o*-BnO-DMBI increase the conductivity by three orders of magnitude, confirming that a doping effect takes place. The increase for N2200 as a host material is even higher with a conductivity of up to $10^{-1}\,S\,m^{-1}$ for *o*-BnO-DMBI as dopant and $10^{-2}\,S\,m^{-1}$ for *o*-MeO-DMBI and *o*-AzBnO-DMBI.

A detailed comparison of the differences in conductivity as indicator for the doping efficiency however is difficult: Recent studies found a tendency of related DMBI-derivatives to phase separate at high concentrations in N2200 and PCBM [127, 130]. This could change the amount of dopants that is actually able to undergo charge transfer, falsifying the calculation of a doping efficiency. In contrast to the rich absorption spectra of pristine and doped P3HT in the visible spectral range, the spectra of doped PCBM and N2200 do not reveal prominent features such as polaron absorption upon doping. Spectra for pristine PCBM, *o*-MeO-DMBI, and *o*-BnO-DMBI as well as doped PCBM are shown in Figure A.2 in the appendix. Corresponding spectra of pristine and doped N2200 are given in Figure A.3 and Figure A.4 in the appendix.

6

INFLUENCE OF SOLVENT UPON DOPING: PARADIGM CHANGE IN PROCESSING

As discussed in the previous chapter, the morphology of P3HT thin films can have a severe impact on charge transport properties. This raises the question if an equivalent importance of the structural order in case of doped P3HT is given. One of the first who studied this connection were Gao *et al.* By comparison of (doped) regiorandom with regioregular P3HT and J-aggregate nanofibers with less ordered polymorphic H-aggregate nanofibers, they emphasize the need for highly ordered domains of P3HT to efficiently separate charges, which is the key to a high overall doping efficiency [20, 21, 131].

For pristine P3HT, the deliberate tuning of thin film morphology and structural order has been subject of intense research in the past [92, 102, 132, 133]. As is was discussed also in the previous chapter, the boiling point of a solvent regulates the amount of π-π stacking in thin films [107, 134]. In the past, there were mainly two solvents used in the preparation of P3HT:F_4TCNQ thin films: chloroform [113, 135, 136] and chlorobenzene [20, 97, 131, 137]. Although discrepancies between studies of P3HT:F_4TCNQ processed from these two solvents were noticed [2], no thorough investigation was performed in literature prior to the one presented herein.[1] As discussed in Section 5.1.2, chlorobenzene with the higher boiling point (131 °C versus 64 °C for chloroform) allows the film to dry slower, enabling the formation of a higher degree of order in the case of pristine P3HT. As the following measurements show, this direct relation is overruled in the case of mixed solutions of P3HT and F_4TCNQ. A first hint that an additional mechanism is at work in mixed solutions of P3HT and F_4TCNQ was given by Duong *et al.* who found that the temperature of the blend solution prior to spin coating impacts the thin film conductivity [137].

This chapter presents a thorough comparison of F_4TCNQ-doped P3HT thin films processed from chloroform and chlorobenzene under identical conditions. First, electron diffraction measurements as well as infrared and UV-Vis spectroscopy reveal the structural properties of the thin films. Conductivity measurements are presented to underline the importance of the observed differences and UV-Vis spectra of solutions shed light on the underlying mechanisms.

1 The study presented in this chapter was published in following publication: L. Müller et al., 2016, *Charge-Transfer-Solvent Interaction Predefines Doping Efficiency in p-Doped P3HT Films*, [89].

6.1 ASSESSING THE STRUCTURE: ELECTRON DIFFRACTION & UV-VIS ABSORPTION SPECTROSCOPY

All thin films investigated in this chapter were spin-cast from blend solutions at 50 °C with a doping ratio of 10:1. In Figure 6.1, radial electron diffraction profiles are shown for pristine as well as F_4TCNQ-doped P3HT processed from chloroform and chlorobenzene. Corresponding bright-field images and diffraction patterns are shown in the Appendix (Figure A.5). In Figure 6.1, analogue to Figure 5.2 in the previous chapter, the characteristic peaks of (100)-orientation (lamellar stacking, 1.68 nm) as well as the (010)-orientation (π-π stacking, 0.38 nm) are visible in the undoped thin films. The lamellar stacking shows an increase in peak height in films from chlorobenzene upon doping, whereas this peak only broadens in the case of chloroform. The intensity of the π-π stacking peak does not change significantly from chlorobenzene, but there is a strong increase in π-π stacking for thin films spin-cast from chloroform in the doped case. This in-

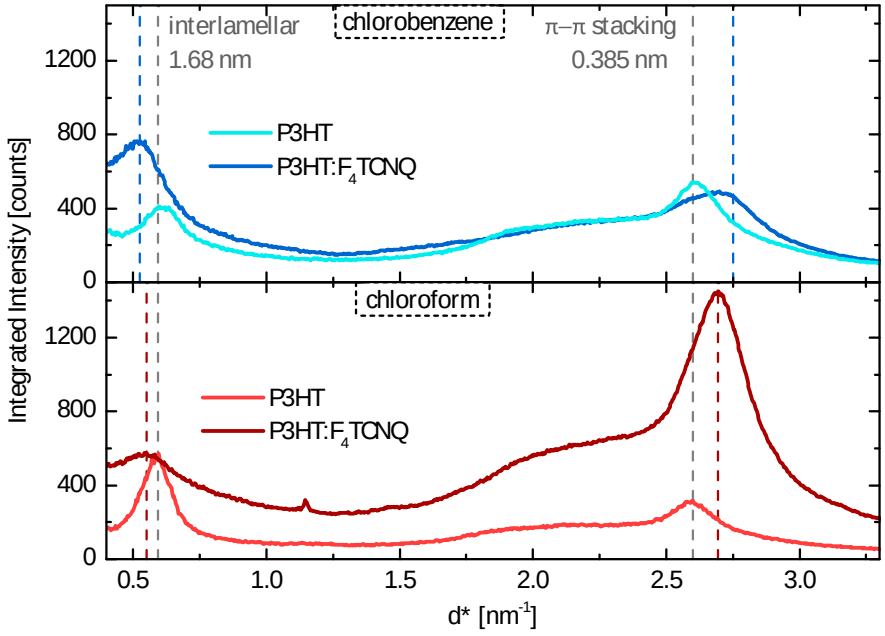

Figure 6.1: Radial profiles of electron diffraction patterns measured on thin films of P3HT:F_4TCNQ and pristine P3HT. Chlorobenzene (top, blue) and chloroform (bottom, red) were used as solvents. Characteristic stacking distances are marked with dashed lines.

crease can be attributed to either a different orientation of the crystallites with respect to the substrate (and hence the probing electron beam) or an increase of the degree of order. In detail, the number of aggregated chain segments or the size of the stacks and therewith the length of planarized chain segments could increase to evoke the observed change in π-π stacking. To discuss the possibility of an alignment change, it is illustrative to study the work of Scholes *et al.*,

who observed increased orientation isotropy for low doping concentrations with the solvent *o*-dichlorobenzene [24]. However, for higher doping concentrations towards the concentration used herein, a decrease in isotropy was observed, which hence does not support the assumption that a change in orientation could be responsible for the observed effect. Although this cannot completely rule out a change in orientation, the possibility of a higher amount of structural order as main driver for the increase in π-π stacking remains more likely, which is furthermore supported by UV-Vis and IR spectra shown in the following.

In addition to the change in peak intensities upon doping, there is also a change in peak positions, representing a change in stacking distances. The lamellar stacking increases from 1.71 nm (1.64 nm) for pristine P3HT films from chloroform (chlorobenzene) to 1.86 nm (1.96 nm) in doped films. At the same time, the π-π stacking distance decreases for chloroform-cast thin films from 3.86 Å for pure P3HT to 3.71 Å in the doped case. For chlorobenzene-cast films, a double-peak is visible, composed of one contribution with a spacing comparable to that of pristine P3HT and one shifted to smaller spacings. This finding allows for the interpretation of two separate phases that are present in thin films spin-cast from chlorobenzene: ordered domains of pure and hence undoped P3HT and domains where both P3HT and F_4TCNQ are present. Note that with this diffraction technique, only ordered domains are probed and no direct statement about the amorphous regions between crystallites can be made. The underlying mechanism behind the shift of crystalline spacings is still discussed in literature and opposing positions exist, claiming that F_4TCNQ molecules incorporate into P3HT crystallites [97, 138] or reside in the side chains and therefore mainly influence the lamellar stacking [22, 139]. The origin of this shift in π-π spacing upon doping is discussed in detail in Chapter 8 with additional electron diffraction data of P3HT:Mo(tfd-CO_2Me)$_3$ and DFT-calculations of charged P3HT crystallites. An explanation based on the formation of F_4TCNQ-crystals can be excluded based on IR measurements discussed in the following. In summary, the electron diffraction data point towards a more ordered thin film from the low-boiling point solvent chloroform, which—based on the behavior of pristine P3HT—is not intuitively understandable.

A closer look at UV-Vis spectra of pristine P3HT from both solvents in Figure 6.2a reveals a clearer vibronic structure and a red-shifted absorption for films spin-cast from the high-boiling point solvent chlorobenzene. Additionally, the absorption at the energy of the 0-0 vibronic peak of the thin film from chlorobenzene is higher than that of the film from chloroform when normalized to the 0-1 vibronic peak at 2.2 eV. This confirms what was already discussed in Chap-

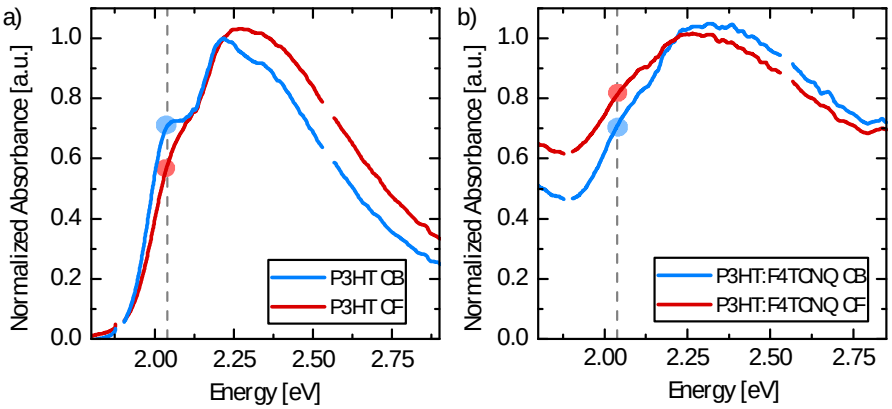

Figure 6.2: Normalized UV-Vis absorbance spectra of F_4TCNQ-doped (right) and pristine (left) P3HT, spin coated from chlorobenzene (blue) and chloroform (red). The spectra are normalized to the 0-1 transition at 2.2 eV. The 0-0 transition at 2.04 eV is marked with a dashed line.

ter 5: The free exciton bandwidth which is directly related to the conjugation length and crystal quality (defined by the ratio of 0-0 to 0-1 vibronic peak) is higher for the high-boiling point solvent chlorobenzene, revealing a more ordered thin film compared to the film spin-cast from chloroform. In the doped case however, the intensity of the absorption at the energy of the 0-0 peak is higher for the chloroform-cast thin film compared to the absorption of the film spin-cast from chlorobenzene in spectra that are normalized to the 0-1 vibronic peak. The ratio is inverted compared to the case of pristine P3HT, matching the observations from electron diffraction discussed above. However, due to absorptions of the F_4TCNQ-anion and the P2 polaron peak below the band gap, a thorough analysis is not possible. The spectra of doped thin films are therefore not fitted to extract the free exciton bandwidth W.

6.2 CHARGE TRANSFER & POLARON DELOCALIZATION: INFRARED SPECTROSCOPY

To investigate possible differences in charge transfer and polaron properties, IR spectra of thin films of pure and doped P3HT from chloroform and chlorobenzene are analyzed.[2] Figure 6.3a displays overview spectra with the broad polaronic excitation and IRAV-modes, whereas Figure 6.3b focuses on the spectral region in which the C≡N-stretching vibration absorbs. Since a detailed discussion of the spectral features of pure and doped P3HT is given in Section 5.2.1, the following analysis focuses on the differences and their implications. Doped films from both solvents exhibit broad polaron absorptions of

2 The measurement was performed by Tobias Glaser from the group of Prof. Pucci at the Kirchhoff-Institute for Physics, Heidelberg University.

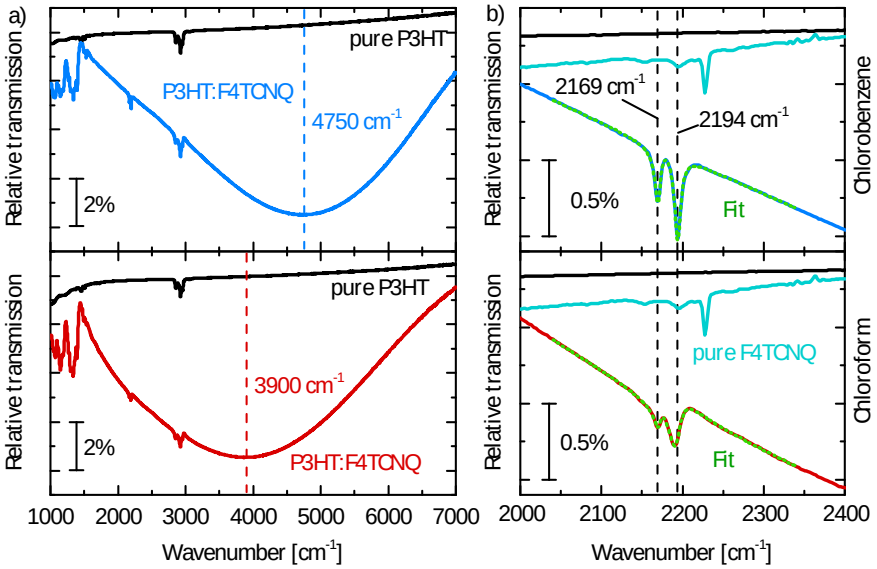

Figure 6.3: a) Relative transmittance of P3HT and P3HT:F_4TCNQ spin cast from chlorobenzene (top) and chloroform (bottom). The dashed lines mark the position of the broad polaron absorption of doped P3HT. b) The peaks shown originate from the excitation of the C≡N-stretching vibration of F_4TCNQ that shifts upon charging of the F_4TCNQ molecule. The dahed green line shows a fit of these peaks.

comparable strength. Remarkably, the peak of this polaron absorption in films from chloroform is positioned at 3900 cm^{-1}, 850 wavenumbers lower in energy than the polaron peak of films from chlorobenzene (4750 cm^{-1}). Figure 6.3b reveals a shift of the C≡N-stretching vibration from 2228 cm^{-1} to 2194 cm^{-1} for films from chlorobenzene. Due to the red-shifted polaron absorption, the interference of the discrete vibration with the broad electronic excitation is stronger in the case of films from chloroform. Hence, the analysis of the peak position in the case of chloroform as solvent is only possible with a Fano-type fit of the peaks (green dashed lines in Figure 6.3b). As explained in Section 5.2.1, a detailed discussion of the fits is not conducted in this thesis. The outcome of the fit, however, is that also the peak position in films from chloroform is shifted to 2194 cm^{-1}. Since the shift of the spectral position of the C≡N-stretching vibration increases linearly with increasing share of the charge on the F_4TCNQ molecule [120–123], an integer charge transfer can be identified in both thin films. The non-existing absorption at the wavelength of the neutral F_4TCNQ at 2228 cm^{-1} furthermore excludes the existence of pure F_4TCNQ-crystals, since these would not contain P3HT and hence could not transfer a charge.[3] The red-shift of the polaron in case of films from chloroform can be explained by a stronger polaron de-

3 Based on the signal-to-noise ratio, dopant concentrations down to 1:100 can be detected reliably with film thickness and integration time used for these measurements.

localization [22, 140]. Whereas the intensity of the DP1 polaron peak between 500 cm^{-1} and 1500 cm^{-1} relates to the strength of interchain delocalization, the P1 polaron peak mainly describes intrachain delocalization. Since the intensity of the DP1 peak does not strongly differ between thin films from chloroform and chlorobenzene, the shift of the P1 peak can be attributed to a higher intrachain delocalization. Despite of the shift in P1 absorption, the spectral shape and position in both films still represent 1D polarons [54]. In order to enable the observed higher intrachain delocalization in films from chloroform, a higher conjugation length is necessary, which is directly related to the degree of structural order in P3HT. This finding fits to the observation from electron diffraction, where a higher amount of π-π stacking is measured in films from chloroform. Summarizing, all measurements presented to this point imply more order in F_4TCNQ-doped P3HT films from chloroform compared to chlorobenzene. This is contradictory to the properties of thin films of pristine P3HT, for which the higher boiling point of chlorobenzene leads to more ordered thin films.

6.3 IMPACT ON CHARGE TRANSPORT

Before the origin of this behavior is approached in the next section, the consequences of the higher amount of order in films from chloroform are analyzed in terms of conductivity these films exhibit. Figure 6.4 shows conductivity measurements of pristine P3HT as well as F_4TCNQ-doped P3HT thin films. The conductivity of pristine films was calculated from IV-measurements. Since the impact of contact resistance increases with decreasing thin film resistance, the four-point probing technique was used in the case of doped thin films which exhibit a conductivity orders of magnitude higher than that of pristine P3HT. Figure 6.4a reveals a higher conductivity of pristine P3HT spincast from the high-boiling point solvent chlorobenzene compared to chloroform, which is in line with the UV-Vis measurements of pristine P3HT thin films (Figure 6.2) and the literature [33, 107, 109]. This interrelation is inverted in the case of F_4TCNQ-doped P3HT, displayed in Figure 6.4b: Films of P3HT:F_4TCNQ show a significantly higher conductivity of 4.5 $S\,m^{-1}$ when spin coated from chloroform compared to chlorobenzene (0.3 $S\,m^{-1}$). This highlights the practical importance of the investigated effect. The absolute values of a few $S\,m^{-1}$ for P3HT:F_4TCNQ in the given concentration match roughly with expectations from literature [97]. However, a detailed comparison remains difficult since the conductivity is very sensitive to additional parameters such as the regioregularity [141] or the temperature of the P3HT-F_4TCNQ blend prior to spin coating [137].

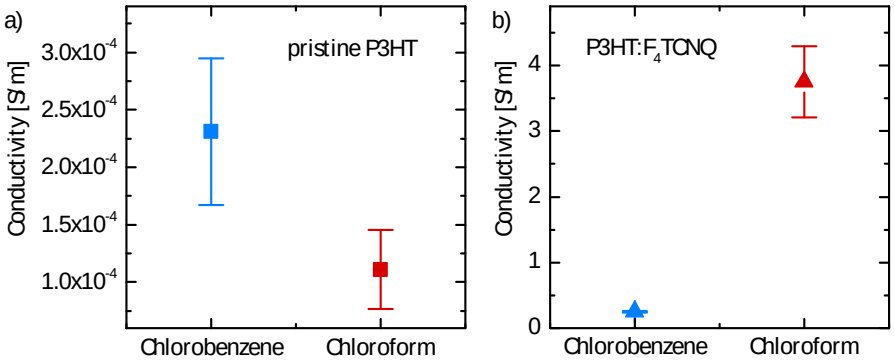

Figure 6.4: Lateral conductivity of pristine (left) and F_4TCNQ-doped (right) P3HT thin films. The conductivity of undoped P3HT was extracted fom IV-measurements, whereas the four-point probe technique was applied for doped P3HT.

6.4 APPROACHING THE UNDERLYING MECHANISM: UV-VIS SPECTROSCOPY ON SOLUTIONS

The effects observed and discussed so far were obtained on already dried thin films. Since all processing steps were kept identical between the films from chloroform and chlorobenzene, the degree of order that forms upon drying could already be predefined in the solution state by interactions of solvent and solutes: single P3HT chains and F_4TCNQ molecules. To investigate the blends, UV-Vis spectra of the mixed solutions were recorded. These and corresponding fits are shown in Figure 6.5 for chloroform and chlorobenzene. As fit inputs,

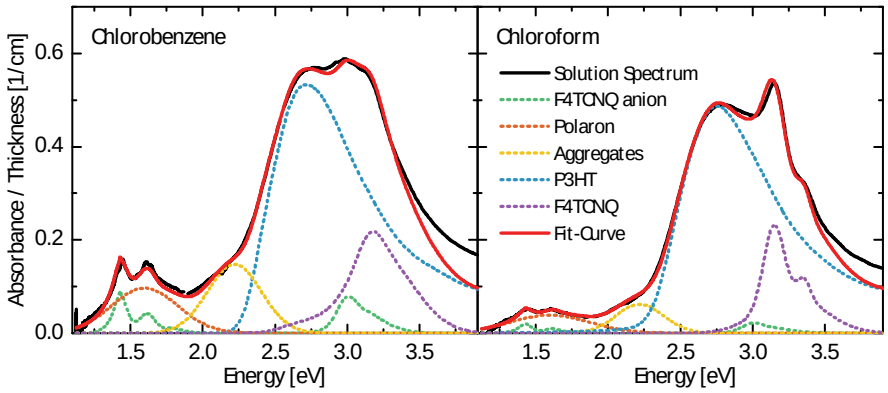

Figure 6.5: UV-Vis absorbance spectra of doped P3HT dissolved in chlorobenzene (left) and chloroform (right). The black line shows the measured spectrum and the red line represents a fit composed of the shown components (dotted lines). Pristine dissolved F_4TCNQ (purple) and P3HT (blue) were measured and used as fit input. The F_4TCNQ anion spectrum (green) was extracted from [88, 113] and the aggregate (yellow) and polaron (orange) contribution was approached with a gaussian.

several contributions were taken into account:

- neutral, disordered P3HT and F_4TCNQ. The spectra were recorded separately with dissolved P3HT and F_4TCNQ.
- charged F_4TCNQ (labeled as F_4TCNQ anion). The spectrum was extracted from references [113] and [88] and used as input for the fit.
- charged P3HT (polaron). The polaron is approached with a gaussian. From the fits to the spectra, the true nature of the charged P3HT absorptions cannot be deduced: It could originate from polarons or bipolarons, which were described as the equilibrium charge storage configuration in the solution state in the past [134, 142].
- P3HT aggregates (ordered domains). To minimize the amount of fitting parameters, this contribution is approached with a gaussian, centered at 2.2 eV. Physically correct, this contribution would be fitted with a Franck-Condon series as done for pristine P3HT in Section 5.1.2. Since the spectra of pristine dissolved P3HT do not show additional absorptions in the spectral range below 2.5 eV, the aggregates are to be comprised of charged P3HT.

Detailed fit parameters are listed in the appendix, Table A.2. A comparison of the measured spectra and corresponding fits reveals significantly stronger absorptions below 2.5 eV in solutions of chlorobenzene. In this spectral range, charged P3HT and F_4TCNQ as well as P3HT aggregates absorb. While the correlation between an increase in absorption of charged P3HT and charged F_4TCNQ is clear, the question arises, why the measured spectra indicate a correlation of the absorption of these charged species with P3HT aggregate formation. Gao, Niles, and Grey answer this question with the finding that polaron and F_4TCNQ-anion absorptions only occur in solutions of regioregular P3HT, whereas they are not observed in regiorandom P3HT, which is not able to form ordered structures [20]. An interplay between the ability to form ordered structures and a further stabilization of the doping and polaron due to the planarization upon charge transfer [131] and aggregation could be a possible mechanism. These findings imply that F_4TCNQ-doped P3HT in chlorobenzene already forms ordered domains in the solution state whereas this aggregate formation is significantly smaller in chloroform and not present at all in pristine P3HT. Such an aggregate formation in chlorobenzene solutions was also observed by Jacobs *et al.* [25].

The question why such aggregates form in chlorobenzene solution can be answered by analysis of the solubility. It was shown in the past that for pristine P3HT, the addition of a solvent that poorly dissolves P3HT leads to precipitation of ordered aggregates (for regioregular P3HT) [134]. However, both pristine P3HT and F_4TCNQ are known

to dissolve without aggregation in the used concentrations in chloroform [49, 107, 113, 131, 136, 137] and chlorobenzene [20, 88, 97, 131]. This can also be deduced from the UV-Vis spectra of solutions in Figure 6.5. The feature of P3HT aggregates at 2.2 eV only emerges in blend solutions and mainly in chlorobenzene. This implies that not the solubility of the pristine materials in chloroform and chlorobenzene is crucial, but the solubility of the charged molecules or even molecule-pairs in the case of P3HT:F_4TCNQ-complexes. Being polar themselves due to the charge transfer, the solubility of charged molecules can strongly depend on the polarity of the solvent. The question if charge transfer takes place at all already in solution can be answered by the observation of a rapid color-change upon mixing F_4TCNQ and P3HT solutions, indicating immediate charge transfer. A possible parameter to evaluate the polarity of a solvent is the normalized molar electronic transition energy of a solvatochromic dye E_T^N (whereas a higher value corresponds to a higher polarity): $E_T^N(CB) = 0.188\,\mathrm{kcal\,mol^{-1}}$ compared to $E_T^N(CF) = 0.259\,\mathrm{kcal\,mol^{-1}}$ [143]. This implies a better solubility of charged molecules and hence less aggregation in chloroform compared to chlorobenzene—which is exactly what is observed in the UV-Vis spectra. This effect of aggregation is expected to become more and more apparent when increasing the concentration of charged molecules from pristine P3HT towards highly doped P3HT. In addition to the static polarity, polarizability effects which are accounted for with the dielectric constant might play a role: The higher dielectric constant of 5.54 for chlorobenzene compared to 4.77 for chloroform [144] could, for instance, facilitate the formation of aggregates due to an increased screening of charges on dopant and host.

6.5 FROM BLEND SOLUTIONS TO THIN FILMS

What is the mechanism that leads from a state where aggregation is observed in chlorobenzene solutions to dried thin films which are less ordered and less conductive than those from chloroform? Several aspects might play a role here. First, there is evidence in literature that the aggregates forming in solution could be made up of aggregated P3HT with F_4TCNQ-molecules surrounding them [25]. In the process of film formation, this could hinder the inter-connectivity of such aggregates *via* tie-chains, which are known to be crucial for the overall conductivity [18, 112]. However, this mechanism alone can not explain the significantly more pronounced π-π stacking in films spin-cast from chloroform. In chloroform, several prerequisites for the formation of an ordered P3HT film are fulfilled. First, P3HT and F_4TCNQ are homogeneously distributed in the solution. Second, as charge transfer takes place already in solution, the backbone planarity is significantly increased [131]. This is an ideal starting point for the

formation of crystallites upon drying since the backbones need to planarize in any case to be able to form π-π stacks [18, 103, 104]. In chlorobenzene solutions, host and dopant molecules are not homogeneously distributed and already pre-aggregated. These aggregates seem to hinder the formation of a degree of order comparable to the one arising from chloroform solutions. This picture fits to the observed π-π double-peak in films from chlorobenzene and the strong π-π stacking measured in films from chloroform with electron diffraction (Figure 6.1).

6.6 DISCUSSION

Studies on P3HT:F_4TCNQ in the past often used either chloroform or chlorobenzene, leading to inconsistencies as recently noticed by Salzmann and Heimel [2]. This work can fill the gap and help to resolve the open questions. As a summary, the whole process of P3HT and F_4TCNQ interacting in solution and the formation of more or less ordered thin films is depicted in Figure 6.6. Note that—as discussed in Chapter 8—the dopants are believed to reside in the lamellar stacking and not in the π-π stacking of P3HT crystallites which is indicated in the zoom-in in of Figure 6.6. Concluding, the doping

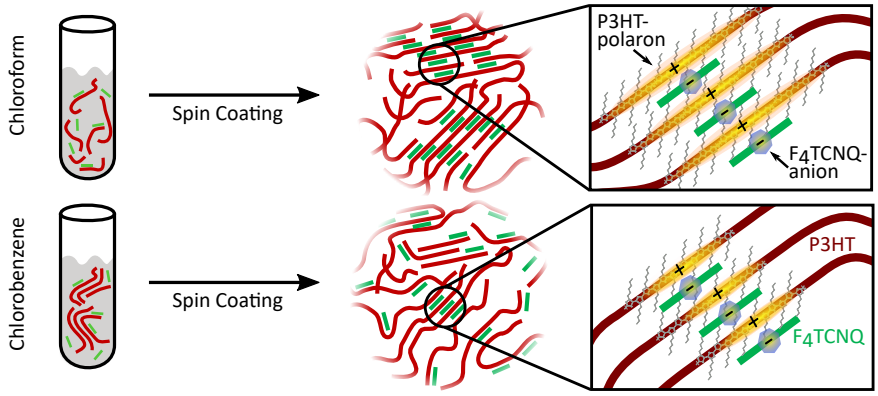

Figure 6.6: Schematic drawing of the formation of order from the dissolved state to dried thin films for P3HT spin cast from the solvents chloroform and chlorobenzene.

of P3HT in case of chloroform as solvent led to an increase of order in terms of π-π stacking compared to undoped P3HT, measured with electron diffraction. This effect can be traced back to interactions of dopant, polymer, and solvent already in the solution state, leading to aggregation in chlorobenzene solutions. These aggregates exhibit distinct absorptions around 2.2 eV and enable furthermore the observation of P3HT polaron and anion absorptions. The solvent polarity is identified as main driving factor. In dried thin films, the increased π-π stacking in films from chloroform leads to increased conjugation length of the polymer chains which allows the polarons to delocal-

ize more. This induces a red-shift of the P1 polaron absorption in IR spectra. As a consequence, the lateral conductivity is significantly higher in thin films from chloroform. This finding demonstrates that the processing guidelines for pristine materials cannot be transferred to doped materials. The charging enables additional mechanisms that in the shown case dominate the thin film formation. In the case of P3HT:F_4TCNQ, the boiling point of the solvent hence does no longer represent the most important solvent parameter in the production of highly conductive thin films as it is the case for pristine P3HT. While this relationship can be seen as general, additional factors such as the overall solubility of dopant and host might also play a role in other material systems.

7

COMPARISON OF BLEND AND SEQUENTIAL DOPING

As discussed in the previous chapter, the processing of doped polymer layers from blend solutions demands for extensive knowledge about the materials as well as interactions between materials and solvents. Additionally, solvents are needed that dissolve both the polymer and the dopant. Especially in case of F_4TCNQ, this is challenging since a solubility is only given in comparably low concentrations of up to $1\,g\,l^{-1}$ whereas P3HT for example is soluble with tens of $g\,l^{-1}$. In the past, doped thin layers were mainly produced from blend solutions or by simultaneous thermal evaporation in vacuum (which is not possible for polymers such as P3HT). However, one property of small molecule dopants gained increasing attention recently: the ability to diffuse readily at room temperature in and into P3HT layers [145, 146]. Such dynamic dopant movements in organic semiconducting materials are analyzed in detail in Part II of the results and discussion. Here, only a brief introduction is given and equilibrium situations are analyzed. One way to utilize this diffusion property is to thermally evaporate dopant molecules in vacuum on a solution-processed P3HT thin film. Although this technique allows for a precise control of critical parameters like dopant concentration, substrate temperature, evaporation rate, and more, it contradicts the original intention to use solution-processable polymers in the first place: the potential to print—ideally all parts of—organic semiconductor devices from solution.

A possible solution to this problem was recently introduced by Scholes *et al.* and Jacobs *et al.* They propose a technique with which a sequential processing of small molecule dopants from solution becomes possible: by spin coating the dopants from a solvent that on the one hand dissolves the dopant, but on the other hand does not dissolve the underlying P3HT layer [24, 25]. Such orthogonal solvents can be found for the combinations of P3HT with F_4TCNQ and also with $Mo(tfd\text{-}CO_2Me)_3$: While the beforehand mentioned solvents like chloroform or chlorobenzene are used for P3HT, acetonitrile dissolves both dopants without impact on a P3HT thin film. As described in Section 4.2, dopant and host material are separately dissolved using the orthogonal solvents first. P3HT is then spin coated, and the dopant is subsequently spin-cast on the already dry P3HT thin film. The additional benefit of this technique is that the underlying P3HT layer can be tuned in terms of film thickness and morphology as described in Chapter 5 before getting in touch with the dopant.

In the following, differently doped P3HT layers are compared to shed light on whether comparable film properties can be achieved. Although sequentially spin coated F_4TCNQ-doped P3HT layers were shown to achieve comparable and even higher doping efficiencies than films from blend solutions [25], a comprehensive comparison including sequential deposition from thermal evaporation was not yet shown for the dopant Mo(tfd-CO_2Me)$_3$. This chapter aims at comparing the properties with electron diffraction and infrared spectroscopy.

7.1 ANALYSIS OF THE STRUCTURAL ORDER: ELECTRON DIFFRACTION

Figure 7.1 displays radial profiles of electron diffraction patterns for differently doped P3HT thin films. The left part focuses on the diffraction signal of the (100)-orientation (lamellar stacking) with a spacing of around 1.6 nm and the right part shows the region around 3.8 Å where the (010)-orientation (π-π stacking) becomes visible. *P3HT* represents the undoped reference profile with clearly visible peaks from lamellar as well as π-π stacking. *P3HT ac* is a control experiment to study the impact of pure acetonitrile on the ordered fraction of P3HT. Jacobs *et al.* assume that acetonitrile is capable of swelling only amorphous regions of P3HT without swelling or dissolving crystallites [25], which was recently supported by X-ray diffraction measurements [22]. In the electron diffraction profile of *P3HT ac*, it can be seen that upon spin coating pure acetonitrile on top of a dried P3HT film, both spacings remain visible, although the ratio of intensities between them changes in favor of lamellar stacking. Importantly, the stacking distances do not change, implying that ordered regions in the P3HT retain their structure. *P3:Mo-mix* depicts a P3HT:Mo(tfd-CO_2Me)$_3$ thin film that was prepared from a blend solution with a defined doping ratio of 10:1. No signal of lamellar stacking is visible in this case. The π-π stacking however can still be observed, although the spacing decreased by roughly 0.08 Å. Such a shift in π-π spacing was already observed for F_4TCNQ-doped P3HT in Chapter 6. Possible origins of this shift in π-π spacing are discussed in detail in Chapter 8. The formation of phase-separated Mo(tfd-CO_2Me)$_3$-crystals can be excluded as reason for this shift since ordered domains of Mo(tfd-CO_2Me)$_3$ do not show a spacing comparable to that of either the (100)- or (010)-orientation of P3HT (purple dotted line labeled as *Mo* in Figure 7.1). An exact analysis of the absolute peak intensity is not performed here since an identical alignment of the transmission electron microscope would be required for each measurement. Variations in the electron dose can alter the measured peak intensity and small deviations in film thickness and doping ratio would further falsify intensity analyses. *P3:Mo-seq-s* describes sequentially doped P3HT with the dopant being applied from solution. In this

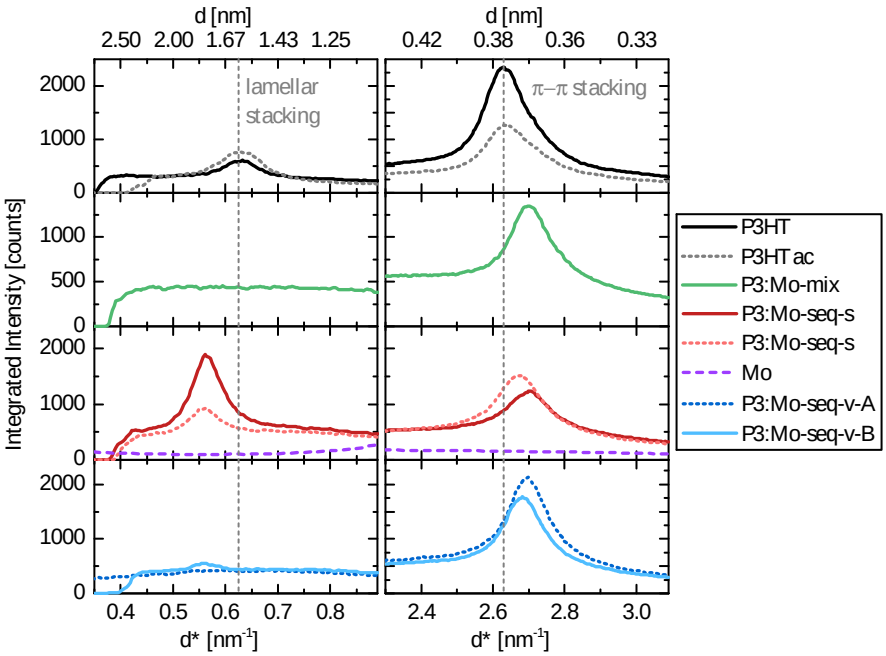

Figure 7.1: Radial profiles of electron diffraction patterns measured on thin films of pristine and differently doped P3HT. P3HT ac: P3HT thin films washed with acetonitrile. P3:Mo-mix: P3HT & Mo(tfd-$CO_2Me)_3$ both dissolved in chlorobenzene and mixed prior to spin coating. P3:Mo-seq-s: Mo(tfd-$CO_2Me)_3$ spin coated from acetonitrile onto an already dried P3HT thin film. P3:Mo-seq-v: Mo(tfd-$CO_2Me)_3$ evaporated with (15 ± 5) Å min^{-1} (A) and 2.6 Å min^{-1} (B) onto an already dried P3HT film in UHV conditions.

case, Mo(tfd-$CO_2Me)_3$ was dissolved at a concentration of 1 g l^{-1} in acetonitrile and spin coated on top of the dried P3HT film. Due to the ability of Mo(tfd-$CO_2Me)_3$ to diffuse into the P3HT film [146] which is further facilitated by the supposed swelling [22, 25], this technique leads to intermixed films of P3HT and Mo(tfd-$CO_2Me)_3$. It can be seen that in this case, the lamellar spacing is still observed and hence not destroyed by the sequential deposition of Mo(tfd-$CO_2Me)_3$. The two profiles shown demonstrate that with this technique, the local structural order can vary. Some regions show an even stronger signal from the lamellar stacking compared to the π-π stacking. Remarkably, a shrinkage of the π-π spacing comparable in magnitude to the mixed doping is observed. Additionally, the spacing of the lamellar stacking increases, just as for the case of F_4TCNQ-doped P3HT in Chapter 6. As third doped P3HT sample, two profiles named *P3:Mo-seq-v* are shown in Figure 7.1. Both profiles are recorded from P3HT films with thermally evaporated Mo(tfd-$CO_2Me)_3$ on top. They differ in the rate the Mo(tfd-$CO_2Me)_3$ was evaporated (*P3:Mo-seq-v-A* with 10 Å min^{-1} to 20 Å min^{-1} and *P3:Mo-seq-v-B* with 2.6 Å min^{-1}). As in the case of the mixed doping technique, no signal of lamellar stacking

is observed for the evaporation rate *A*, and only a small peak is visible for evaporation rate *B*, which is shifted to a larger spacing compared to pristine P3HT. As in both differently doped samples before, the π-π stacking remains visible, but shifted to smaller spacings for both evaporation rates.

Since the change in π-π spacing is analyzed in detail in the following chapter, the discussion presented here focuses on the lamellar spacing. The extinction of the lamellar stacking peak in the case of mixed doping could be due to a residence of Mo(tfd-$CO_2Me)_3$ molecules at the side chains of P3HT crystallites. With this, the formation of well ordered lamellar stacking would be inhibited. The observation of this peak in the sequential doping from solution would fit to this hypothesis when keeping in mind that in this case, lamellar stacking is already formed in the pristine P3HT film prior to the doping. The supposed swelling effect of acetonitrile in this case would not tear apart the ordered domains in the (100)-orientation. Even for an infiltration of the lamellar stacking by the comparably large Mo(tfd-$CO_2Me)_3$ molecules, the crystallites in the lamellar stacking directions would sill be preserved—with a larger lamellar spacing. However, efficient doping in terms of a conductivity enhancement and a peak shift of the π-π spacing is observed. This hints to a doping mechanism where charged dopant molecules reside at the boundary of crystallites or at the side chains in lamellar direction. In this situation, the positive charges are transferred to the inside, the polymer backbone, as previously proposed for a different host:dopant system by Gao, Niles, and Grey [20]. At first sight, the (almost complete) disappearance of the lamellar spacing peak of the sequential doping from thermal evaporation of the dopant in Figure 7.1 (*P3:Mo-seq-v*) contradicts this idea. Also here, the lamellar stacking is formed prior to doping and ideally should be preserved by evaporation of the dopant. A possible explanation can be given by the excess energy that dopants have when they impinge the polymer film due to the process of thermal evaporation. To explain the observed diffraction profiles, this energy would need to be larger for a higher evaporation rate which is reasonable since the evaporation rate is controlled by the temperature and hence energy that is transferred to the dopant molecules. A higher evaporation rate would then lead to less lamellar stacking, which is observed. Due to the introduced energy, Mo(tfd-$CO_2Me)_3$ molecules could not only intercalate in the lamellar spacing but even tear apart crystallites in this orientation. However, the magnitude of this effect is surprising since the evaporation temperature of Mo(tfd-$CO_2Me)_3$ in vacuum conditions is comparably low (~ 130 °C) and a heating of the substrate during evaporation is not indicated by in situ IR measurements in comparable experiments. Additionally, the dopants would have to "carry" this energy through the complete film thickness of

50 nm. A future experiment could investigate this phenomenon with evaporation of Mo(tfd-$CO_2Me)_3$ onto cooled samples, where effects of introduced energy should be less pronounced.

7.2 POLARON DELOCALIZATION & CHARGE TRANSFER: INFRARED SPECTROSCOPY

To expand the comparison further, Figure 7.2 displays IR spectra of differently doped P3HT films, measured by Vipilan Sivanesan.[1] *P3:Mo-seq-s* labels sequentially doped P3HT from solution (Mo(tfd-$CO_2Me)_3$ from acetronitrile). *P3:Mo-seq-v* describes sequentially doped P3HT by thermal evaporation of Mo(tfd-$CO_2Me)_3$. The abbreviations *LT* and *RT* denote low temperature (190 K) and room temperature and describe the temperature at which the substrate was kept during evaporation of the dopant. However, the spectra shown are all measured at room temperature, the *LT*-sample was hence allowed to equilibrate to room temperature before the spectrum was recorded. *P3:Mo-mix* is the P3HT:Mo(tfd-$CO_2Me)_3$ thin film that was processed from blend solution. The spectra are shifted but not stretched or compressed along the y-axis to facilitate a comparison of peak positions. Figure 7.2 reveals that all sequentially doped P3HT thin films show

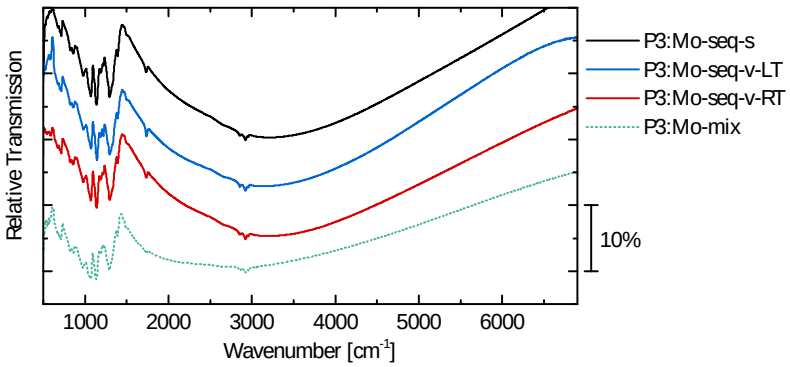

Figure 7.2: Relative transmittance at normal incidence of sequentially and blend (P3:Mo-mix) doped P3HT thin films. P3:Mo-seq-s: Mo(tfd-$CO_2Me)_3$ spin coated from acetonitrile onto a dried P3HT thin film. P3:Mo-seq-v: Mo(tfd-$CO_2Me)_3$ evaporated onto dried P3HT film in UHV conditions. Whilst Mo(tfd-$CO_2Me)_3$ was evaporated at 190 K (LT) and room temperature (RT) onto P3HT thin films, IR-spectra were measured at room temperature. The spectra are shifted with respect to each other in direction of the y-axis.

a comparable overall shape of the spectrum. The broad electronic excitation of the positively charged P3HT (P1 polaron absorption) does not differ significantly in shape and position. It peaks for all three processing conditions at roughly 3100 cm^{-1}. Furthermore, the IRAV-modes below 1500 cm^{-1} resemble each other in appearance. In con-

1 Group of Prof. Pucci, Kirchhoff-Institute for Physics, Heidelberg University

trast, the polaron peak of the sample from mixed doping is shifted to lower wavenumbers, peaking at around 2700 cm^{-1}. The observation of almost identical P1 polaron absorptions from dopant evaporation onto cooled P3HT thin films and sequential processing from a solvent questions the importance of swelling that was highlighted as fundamental for sequential doping recently [22].

The differences between mixed and sequentially doped P3HT films can be rationalized with the different morphologies these films develop during film formation. While all films for the sequential doping are made of pristine P3HT prior to doping, both Mo(tfd-CO_2Me)$_3$ and P3HT are present during film formation for *P3:Mo-mix*. As it is discussed in Chapter 6 in detail, the interactions between solutes and solvent can largely influence the thin film morphology and with that the structural order. The lower energy of the polaron peak in the mixed case points towards a more delocalized polaron which is connected to a higher conjugation length in such films. This is surprising, since this film was spin cast from chlorobenzene, which showed inferior formation of structural order in case of P3HT:F_4TCNQ. However, the excellent solubility of Mo(tfd-CO_2Me)$_3$ compared to F_4TCNQ could counterbalance the diminishing solubility of charged species in chlorobenzene which would explain the observed behavior. The similarities between the sequentially doped films in the IR spectra point towards an almost unchanged structure in the (010)-orientation (π-π stacking), although the presence of lamellar stacking varies strongly between the samples as shown above in Figure 7.1. Spectra of sequentially doped films of different temperatures onto which Mo(tfd-CO_2Me)$_3$ was evaporated do not differ significantly. As discussed in part two of this thesis, the diffusion of small molecule dopants is a temperature-activated process. Anticipating the results discussed in that chapter, Mo(tfd-CO_2Me)$_3$ does not diffuse into the P3HT layer at a temperature of 190 K (*LT*). It can therefore be safely assumed that except for the upper layers of P3HT, the P3HT and its structure is not influenced by the evaporation of Mo(tfd-CO_2Me)$_3$ molecules. Just upon equilibrating towards room temperature, the dopant molecules start to diffuse into the P3HT film. The observation that both the cooled and not cooled P3HT reveal a similar IR transmittance spectrum in the doped case furthermore supports that the intrachain order and conjugation length—which is stabilized by stacking along the π-π direction—is not altered significantly by diffusion of Mo(tfd-CO_2Me)$_3$ into the P3HT layer.

Since the position of the characteristic C=O-stretching vibration of Mo(tfd-CO_2Me)$_3$ does not shift measurably upon doping, a reliable evaluation of the amount of charge transfer cannot be made. However, conductivity measurements indicate comparably strong doping in all cases, ruling out a partial charge transfer which was described

to be much less efficient in generating free charges [2, 14]. Furthermore, the varying amount of order in the lamellar stacking direction is not expected to heavily influence charge transport since the interchain conductivity in this direction is in any case significantly lower compared to the intrachain and interchain conductivity in π-π stacking direction (due to the bad electrical conductivity of the side chains) [132]. A detailed comparison of conductivity and doping efficiency is not given here due to the numerous parameters that—additionally to the doping concentration—impact these quantities. Among them are the effects of temperature while evaporation, including a desorption of dopants in the vacuum that would reduce the total number of dopants in the film, the undefined number of dopant molecules that enter the film in case of solution sequential doping, and more.

7.3 SUMMARY

In summary, different sequential and mixed doping techniques seem to mainly affect the structure of P3HT thin films in the lamellar stacking as it could be deduced from electron diffraction measurements (Figure 7.1). One possible explanation for the observed effects is a residence of dopant molecules in or at the side chains which is detrimental for the formation of order in the lamellar direction. Whereas the π-π spacing shrinks upon doping for all doping techniques, IR spectroscopy (Figure 7.2) implies only minor differences in intrachain order and the connected conjugation length between all sequentially doped samples, as concluded from the position of the P1 polaron absorption. The following chapter focuses on the origin of the decrease in π-π spacing.

8

INFLUENCE OF DOPING ON CRYSTALLINE PACKING IN POLYMERS

As noted in the previous chapter, the lattice spacing in the π-π stacking direction shrinks upon doping. The following gives a brief overview of existing related observations in literature and prevalent hypotheses that could explain this effect. After a discussion of the π-π stacking measurements conducted for this thesis, a novel approach to explain the observed change in lattice spacing is presented.

The impact of doping on the structural order of organic semiconducting polymers was mainly investigated on the prominent example of P3HT:F_4TCNQ in literature. Duong *et al.* observed a change in crystal packing at doping concentrations exceeding a dopant molar fraction of 0.03 [97, 137]. They propose the formation of mixed crystals of P3HT and F_4TCNQ that lead to a shift of the π-π spacing and the formation of a double peak in X-ray diffraction. This picture was picked up by numerous publications, which led to the prevalent believe that the change in π-π spacing upon doping is caused by intercalation of F_4TCNQ molecules into the π-π stacking of P3HT crystallites [24, 25, 88, 97, 137, 138]. The observed shorter spacing in X-ray [24, 97, 137, 147] or electron [25, 89] diffraction would then no longer be the π-π stacking of adjacent P3HT chains, but the spacing between P3HT chains and the planar, intercalated F_4TCNQ molecules. However, Gao *et al.* draw a picture in which F_4TCNQ is located at the boundaries of ordered domains. The transferred charges in this picture separate into the crystallites in an energetically more favorable state, which is caused by the higher conjugation length of the more planar P3HT chains in such a crystal, allowing the charge to delocalize stronger in comparison to unaggregated chains [20, 21, 148]. More recently, Scholes *et al.* present measurements implying that the picture of F_4TCNQ intercalating into the π-π stacking of P3HT might be wrong [22], which is supported by a work that finds no alignment of F_4TCNQ molecules with the π-π stacking direction in strongly aligned rubbed P3HT thin films [139]. The following sections provide further evidence that an intercalation of dopants cannot be responsible for the shrinking π-π spacing. Furthermore, DFT calculations are utilized to shed light on the underlying mechanism that induces changes in π-π stacking of P3HT crystallites upon doping, which was not yet discussed thoroughly in literature.

8.1 MEASURING THE STACKING DISTANCES IN CRYSTALLITES: ELECTRON DIFFRACTION

As it was briefly mentioned in the previous chapter, the shrinkage of π-π spacing in P3HT crystallites is observed independent of dopant (F_4TCNQ and Mo(tfd-CO_2Me)$_3$) and doping technique (mixed and sequential doping from solution or thermal evaporation), as summarized in Figure 8.1. This graph shows the π-π spacing measured by electron diffraction in a TEM for untreated and acetonitrile-washed pristine P3HT (*P3HT* & *P3HT ac*), P3HT:Mo(tfd-CO_2Me)$_3$ (*P3:Mo*), and P3HT: F_4TCNQ (*P3:F4*). Three different doping techniques are compared for P3HT:Mo(tfd-CO_2Me)$_3$: films spin cast from a blend solution (*mix*), sequential doping from acetonitrile solution (*seq-s*), and thermal evaporation of Mo(tfd-CO_2Me)$_3$ (*seq-v*). The value of π-π spacing for F_4TCNQ-doped P3HT is displayed for spin cast films from blend solutions in the solvents chloroform (*CF*) and chlorobenzene (*CB*). The complete diffraction profiles are shown in previous chapters (Figure 6.1 for P3HT: F_4TCNQ and Figure 7.1 for P3HT:Mo(tfd-CO_2Me)$_3$). Doping concentrations for the blend doping are 10:1. The exact amount of dopants in the films prepared by sequential doping is not exactly known, but expected to be comparably high. As it can be

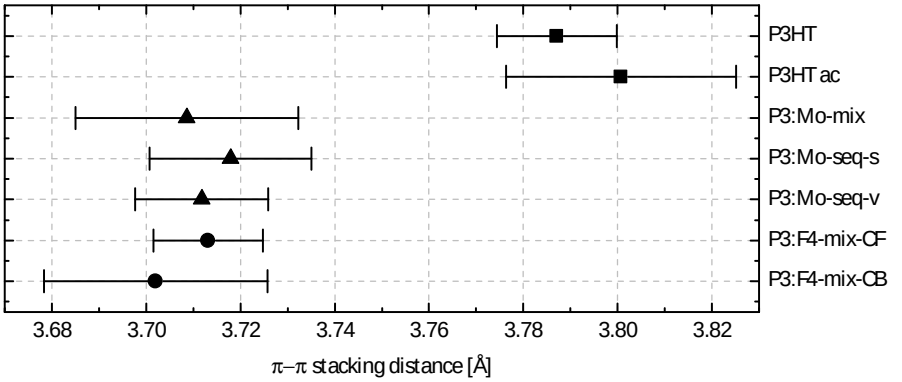

Figure 8.1: π-π stacking distances extracted from electron diffraction measurements for doped and undoped P3HT. Irrespective of doping technique and dopant, the π-π stacking distance is smaller in doped compared to pristine P3HT. The errors originate from sample-variation as well as from local variations on the measured samples.

seen in Figure 8.1, pristine P3HT reveals a spacing of (3.79 ± 0.01) Å in contrast to spacings around 3.71 Å for doped P3HT. Within the error that is calculated from deviations of measurement spots on the same sample and measurements of different samples, all values are equal. This means that the π-π spacing shrinks independent of dopant and doping technique by roughly (0.08 ± 0.01) Å. If, as usually assumed, the intercalation of the dopant into π-π stacks of P3HT chains would be the main driving factor for the observed shift, Mo(tfd-CO_2Me)$_3$

should induce a different spacing compared to the differently sized F_4TCNQ. While F_4TCNQ is a flat molecule which can be imagined to easily fit in between the backbones of quite flat adjacent P3HT chains, Mo(tfd-CO_2Me)$_3$ has a three-dimensional structure and larger spatial dimensions. Figure 8.2a shows the three-dimensional optimized geometry of Mo(tfd-CO_2Me)$_3$. To estimate the height of such a molecule, the distance between planes spanned by the three topmost fluorine atoms A_1 and the plane spanned by the lowest three hydrogen atoms A_2 is calculated to 6.15 Å. From this rough estimation, it becomes clear that an intercalation of Mo(tfd-CO_2Me)$_3$ in between P3HT chains in the π-π stacking direction would be unlikely to cause diffraction patterns similar to that of F_4TCNQ-doped P3HT, including the same shift of 0.08 Å in π-π spacing. For comparison, the molecular structure of F_4TCNQ in a top- and side-view is displayed in Figure 8.2b and c.

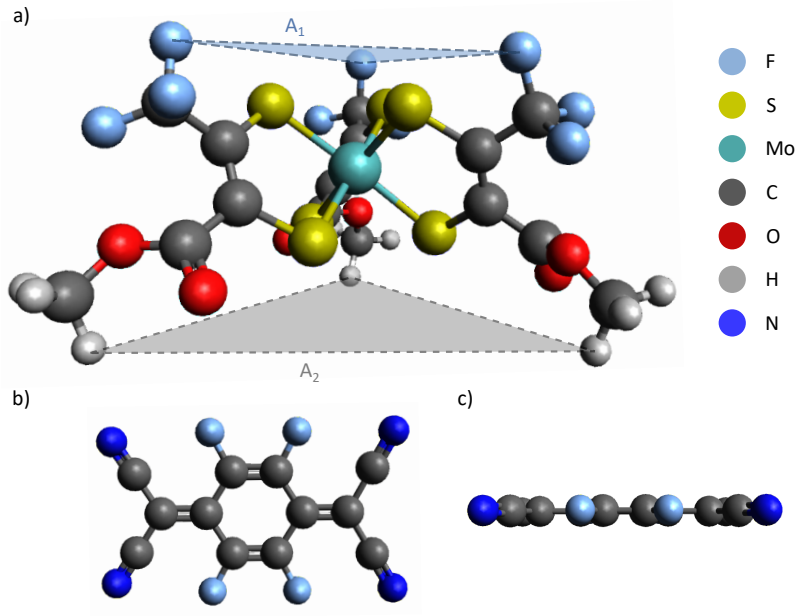

Figure 8.2: 3D molecular structures of Mo(tfd-CO_2Me)$_3$ (a) and F_4TCNQ (b, c). The planes A_1 and A_2 are used to estimate the height of a Mo(tfd-CO_2Me)$_3$ molecule. The colors represent different atomic species as given in the legend.

Further evidence that such a change in π-π spacing is a general phenomenon is given by literature: Thelen *et al.* observed a shrinkage of π-π spacing upon electrochemical doping P3HT with bis(trifluoromethanesulfonyl) imide ($TFSI^-$) anions [147]. They—as confirmed by Guardado and Salleo—conclude that, at voltages high enough, the $TFSI^-$ anions are able to enter the alkyl side chain regions of crystallites, which represent the connecting elements in lamellar stacking direction [149]. This leads to an irreversible expansion of the lamellar spacing, similar to what is observed in molecular doping in this thesis (see Figure 6.1 for P3HT:F_4TCNQ and Figure 7.1 for

P3HT:Mo(tfd-$CO_2Me)_3$). Based on the molecular packing calculated by Himmelberger *et al.* [150], the geometric effect of straightening alkyl side chains initialized by intercalated anions is given as one possible explanation for the contraction of π-π stacking in this case [149]. The planarization of P3HT chains upon doping was given as alternative explanation in the past [23]. Interestingly, a contraction of π-π stacking is not only observed for P3HT, but also for the polymer PBTTT[1], doped with F_4TCNQ [151]. This polymer also develops a semi-crystalline structure with crystallites made of lamellar and π-π stacked polymer chains [152]. The amount of shrinkage found by X-ray diffraction is quite comparable to the one found for electrochemical doping of P3HT [147, 149]. The finding that a contraction of π-π spacing is measured for two different polymers and strongly differing dopants, ranging from small ions to the planar F_4TCNQ molecule and the voluminous Mo(tfd-$CO_2Me)_3$ dopant, questions the mere straightening of alkyl side chains by intercalation of dopants as explanation. In the following section, the charging of the polymer backbone that is common to all previously described material combinations and processing techniques, is investigated as possible basic cause of the smaller π-π stacking distance for the first time.

8.2 APPROACHING THE UNDERLYING MECHANISM: DFT CALCULATIONS

Density functional theory (DFT) calculations are shown in the following as an approach to access the structural change of P3HT or similar crystals upon charging. The DFT calculations were performed by Wenlan Liu.[2] Equilibrium geometries of the bulk P3HT and polythiophene were calculated with the PBE [153] functional in combination with the projector-augmented wave (PAW) method [154, 155], which are implemented in the VASP code [156, 157]. The oligomers structures were optimized at the B3-LYP/TZVP level [158–162] with the TURBOMOLE program package [163], and localized molecular orbitals were obtained with a modified Pipek-Mezey method [164, 165]. Since an atomistic reproduction of complete P3HT thin films with DFT is not possible with computing power available to date, simplifications and reductions to smaller systems have to be made. The question arises, which minimal system still appropriately describes the real situation, but at the same time, keeps the need for computational power at a reasonable level.

For the calculations shown here, a dimer system of two molecules with a variable amount of thiophene units with and without side chains is chosen. The distance between these chains represents the π-π spacing . Since the thiophene units are not completely planar, but

1 poly(2,5-bis(3-tetradecylthiophen-2-yl)thieno[3,2-*b*]thiophene)
2 Group of Andreas Köhn, University of Stuttgart.

instead tilted with respect to each other [103, 104], parallel planes are introduced for which the sum of the root mean square deviations (RMSD) of the distances between the atoms and the respective plane is minimized. However, P3HT chains are more planar in ordered structures compared to single chains and planarize even more when charged [103, 131], reducing the error introduced by this approach. Since P3HT as a polymer is comprised of chains that contain tens to hundreds of thiophene units, depending on the molecular weight, the question arises how many thiophene units are necessary to appropriately describe the charging upon doping. Previous studies point to an interaction of one F_4TCNQ molecule with four thiophene units [20, 49, 97, 120], which is used here as minimum meaningful length. First calculations to understand the basic properties of this system consider the dimer of two molecules made of four thiophene units each (quaterthiophene, 4T) without side chains, as shown in Figure 8.3a. The system with alkyl side chains is depicted in Figure 8.3b. Before discussing the calculation of spacing between the molecules, a closer look at the electronic orbitals is instructive.

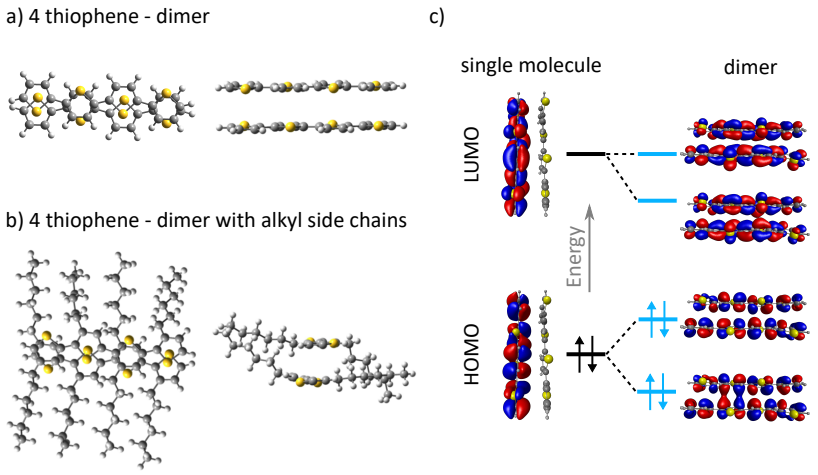

Figure 8.3: a, b) Relaxed 3D molecular structures of a quaterthiophene dimer without (a) and with (b) alkyl side chains in. c) Highest occupied (HOMO) and lowest unoccupied (LUMO) molecular orbital of the single quaterthiophene as well as the dimer.

Figure 8.3c shows the HOMO and LUMO energetic position of the single molecule and of the dimer. It can be seen that for the dimer, a splitting occurs due to interaction of the single orbitals. In the ground (uncharged) state, the LUMO orbitals are not occupied, whereas the HOMO is fully occupied. Upon p-doping, one electron is removed from the system. Due to the pursuit of energy minimization, this electron is missing in the upper level of the depicted two HOMO states, which is an antibonding molecular orbital in contrast to the lower bonding orbital. From this rather elementary consideration, it becomes clear that in the p-doped state, the bonding orbital is weighted

stronger compared to the antibonding orbital, making a decrease of the π-π spacing plausible.

DFT calculations to access the π-π spacing directly were carried out on the same dimer system with and without side chains for a varying number of thiophene units. Figure 8.4a shows the π-π spacing of the neutral dimer in blue and the positively charged (cation) dimer in red. The difference between the corresponding neutral and cationic values represents the decrease of π-π spacing that in a second step can be compared to the shift observed with electron diffraction for p-doped P3HT. The spacing of the neutral dimer is larger than the spacing of the charged system for all lengths calculated. Two effects are visible. First, the π-π spacing decreases for the neutral dimer when increasing the chain length from four units up to 14 units. At the same time, the spacing of the cation increases between four and eight units, reaching a steady state then. This leads to a decrease of the difference in π-π stacking between the neutral and charged state Δ_1 for increasing length of the dimer.

The observation that the π-π spacing is generally smaller for the charged system shows that already the charging without any dopant molecules present affects the system in the direction that is observed with electron diffraction on real doped P3HT samples. The decrease of spacing of the neutral dimer with increasing length can be explained by a relaxation of the system when increasing the size. For the cation, the charging effect decreases with increasing length, since the single additional charge can delocalize stronger, weakening the effect per single thiophene unit. Both effects combined then lead to a decrease of π-π stacking contraction for larger dimers. However, when concerning the finding from literature that the dopant F_4TCNQ interacts only with four thiophene units, the spacing distance Δ_1 for four thiophene units should be the most relevant. For the system without side chains, Δ_1 is calculated to be 0.08 Å, which fits well to the measured value of (0.08 ± 0.01) Å from electron diffraction of differently doped P3HT (see Section 8.1).

Figure 8.4b shows π-π spacing calculations of the same system, but with two charges (bication). For this system, the spacing of the cation is large for a small length, reaches a minimum for eight thiophene units length and increases again for longer dimers. The absolute values from eight units to higher length are—as for the cationic case—smaller than the spacing of the neutral dimer. The observation that the system reaches the minimal π-π spacing distance for exactly eight units length when charged twice shows that the calculations are consistent with the system of one charge that reached its minimum at four units. Below eight units, the dimer is over-saturated with positive charges, leading to a coulombic repulsion of the molecules. For eight units, the system is saturated and dilutes for longer dimers. The difference between neutral and bicationic spacing for eight units

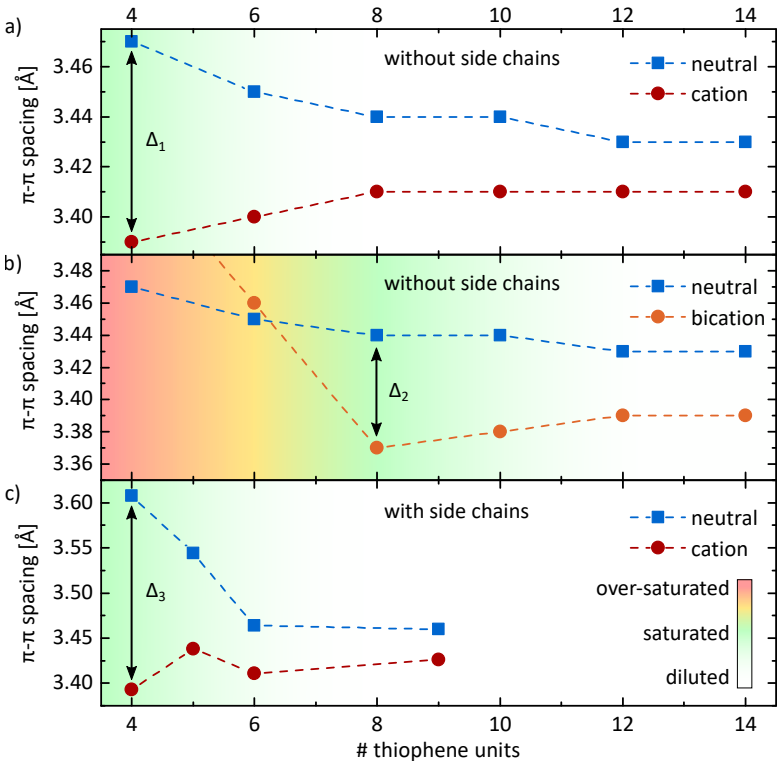

Figure 8.4: Calculated π-π spacing distances for neutral (blue), cationic (red), and bicationic (orange) dimers of quaterthiophene (a, b) and quaterthiophene with hexyl side chains (c). The length of the dimer in units of thiophene monomers is given on the x-axis. The background color-gradient indicates the charge-saturation of the dimer for the cationic or bicationic state.

length Δ_2 resembles the 0.08 Å that were observed for four units in the cationic state and electron diffraction measurements of real doped P3HT.

To take one step towards a more realistic system, Figure 8.4c shows calculations of the π-π spacing for a neutral and singly charged dimer with alkyl side chains, reproducing the chemical structure of P3HT. A decreasing spacing of the neutral dimer for increasing chain length shows the same trend as without side chains. Furthermore, the spacing of the charged dimer is smaller compared to the neutral system, preserving the general trend. The spacing of the cation is minimal with four thiophene units also with side chains, but does not monotonically increase with increasing length—a local maximum is reached for five units length. The absolute spacing difference between neutral and cationic dimer at four units length $\Delta_3 = 0.22$ Å however is much larger than measured experimentally and calculated without side chains.

8.3 DISCUSSION

The DFT calculations for dimers with and without side chains show a clear trend of decreasing π-π spacing upon removing one electron from the system. This fits to the measurements presented in this thesis and observations by others for doped P3HT as well as doped PBTTT [22, 24, 25, 88, 89, 97, 137, 138, 147, 149, 151]. The question if the absolute amount of change in π-π spacing that is induced by a charging of the crystallite is enough to fully explain the experimentally observed shift is not easy to answer. From the calculations shown in Figure 8.4, the dimer structure with side chains (c) is closest to the real situation. Nevertheless, the system is still strongly simplified. Crystallites in real P3HT thin films consist not only of a dimer structure with a few thiophene units in length but can be much larger [24, 93, 166], depending on material properties like the regioregularity and processing conditions as shown in Chapter 5. Although a larger crystal domain is able to host more than one charge, delocalization effects can play a role, which strongly affect the amount of π-π spacing change as shown in Figure 8.4c: a difference of 0.22 Å is calculated for four thiophene units dimer length and an increase to six units already decreases this value to 0.05 Å. Additionally, the influence of side chains can be strong as the differences between the calculations of dimers with and without side chains illustrate. Furthermore, the calculated dimer system with side chains differs from a real dimer which is embedded in a surrounding of amorphous P3HT or other ordered P3HT chains in a larger crystallite. The alignment of chains can be strongly influenced by the surrounding and reversely influences the packing of polymer chains [150]. As suspected by Scholes *et al.*, dopant molecules located at or in the side chains could further change the angle of the side chains relative to the backbone, enabling a registry shift in along the backbone direction [22].

A combination of the considerations leads to the following conclusion: The calculations shown above clearly reveal a decrease of π-π spacing caused by the pure charging without any dopant molecules or restricting surrounding being present. Although this approach of regarding solely the charging provides an important insight by decoupling it from all external influences, it is a weakness at the same time, since absolute values can strongly depend on the exact surrounding. The calculations presented herein therefore cannot exclude that previously suggested mechanisms like the reduced dihedral angle between single thiophene units (planarization of the backbone) [23] upon charging or the reorganization of side chains [139] additionally contribute to the reduction of π-π spacing in doped P3HT crystallites. Although still considered as possible option to date [23, 138], the intercalation of dopant molecules as cause for the shift is found to be

rather unlikely as indicated by the comparison of diffraction data of F_4TCNQ- and Mo(tfd-CO_2Me)$_3$-doped P3HT, which is furthermore supported by recent studies [22, 139].

The results presented in this chapter have implications exceeding the fundamental understanding of molecular arrangement. Thelen *et al.* previously found a clear correlation between charge carrier mobility and doping-induced lattice strain dominated by a decrease in π-π spacing [167]. Hence, the effect of charging on the molecular order and the corresponding change of charge carrier mobility would need to be considered charge transport models for organic field-effect transistors. During operation of OFETs, the switching between charge transport of the intrinsic semiconductor with a low current (off-state) and high current in the on-state is achieved by accumulation of a significant charge carrier density at the interface to a dielectric by application of a gate voltage. The magnitude of charge carrier density of $10^{20}\,cm^{-3}$ for sequentially F_4TCNQ-doped P3HT [22] is close to the charge carrier density in a P3HT field-effect transistor, which is typically around $10^{19}\,cm^{-3}$ [41]. Hence, it can be speculated that a charge-induced decrease in π-π spacing comparable to what was described in this chapter for doped P3HT could be expected in the on-state of transistor operation as well. First measurements employing X-ray diffraction in the channel of a bottom-gate P3HT thin film field-effect transistor were initiated at the end of the experimental work for this thesis. However, experimental difficulties did not allow for an evaluation of the obtained data and future measurements have to show if the proposed mechanism can be observed in OFETs. The change in lattice spacing could extend existing transistor models, additionally to previously considered effects like static side-chain and backbone packing, defects in regioregularity, and occurrence of different polymorphs for P3HT [168].

Results & Discussion

Part II

DOPANT DYNAMICS: DIFFUSION & DRIFT OF MOLECULAR DOPANTS

In Part II of the results and discussion, the dynamic processes of diffusion and drift of molecular dopants are discussed with focus on the latter. First, a brief overview summarizes existing literature on dopant diffusion in Chapter 9. Then, the influence of the host morphology on dopant diffusion is discussed on the basis of optical, IR, and photoelectron spectroscopy measurements in Chapter 10. The controlled drift of molecular dopants is investigated in Chapter 11. This dynamic motion is revealed and analyzed with microscopic and spectroscopic techniques. The influence on charge transport is discussed and the emerging current signature that indicates dopant drift is utilized to compare various material combinations to approach the underlying mechanisms. With the long-term goal of a chemical immobilization, the drift behavior of chemically modified n-type dopants is investigated. This part finishes with the demonstration of memristive devices based on the controlled drift of dopants in P3HT. This class of devices recently gained increasing attention due to their potential use in memory technology and neuromorphic hardware.

9

A SHORT LITERATURE REVIEW

Whereas the first part of the results and discussion focused on static properties of doped thin polymer films, Part II is dedicated to the influence of parameters like concentration gradients or externally applied electric fields on the spatial stability of dopants. In state of the art organic electronic devices such as OLEDs or OFETs, doping is usually restricted to spatially confined regions [15, 169, 170]. A diffusion of dopants out of the designated charge transport or injection layers into for example the emission layer of an OLED or the channel of a transistor would severely deteriorate device performance [171–174]. The following motivates, why dopants can be prone to diffusion or drift, and a brief overview of existing studies on the diffusion of dopants is given.

In inorganic semiconductors, dopants occupy vacancy sites in the crystal lattice of the host and are covalently bound to the surrounding atoms. Doping of organic semiconductors fundamentally differs in two points: First, the host material is usually amorphous or semicrystalline, especially in the case of polymers. Second, dopants are weakly bound to the matrix *via* van der Waals forces. After charge transfer between dopant and host, electron and hole are in many cases still localized, which can lead to additional binding *via* Coulombic forces. Many organic polymers undergo glass transition at temperatures between 0 °C and 200 °C, which increases the probability to overcome the already weak bonds that keep dopant molecules at place [19]. The first generation of dopants was based on monoatomic ions such as iodine or electropositive metals such as lithium. Although they allow for a high conductivity, films doped with these dopants showed poor stability due to diffusion and even sublimation of the dopants [5, 6]. Over time, larger molecular dopants were developed, ranging from the size of F_4TCNQ to bulky molecules like $Mo(tfd\text{-}CO_2Me)_3$ or $C_{60}F_{36}$. Surprisingly, even though $C_{60}F_{36}$ allowed for thermally more stable hole transport layers in OLED devices with the host BF-DPB[1] [175], it was shown to diffuse into the small molecule host MeO-TPD[2] at room temperature [145]. However, the time scales differ compared to the much smaller F_4TCNQ, which readily forms well mixed films when thermally evaporated onto films of the same host material [145]. There are several studies that find or exclude diffusion of various dopants, depending on the host-dopant combination and external parameters such as the temperature. Gao

1 N,N′-[(Diphenyl-N,N′-bis)9, 9,-dimethyl-fluoren-2-yl]-benzidin
2 N,N,N′,N′-tetrakis(4-methoxyphenyl)benzidine

and Kahn find spatial stability of F_4TCNQ in the small molecule host α-NPD[3] up to 80 °C [176], whereas Tyagi, Tuli, and Srivastava observe diffusion already at room temperature [173]. Duhm *et al.* also find diffusion of F_4TCNQ in the more crystalline host CBP[4] [177] and several other studies investigate a dopant diffusion in small molecule host materials [83, 178, 179].

Whereas small molecule host materials are usually amorphous or crystalline, polymers often exhibit a semi-crystalline structure, which is tunable by processing conditions such as the used solvent or annealing steps, as shown in Chapter 5. A complete understanding of which parameters control dopant diffusion in such systems is not yet established. Previously, diffusion of F_4TCNQ was for example observed in the semi-crystalline polymer PBTTT and P3HT [145, 180]. In the semi-crystalline polymer P3HT, the F_4TCNQ-derivative F_4MCTCNQ[5], which possesses greater solubility compared to F_4TCNQ [27], was shown to diffuse more slowly than F_4TCNQ [181]. The reason for this behavior is not yet fully understood. Molecules as large as C_{60} are able to diffuse in and into P3HT at temperatures exceeding 50 °C [182]. Dai *et al.* could show that the small molecule dopant Mo(tfd-CO_2Me)$_3$ diffuses into regioregular P3HT at room temperature, whereas this diffusion was significantly suppressed when mixing P3HT with the C_{60}-derivative ICBA[6] prior to contact with the dopant [146]. This suggests a major influence of the host morphology in terms of free volume and possible pathways that dopants can take. When available volume is occupied, pathways are no longer accessible for a diffusion of dopants. However, a detailed comparison of host materials to gain insight into mechanisms that allow for the formation of free volume and accessible pathways is difficult due to varying processing conditions and different measurement techniques used in existing studies. One approach was made by Li *et al.*, who replaced the alkyl side chains of P3HT with poly(ethylene oxide) (PEO) side chains [183]. They show evidence that F_4TCNQ interacts with the PEO side chains, rendering the new polymer more attractive than P3HT. In their experiment, this leads to a migration of F_4TCNQ from P3HT into the new polymer [183]. A comparable study by Kroon *et al.* found a higher thermal stability of a F_4TCNQ-doped polymer with PEO side chains compared to P3HT doped with F_4TCNQ , indicating that side chain engineering might be one way to hinder dopant molecules from migrating into adjacent layers [184].

The following chapter follows another approach by comparing two host systems that only differ in structural order, but not in chemical composition or processing conditions: regiorandom and regioregular P3HT.

3 N,N′-diphenyl-N,N′-bis(1-naphthyl)-1,1′ -biphenyl-4,4′-diamine
4 4,4′-bis(N-carbazolyl)biphenyl
5 tetrafluoromethyl-oxycarbonyltricyanoquinodimethane
6 indene-C_{60} bis-adduct

10

DOPANT DIFFUSION IN DEPENDENCE ON THE THIN FILM MORPHOLOGY

P3HT is well suited for a study in which only the structural order between samples should be changed. The regioregularity, which is defined by the order of linked thiophene units (see Chapter 4) has large impact on the formation of ordered domains in thin films. As discussed in Chapter 5, regioregular P3HT has a semi-crystalline structure in contrast to amorphous regiorandom P3HT. Furthermore, the degree of crystallinity can be tuned by the regioregularity, whereas single crystals covering whole P3HT films cannot be achieved. In the following, the influence of structural order on the diffusion properties of the small molecule dopants F_4TCNQ and $Mo(tfd\text{-}CO_2Me)_3$ is discussed.

10.1 SEQUENTIAL DOPING OF DIFFERENTLY ORDERED P3HT FILMS

Figure 10.1 shows UV-Vis absorption spectra of differently ordered F_4TCNQ-doped P3HT thin films. *P3HTrra:F_4TCNQ-seq-s* abbreviates regiorandom P3HT, doped sequentially from acetonitrile solution. The highly regioregular P3HT (RR= 96.7 %) is labeled as *P3HTrr*, whereas *P3HT* is still considered regioregular, but with a lower regioregularity of 93.7 %. As it is discussed in Chapter 5, the differences in the UV-Vis absorption spectra of the undoped P3HT (black lines in Figure 10.1) directly relate to differing degrees of order. To approach the question, whether the structural order in such thin films impacts the diffusion behavior of small molecule dopants in and into these films, sequential doping with F_4TCNQ from acetonitrile solution was performed on all three samples. As introduced in Chapter 5, characteristic absorption features appear, originating from the absorption of the charged P3HT (P2 polaron) around 1.5 eV and the F_4TCNQ anion with a double-peak structure below the bandgap of P3HT and around 3 eV. The dotted line in Figure 10.1 shows the absorption of a 10:1 P3HT:F_4TCNQ thin film that was processed from a blend solution. This spectrum serves as reference for the sequentially doped samples. It can be seen that the characteristic doping-related absorptions show up in intensities that are comparable to the film spin coated from blend solution. This observation is independent of the thin film morphology and comparable intensities show up for regiorandom as well as both regioregular P3HT films. Interestingly, the position of the P2 polaron absorption does not seem to shift significantly with changing degree of order and hence conjugation length as the P1 component of the

polaron in the IR spectral region does (see Chapter 6). The observa-

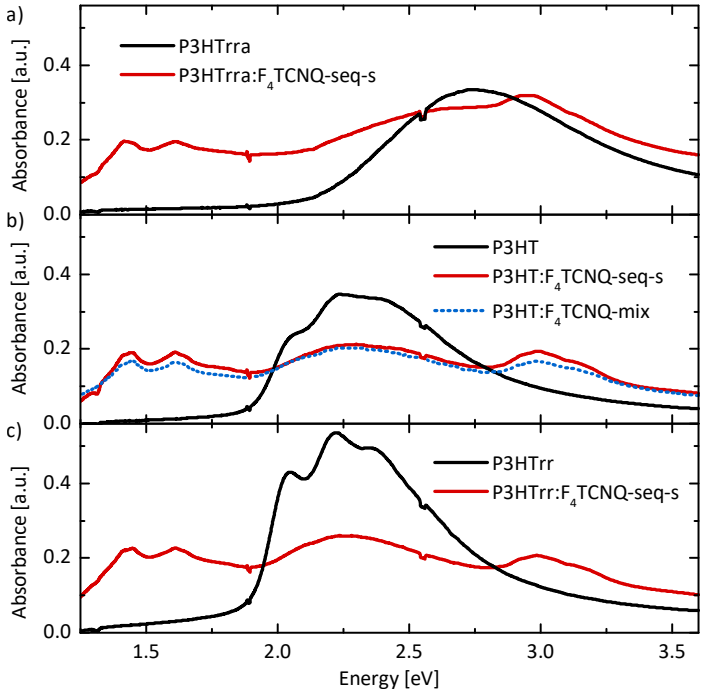

Figure 10.1: UV-Vis absorption spectra of (doped) regiorandom P3HT (a), P3HT with high regioregularity (b), and very high regioregularity (c). F_4TCNQ was sequentially processed onto dried P3HT films from acetonitrile solution (-seq-s, red solid lines). The absorption spectrum of a 10:1 F_4TCNQ-doped P3HT film that was processed from blend solution is given in (b) as reference (-mix, blue dotted line).

tion that the doping-related absorption features emerge independent of the film morphology is a clear hint that not only a doping at the interface of separated dopant and polymer layers occurs as it would be expected for no diffusion of F_4TCNQ into P3HT. Rather, the dopant must be embedded in the whole volume of the thin film to cause such strong absorption features. This can only be explained in terms of a dopant diffusion into the P3HT films. However, the doping technique of sequentially processing the dopant from acetonitrile solution may also play a role in the observed diffusion. A swelling of the amorphous domains is expected to take place [22, 25, 185]. The enlarged free volume forming during such a swelling may permit a diffusion that could be inhibited in a case of no additional solvent present. Due to the high volatility of F_4TCNQ, it is not easily evaporated in a controlled manner in vacuum, rendering this control experiment difficult. Furthermore, since only the final equilibrium state can be observed with this technique, it is not clear if the films behave comparable or if other dynamics that are related to the structural order determine for example the diffusion constant and dopant mobility.

To check if the observed dopant-diffusion in P3HT is dominated by solvent-effects and differently ordered P3HT films impose different degrees of freedom to molecular dopants, or if the structural order actually does not significantly impact dopant diffusion in terms of mobility and diffusion constant, IR and Photoelectron spectroscopy measurements of Mo(tfd-CO_2Me)$_3$-doped P3HT are discussed in the next section.

10.2 A DETAILED ANALYSIS WITH PHOTOELECTRON & INFRARED SPECTROSCOPY

The study described in this section is currently in preparation for publication.[1] Since the experimental contribution of the author of this thesis is limited to the determination of the thin films' morphology *via* electron diffraction, the results are only briefly summarized to provide a basis for the discussion of dopant drift in the next chapter.

In this study, the dopant Mo(tfd-CO_2Me)$_3$ is sequentially evaporated in UHV onto already dried P3HT films of 50 nm thickness and varying regioregularity. Electron diffraction measurements of such films are displayed in Figure 5.2 (Chapter 5), showing that regiorandom P3HT (P3HTrra) has a fully amorphous morphology, whereas regioregular P3HT (P3HT, RR = 93.7 %) is semi-crystalline. It therefore possesses amorphous and crystalline domains. When evaporating Mo(tfd-CO_2Me)$_3$ onto these layers, IR transmission spectroscopy can be used to observe the occurring charge transfer in terms of the broad electronic excitation that can be assigned to the P1 polaron absorption of the charged P3HT. It is observed that within the measurement time of a few minutes, this polaron peak strongly emerges beyond the value that would be expected for only a surface coverage. This effect can be shown for both P3HT and P3HTrra, revealing that Mo(tfd-CO_2Me)$_3$ readily diffuses into these layers upon arrival at the surface. To determine whether this diffusion is temperature-activated, the same experiment is performed with P3HT films cooled to −80 °C. In this case, a separate, neutral layer of Mo(tfd-CO_2Me)$_3$ forms at the surface of the P3HT film, showing no charge transfer except of the inter-facial layer between P3HT and Mo(tfd-CO_2Me)$_3$. Continuous measurement of IR spectra during warm up to room temperature show that between 5 °C and 10 °C, the spectral signatures that indicate charge transfer (IRAV modes below 1500 cm^{-1} and the P1 polaron absorption) increase significantly. This shows that the diffusion is a thermally activated process.

1 Patrick Reiser, Lars Müller, Vipilan Sivanesan, Robert Lovrincic, Stephen Barlow, Seth R. Marder, Annemarie Pucci, Wolfgang Kowalsky, Wolfram Jaegermann, Eric Mankel, and Sebastian Beck: *Diffusion Properties of Molecular Dopants in Sequentially Doped Semiconducting Polymers*, in preparation.

Whereas these results prove that diffusion of Mo(tfd-$CO_2Me)_3$ generally takes place in regiorandom and regioregular P3HT, it is not clear if there are differences in diffusion constants and mobility. To evaluate this, photoelectron spectroscopy can be deployed to investigate the concentration of different atomic species at the surface of the thin films. This technique is sensitive to the first few nanometers since the mean free path of the electrons investigated is restricted to this length scale. This allows to monitor the decrease of Mo(tfd-$CO_2Me)_3$ concentration at the surface while it diffuses into the P3HT film. Tracking this surface concentration over time, the diffusion behavior can be extracted. It has to be noted that—due to experimental limitations—the measurements can only be performed after evaporation, when a large amount of dopants already diffused into the film. Hence, the extracted properties represent diffusion in the case of almost saturated P3HT films. Figure 10.2 shows the molar fraction of Mo(tfd-$CO_2Me)_3$ molecules to P3HT monomers for P3HT (a) and P3HTrra (b). The values are extracted using the emission spectra of 1s electrons of fluorine, which is solely present in the dopant, and carbon. The solid lines represent fits assuming Fickian diffusion that is locally independent of the dopant concentration. The dashed lines show the concentration development if only desorption of dopant molecules into the vacuum is considered ($0.05\,\mathrm{nm\,h^{-1}}$). The color scale represents different nominal layer thicknesses of Mo(tfd-$CO_2Me)_3$ that were evaporated onto the P3HT thin films.

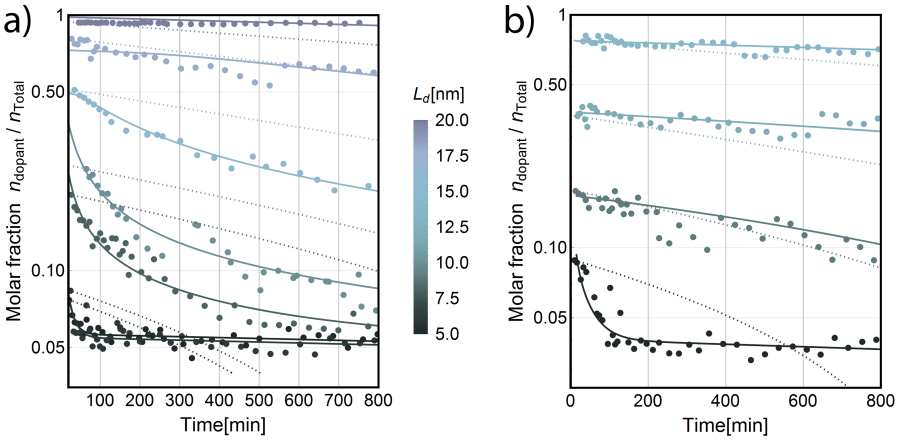

Figure 10.2: Surface molar fraction of Mo(tfd-$CO_2Me)_3$ molecules to P3HT monomers for P3HT (a) and regiorandom P3HT (b). The relative errors for molar fractions are estimated to be 15 %. Solid lines represent fits to the data according to a Fickian diffusion model. The dashed lines show the time dependence assuming solely desorption with a rate of $0.05\,\mathrm{nm\,h^{-1}}$ of a top layer of dopants on P3HT.

It can be seen that for regioregular P3HT, the surface molar fraction shows minor changes for high nominal layer thicknesses and increasingly strong changes for low layer thicknesses of Mo(tfd-$CO_2Me)_3$

in the displayed time span of 800 min. P3HTrra shows a comparable trend. However, a strong change is observed at much lower amounts of dopant compared to regioregular P3HT. Additionally, the slope of molar fraction, especially at low dopant loading differs significantly from the dashed lines that describe desorption only—for both regiorandom and regioregular P3HT. The fits assuming Fickian diffusion in both cases match the observed trends.

Especially when observing a fast change in surface molar fraction, the strong discrepancy between the observed behavior and the dashed lines in Figure 10.2 that only consider desorption shows that such a desorption cannot fully explain the decrease in surface dopant concentration. Therefore, a diffusion is confirmed with this method. Due to the sensitivity of the electronic orbitals to a charging of the dopant molecule, photoelectron spectroscopy can distinguish between charged and neutral $Mo(tfd\text{-}CO_2Me)_3$. At the surface of both regiorandom and regioregular P3HT, the amount of charged $Mo(tfd\text{-}CO_2Me)_3$ seems not to change, whereas the amount of neutral $Mo(tfd\text{-}CO_2Me)_3$ decreases. Additionally, the surface concentration of charged dopant molecules for low dopant film thicknesses does not decrease to values that would be expected for a homogeneous distribution of dopants throughout the volume of the P3HT thin film. This points to a diffusion of mainly neutral dopants, which fits to the observation of Li *et al.* that the diffusion constant of neutral F_4TCNQ in P3HT is significantly higher than that of charged F_4TCNQ [181]. The increasingly fast change in molar fraction when comparing higher to lower layer thicknesses (which directly relates to the absolute amount of dopant molecules) shows that a faster diffusion takes place when less $Mo(tfd\text{-}CO_2Me)_3$ molecules already occupy available sites in the volume of P3HT. The fits reveal a lower diffusion constant for the fully amorphous regiorandom P3HT compared to the regioregular one. Additionally, the diffusion constant decreases exponentially with increasing dopant concentration. This can be rationalized by considering the decrease in available sites that $Mo(tfd\text{-}CO_2Me)_3$ molecules can occupy if the film is already filled with a certain amount of molecules. The highest values of the diffusion constant D extracted from the fits in Figure 10.2 are in the order of $10^{-15}\,cm^2\,s^{-1}$. However, note that this diffusion constant is only valid for the case of almost saturated P3HT films, since the immediate diffusion upon thermal evaporation that was observed by IR spectroscopy takes place prior to the measurements shown in Figure 10.2.

The observed lower diffusion constant of $Mo(tfd\text{-}CO_2Me)_3$ in regiorandom P3HT compared to regioregular P3HT at similar amounts of dopant molecules available requires a detailed evaluation. Keeping in mind the spatial dimensions of $Mo(tfd\text{-}CO_2Me)_3$ as discussed in Chapter 8, it is clear that $Mo(tfd\text{-}CO_2Me)_3$ does not move in the π-π

stacks of P3HT crystallites. However, the amorphous regions and the interlamellar spacing of ordered domains remain as possible pathways for a diffusion. In comparison to the amorphous regions, ordered domains usually exhibit denser packing, pointing to a more likely movement in the amorphous regions. Additionally, as shown in Figure 7.1, thermal evaporation of Mo(tfd-$CO_2Me)_3$ is to a certain degree able to break up the lamellar stacking of P3HT crystallites, forming new amorphous regions. The fractional free volume of the amorphous P3HT would be expected to be larger than that of regioregular P3HT [99, 186]. However, this expectation does not match with the observed slower diffusion in P3HTrra. One possible explanation can be based on the influence of crystallites. Upon formation of the denser ordered domains, the local density at the grain boundaries would be reduced. This could enable a better diffusion in the vicinity of crystallites. The work of Lee and Dadmun supports this hypothesis by finding that the non-crystalline regions in regioregular P3HT possess a lower density than completely amorphous P3HT [187].

Summarizing, the small dopant molecule Mo(tfd-$CO_2Me)_3$ readily diffuses into regioregular and regiorandom P3HT as shown with IR spectroscopy. The diffusion process is thermally activated with activation temperatures around 5 °C. The diffusion rate of Mo(tfd-$CO_2Me)_3$ for almost saturated P3HT films is higher in semi-crystalline regioregular P3HT compared to fully amorphous regiorandom P3HT, as found by monitoring the change of surface molar fraction of Mo(tfd-$CO_2Me)_3$ molecules on a P3HT thin film with time-dependent photoelectron spectroscopy. The difference between regiorandom and regioregular P3HT points to the importance of irregularities in local density, which can form at grain boundaries, for the diffusion process.

11

CONTROLLED DRIFT OF SMALL MOLECULE DOPANTS

In the previous chapter, the diffusion of molecular dopants in polymers was discussed. Such a diffusion is driven by a concentration gradient and is not unique for molecules that undergo charge transfer with a host material. However, charged dopant molecules—although potentially bound by coulombic forces—might be affected by electric fields. In an ideal case, the coulombic binding is weak because efficient doping would generate free charges that can contribute to charge transport in the host material—and would not be bound to the dopants. The following sections show that such a drift can indeed occur and investigate the consequences this drift has for charge transport and the application of doping. To the knowledge of the author, the possibility of a directed drift of molecular dopants was not studied thoroughly in the past: Tyagi *et al.* observe an increased diffusion length upon application of an electric field in F_4TCNQ-doped hole transport layers of OLEDs [26]. They use the small molecule α-NPD as hole transport material, which shows already a limited diffusion of F_4TCNQ [173, 176], rendering a strong dopant drift unlikely. Second, Li *et al.* mention the general possibility of a dopant drift with electric field stress, but do not investigate this [27]. Rep *et al.* report on effects that lead to observations comparable to the ones studied in this chapter [188]. They investigate the redistribution of Na^+ ions that leave an alkali-rich glass substrate at high electrical fields and induce higher local charge carrier densities in the bulk and near the respective contact [188].

In the following, the fundamental mechanisms of an electric-field-induced drift of molecular dopants are examined on the polymeric host material P3HT, in which many dopants already show a strong tendency to diffuse. To approach the underlying mechanisms, different host materials and dopants are compared, ranging from polymers to small molecules, including both p-type as well as n-type dopants and hosts. Finally, the application of dopant drift in memristive devices is evaluated.[1]

1 Some of the results presented in this chapter are published in the following article: L. Müller et al., 2017, *Electric-Field-Controlled Dopant Distribution in Organic Semiconductors*, [124].

11.1 MICROSCOPIC AND SPECTROSCOPIC CHARACTERIZATION OF DOPANT DRIFT IN P3HT

To verify that the dopants F_4TCNQ and Mo(tfd-CO_2Me)$_3$ can be prone to a drift upon application of an external electric field in P3HT, two-electrode devices with a defined channel of doped P3HT were studied with optical microscopy as well as spatially resolved IR spectroscopy. The geometry used is schematically shown in Figure 11.1.

11.1.1 *Optical Microscopy*

For optical microscopy, the two gold electrodes were thermally evaporated onto glass substrates. Hereafter, the P3HT layer was spin coated either from blend solution in the case of P3HT:Mo(tfd-CO_2Me)$_3$or as pristine material with subsequent sequential deposition of the dopant from acetonitrile solution for P3HT:F_4TCNQ. While one of the electrodes is grounded, the second electrode is biased with different voltages, leading to a defined electric field over the channel of varying length (125 µm in most cases). The electrode structure for the experiment shown in Figure 11.1 was imaged during application of certain voltages for defined times with an optical microscope.

Figure 11.1a displays an optical micrograph after an electric field of 1.2 V µm^{-1} was applied in a way that the left electrode was biased negatively whereas the right electrode was grounded. It can be seen that in the channel, two regions form: One with a greyish appearance and one with a purple color near the negative electrode. Before application of the field, the whole channel appeared in the greyish color. This measurement was performed in the transmission mode. Figure 11.1b displays an analogue experiment for P3HT:Mo(tfd-CO_2Me)$_3$. Here, the negative bias was applied on the right electrode, leading also to the formation of two distinct regions in the channel: One comparably small region that appears brighter and the rest of the channel, which remains darker. Before application of the field, the whole channel appeared in this darker color. The measurement for P3HT:Mo(tfd-CO_2Me)$_3$ was performed in the reflection mode, which is the reason for the differing appearance of the colors and electrodes between Figure 11.1 a and b. It should be noted that the appearance with the two distinct regions remains stable upon turning off the electric field at least for the duration of the experiment (minutes to hours).

To understand the two states forming, it is instructive to take a look at the absorbance spectra of the materials involved: pristine, F_4TCNQ-doped, and Mo(tfd-CO_2Me)$_3$-doped P3HT (see Figure 5.5 in Chapter 5). Pristine P3HT absorbs mainly between 2.0 eV, corresponding to 600 nm, and 2.75 eV (450 nm), giving the P3HT film a purple appearance. P3HT: F_4TCNQ shows additional absorption features at higher and lower energy, leading to a broader absorption and hence a more

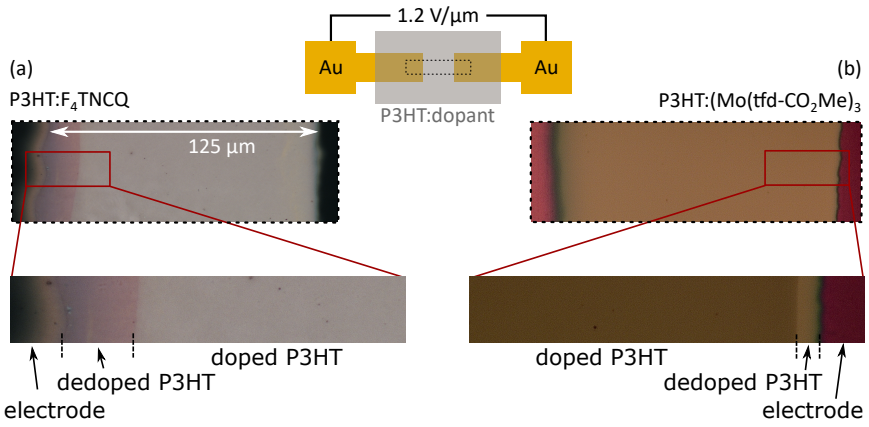

Figure 11.1: Optical micrographs of P3HT doped with F_4TCNQ (transmittance mode, a) and Mo(tfd-CO_2Me)$_3$ (reflection mode, b) in a channel between two gold electrodes after application of 1.2 V µm^{-1} for 30 s as depicted in the schematic. The red area in (a) and the brighter region in (b) indicate dedoped P3HT.

greyish appearance. For P3HT:Mo(tfd-CO_2Me)$_3$, the difference is less pronounced since charged Mo(tfd-CO_2Me)$_3$ does not have specific absorptions in the visible range. Therefore, only the P2 polaron absorption of P3HT around 1.5 eV adds in case of doping with Mo(tfd-CO_2Me)$_3$. The purple region in Figure 11.1a and the brighter region in Figure 11.1b can therefore be interpreted as undoped P3HT. This is a first indication that the application of an electric field high enough is able to induce a drift of dopants. This drift is directed along the field lines of the electric field from the negative towards the positive electrode, since the dopants are of p-type, and hence negatively charged. As a result, the drift leads to the formation of an undoped region of a certain width close to the negative electrode. Figure A.7 in the appendix shows that the length of this dedoped region increases linearly with the electric field applied to the doped polymer on the example of P3HT:F_4TCNQ. The factors that determine the exact width of the region are discussed in the following sections. It should be additionally noted that this drift, leading to the formation of a dedoped region, only occurs above a certain threshold electric field on time scales of seconds. A real time video, showing the formation of the dedoped region at different electrodes, depending on the polarity of the electric field, can be seen in the supporting information of [124].[2] The video is captured with the optical microscope on the example of P3HT:F_4TCNQ for different field strengths.

2 http://onlinelibrary.wiley.com/doi/10.1002/adma.201701466/abstract

11.1.2 *Spectroscopic IR-Microscopy*

Although the optical micrographs discussed in the previous section provide evidence for a dopant drift due to the similarities of absorption spectra and color of the regions that are thought of as dedoped, a proof has to be given that indeed the majority of dopants leaves this volume. One technique that is predestined for such an investigation is IR spectroscopy, since the whole volume of the illuminated spot is measured in the transmission mode and the dopants have unique absorption features: the C≡N stretching mode in case of F_4TCNQ, and the C=O stretching mode in case of Mo(tfd-CO_2Me)$_3$. The limitation of a rather large spot size can be circumvented with a spectroscopic IR microscope, which is able to focus the IR beam down to micrometers and allows to record full spectra of this spatially limited region. Such a spectroscopic microscope is operated by the group of Professor Pucci at the Kirchhoff-Institute for Physics, where the subsequently shown measurements were performed.[3] On a CaF_2-substrate, the same electrode structure as depicted in Figure 11.1 was used, and two positions near the electrodes were chosen to monitor the spectra after application of certain electric fields (A & B). The black lines in Figure 11.2 show the IR transmission spectra at positions A and B before application of an electric field. Figure 11.2a shows an overview spectrum, whereas Figure 11.2b displays a zoom in to the spectral range of the C=O stretching vibration that is specific for Mo(tfd-CO_2Me)$_3$ at position A. It can be seen that in the unbiased state, both positions reveal the spectral signature of Mo(tfd-CO_2Me)$_3$ -doped P3HT with the broad polaron absorption around 2500 cm^{-1} and IRAV modes below 1500 cm^{-1}. The C=O peak at 1737 cm^{-1} is also visible. When applying 1.8 V μm^{-1} for 90 s the first time, the spectra do not change significantly. The origin of this is not clear. After inverting the voltage, the spectral shape changes significantly. At position A, the P1 polaron peak and the IRAV modes strongly decrease to the baseline that would be expected for pristine, undoped P3HT. Additionally, Figure 11.2b reveals that the C=O stretching vibration is no longer detectable. At position B, the P1 polaron peak and the IRAV modes increase. In this configuration, the electrode near position A was biased negatively, the electrode near position B positively. A further inversion of the field and application for 90 s inverts this picture: the polaron and IRAV modes gain intensity again at position A, whereas they decrease in intensity at position B.

An explanation of the observed effects can be given by a drift of dopants. When a positive voltage is applied at the electrode near position A and a negative voltage at the position near position B, the negatively charged Mo(tfd-CO_2Me)$_3$ molecules are forced towards

3 Measurements were performed together with Vipilan Sivanesan and Jakob Bernhardt under the supervision of Dr. Sebastian Beck.

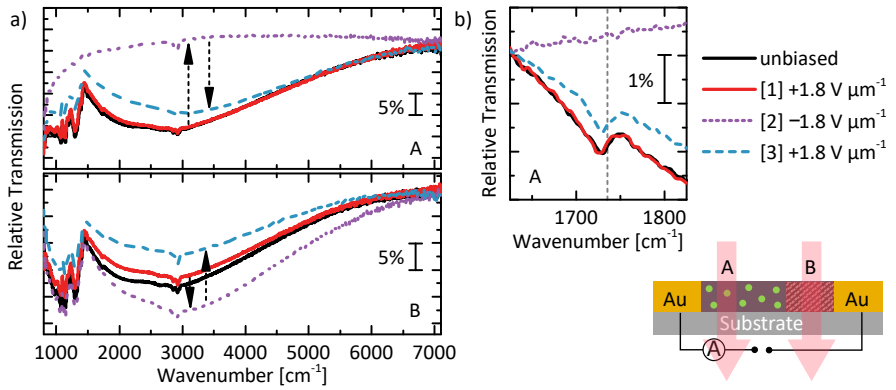

Figure 11.2: Spatially resolved IR relative transmission spectra of P3HT:Mo(tfd-CO_2Me)$_3$ spin cast from 10:1 blend solutions, measured in a channel near the two electrodes (positions A & B) as depicted in the schematic. Spectra are measured before and in between application of electric fields of alternating polarity to form a dedoped region near one of the electrodes. (a) shows an overview spectrum with the broad P1 polaron absorption of charged P3HT and the IRAV modes below 1500 cm^{-1}, depending on the position and applied voltage. (b) shows the spectral region of the C=O stretching vibration that can be used as a direct indicator for the presence of Mo(tfd-CO_2Me)$_3$ in the beam spot.

position A. If they drift in this direction, a depletion region must form at position B, leaving undoped P3HT there. Ideally, no signature of the dopant (peak of the C=O stretching vibration) and no signature of doped and hence charged P3HT (IRAV modes and P1 polaron absorption) is observed in this dedoped region. At position A, the dopants would accumulate and hence, the doping-related signals would increase. This state together with the IR beam at position A and B is schematically drawn in Figure 11.2. The imperfections of the measured spectra in terms of spectral shape and not fully diminishing doping signature can have several reasons: First, the process could lead to irreversible change of host and dopant. Since a spot size of 21 µm was necessary to achieve a decent signal to noise ratio, the electric field strength had to be strong enough to create a dedoped region with a width of these 21 µm plus a few additional micrometers. These are necessary since interactions of beam and electrodes should be avoided to obtain a reliable spectrum. This trade-off between a perfect spectrum and closest position to the electrode possible can also explain unwanted baseline effects as seen for example in Figure 11.2a around 1000 cm^{-1}. The mentioned strong fields could lead to irreversible changes in the P3HT morphology and with this change the spectra and ability of Mo(tfd-CO_2Me)$_3$ to move. As shown in subsequent sections on the electrical implications this drift has, a drift at moderate field strengths can be initiated many times without signif-

icant effect on the electronic properties. As comparison, Figure A.8 in the appendix shows similar measurements for the material combination P3HT:F_4TCNQ. Also in this case, the drift can be proven with the spectral signatures of the polaron, IRAV, and the C≡N stretching vibration of F_4TCNQ that appear or disappear at a position near the electrode.

11.1.3 *Calculation of Dopant Mobility*

From the data presented in the previous sections, a drift mobility of the dopants can be estimated. For this calculation, the volume that the dopants leave in a certain time and under a certain electric field strength is evaluated. Figure 11.3 shows a schematic drawing of a P3HT thin film between two electrodes. In this P3HT film, a certain number of molecular dopants is present. Figure 11.3a describes the initial state with a homogeneous distribution of dopant molecules throughout the P3HT layer. Figure 11.3b describes the final state, where the dopants were forced towards one electrode by the externally applied voltage that defines the electric field. To calculate the mobility, the volume V is necessary, as well as the area A the dopants pass through.

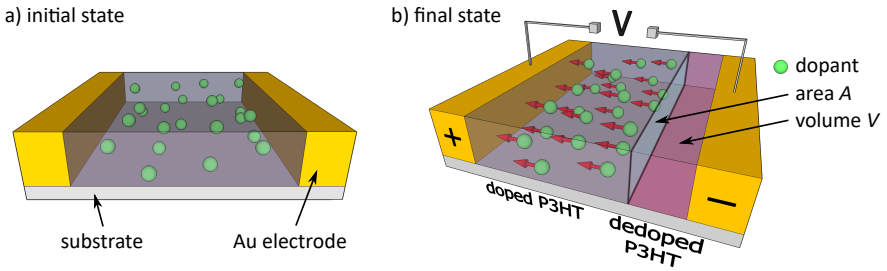

Figure 11.3: a) Schematic of a doped P3HT film in between two electrodes. b) Schematic showing the formation of a dedoped region near the negative electrode, formed through the dopant drift that is indicated by red arrows. The depleted volume V and the area A the dopants leave through are indicated.

The particle (dopant molecules) current density is defined as

$$j = q \cdot \frac{\Delta N}{\Delta t} \cdot \frac{1}{A}, \tag{11.1}$$

where A a the area the dopants pass through, as depicted in Figure 11.3b. ΔN gives the number of charged dopants with the charge q, that leave the considered volume in the time Δt. The dopant current density j also depends on the dopant density n, the electric field E, the charge of the dopants q, and their mobility μ:

$$j = q \cdot n \cdot \mu \cdot E. \tag{11.2}$$

When d is the length of the dedoped volume, $V = A \cdot d$ is given. The density of dopant molecules in this volume is then calculated by $n = N/V = \frac{N}{A \cdot d}$. Combining Equation 11.1 and Equation 11.2 leads to the mobility

$$\mu = \frac{\Delta N}{N} \cdot \frac{d}{\Delta t \cdot E} = \frac{d}{\Delta t_{\Delta N = N} \cdot E} . \tag{11.3}$$

$\Delta t_{\Delta N = N}$ is defined as the time when all dopants have left the volume V. This value is experimentally difficult to obtain since the concentration is only detectable down to a certain amount of dopant molecules, and the detectivity is dependent on the measurement technique.

The mobility of F_4TCNQ can be estimated with Equation 11.3 from the recording of the dopant drift in the optical microscope, which was introduced in Figure 11.1. From these recordings, the time Δt from a homogeneous distribution of dopants to the formation of the dedoped region is extracted. With the electric field that is defined by the channel length and the applied voltage, and the length of the dedoped region d which is measured with the optical microscope, the mobility is calculated. Mobility values for F_4TCNQ are evaluated for 12 cycles with electric fields from $0.32\,V\,\mu m^{-1}$ to $1.6\,V\,\mu m^{-1}$. Since the error of determining the time Δt is too high to resolve a trend, and the aim of this estimation is to obtain the order of magnitude such a mobility has, the values at different electric fields are averaged. As result, the mobility of F_4TCNQ in P3HT is found to be $(7 \pm 4) \times 10^{-8}\,cm^2\,V^{-1}\,s^{-1}$.

The mobility of Mo(tfd-CO_2Me)$_3$ in P3HT is estimated with the same formalism, but from spatially resolved IR spectroscopy. V in this case is defined as the volume that is illuminated by the measurement spot with diameter $d = 21\,\mu m$. This measurement spot is located near the negative electrode from which the dopants are pushed away by the electric field. For this evaluation, a constant electric field of $1.7\,V\,\mu m^{-1}$ was periodically applied for 10 s per cycle. After each voltage pulse, an IR spectrum was recorded at the chosen spot near the negative electrode and the signal of the C=O stretching vibration is used as a measure of the dopant concentration. For $\Delta t \approx 40\,s$, $\Delta N = N$ is fulfilled, since no signal of the dopant is detected after this time. Considering the signal to noise ratio and the given measurement conditions such as the film thickness and integration time, the doping concentration has decreased to 10 % or less of the original concentration of 10:1. This only represents the upper limit and the vanishing polaron peak and IRAV modes in the dedoped region further point towards a negligible number of remaining dopant molecules. With the considerations given above, the drift mobility of Mo(tfd-CO_2Me)$_3$ in P3HT is evaluated to $(3 \pm 1) \times 10^{-9}\,cm^2\,V^{-1}\,s^{-1}$.

11.1.3.1 *Discussion*

Summarizing the calculations of the previous section, F_4TCNQ seems to have a higher mobility of $(7 \pm 4) \times 10^{-8}\,cm^2\,V^{-1}\,s^{-1}$ compared to $(3 \pm 1) \times 10^{-9}\,cm^2\,V^{-1}\,s^{-1}$ for Mo(tfd-CO_2Me)$_3$ in P3HT. This would be expected from the basic idea that the mobility is limited by available sites the molecules can transfer to. As the F_4TCNQ molecule is smaller than Mo(tfd-CO_2Me)$_3$ (compare Figure 8.2 in Chapter 8), more possible sites are available for a movement. Although this simple derivation allows for the estimation of the order of magnitude of the drift mobility, several simplifications are made. First, the formation of an additional voltage drop at the electrode is neglected. It is shown in a following section that this voltage drop can be of significant strength. With such an imperfect contact, the electric field that drops over the doped semiconductor is decreased significantly and the mobility is underestimated. Additionally, once the dedoped region is forming, the electric field is not constant throughout the channel, which is assumed in the simple model for the mobility. As second estimation, all dopants are assumed to drift with the same speed, which leads to a resulting averaged value. Since the electronic properties of P3HT already change at low doping concentrations [2, 113], a minority of fast dopants or some slow dopants could already lead to detectable changes. Furthermore, in this model, the positive electrode towards which the dopants drift is not implemented as a boundary. The accumulation of dopants at this electrode and the general concentration gradient of dopants could lead to an additional internal electric field. Hence, a correct theoretical description of the dopant drift in an electric field would require a coupled set of drift-diffusion equations together with the Poisson equation for both charge carriers and dopants, as theoretically described in Section 2.6. An implementation of this model is beyond the scope of this thesis.

To compare the calculated mobility with measurements of diffusion coefficients from literature, the Nernst-Einstein relation can be used as first ansatz:

$$D = \frac{\mu k_B T}{q}\,. \tag{11.4}$$

Here, D is the diffusion coefficient, k_B is Boltzmann's constant, T the temperature, and q the charge of particles that diffuse—in this case the dopants that drift and diffuse. Their charge is assumed to be unity, since integer charge transfer is observed both dopants in P3HT (see Chapter 5). However, it is not clear if the Nernst-Einstein relation holds in this case for a solid polymer and (charged) dopant molecules that generate counter-charges wherever they are. Using Equation 11.4 to calculate the diffusion coefficient from the measured drift mobility of F_4TCNQ yields a value of $10^{-9}\,cm^2\,s^{-1}$. A comparison of this number to the measured diffusion coefficients of neutral and

ionized F_4TCNQ by Li *et al.* reveals large discrepancies: $D_{F4\text{-neutral}} = 10^{-12}\,cm^2\,s^{-1}$ and $D_{F4\text{-anion}} = 10^{-14}\,cm^2\,s^{-1}$ [181]. Previous studies on ionic currents in (also solid) electrolytes found that the Nernst-Einstein relation in these cases holds for low ion concentrations, whereas ion-pairs form neutral complexes that contribute to diffusion but not to a directed drift at high concentrations. This leads to an overestimation of the drift current with the Nernst-Einstein relation [189–191]. In the present case of charged dopant molecules, the relation is inverted: the equation leads to higher diffusion constants than observed. This deviation can have various reasons. First, as described above, the model used for calculation of the drift mobility neglects several effects such as the boundaries represented by the electrodes. Second, the validity of the Nernst-Einstein relation is questionable in this case. Although an integer charge transfer is measured for F_4TCNQ, many dopant anions and polymer cations are still coulombically bound. This becomes clear by estimations of the doping efficiency of F_4TCNQ in P3HT: Pingel and Neher find, that only 5 % of all dopants introduced generate free charge carriers that contribute to the conductivity [113]. This observation in turn means that many charged dopants are coulombically bound to the countercharge located on the polymer. While this effect is originally unintended, it might help to significantly reduce the diffusion of dopants. Application of an electric field could overcome this coulombic bond and dissociate the polymer-dopant pair, rendering the Nernst-Einstein relation invalid for this specific problem. This model is in line with the observation of a threshold field strength, above which the drift is initiated, which is further discussed in the following sections.

Although it is not possible to directly compare the drift mobility with diffusion measurements from literature, it is instructive to take a closer look at the numbers to get an picture of the stability of such dedoped regions with dimensions of micrometers. With a drift mobility of $10^{-8}\,cm^2\,V^{-1}\,s^{-1}$ at room temperature, F_4TCNQ molecules are able to drift one micrometer in a field of $1\,V\,\mu m^{-1}$ per second. Taking into account the highest diffusion constant found by Li *et al.* ($D_{F4\text{-neutral}} = 10^{-12}\,cm^2\,s^{-1}$), F_4TCNQ molecules exhibit a diffusion length of 10 nm per second—two orders of magnitude smaller than the drift length.

11.2 CONSEQUENCES OF DOPANT DRIFT ON CHARGE TRANSPORT

In the previous sections, the drift of F_4TCNQ and Mo(tfd-CO_2Me)$_3$ in P3HT was proven and characterized. This section is dedicated to the consequences such a drift has on electric properties. As discussed in Chapter 5, the conductivity of doped P3HT can be higher by more than four orders of magnitude compared to pristine P3HT. Therefore, the formation of a dedoped region with dimensions of 10 % or more

of the total channel length can have severe effects on the total channel resistance. Additionally, doping strongly decreases contact resistance [192–194]. Hence, the total resistance of the system should further increase in case of a directed drift away from one electrode.

11.2.1 *Electrical Characterization*

To study the actual impact, current-voltage (IV) curves were recorded on lateral two-electrode devices comparable to the ones used for the studies described in the previous chapters. Figure 11.4 shows IV curves for pristine P3HT as well as P3HT:F_4TCNQ and P3HT:Mo(tfd-CO_2Me)$_3$ for increasing voltages and hence electric field strengths. Both doped thin films were spin cast from a blend solution of host and dopant in chlorobenzene and a doping ratio of 10:1. As it can be seen for pristine P3HT in Figure 11.4a, the current increases linearly with increasing voltage and the absolute current values are as low as a few nanoampere. No hysteresis is observed for increasing and decreasing sweeping direction. For Mo(tfd-CO_2Me)$_3$-doped P3HT, the current at low electric fields increases also linearly, but with absolute values of milliampere (Figure 11.4b). Further increasing electric field strength leads to a superlinear increase of the current until it reaches a peak at around $0.6\,\mathrm{V\,\mu m^{-1}}$. For higher fields, the current decreases for increasing voltage, showing a negative differential resistance of the device. In the backward direction from high voltages to zero, a strong hysteresis is observed, as the current is constantly lower than for equal voltages in the forward sweep. F_4TCNQ shows a comparable behavior but a sharper peak. Additionally, the peak occurs at higher electric fields between $2.8\,\mathrm{V\,\mu m^{-1}}$ and $3\,\mathrm{V\,\mu m^{-1}}$. The curves R_1, R_2, and R_3 represent three different scan rates of $0.008\,\mathrm{V\,\mu m^{-1}\,s^{-1}}$, $0.041\,\mathrm{V\,\mu m^{-1}\,s^{-1}}$, and $0.11\,\mathrm{V\,\mu m^{-1}\,s^{-1}}$. For faster scan rates, the peak is shifted to higher electric fields. In the back sweep, the current is similar for all scan rates.

The IV characteristics of pristine P3HT resembles that of an intrinsic semiconductor: The overall current is low compared to the doped case, and a linear increase following Ohm's law without hysteresis is observed. In the doped case however, strong deviations occur. The current which is roughly six orders of magnitude higher confirms successful doping. The occurrence of a peak with following negative differential resistance can be rationalized with the dopant drift starting above a certain field strength. Once the dopants move, a dedoped region with significantly larger resistivity forms, increasing the overall resistance of the two-electrode device. This leads to a decrease of current. With increasing field strength, this region grows, increasing the total resistance even further. Once the electric field starts to decrease again in the backward sweep, the dedoped region remains, since the diffusion is too slow to equalize the dopant concentration within the

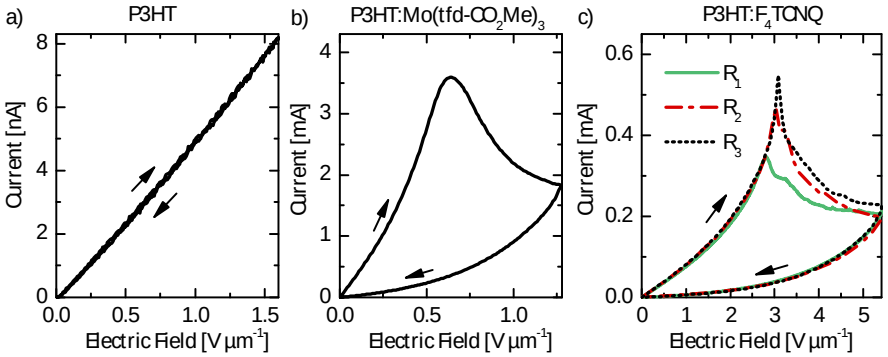

Figure 11.4: Current-voltage measurements of P3HT (a), P3HT:Mo(tfd-$CO_2Me)_3$ (b), and P3HT:F_4TCNQ (c). The electric fields calculated from the voltage and channel length are given on the x-axes to allow for a better comparison. The sweeping direction is indicated by arrows. In (c), measurements with increasing scan rates $R_1 = 0.008\,V\,\mu m^{-1}\,s^{-1}$, $R_2 = 0.041\,V\,\mu m^{-1}\,s^{-1}$, and $R_3 = 0.11\,V\,\mu m^{-1}\,s^{-1}$ are given.

measurement time (as calculated in the previous Section 11.1.3). As a consequence, the resistance of the whole electrode structure remains at its maximum value, leading to the large hysteresis with an overall lower current in the back-sweep.

Comparison of F_4TCNQ-doped with Mo(tfd-$CO_2Me)_3$-doped P3HT shows that the peak is reached at lower field strength for the larger dopant. A possible explanation is based on the spatial separation of electron and hole: As discussed in the previous section, a large number of dopants is initially still coulombically bound to the polymer chain. The strength of this bond is related to the spatial separation of electron on the dopant and hole on the polymer chain. As discussed in previous chapters, a higher degree of crystallinity with larger conjugation lengths of the polymer leads to a stronger delocalization of the polaron, which increases the mean distance between hole and electron [22]. This in turn increases the doping efficiency due to a larger number of free charges that can contribute to charge transport [20, 21]. A comparable effect could be responsible for the lower threshold electric field of Mo(tfd-$CO_2Me)_3$-drift compared to F_4TCNQ-drift in P3HT. Whereas F_4TCNQ is a rather small and planar molecule, not allowing for a strong spatial separation of electron and hole, Mo(tfd-$CO_2Me)_3$ is a volumetric molecule. Figure 11.5 visualizes the spin density of negatively charged Mo(tfd-$CO_2Me)_3$, with the negative charge displayed in red.[4] This reveals that the negative charge is mostly located at the molybdenum core in the center of the molecule. This initially separates the charges more than in the case of F_4TCNQ and might require a smaller electric field to overcome

4 The spin density was calculated by Wenlan Liu.

the coulombic bond. Additionally, the local structure of the formed films may vary, depending on effects like solubility of the dopant and interactions of solute and solvent as shown in Chapter 6. As an example, a lamellar stacking is not observed anymore for mixed doping of P3HT with Mo(tfd-CO_2Me)$_3$ (see Figure 7.1), whereas this stacking is preserved in the case of F_4TCNQ (see Figure 6.1). This might permit Mo(tfd-CO_2Me)$_3$ to move more freely than F_4TCNQ, which is most likely located at the alkyl side chains in the lamellar stacking.

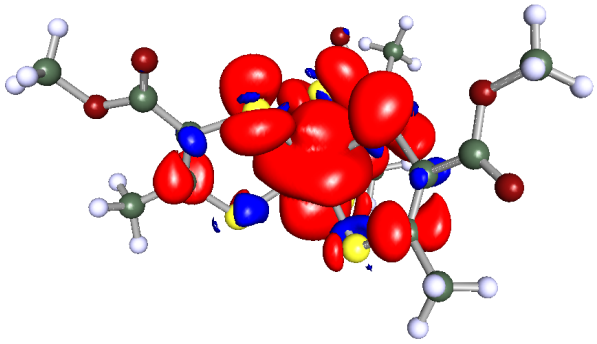

Figure 11.5: DFT calculations of the spin density distribution of a singly charged Mo(tfd-CO_2Me)$_3$ molecule. Red indicates a negative, blue a positive spin density. The electron is located mainly at the core of the molecule.

The superlinear increase of current observed for both F_4TCNQ- and Mo(tfd-CO_2Me)$_3$-doped P3HT for electric fields below the field at which the current peaks can have several reasons. One possibility is a contribution of the ionic displacement current that occurs when a drift is initiated. In this case, a mixed ionic-electronic current would be observed leading to an overall superlinear increase. However, chronoamperometric current measurements at constant electric fields presented in a following section do not support this hypothesis, since no drift signature is observed for electric fields significantly smaller than the value around which the current peaks. A comparison of the current at 0.5 V µm^{-1} in Figure 11.9 for P3HT:Mo(tfd-CO_2Me)$_3$, where no drift signature is observed, but the apparent superlinear increase in current (Figure 11.4) at this field strength illustrates this point. A second possible explanation can be given by the coulombic bond that can inhibit a separation of electron on the dopant and hole on the polymer, hence decreasing the doping efficiency. The applied electric field exerts a force on electron and hole in opposite directions and hence seeks to separate them, which would increase the absolute number of holes that can participate in charge transport. A theoretical study which finds an increasing hole delocalization for increasing electric field strengths supports this hypothesis [195]. The result would be an increase of charge carrier density with increasing electric field and hence the conductivity and current which is measured in Figure 11.4. In future measurements, the polaron delocalization

could be accessed by IR spectroscopy while electric fields are externally applied to prove this hypothesis. Another possibility could be a transition to a space charge limited current (SCLC) regime, where the current increases quadratic with voltage [35]. However, Figure A.9 in the appendix shows that an SCLC behavior does not represent the measured current sufficiently.

As shown on the example of P3HT:F_4TCNQ in Figure 11.4c, the scan rate determines at which electric field the peak is measured. This points to rather slow dynamics of the initiation of a collective dopant drift. Although the variation of the peak position for this examples is below 10 % for scan rates ranging from $0.008\,\mathrm{V\,\mu m^{-1}\,s^{-1}}$ to $0.11\,\mathrm{V\,\mu m^{-1}\,s^{-1}}$, a scan rate slow enough so that the system can reach its equilibrium before the next voltage step is set should be chosen for a detailed comparison of peak positions as indicator for a threshold electric field.

11.2.2 *Scanning Kelvin Probe Microscopy*

The analysis of current-voltage characteristics is able to unravel the consequences of a directed dopant drift on the resistance and hence performance of doped thin films. However, from such measurements it is not possible to infer which effects and to which amounts they contribute to the overall increase in resistance. Two contributions can play a key role: First, the mere conductivity of the dedoped region which should be greatly reduced when most dopants leave this part of the thin film. Second, the contact resistance which is known to be strongly reduced upon doping at an interface [192–194]. To shed light on this question, Scanning Kelvin Probe Microscopy (SKPM) is a suitable method. For the measurements shown in Figure 11.6, two-electrode devices on glass with a channel length of 140 µm and P3HT:Mo(tfd-CO_2Me)$_3$ with a doping ratio of 10:1 was spin cast from a blend solution.[5] The SKPM settings are listed in Chapter 3.

For the measurements shown in the following, different voltages were subsequently applied to the electrodes, leading to electric fields between $0\,\mathrm{V\,\mu m^{-1}}$ and $2.86\,\mathrm{V\,\mu m^{-1}}$. For each step, an optical micrograph was recorded, as displayed in Figure 11.6a. The purple area on the right side is the negative electrode, and the greyish material left of it is P3HT:Mo(tfd-CO_2Me)$_3$. It can be seen that with increasing field strength, a dedoped region of increasing width is formed. The positive electrode is not displayed to obtain comparable scales as for the SKPM images, which are restricted by the maximum scanner range. Figure 11.6b shows SKPM images of the regions displayed in the optical micrographs. The bright region on the right side is the gold electrode, the darker regions left of it are the dedoped regions

5 The SKPM measurements shown here were performed by Seon-Young Rhim and Sebastian Hietzschold.

and the Mo(tfd-$CO_2Me)_3$-doped P3HT. Line scans of these images are shown in Figure 11.6c. The region of x-values above 32.5 µm is assigned to the electrode. For the measurements shown, a bias voltage of 5 V, corresponding to 0.04 V µm^{-1}, was applied, and the potential distribution along the channel was measured. From this potential distribution, the voltage drop and hence the local resistivity can be spatially resolved. For field strengths up to 0.72 V µm^{-1}, a continuous voltage drop over the doped P3HT insinde the channel is observed. Additionally, the surface potential does not show an extra step at the electrode, supporting the assumption of negligible contact resistance in the case of highly doped P3HT at the electrode. For 0.72 V µm^{-1}, the surface potential drops sharply at the electrode. At higher electric fields, there is no longer only one defined potential step, but a second which contribution becomes more prominent with an increasing electric field.

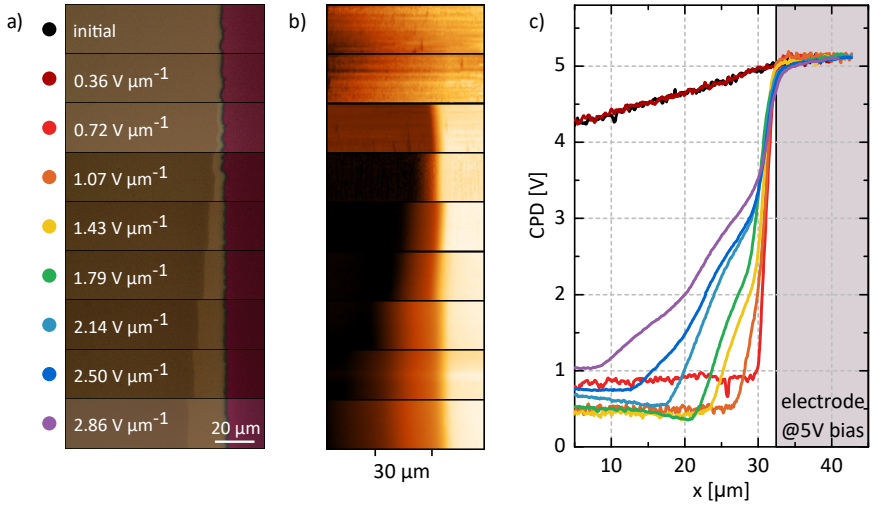

Figure 11.6: a) Optical micrographs of a lateral two-electrode structures (only the right electrode is visible in purple color). P3HT:Mo(tfd-$CO_2Me)_3$ at a concentration of 10:1 from blend solutions covers the structure with a thickness of 50 nm. For each measurement cycle, an electric field of given strength was applied for 60 s, followed by recording of an optical micrograph and ambient SKPM measurements on the same spot. b) SKPM measurements recorded with a bias of 5 V, corresponding to a field of 0.04 V µm^{-1}, which is below the threshold for a dopant drift. c) Contact potential difference profiles extracted from the SKPM images in (b).

The optical micrographs presented in Figure 11.6a resemble the behavior observed and described in Section 11.1: The changed optical absorption in the visible spectral region due to dedoping of the P3HT host matrix can be observed in the optical microscope, and an increasing width is found for increasing electric fields. Furthermore, no such region is observed below a certain threshold field, in this case for the

applied field below $0.72\,\mathrm{V\,\mu m^{-1}}$. For such low fields, the voltage drops linearly across the channel, as it would be expected for a spatially independent resistance of the channel. The observation that no voltage drop is found directly at the interface of P3HT:Mo(tfd-$CO_2Me)_3$ to gold shows that the contact in this case is ohmic [194]. The greatly increased charge density due to doping leads to a mechanism comparable to the band bending in crystalline inorganic semiconductors: a narrower space charge region forms when increasing the charge carrier density, greatly enhancing the tunneling and hence injection and extraction of charges [192–194, 196]. The sharp step in surface potential directly at the electrode for higher electric fields can then be assigned to the changed contact resistance when a dedoped region forms at the interface. The contact is no longer ohmic and a share of the potential that depends on the ratio of contact and channel resistance drops at the interface to the electrode. This explains the trend in line scans for increasing field strength in Figure 11.6: As the the dedoped region grows, its resistance increases and is comparable in magnitude to the contact resistance—whereas both are significantly larger than the resistance of the doped P3HT in the channel. At the example of fields around $2\,\mathrm{V\,\mu m^{-1}}$, both voltage drops are clearly visible and comparable in magnitude. The additional second kink in potential drop for high electric fields above $2\,\mathrm{V\,\mu m^{-1}}$ is not straightforward to explain and might be related to the measurement procedure of applying higher and higher voltages in a stepwise manner.

11.2.3 *Discussion*

The results presented in this section demonstrate the practical impact of a directed dopant drift when comparing the used electric fields with device-relevant parameters: A state of the art OLED for example consists of several layers with a total thickness of around 150 nm and is operated at around 5 V [77]. This leads to electric fields that exceed the observed drift threshold fields, showing that a drift of dopants in transport and injection or extraction layers could have severe impact on the device performance. However, the ability to drift in general—as shown in the subsequent section—and the fields that are necessary to induce such a drift (see Figure 11.4) are material-dependent. The mere size of a molecule seems not to be the critical parameter for the threshold electric field. Mo(tfd-$CO_2Me)_3$ as larger molecule compared to F_4TCNQ shows drift above fields of around $0.7\,\mathrm{V\,\mu m^{-1}}$ compared to roughly $2.8\,\mathrm{V\,\mu m^{-1}}$ for F_4TCNQ. As discussed, the localization of the charge inside the dopant molecule and the resulting separation of electron and hole might be a decisive factor since it defines the coulombic binding of the dopant molecule to the polymer which has to be overcome in case of a field-induced drift. This can also play a role in the observed higher conductivity of Mo(tfd-$CO_2Me)_3$-

doped P3HT compared to P3HT:F_4TCNQ for equal concentrations (see Chapter 5).

11.3 APPROACHING THE UNDERLYING DRIFT MECHANISM: MATERIAL COMBINATIONS & PARAMETER VARIATION

One way to unveil a drift of dopants in a host matrix is to record the current for increasing voltages applied to a two-electrode lateral structure as shown in Section 11.2.1. However, with this method, the scan rate influences the result and high fields can irreversibly damage the thin film. An other way to approach the drift electrically is to apply constant voltages and hence electric fields of alternating polarity to doped P3HT in the same architecture. The measurement principle is depicted schematically in Figure 11.7. Starting from a state where a dedoped region already formed, the initial overall conductivity is comparable low (region A). Applying a positive bias to the electrode close to the depleted region leads to a drift of negatively charged dopants towards this electrode, filling up the dedoped region and increasing the overall conductivity up to a certain level (point B). At some point, the drift leads to the formation of a dedoped region at the opposite electrode, which decreases the conductance and hence the current again (region C). When inverting the applied voltage, the

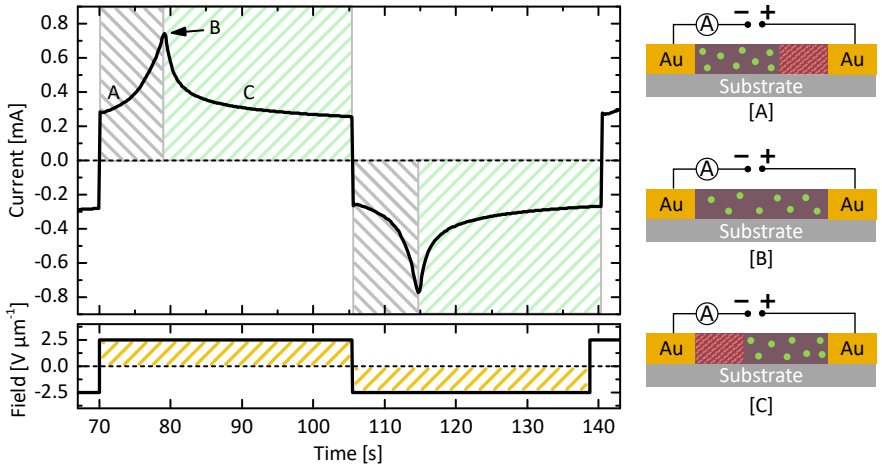

Figure 11.7: Exemplary measurement of current for a constant voltage that is applied for 35 s on a 200:1 P3HT:Mo(tfd-CO_2Me)$_3$ thin film, then inverted. The electric field is displayed in the bottom part. In the initial state, a dedoped region already exists. This region fills up with dopants, leading to an increase in current (A). After the current has reached its maximum (B), a dedoped region forms at the opposite electrode (C). Inversion of the voltage initiates the same process in opposite direction.

same process is initialized, but in the opposite direction. The signature of this current response over time, the corresponding electric field, and a schematic drawing of the device states is shown in Fig-

ure 11.7. The time at which the peak is reached depends on the electric field strength, whereas high field strengths correspond to faster drift speeds according to $|\vec{v}_D| = \mu \cdot |\vec{E}|$. Here, $\vec{v}_D$ is the drift velocity, μ the drift mobility, and $\vec{E}$ the electric field.

To confirm that the measured current is governed by the described mechanism, Figure 11.8 shows optical micrographs of a device where voltage pulses of 30 s duration and alternating polarity were applied. While the microscope images were taken, the current response of the device was recorded to correlate the observed behavior. For this example, P3HT was doped sequentially with F_4TCNQ from solution. As it can be seen in Figure 11.8, the images with a homogeneous dis-

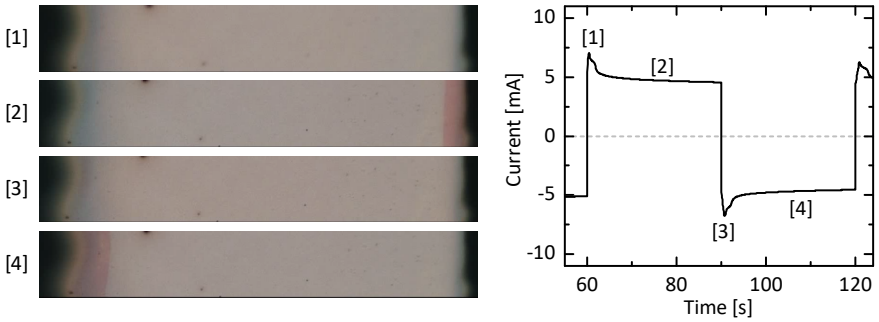

Figure 11.8: Optical microscope images of a P3HT:F_4TCNQ thin film between two electrodes (black), recorded during application of a constant voltage of alternating polarity for 30 s each. (1,3) display the state at which the dopants are distributed homogeneously. In (2,4), the dedoped region is visible near one of the electrodes. The corresponding current is given on the right side.

tribution of dopants (1,3) coincide with the peak currents as expected for the previously described model. When the current has decreased after reaching the peak, the optical signature of a dedoped region is visible in the micrographs (2,4). In the following, this current signature is utilized to study and verify an electric-field-induced drift of various dopant molecules in different host materials to check if different material classes allow for a determination of parameters that enable or inhibit a dopant drift.

11.3.1 *Influence of Host Matrix and Dopant Size*

Figure 11.9 shows electrical measurements where voltage pulses of a defined duration and alternating polarity were applied to different host-dopant combinations. After three cycles each, the electric field strength was increased to finally reach a value that induces a drift, if possible. For P3HT:F_4TCNQ and P3HT:Mo(tfd-CO_2Me)$_3$ in Figure 11.9a and b, the current for a constant electric field is constant below the threshold for a dopant drift, as it would be expected for a stable doped system. Above electric fields that induce a dopant drift,

the signature that was introduced in Figure 11.7 is clearly visible, confirming the occurrence of a directed drift motion. The observed threshold values of $2\,V\,\mu m^{-1}$ to $3\,V\,\mu m^{-1}$ for F_4TCNQ and around $0.75\,V\,\mu m^{-1}$ for Mo(tfd-$CO_2Me)_3$ at doping concentrations of 10:1 are in line with the values estimated from current-voltage characteristics presented in Figure 11.4. Figure 11.9b and c show similar measurements for both F_4TCNQ and Mo(tfd-$CO_2Me)_3$ in the small molecule host material Spiro-MeOTAD. In contrast to the semi-crystalline polymer P3HT, no drift signature is observed up to electric fields of $8\,V\,\mu m^{-1}$ for both dopants in Spiro-MeOTAD.

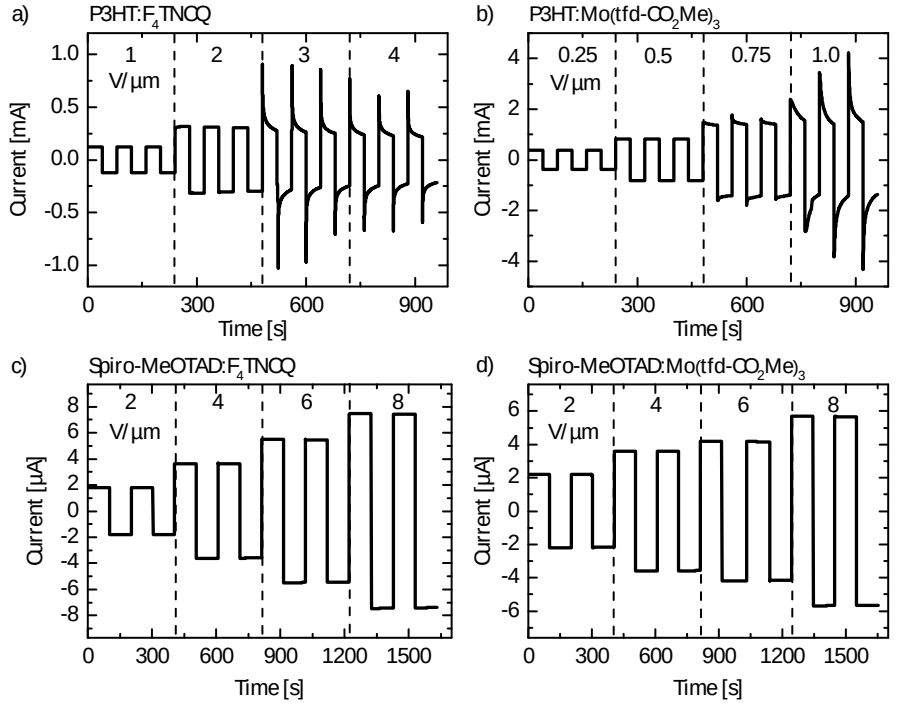

Figure 11.9: Currents at various alternating electric fields for doped P3HT (a,b) and Spiro-MeOTAD (c,d). A drift signature is visible for doped P3HT but not for Spiro-MeOTAD for fields up to $8\,V\,\mu m^{-1}$.

Discussion

The current measurements of doped P3HT corroborate the findings presented in the previous sections and demonstrate that the observed drift and resulting electric properties of such layers are field-dependent and can be controlled reversibly. In contrast to the drift in the polycrystalline polymer P3HT, no drift is observed for the amorphous small molecule Spiro-MeOTAD for neither the dopant F_4TCNQ nor Mo(tfd-$CO_2Me)_3$ up to $8\,V\,\mu m^{-1}$. One possible reason could be no or only partial charge transfer between host and dopant, leading to a strong localization of the charges. This option can be ruled out by the

observation of a conductivity that is increased by a factor of 10^3 for F_4TCNQ and 10^2 for Mo(tfd-$CO_2Me)_3$ with doping concentrations of 10:1. Additionally, integer charge transfer is measured with IR spectroscopy in the case of F_4TCNQ-doped Spiro-MeOTAD. While the shift of the C≡N stretching vibration in F_4TCNQ can be used as measure for the charge transfer, the C=O stretching vibration in Mo(tfd-$CO_2Me)_3$ does not significantly shift upon charge transfer and hence cannot be used as indicator. Although integer charge transfer occurs in the doped Spiro-MeOTAD-layers, the coulombic binding of the charges is presumably still stronger in the amorphous matrix where one dopant interacts with one host molecule compared to the semi-crystalline P3HT, where charges can be delocalized over several thiophene units in the P3HT backbone. This can be inferred from the position of the P1 polaron absorption in the IR spectral range which is strongly blue-shifted for doped Spiro-MeOTAD compared to P3HT [124]. In addition to the delocalization, the charge separation initially could be larger in case of P3HT crystals, where the dopant molecules do not reside in the π-π stacking of the P3HT crystals, but rather in between the side chain stacking. The alkyl side chains might therefore represent a further spatial separation which is not present in Spiro-MeOTAD. These factors could lead to tightly bound electron-hole pairs in case of doped Spiro-MeOTAD which then can only hardly be overcome by an external electric field. The observation of F_4TCNQ not drifting in Spiro-MeOTAD is in line with a lack of diffusion of F_4TCNQ in Spiro-MeOTAD that was observed previously [178]. The separation of charges might not be the only parameter influencing the ability to drift. The structural order of the host matrix needs to provide sites the moving dopants can occupy. Whereas P3HT is made up of crystallites surrounded by an amorphous matrix, Spiro-MeOTAD is fully amorphous [197]. The small molecule Spiro-MeOTAD can fill the volume quite densely due to its mono-molecular structure compared to long polymer chains of P3HT. This could hinder a site change of dopant molecules which is a necessary prerequisite for a dopant drift as well as diffusion. A closer look on the morphological parameters that allow for a dopant drift is taken in the following.

11.3.2 *Polymer Morphology: The Necessity of Structural Order*

To find out if the observed differences between the polymer P3HT and the small molecule Spiro-MeOTAD arise from fundamental differences between polymers and small molecules or if the semi-crystalline structure compared to the amorphous nature of Spiro-MeOTAD is decisive, Mo(tfd-$CO_2Me)_3$-doped regiorandom P3HT (P3HTrra) is investigated. As shown with electron diffraction in Chapter 5, the P3HTrra used for this study has a completely amorphous morphology but the same chemical composition. Hence, the materials only differ in struc-

tural order. Figure 11.10a displays—as shown above for P3HT:Mo(tfd-$CO_2Me)_3$—a drift signature measurement with constant electric fields between $1\,V\,\mu m^{-1}$ and $4\,V\,\mu m^{-1}$ that alternate in polarity. It can be seen that a drift signature is not at all visible below $3\,V\,\mu m^{-1}$. For higher field strengths, the current is no longer perfectly constant for constant electric field, but the signature is not comparable in intensity to the one observed for Mo(tfd-$CO_2Me)_3$-doped regioregular P3HT in Figure 11.9b. This impression is corroborated by the current-voltage measurements presented in Figure 11.10b. The current shows a linear dependence on the electric field up to the maximum applied value of $5\,V\,\mu m^{-1}$, which is far above the electric field of $0.6\,V\,\mu m^{-1}$ where drift in P3HT:Mo(tfd-$CO_2Me)_3$ set in (indicated by the current peak) in corresponding IV-measurements (see Figure 11.4). A compa-

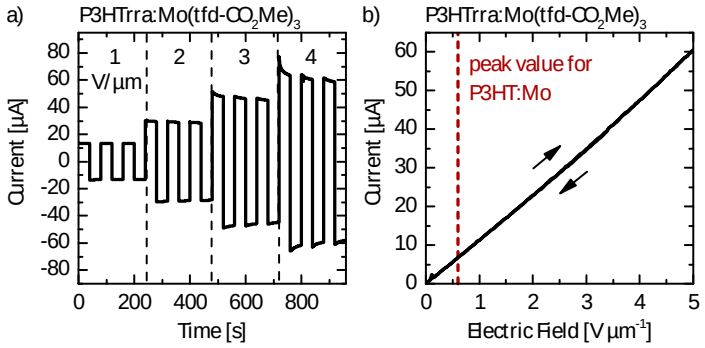

Figure 11.10: a) Current at various alternating electric fields for Mo(tfd-$CO_2Me)_3$-doped regiorandom P3HT (P3HTrra) with a doping ratio of 10:1. b) Current-voltage measurement of P3HTrra:Mo(tfd-$CO_2Me)_3$ with electric field strength marked in red where the current peak is observed for (regioregular) P3HT:Mo(tfd-$CO_2Me)_3$ for a similar doping concentration.

rable result was found in the master thesis of Seon-Young Rhim for F_4TCNQ-doped P3HTrra [198]. This means that the completely amorphous regiorandom P3HT does not allow for a drift at fields as low as for regioregular P3HT. Only the semi-crystalline structure in the examples investigated here seems to provide enough pathways and possible sites for an observable dopant drift. This matches with the results presented and discussed in detail in Chapter 10 on the diffusion of dopants in P3HT and P3HTrra. The main arguments are therefore only shortly reproduced here. First, the density of amorphous regions in between crystallites is found to be lower compared to the density of fully amorphous P3HT [187]. The formation of crystallites which intrinsically have a high density could lead to a decrease of density in the surrounding amorphous regions. Additionally, pathways of even lower density could be formed directly at the border of such crystallites. Further pathways can be given by the lamellar stacking regions, which at least partly widen or completely break up when dopants are introduced (compare the electron diffraction mea-

surements of Mo(tfd-$CO_2Me)_3$-doped P3HT in Figure 7.1). However, to enable a dopant drift over micrometers as observed, such pathways in crystallites must be combined with the ability to move in amorphous regions so that dopants are not stuck in crystalline domains. The observed higher ionization potential of 5.25 eV for regiorandom P3HT [23] could be a further possible explanation if it would lead to less charges transferred between dopant and P3HT. However, this is not supported by IR-spectra of P3HTrra:F_4TCNQ that indicate integer charge transfer for all detectable F_4TCNQ molecules [124].

11.3.3 *Influence of Doping Concentration*

One interesting parameter that likely influences the drift is the dopant concentration. Figure 11.11 shows the value of the electric field strength at which the current peaks in a sweep measurement comparable to Figure 11.4 for different doping concentrations ranging from 25:1 to 100:1 (thiophene units to dopant molecules). The values shown are measured on P3HT:Mo(tfd-$CO_2Me)_3$. The field value at which the current peaks is used as an indicator for the threshold above which the drift is initiated. It can be seen that the field strength needed to initiate a drift of Mo(tfd-$CO_2Me)_3$ in P3HT increases with decreasing doping concentration.

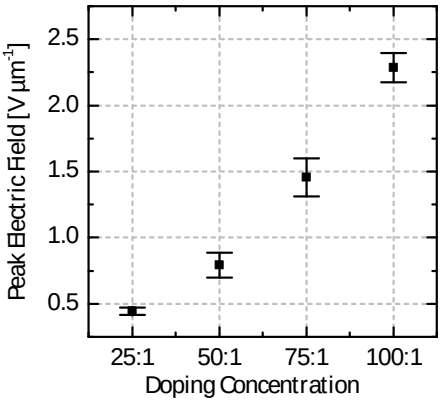

Figure 11.11: Electric field strength at which the current peaks for a varying host:dopant concentration on the example of P3HT:Mo(tfd-$CO_2Me)_3$.

Discussion

Since the absolute number of available jump sites that are available for a dopant molecule decreases with increasing doping concentration, the observed decrease of electric field strength that is needed to initiate a drift for increasing dopant concentrations is not apparent. One effect that could contribute to an explanation was found by Mityashin *et al.*: In their work, the overall charge generation ef-

ficiency upon doping, composed of the probabilities of ionization, recombination, and dissociation is investigated. They find that generated electron-hole pairs, located on dopant and host, respectively, can only overcome the Coulomb dissociation barrier when the energetic disorder that is introduced by neighboring dopant molecules is large enough [45]. Hence, a minimum doping concentration is needed to efficiently generate free charge carriers. Theoretical investigations analyzing the density of states and the correlated charge-carrier transport support this finding [199]. Furthermore, the observation of weak and strong doping regimes in F_4TCNQ-doped P3HT at low and high dopant loadings by Duong *et al.* would fit into this picture, although it was attributed to changes in structural order by the authors [97]. Olthof *et al.* further provide evidence that (in a n-doped material) the activation energy for molecular doping and hence charge separation increases strongly for a decreasing doping concentration due to trap filling at low concentrations [200]. The charge separation that is needed for a high doping efficiency could additionally be a necessary prerequisite for a dopant drift, since it lowers the barrier that has to be overcome by the electric field to separate the charged dopant from the oppositely charged host. Therefore, the increased energetic disorder at higher doping levels should lead to lower drift threshold electric fields which is in line with the measurement.

11.4 A PATHWAY TO STABLE ELECTRICAL DOPING: CHEMICAL IMMOBILIZATION

Except for some specialized applications that are discussed in the following Section 11.5, a diffusion and drift of dopants is not desired since it can lead to severe device degradation or even failure, for instance in OLEDs [26, 174]. In the following, several approaches to decrease the dopant mobility are summarized.

As shown for the example of $C_{60}F_{36}$ compared to F_4TCNQ as dopant in P3HT, a strong increase of the dopant's molecular size does reduce its ability to diffuse [145, 201]. However, as discussed in the previous sections, a size comparable to that of Mo(tfd-CO_2Me)$_3$ is not enough and even larger molecules may modify the structural order of the host material which might lead to unwanted side-effects. A second approach to inhibit dopant mobility in a host matrix is to fill the free volume with a material that ideally does not alter the electrical or optical characteristics of the system. It was shown that this idea works on the example of P3HT mixed with the C_{60}-derivative ICBA: The dopant Mo(tfd-CO_2Me)$_3$ could no longer enter this material blend whereas is readily diffuses into pristine P3HT [202]. However, ICBA is a known electron conductor and is used as photovoltaic blend in combination with P3HT, hence changing the properties of the P3HT system. Whereas this approach works for Mo(tfd-CO_2Me)$_3$, the sequential

doping of P3HT:PCBM with the smaller F_4TCNQ leads to fully doped P3HT. Similar to ICBA, PCBM is another soluble C_{60}-derivative. Sequential doping works with both application of F_4TCNQ from acetonitrile solution or by vapor-doping at ambient atmosphere (for details about vapor doping, see [23, 151]). UV-Vis absorption spectra of the doped and pristine thin films are shown in Figure A.6 the appendix. However, in case of the doping from solution, a solvent-induced swelling could assist the diffusion into the film, and elevated temperatures of the host film in case of the vapor doping could also facilitate diffusion of F_4TCNQ into P3HT:PCBM. Although these measurement cannot exclude that F_4TCNQ might not be able to enter the blend at room temperature and without solvent present, a stability especially for a wide temperature range is desirable from an application point of view.

Next to a modification of the possible site choice in the host material, it would be possible to adjust the adjacent layers in such a way that it is energetically favorable for the dopant molecules to reside in the intended layer. However, the electrical characteristics can still be strongly altered even when dopants drift in a single layer as shown in the previous sections. Alternatively, a structural modification to induce a chemical reaction that binds the dopant to specific groups like the side chains is possible. This approach was demonstrated on a bilayer system of a polar polythiophene and the non-polar P3HT [183]. In this study, the dopant F_4TCNQ tends to reside in the polythiophene with polar side chains, even upon heating to temperatures beyond the 80 °C sublimation temperature of F_4TCNQ [183]. While side-chain engineering can be a promising route, it additionally changes the structural order and potentially introduces unwanted side-effects that limit the doping efficiency [183].

Instead of chemically modifying the host material, the dopant itself can be equipped with an anchoring group that chemically binds to ideally any host material. Following this approach, a DMBI-derivative that acts as n-dopant was synthesized.[6] For a discussion of the doping properties, see Section 5.3. As reactive group that does not need specific target groups to react with, an azide group (N_3) is attached to the dopant. One possible binding mechanism can be an insertion to a C-H bond of organic host materials [29, 30, 87]. As described in Section 5.3, *o*-MeO-DMBI and *o*-BnO-DMBI are used as literature-known dopant and modified reference to the *o*-AzBnO-DMBI with attached azide. This reaction of the azide is intended to be activated by either UV-light at wavelengths of $\leqslant 254$ nm or temperature above 119 °C. In this way, the dopant can be introduced to the host material prior to or after film formation and an activation can be triggered at any time.

6 Synthesis was carried out by Simon Benneckendorf in the group of Prof. Bunz at the Institute of Organic Chemistry (OCI) at Heidelberg University.

Since it is difficult to directly prove diffusion or the lack thereof with the methods available, the electric-field-induced drift as indirect indicator for the ability to diffuse and a possible immobilization is investigated. For comparison, two different host systems are analyzed: the small molecule PCBM and the semi-crystalline polymer N2200. A first hint that diffusion of the DMBI-derivatives might take place in N2200 is given by long-term conductivity measurements that are displayed in Figure A.11 in the appendix. These show a strong decrease of the thin film conductivity over time, which however could also be caused by material degradation. Therefore, drift measurements are analyzed in the following. Figure 11.12a shows the current for increasing electric fields for pristine PCBM, PCBM:*o*-MeO-DMBI, and PCBM:*o*-BnO-DMBI processed from blend solutions in chloroform at doping concentrations of 10:1. Whereas pristine PCBM shows currents at the detection limit (10^{-11} A), the currents for doped PCBM are orders of magnitude higher, proving that doping takes place. As apparent, there is no peak and decrease of current up to fields of $8\,\mathrm{V\,\mu m^{-1}}$ (compare Figure 11.4, where such a peak is shown for P3HTMo(tfd-CO_2Me)$_3$), pointing towards a lack of drift for the investigated fields in the small molecule host material PCBM. Figure 11.12b-d show current measurements over time for alternating and stepwise increasing constant electric fields for the polymer N2200 doped with *o*-BnO-DMBI, *o*-MeO-DMBI, and *o*-AzBnO-DMBI. For these material combinations, a drift signature is observed, but for comparably high fields above roughly $8\,\mathrm{V\,\mu m^{-1}}$.

Discussion

The lack of diffusion signature for the small molecule host material PCBM can be rationalized analogue to the p-doped Spiro-MeOTAD. The possibility of a (not necessarily crystalline) close packing probably does not provide enough free volume and sites the dopant can jump to. Furthermore, a rather localized charge on the PCBM with a dopant molecule located directly next to it might impose strong coulomb interaction that cannot be overcome by the fields used herein. Due to a limited amount of available dopant material caused by the synthetic complexity and the small-molecule-like character of PCBM, which analogue to Spiro-MeOTAD did not show a tendency for a drift, all further measurements were carried out with the polymer N2200. This polymer is widely used as n-type material for organic field-effect transistors [80] and exhibits a semi-crystalline structure [203–205]. In contrast to doped P3HT, all three n-type dopants investigated did not show a drift signature up to around $8\,\mathrm{V\,\mu m^{-1}}$. Above, a drift signature becomes clearly visible, showing an electric-field-induced drift. However, the measurements in Figure 11.12b-d consistently show non-idealities like multiple peaks or small current breakdowns which can be assigned to the high field strength that possi-

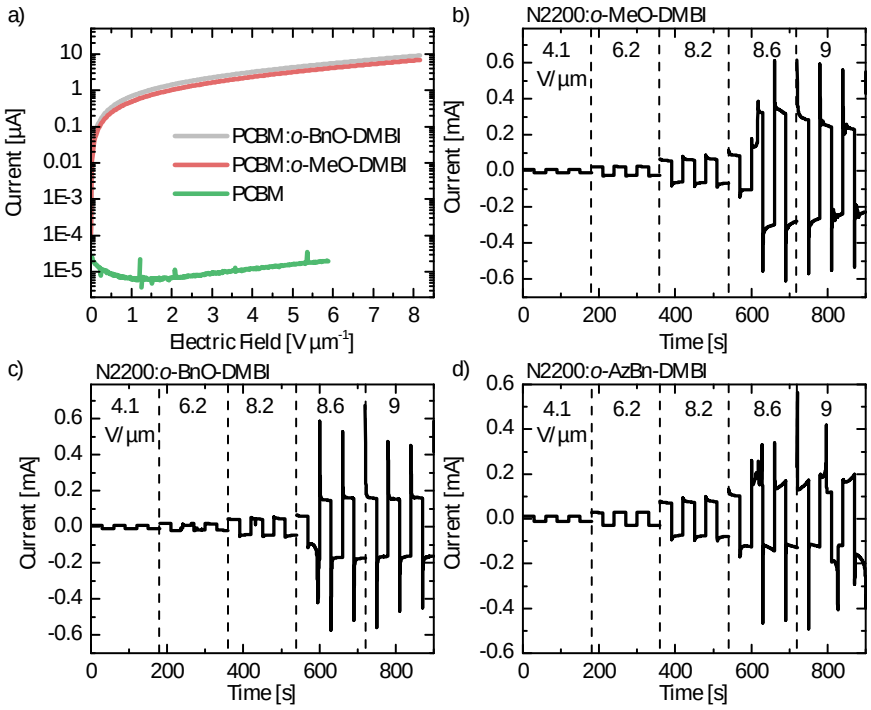

Figure 11.12: a) Current-field measurement for PCBM, PCBM:*o*-MeO-DMBI, and PCBM:*o*-BnO-DMBI showing no peak and hence no drift. b) - d) Currents at various alternating electric fields for N2200 doped with *o*-MeO-DMBI (b), *o*-BnO-DMBI (c), and *o*-AzBnO-DMBI (not activated) (d). A drift signature is visible for fields above roughly 8 V µm^{-1}.

bly damages the host material Furthermore, high dopant velocities once a drift is initiated could further locally damage the N2200 thin film. In addition to comparable doping efficiencies (see Section 5.3), the drift behavior in N2200 is similar for the three chemically modified DMBI-derivatives, showing that the addition of the benzene ring and the (not activated) azide group do not significantly alter the dopants' drift properties. With this basis, an activation with UV-light for 17 min at a wavelength of 254 nm and by thermal annealing at 130 °C for 10 min was tested. The UV-Vis absorption spectrum does not change significantly upon thermal activation in N2200, as displayed in Figure A.10 in the appendix. On the other hand, the absorption of the azide (N_3 group) in the infrared wavelength region vanishes for both techniques, indicating an activation as intended [206]. However, the observed drift signature above 8 V µm^{-1} remains unchanged independent of the pre-treatment and resembles the one shown in Figure 11.12d. One possible reason for this behavior could be a Ketinimine expansion: a reaction of the azide group with the dopant molecule itself [30, 207] instead of the desired binding to the host. To inhibit this reaction, a further chemical modification of the benzene ring with four fluorine atoms that can sterically hinder this reaction [208] is planned for the future. The fluorine atoms present in

such a modified version of the azide dopant *o*-AzBnO-DMBI would further allow to study a diffusion of the dopant molecules through a layer of N2200 with photoelectron spectroscopy. In this way, the comparably high electric fields that are necessary to initiate the drift can be avoided and the mobility of the dopants could be accessed without strong external influences.

11.5 APPLIED DOPANT DRIFT IN MEMRISTIVE DEVICES

A mobility of dopant molecules is usually unwanted as it represents one source of device degradation. Dopants diffusing out of the designated charge transport or injection layers in OLEDs or OFETs into adjacent layers or the channel can strongly alter device performance [171–174] and even a drift inside a single thin film can have a severe effect on the overall conductance as shown. However, the controlled motion of dopant molecules between two electrodes and the resulting control over the total resistance of the device has potential applications as a so-called memristive device or memristor. Such devices are subject to increasing research for a wide range of applications such as non-volatile memory, neuromorphic circuits, chaotic systems, and analog circuit design [209]. In the following sections, a proof of principle memory and memristive device based on a dopant drift is introduced. The device characteristics concerning memory and neuromorphic applications are measured and evaluated in the context of a general introduction, and an overview of existing systems and approaches is given. A general introduction to the memristor and memristive devices can be found in Section 2.7.

11.5.1 *Memory Applications*

To store information in a classical computing approach, two defined states (0/1) are required. A memristive device can achieve this with switching between a low resistance state (LRS) and a high resistance state (HRS). After the theoretical introduction of the memristor by Leon Chua in 1971 [62], the first working memristive device was presented by scientists from the HP Labs in 2008 [209]. Since then, the idea to get rid of the need for a separation of volatile and non-volatile memory in modern computers by replacing both with a non-volatile memristive memory was pursued by several large IT companies and researchers. The technology which in terms of computer memory is usually referred to as resistive random-access memory (ReRAM) is one candidate to succeed current memory technologies [210]. Due to the ambiguous usage in literature and the initiative by Chua himself to merge all resistance switching memories with two terminals into the category of memristors [65, 211], the term memristor is used in the following as synonym for memristive device. Memristors can

be classified into three main categories: molecular and ionic thin-film memristors, 3-terminal memristors, and spin-based or magnetic memristors [212]. The devices shown in this thesis belong to the first class. Various forms of memristors were developed, ranging from devices based on inorganic semiconductors with excellent down-scaling properties, succeeded from the development of processor technology in the past decades, to devices made of organic semiconductors with new properties such as processing on flexible substrates or the processability from solution by printing techniques. Hence, a conclusion about properties like reading and writing speed, temporal stability, the ability to distinguish between on- and off-state, and the cost and size of basic memory units is not generally possible.

11.5.1.1 *Switching Between two States*

With the possibility to initiate and control a drift of dopants for the material system presented in this thesis on a length scale of micrometers, and a diffusion-driven tendency to reach the equilibrium state orders of magnitude slower than the drift, this effect can be utilized to store information. Figure 11.13 shows schematic of a vertical two-electrode device with the electrodes made of silver and the active layer made of P3HT:Mo(tfd-$CO_2Me)_3$, processed from blend solution at a doping ratio of 25:1. The film thickness for the measured devices was 3.5 µm. An additional layer of MoO_3 between the doped P3HT and the top electrode was thermally evaporated to ensure a good injection even in the case of less dopants near this electrode [213]. A voltage of −10 V (2.9 V µm^{-1}), applied for 4 s, was then used to generate a dedoped region near the bottom contact, which strongly increases the overall resistance of the device (OFF-state). With a voltage of 9 V (2.6 V µm^{-1}), applied for 0.5 s, the dedoped region is filled again with dopants, but a dedoped region is not yet established at the opposite electrode. This state has the lowest possible overall resistance (ON-state). By reading the state with a voltage below the threshold for a dopant movement (−0.1 V = 0.03 V µm^{-1}), applied for 0.1 s, the state is maintained. The graph on the right side of Figure 11.13 displays the readout at ON- and OFF-state for 20 switching cycles. By averaging over the readout time span of 0.1 s, the displayed error bars were obtained. With these parameters, an on-off-ratio greater than 10^2 was achieved. Furthermore, switching times down to 80 ms were realized in the master thesis of Seon-Young Rhim with a reduction of the on-off-ratio to one order of magnitude [198].

The results presented herein represent a proof of concept. Variation of material combinations, doping concentrations, film thicknesses, and measurement parameters could yield better performance. The large difference of contact resistance between doped and undoped material near an electrode as shown with SKPM measurements in Section 11.2.2 could be further exploited with a change of electrode ma-

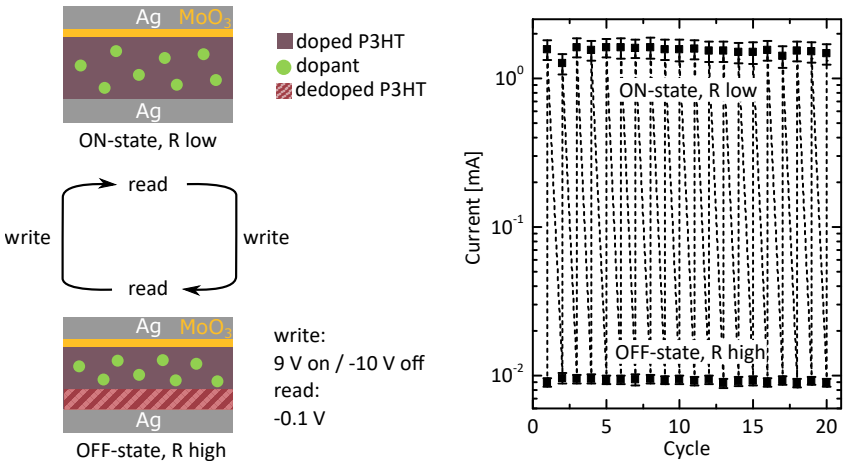

Figure 11.13: Left: Schematic illustration of a memory device with a dedoped region generated at the bottom electrode in the off-state and a homogeneous distribution of dopants in the on-state. Right: Absolute current at −0.1 V (0.03 V µm^{-1}) in the states "ON" and "OFF" for subsequent switching cycles.

terials as proposed by Smits *et al.* [214]. Whereas memory devices based on organic materials often suffer from low switching speeds or stability issues, new concepts like the use of transition-metal complexes reveal a potential comparable to oxide-based memory devices, which represent the most promising candidate in terms of application potential today [215]. To allow for a classification of the working principle presented herein, related approaches are introduced in the following.

Polymer-based memristive devices generally make use of a variety of material properties and mechanisms. Examples are conformation changes of molecules [216, 217], ionic conduction [216, 218], charge transfer [216–218], space charge effects and trap states [216–218], and the formation of highly conductive metallic current bridges or carbon-rich filaments [216–218]. Many approaches utilize small ionic additives like NaCl, $LiCF_3SO_3$, or iodide, which are highly mobile and hence allow for fast switching [214, 219, 220]. However, this high mobility usually demands for a separate layer which releases the ions upon application of an electric field into a polymer [219, 220]. This increases the structural complexity to a minimum of two layers between the electrodes. The concept presented herein in contrast uses dopant molecules that can be much larger in size, such as $Mo(tfd\text{-}CO_2Me)_3$, which could strongly increase the retention time. However, this approach inherently represents a trade-off between retention time and switching time which also depends on the overall film thickness. The structure of memristive devices in the past varied from only one layer between two electrodes [221, 222] like the one presented herein to more complicated structures such as three-electrode devices [223, 224].

11.5.1.2 *Stability of Memory Operation*

To assess the longevity of the memristive device for many switching cycles between the on- and off-state, an exemplary long-term measurement is shown in Figure 11.14. For this measurement, P3HT:Mo(tfd-$CO_2Me)_3$ at a concentration of 75:1 was processed from blend solution. The operation is similar to the one introduced in the previous section with a readout time span of 0.1 s that is resolved on the right side of Figure 11.14.

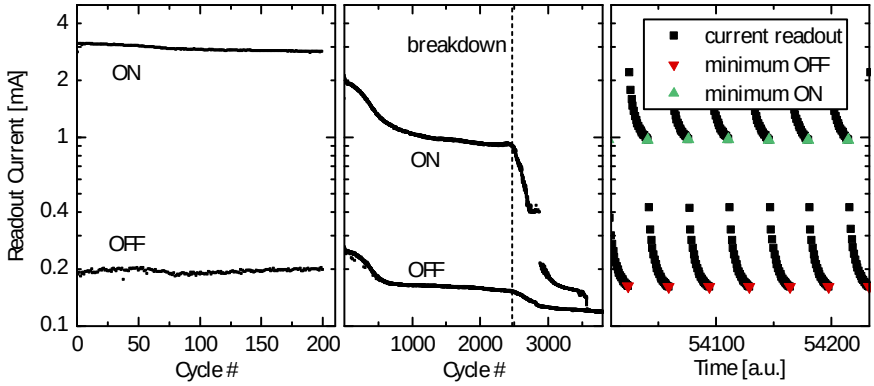

Figure 11.14: Absolute readout current in ON and OFF state with −0.1 V readout voltage. Data points for on- and off-state in the left and center part are taken as the minimum of the readout current in the measurement time span of 0.1 s as shown in the right part.

During this readout, the current relaxes to a minimum value which is shown as ON and OFF in the left and center part of the graph. For this exemplary set of parameters, the on-off-ratio is maintained up to roughly 2500 switching cycles. After the first 500 cycles, the on- and off-conductance decrease similarly to a new equilibrium state, not changing the on-off-ratio. After 2500 cycles, the on-state breaks down and finally converges with the off-state. This could either be explained by a material degradation or a loss of optimum operating parameters. For this kind of devices, the on-state is reached when a homogeneous distribution of dopants is established. Since further application of the voltage that led to this state initiates the formation of a dedoped region at the opposite electrode, decreasing the conductance again, a tracking of the maximum conductivity would be desirable for a stable operation of the memristive device over long time scales and many switching cycles. A material degradation can be further minimized by limiting the voltage, which however also decreases the achievable width of the dedoped region and hence the on-off-ratio. Since the device presented herein is not optimized and the cycle-stability of memristive devices as well as retention times in literature vary strongly—depending on operation conditions and technology [218]—a detailed comparison is not performed here.

11.5.2 *Operation as Memristive Device*

As theoretically described in Section 2.7, a memristive device is characterized by an odd-symmetric current-voltage Lissajous figure [62, 211]. Hence, the IV curve of a memristive device shows a pinched hysteresis loop where the current is zero for no voltage applied and additionally shows a strong hysteresis. This behavior can be reproduced with a device of doped P3HT between two electrodes similar to the memory device schematically illustrated in Figure 11.13 in the previous section. Figure 11.15 shows such a current-voltage characteristic for which the voltage is sweeped between −3 V and 4 V. Hence, this device can be described as voltage-controlled memristive one-port [65]. For this example, P3HT:Mo(tfd-CO_2Me)$_3$ with a concentration of 25:1 and a thickness of 3.5 µm was measured with a scan speed of 3 V s^{-1} in a vertical two-electrode architecture.

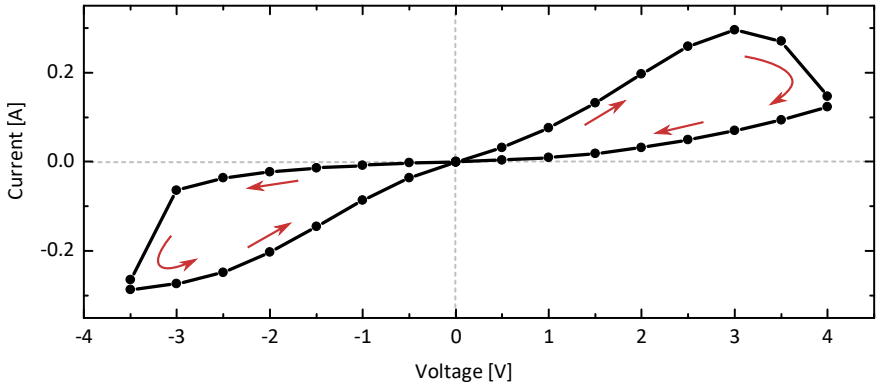

Figure 11.15: Current-voltage sweep between −3 V and 4 V showing a pinched hysteresis loop, characteristic for a memristor.

11.5.3 *Memristive Devices for Neuromorphic Computing*

To date, classical computation in many cases is based on the von Neumann architecture, which determines a separation of computation and storing of data, defining a sequential processing of information. Although current technology is able to emulate increasingly complex structures such as the brain functionality of a mouse or a cat [225–227], the need for parallel computation leads to an exponential growth of energy dissipation with increasing brain size [228]. The key properties of biological neuronal systems are a large connectivity of single neurons—on average 7000 synaptic connections each [229]—that enables energy efficient parallel computation and the fusion of memory and computation [230, 231].

One mechanism that is believed to be paramount for biological systems to learn and function is the property of synapses to adjust the synaptic weight between two neurons. This synaptic weight is deter-

mined by the ionic flow between the neurons through the synapse. This resembles the fundamental property of memristive systems: the conductance of the system is not constant but defined by the device history. Memristive devices that possess this property can potentially represent a biological synapse in a neuromorphic system. Such a system reproduces the computation of a brain in for example a crossbar architecture with devices that represent pre- and post-synaptic neurons and memristive devices representing the synaptic connections in between the neurons. Figure 11.16c illustrates the analogy. Such crossbar architectures recently succeeded in data classification and image recognition [232, 233]. Furthermore, the high level of parallelism inherent to such systems is believed to potentially reduce energy costs for neuronal algorithms by six orders of magnitude compared to simulated neuronal networks [232, 233]. Figure 11.16a illustrates the growing research interest for memristive technology in recent years. Shown are the citations per year that are listed in the topic *memristor* according to *Web of Science* [234]. The growing research activity in the memristive context and the upcoming need for an analysis of big amounts of data with new approaches like deep learning with neural networks promises synergistic developments [233].

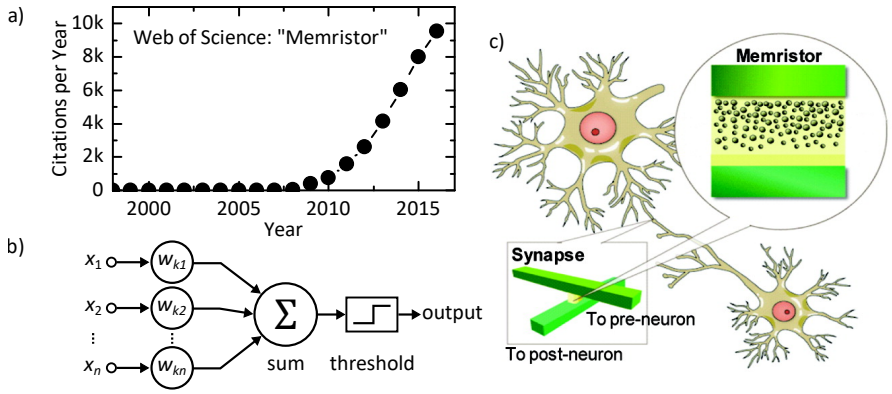

Figure 11.16: a) Temporal evolution of citations per year for the topic *memristor* according to Web of Science. b) McCulloch-Pitts neural model in a symbolic representation. c) Schematic of a synapse connecting two biological neurons. The inset illustrates a memristor connecting the pre- and post-synaptic neuron in a crossbar architecture. (c) is reprinted with permission from [228]. Copyright 2010, American Chemical Society.

Figure 11.16b summarizes the working principle of neural communication with the McCulloch-Pitts neural model in a symbolic representation [235]. Each input x_i represents the signal of an adjacent neuron connected to the neuron k that is considered in this model. These signals are weighted with factors x_{ki}. The weighted input signals sum up and, if surpassing a certain threshold, the neuron is activated. The weighting of the signals is achieved with a change of signal conductance, depending on the synapses history, which is mimicked

by many memristive techniques. Synaptic functions such as short- and long-term potentiation (STP, LTP) as well as spike-timing dependent plasticity (STDP) were reproduced with memristive devices in the past [63, 236]. Recently, organic memristors gained attention as they provide features such as flexibility, low power consumption, bio-compatibility, and the potential to act as direct interface to the brain [237–241]. Limitations in performance and stability that originate from mechanisms such as the slow kinetics of ion diffusion and others are currently tackled by new concepts like decoupling the reading from the writing process in a three-terminal device [224].

11.5.3.1 *Long Term Potentiation & Depression*

This section focuses the capability of the dopant-drift based memristive devices to be operated in a pulsed mode for long term potentiation (LTP) and depression (LTD), two important properties of synapses. In addition to the two extreme states of a homogeneous distribution of dopants and the formation of a large dedoped region, intermediate states with different widths of a dedoped region and resulting intermediate conductance states of the overall device would be necessary. The set-up shown in Figure 11.17d serves to investigate if such a mode is possible with the shown devices. A function generator that sends voltage pulses of defined intensity, duration, and repetition rate is connected to a source measure unit (SMU) that provides a constant low voltage which is used to read out the conductance state in between the voltage pulses. This readout voltage has to be small enough not to initiate a drift of dopants to not alter the current state of the device. 5 mV, corresponding to a field of 1.42 mV μm^{-1} are used in the shown example. In addition to supplying the readout voltage, the source measure unit constantly reads the current flowing through the circuit, in which the function generator, the SMU, and the memristive device are connected in series. Figure 11.17a-c display readout currents for a pulse width between 100 ms and 200 ms and pulse heights of 6 V and 8 V. The frequency was set to 1 Hz for all measurements shown. After a defined number of pulses depending on how fast the final states are reached, the pulses voltage polarity is inverted.

It can be seen that for all shown parameters, the device can be brought to the low conductance state with a small current step size, whereas the high conductance state is reached with fewer pulses. An increase of the pulse height from 6 V to 8 V leads to a larger current change per pulse, meaning that less pulses are needed to switch between low and high conductance. An increase of the pulse duration from 100 ms to 200 ms has a similar effect on the speed with which the two final states are reached. Whereas many single steps from a high conductance to the low conductance can be accessed also at higher voltage and longer pulse width, the switching speed for high voltages

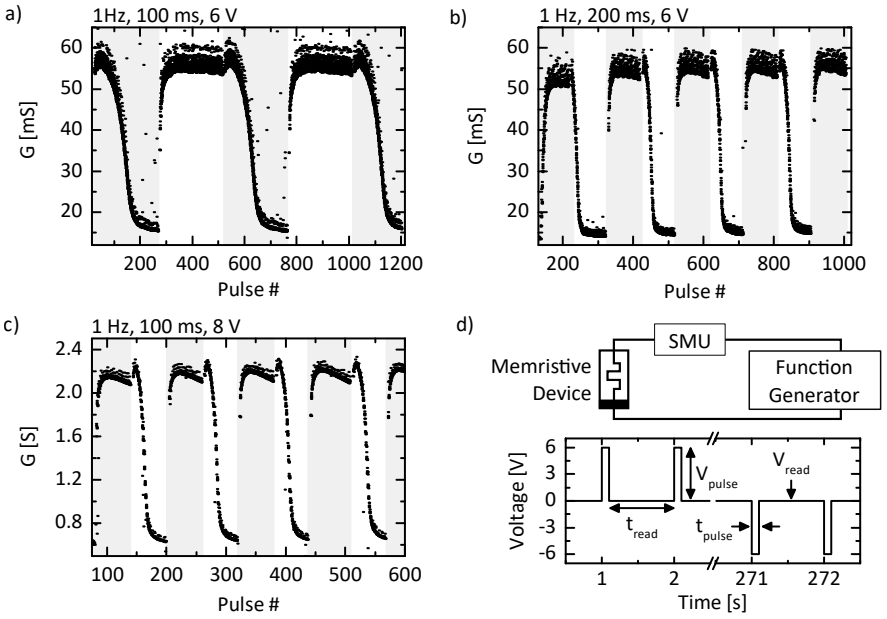

Figure 11.17: a) - c) Pulsed operation of the memristive device displayed in Figure 11.13 showing long term potentiation and depression. The conductance G is incrementally changed in steps between the high and low conductance state. d) The setup that was used to apply pulses and measure the conductance, together with a schematic that defines the relevant parameters.

and long pulses in the other direction is too fast to resolve small conductance steps. Hence, only a short pulse width grants that the device can be adjusted to many conductance states in both switching directions. Note that the results presented in Figure 11.17 are intended as a proof of principle to show the capability of the dopant-drift based memristive device to operate in a pulsed mode. This mode yields conductance changes that emulate the long term potentiation (LTP) and depression (LTD) of biological synapses. Optimization would need to include—amongst others—the choice of materials, the device layout, the circuit to apply pulses and measure them, as well as the range of parameters that is tested for the voltage pulses.

In this chapter, an electric-field-induced drift of molecular dopants was shown to occur in the semi-crystalline polymer P3HT. Spectroscopic methods and electrical characterization was used to prove the drift, and a variation of host and dopant materials could show that the semi-crystalline morphology of semiconducting polymers is an important prerequisite for a drift at moderate electric fields. The dedoping of a spatial region near the negative electrode as a consequence of the directed drift was shown to strongly reduce the conductance of a two-electrode-structure by increasing the contact resistance and the channel resistance. An approach to immobilize the molecular dopants with a chemical anchor was presented, and the applicability

of a controlled drift in memory and memristive devices was evaluated.

12

CONCLUSION & OUTLOOK

This work presents three novel findings that impact future research on doped organic semiconductors: First, charge transfer upon doping is shown to strongly impact the structural order of doped thin films *via* the interaction of solvent and solute already in the solution state. This result is expected to lead to a redefinition of processing guidelines for the preparation of doped organic thin films from blend solutions. Second, the spatial position of dopant molecules in ordered domains of P3HT which is controversially discussed in literature is clarified and an explanation for the change in crystallite spacings upon doping is presented. The third major outcome of this work is the proof and characterization of an electric-field-induced drift of small molecule dopants in polymers, which can give rise to device degradation, but can also be utilized to realize memory and memristive devices. In the following, the results and consequences of the individual studies presented in this work are discussed, followed by a brief outlook on possible future developments.

Structural Order in Doped Organic Semiconductors

To provide a basis for the analysis of doped thin films, the structural order in the undoped semiconducting polymer P3HT was deliberately changed by controlling the film drying time *via* the boiling point of solvents. The inverse exciton bandwidth extracted from Franck-Condon fits of UV-Vis spectra was shown to correlate (non-linearly) with the thin film conductivity, which allowed following studies to distinguish between changes in doping efficiency and morphology-induced changes in conductivity. The p-type dopant Mo(tfd-CO_2Me)$_3$ was found to outperform the smaller F_4TCNQ in terms of thin film conductivity of p-doped P3HT when prepared from blend solution at the same doping ratio. Future studies could focus on examining the reason for the higher conductivity. This could be either an intrinsically better doping efficiency—possibly induced by the larger spatial separation between the electron on the dopant and the hole on the polymer—or the better solubility of Mo(tfd-CO_2Me)$_3$ and hence improvements in the structural order in the dried thin film.

While the drying time is the dominant parameter that regulates the formation of order in pristine P3HT thin films, this thesis shows that the charge transfer between dopant and host, which already occurs in the solution state, critically modifies the solubility of the charged molecules and thus the development of structural order upon film

formation. Electron diffraction performed in a transmission electron microscope was used to reveal improved structural order in films from chloroform compared to chlorobenzene, which opposes the expected behavior based on the properties of pristine P3HT. Figure 12.1 schematically summarizes these findings. The observed higher amount of π-π stacking in thin films from chloroform directly correlates with a conductivity that is one order of magnitude higher. These results demand for a critical evaluation of not only the boiling point of the solvent and the solubility of the pristine materials, but furthermore the polarity of the solvent to obtain highly ordered and hence conductive doped thin films. Recent studies indicate that an increase in charge carrier mobility upon increasing the amount of structural order dominates the conductivity rise rather than a higher charge carrier density originating from a higher doping efficiency due to a stronger delocalization of charges in larger crystallites [22, 23].

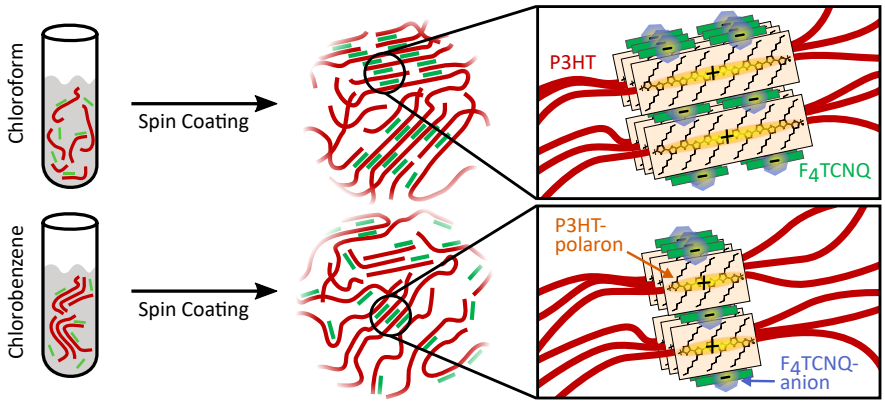

Figure 12.1: Schematic that summarizes the effect of solvent polarity on aggregation in solution, the resulting formation of strucutral order in the thin film, and the spatial position of dopants in the lamellar stacking of P3HT crystallites. The polaron delocalization is defined by the conjugation length and thus crystallite size.

The described increasing complexity of film formation when processing a blend of dopant and host recently led to the development of a sequential doping method based on the diffusion of dopants into a polymer film [24, 25]. This thesis provides a comparison of P3HT doped with the two differently sized dopants F_4TCNQ and $Mo(tfd\text{-}CO_2Me)_3$ and three doping techniques: doping from blend solution, sequential doping from solution, and sequential doping by thermal evaporation of the dopant onto a P3HT thin film. Recent literature hypothesizes that a swelling induced by the solvent in case of a sequential doping from solution is essential for efficient diffusion and thus doping of polymer thin films [22, 24, 25]. The results presented herein question this belief since a comparably strong diffusion and doping occurred when the large dopant $Mo(tfd\text{-}CO_2Me)_3$ was thermally evaporated in vacuum. Furthermore, this thesis shows that

electronic excitations do not differ between films doped sequentially from solution or evaporation although the crystalline structure in the lamellar stacking direction varies strongly. To further optimize doping of P3HT and comparable materials, a thorough understanding of diffusion paths and crystallite stability upon sequential doping is essential. In the future, electron diffraction could be used to deepen the understanding on how varying processing conditions in sequential doping correlate to the change in lamellar stacking of P3HT.

One important finding of the TEM electron diffraction analysis of various sequential doping techniques and molecular dopants is a similar decrease of spacing in the π-π stacking direction of P3HT crystallites, independent of the dopant size (F_4TCNQ compared to Mo(tfd-CO_2Me)$_3$) and doping technique. This implies that dopants do not reside inside the π-π stacking of P3HT, a question which is currently controversially discussed in literature [22, 25, 88, 97, 138, 139]. Furthermore, this thesis provides a novel alternative explanation for the change in π-π spacing: the charging of the P3HT backbone that is inherent to all doping techniques for which a shift can be observed. Density functional theory calculations of charged P3HT dimers without any dopant present support this ansatz, which is reported here for the first time. Future studies could experimentally investigate the change in π-π spacing upon charging P3HT without any dopant present to support the theoretical studies. This could be realized with a transistor device, in which a gate voltage induces charge carrier densities comparable to the density generated by doping. However, the necessity for a gate electrode excludes transmission measurements, which leaves X-ray diffraction as a possible alternative. The sequential doping methods available now allow for a separation of the structure formation and the doping process, which can be used to better understand the mechanisms governing the doping efficiency [22, 23]. However, the effect that enables this sequential processing—the diffusion of dopants—is detrimental for many applications where doping is intended to be spatially restricted to a single layer of a multi-layer device, for instance in OLEDs or OFETs.

Dynamic Processes: Diffusion and Drift of Dopants

Although dopant diffusion has been known for a long time, the morphological prerequisites and underlying mechanisms describing the diffusion of small molecule dopants in organic semiconductors are poorly understood. Within this thesis, it is shown that P3HT thin films with different degrees of order, ranging from completely amorphous to semicrystalline thin films can be doped successfully with the sequential doping technique from solution up to doping levels comparable to blend doping. To exclude the influence of solvent swelling on the diffusion properties, a study that combined morphological and

spectroscopic investigations was carried out, to which electron diffraction measurements of differently ordered P3HT thin films presented in this thesis contributed. Without any solvent swelling of the P3HT film, the dopant Mo(tfd-CO_2Me)$_3$ tends to diffuse slower into fully amorphous P3HT compared to semicrystalline P3HT. Together with the electron diffraction studies of different sequential doping techniques, this result can serve as a basis for future studies that aim at understanding diffusion pathways. With this knowledge, a deliberate change of either the host morphology or the properties of the dopants might be possible to inhibit diffusion and stabilize a desired doping profile.

Although several publications deal with the topic of dopant diffusion in various host-dopant combinations, a possible drift of dopants in an applied electric field was not discussed thoroughly before. This thesis presents the first detailed analysis of an electric-field-induced drift of dopants with a proof of the drift, an estimate of the drift mobility, and the consequences on charge transport and charge carrier injection from electrodes. This drift occurs at moderate, device-relevant electric field strengths above a threshold value in the case of P3HT doped with F_4TCNQ as well as Mo(tfd-CO_2Me)$_3$, whereas it is not observed for moderate field strengths with the small molecule host material Spiro-MeOTAD. Furthermore, a dopant drift does not occur at comparable fields in fully amorphous P3HT. Combined, these findings indicate that the semicrystalline morphology of P3HT which is inherent to many polymers is crucial for a dopant drift. This finding is relevant for the transition from vacuum-deposited small molecules that are currently used in for example OLEDs to solution-processed printed organic semiconductors, where polymers that cannot be thermally evaporated become interesting. Figure 12.2 schematically illustrates the dopant drift. The revealed drift mechanism significantly alters the electrical conductivity of doped thin films and hence can be one mechanism for device degradation.

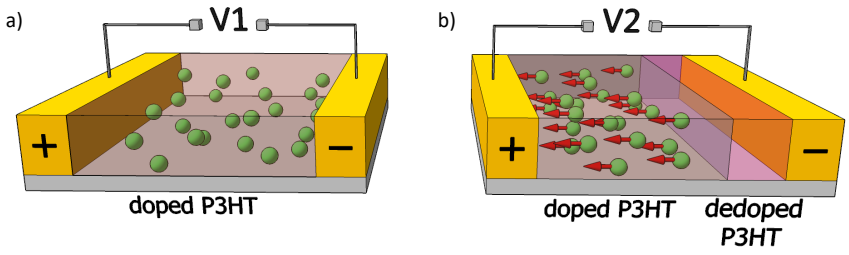

Figure 12.2: Schematic representation of dopant drift under an electric field. a) No drift of molecular dopants takes place if the electric field strength defined by V_1 is below the threshold ($V_1 < V_{th}$). b) For $V_2 > V_{th}$, a drift of negatively charged dopants takes place.

To approach this problem of dopant diffusion and drift, this thesis presents measurements of a joint project of the analytic groups at the

InnovationLab and the Institute of Organic Chemistry of Heidelberg University to develop dopants that can be deliberately immobilized in a host matrix. The dopants that were synthesized with this goal are chemically modified DMBI-based n-type dopants. The chemical modifications do not reduce the ability to electrically dope the small molecule PCBM and the polymer N2200, but are equipped with an azide group that can induce a chemical bond to the host upon activation. However, the dopants synthesized so far did not inhibit a drift at high electric fields, probably due to a reaction with the dopant molecule itself instead of reactions with the surrounding matrix. Further chemical modifications with fluorine atoms could sterically suppress this effect and furthermore allow for a contrast between dopant and host in, for example, photoelectron spectroscopy. Future studies could then investigate the diffusion in addition to the field-induced drift. For the long-term goal of stable electrical doping of any host material, further efforts to bind dopant molecules to the host matrix and the development of a basic understanding of the diffusion and drift processes are essential. Apart of the attempt to immobilize dopants in a host matrix, this thesis shows that the controllable dopant drift can be utilized to deliberately tune the electrical resistance of a two-terminal device. In a proof of concept experiment, an on-off-ratio of 10^2 was achieved in memory operation over 2500 cycles. Furthermore, it was shown that such devices exhibit memristive behavior, and the synaptic properties long term potentiation (LTP) and long term depression (LTD) were successfully demonstrated.

A general conclusion on the status of research on doping of organic semiconductors reveals that there is still no unifying picture that describes the complete range of phenomena, including both doping *via* charge transfer complex (CPX) formation and integer charge transfer (ICT) for both small molecules and polymers. Future work must aim at a broader understanding to provide a reliable basis for the synthesis of new dopants and host materials. A second gap in the fundamental understanding is the discrepancy between observed ionization rate of dopants which can be up to 100 % and the low share of free charge carriers that can contribute to charge transport, which can be as low as 5 % [113]. A clarification of the underlying mechanism, for example a trapping of charges in defect states [200, 242] or Coulombic binding could lead to pathways that might greatly enhance doping efficiency. In addition, the continuous progress in computational power will allow future simulations to not only calculate interactions of a few molecules at a time, but will give access to larger volumes and longer time scales. Finally, the previously identified problems must be approached in the future. This includes the synthesis of spatially stable dopants, whereas an immobilization is ideally induced by external stimulus as it was envisioned with the

DMBI-derivatives analyzed in this thesis. Further chemical modifications that allow to anchor dopants to electrodes for a spatially stable interface doping would be especially desirable for organic field effect transistors [170, 243], and of general interest also for other applications.

In conclusion, the present work provides insight into the fundamental mechanisms that govern doping of organic semiconductors. Beginning with the interplay of dopant, host, and solvent—even before the formation of a doped solid thin film—existing beliefs and established processes must be questioned, since the charging of molecules can affect interactions significantly. This thesis presents the structural measurements that answer the debated question whether dopants infiltrate P3HT crystallites or not—together with a hypothesis that can explain why the lattice spacing changes without the need of a physical presence of dopant molecules in the π-π stacking. In addition to elucidating the role of structural order for the diffusion of dopant molecules in the polymer P3HT, this thesis provides the first comprehensive investigation of an electric-field-induced dopant drift. Beyond the development of a mechanistic understanding of the dopant drift, the practical applicability in memory and memristive devices was demonstrated for the first time.

A

APPENDIX

FITS TO UV-VIS SPECTRA OF P3HT

Table A.1 lists the parameters emerging from the Frack-Condon fit of UV-Vis spectra of P3HT and P3HTrr thin films spin cast from chloroform (CF), chlorobenzene (CB), and dichlorobenzene (DCB). Fits were performed according to Equation 5.2 with the software Wolfram Mathematica 11.

	k	W [eV]	E_{0-0} [eV]	σ [eV]
P3HT CF	0.831	0.158	2.042	0.077
P3HT CB	0.836	0.106	2.026	0.077
P3HT DCB	0.857	0.096	2.028	0.075
P3HTrr CF	0.836	0.158	2.042	0.076
P3HTrr DCB	0.915	0.056	2.028	0.072

Table A.1: Values for amplitude factor k, free exciton bandwidth W, energy of the $0-0$ transition E_{0-0}, and the standard deviation σ emerging from the Franck-Condon fits displayed in Figure A.1.

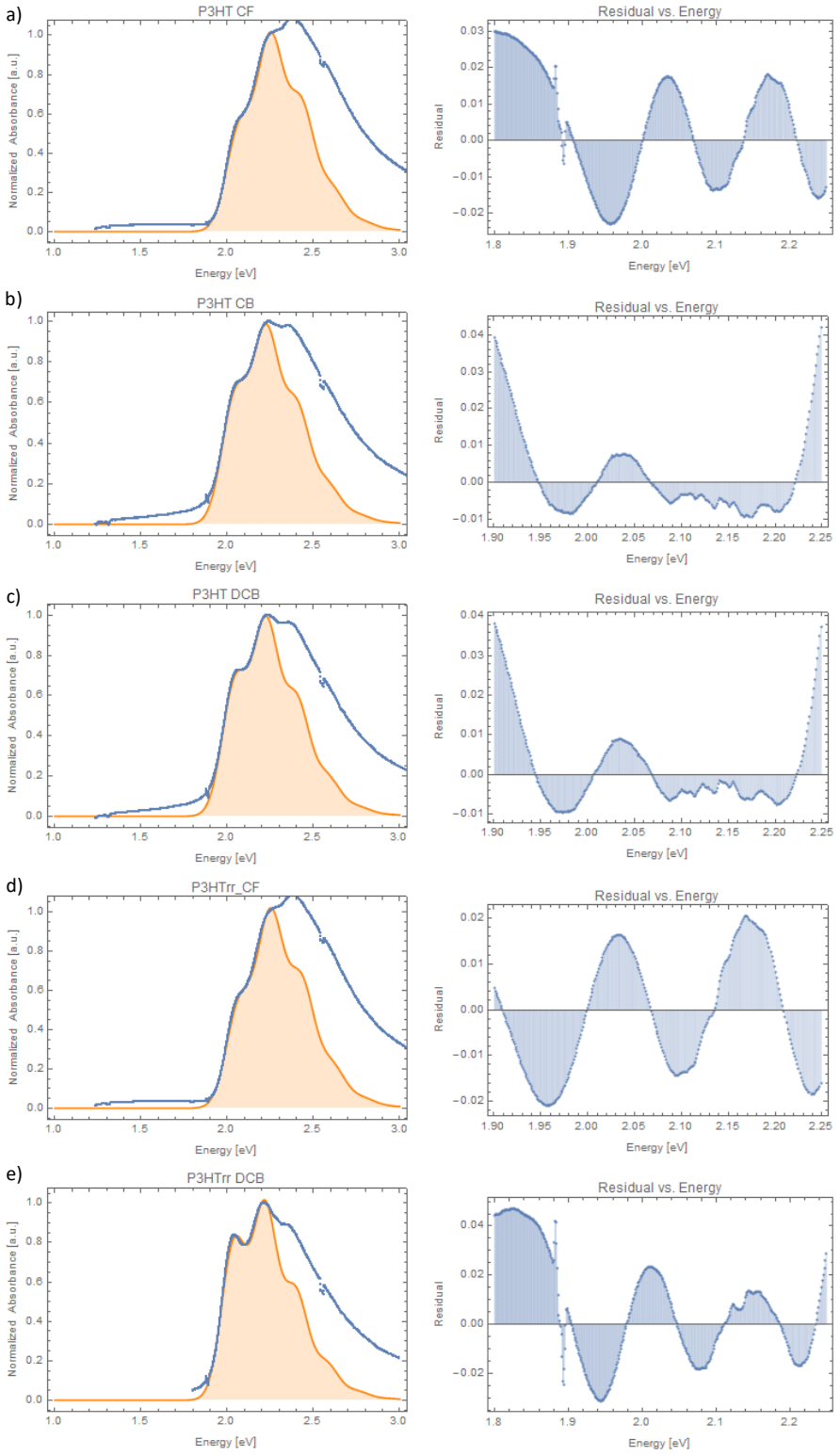

Figure A.1: Franck-Condon fits to UV-Vis spectra of pristine P3HT and P3HTrr spin coated from the solvents chloroform (CF), chlorobenzene (CB), and dichlorobenzene (DCB). The left part shows the UV-Vis spectra in blue and the resulting fits in orange that are composed of contributions described in Section 5.1.2. The right part shows the fit-residuals. The fit was performed between 1.8 eV and 2.25 eV.

CHARACTERIZATION OF DMBI-DERIVATIVES AS N-TYPE DOPANTS FOR ORGANIC SEMICONDUCTORS

UV-Vis Absorption Spectroscopy of N-Doped Organic Semiconductors

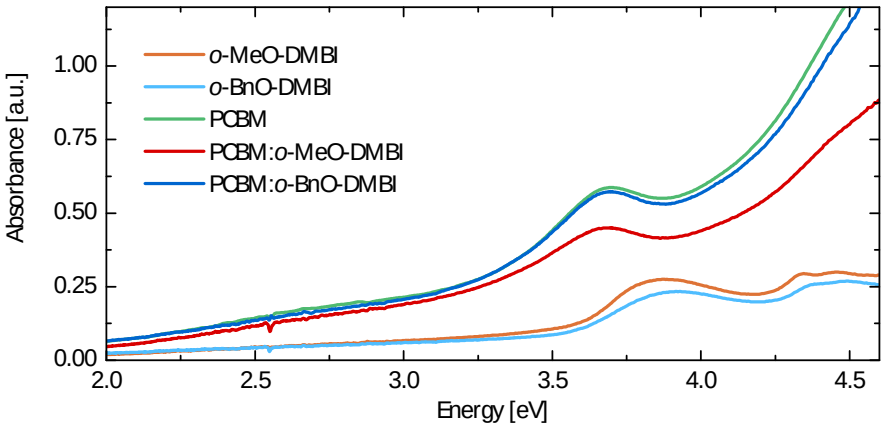

Figure A.2: UV-Vis absorption spectra of pristine PCBM, pristine dopants *o*-BnO-DMBI and *o*-MeO-DMBI, and doped PCBM with doping concentrations of 10:1. Films were spin cast from blend solutions from chloroform.

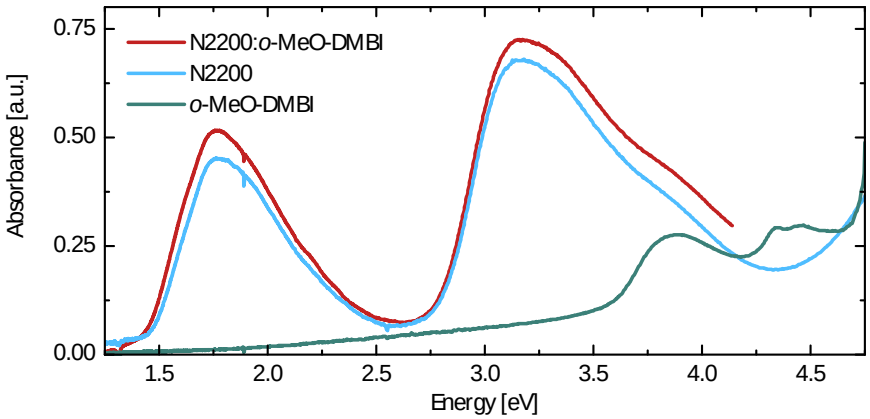

Figure A.3: UV-Vis absorption spectra of pristine N2200, pristine dopant *o*-MeO-DMBI, and N2200:*o*-MeO-DMBI with a doping concentration of 10:1. Films were spin cast from blend solutions from chloroform.

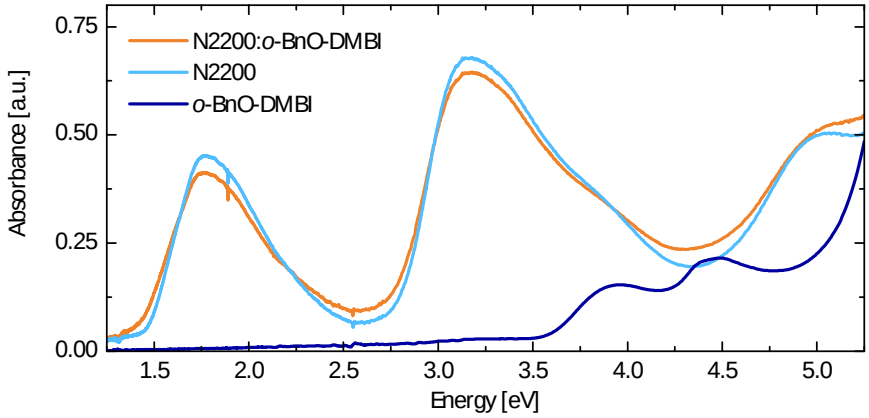

Figure A.4: UV-Vis absorption spectra of pristine N2200, pristine dopant *o*-BnO-DMBI, and N2200:*o*-BnO-DMBI with a doping concentration of 10:1. Films were spin cast from blend solutions from chloroform.

INFLUENCE OF SOLVENT UPON DOPING

Fits to UV-Vis Spectra of dissolved P3HT:F_4TCNQ

Table A.2 lists fit parameters of the Gaussians used to describe the polaron and aggregate absorption in Section 6.4. The software Fityk 0.9.8 was used to fit all contributions at the same time. Except of the Gaussians, all fit inputs were measured or extracted from literature, and adjusted with a scaling factor. The Gaussian function that is used by Fityk is given by

$$G(h, c, w) = h \cdot \exp\left\{\left(-\ln 2 \cdot \left(\frac{x - c}{w}\right)^2\right)\right\}, \tag{A.1}$$

where c denotes the center, h the height, and w the half width at half maximum (hwhm).

	height [cm^{-1}]	center [eV]	hwhm [eV]
chlorobenzene			
polaron	9.68×10^{-2}	1.60	0.27
aggregates	1.48×10^{-1}	2.22	0.22
chloroform			
polaron	3.89×10^{-2}	1.60	0.32
aggregates	6.18×10^{-2}	2.22	0.19

Table A.2: Parameters height h, center c, and half width at half maximum w that emerged from fits of P3HT:F_4TCNQ dissolved in chloroform and chlorobenzene.

TEM Brightfield Images and Electron Diffraction Patterns

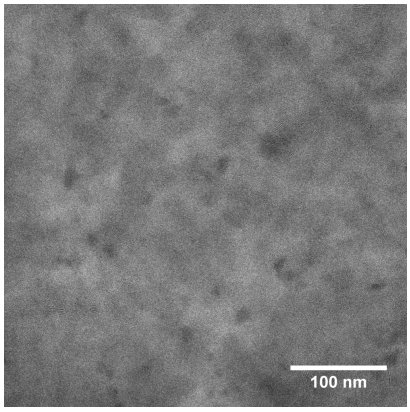

(a) BFTEM of P3HT:F_4TCNQ from CF.

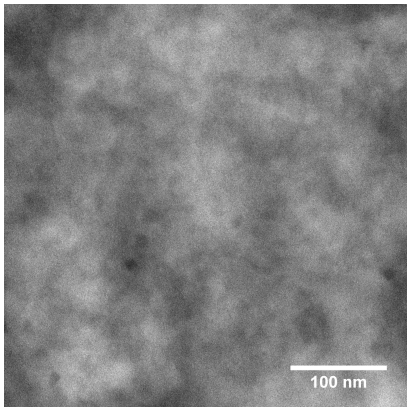

(b) BFTEM of P3HT:F_4TCNQ from CB.

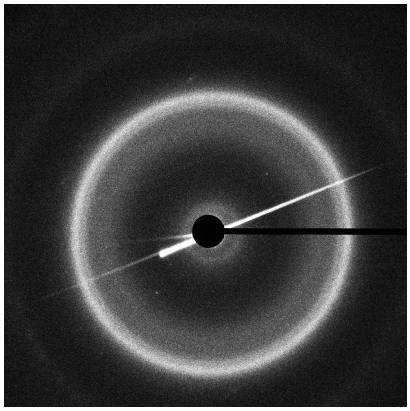

(c) ED of P3HT:F_4TCNQ from CF.

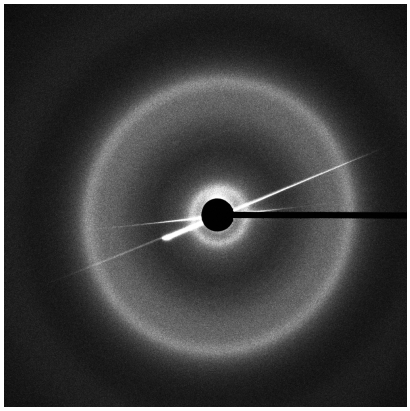

(d) ED of P3HT:F_4TCNQ from CB.

Figure A.5: (a,b) Bright-field transmission electron microscopy (BFTEM) images of F_4TCNQ-doped P3HT with a concentration of 10:1. Films were spin coated from chloroform (CF) (a) and chlorobenzene (CB) (b). (c,d) Electron diffraction (ED) patterns of P3HT:F_4TCNQ spin-cast from chloroform (c) and chlorobenzene (d).

DIFFUSION OF DOPANTS

Figure A.6 displays UV-Vis absorption spectra of sequentially doped P3HT:PCBM blends. For both sequential doping from solution and thermal evaporation, a clear spectral doping signature is visible: the broad P2 polaron absorption around 1.5 eV and the double-peak originating from the charged F_4TCNQ molecule in the same spectral region. This indicates a non-negligible diffusion of F_4TCNQ into the blend P3HT:PCBM. However, solvent swelling or a higher substrate temperature in case of the vapor-doped thin film cannot be excluded.

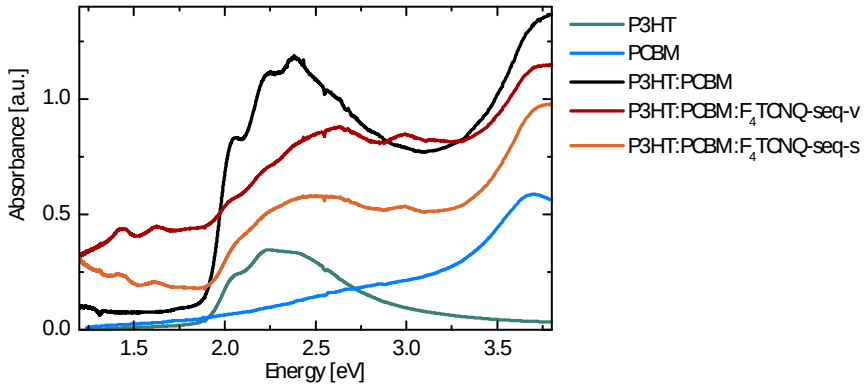

Figure A.6: UV-Vis absorption spectra of pristine P3HT, PCBM, and a blend film as well as P3HT:PCBM sequentially doped with F_4TCNQ from acetonitrile solution (*P3HT:PCBM:F_4TCNQ-seq-s*) and vapor doping (*seq-v*) according to [23]. A strong doping signature (see Chapter 5 for details) is visible in both sequentially doped P3HT:PCBM blends, indicating a diffusion of F_4TCNQ into the mixed films.

CONTROLLED DRIFT OF SMALL MOLECULE DOPANTS

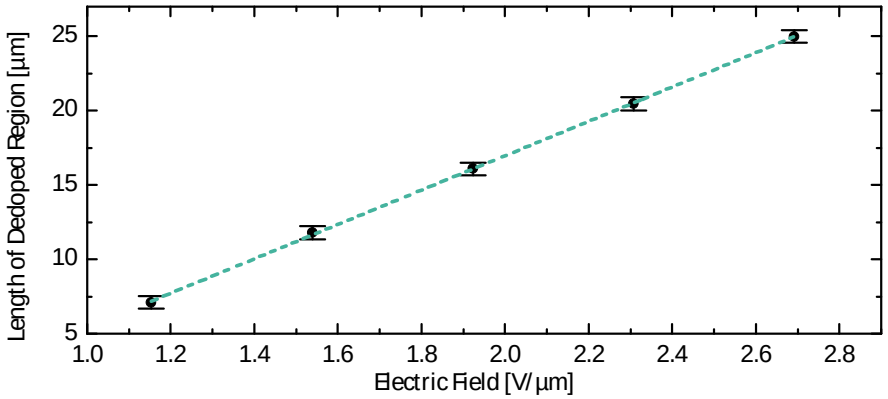

Figure A.7: Length of the dedoped region in a two-electrode device with a channel length of 140 µm, a doping ratio of 50:1 P3HT:Mo(tfd-CO_2Me)$_3$ for electric fields above the threshold for a dopant drift. The dashed linear line is a guide to the eye.

Figure A.8 displays spatially resolved IR spectroscopy measurements of P3HT:F_4TCNQ analogue to the measurements on P3HT:Mo(tfd-CO_2Me)$_3$ in Figure 11.2. The measurement spot was located near the electrode to which the polarity of the electric field given in the legend corresponds. The electric field strength was incrementally increased from $-1.2\,\mathrm{V\,\mu m^{-1}}$ to $-1.4\,\mathrm{V\,\mu m^{-1}}$, then set to $1.8\,\mathrm{V\,\mu m^{-1}}$ and was then inverted again. With increasing field strength, a decrease of the P1 polaron absorption is observed, which increases again after inversion of the voltage. This is in line with a dopant drift, since the negatively charged dopants are expected to be pushed away from the negative

electrode. The peak intensity of the C≡N stretching vibration resembles the strength of the polaron absorption, giving a direct proof that less F_4TCNQ molecules are present in the measurement spot when a negative voltage is applied. The concentration increases again upon application of a positive voltage.

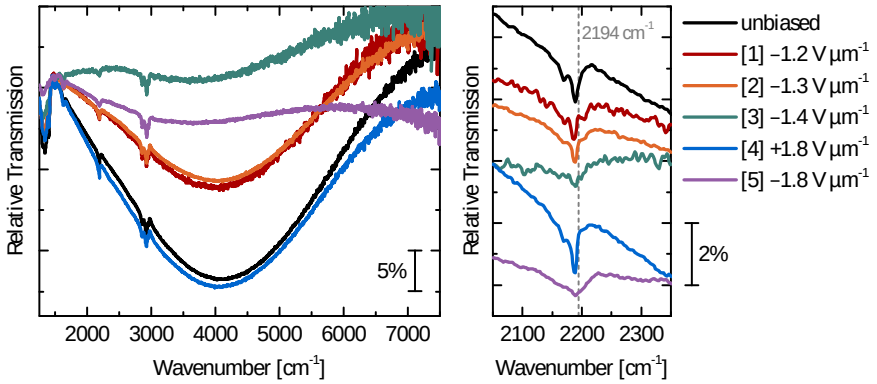

Figure A.8: Spatially resolved IR relative transmission spectra of P3HT:F_4TCNQ in a doping ratio of 10:1, doped by sequential doping from acetonitrile solution. Spectra are measured before and after application of electric fields near the electrode to which the polarity of the electric field in the legend corresponds. The left side displays overview spectra with the broad P1 polaron absorption of charged P3HT and the IRAV modes below 1500 cm^{-1}. The right side shows a zoom-in to the spectral region of the C≡N stretching vibration, characteristic for the F_4TCNQ molecule.

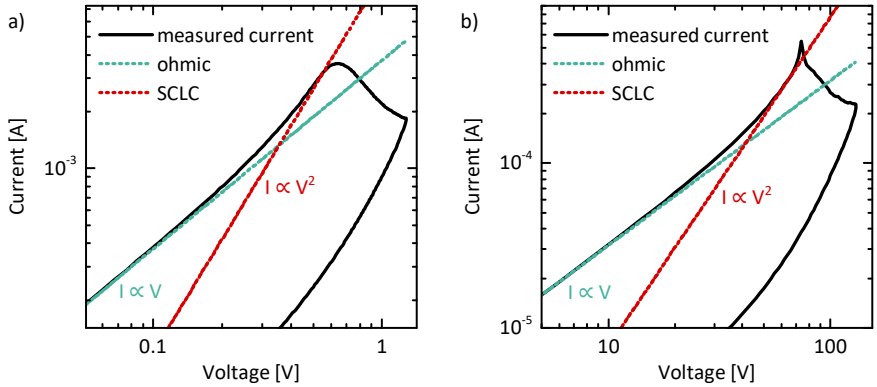

Figure A.9: Double-logarithmic representation of IV measurements where a drift of Mo(tfd-CO_2Me)$_3$ (a) and F_4TCNQ (b) in P3HT sets in above a certain threshold voltage. The two lines represent the ohmic and space-charge limited current (SCLC) regime, in which the current depends on V and V^2, respectively. For low voltages, the current shows ohmic behavior, but the superlinear increase cannot be sufficiently described with SCLC behavior.

CHARACTERIZATION OF DMBI-DERIVATIVES AS N-TYPE DOPANTS FOR ORGANIC SEMICONDUCTORS

UV-Vis spectra of N2200:o-AzBnO-DMBI

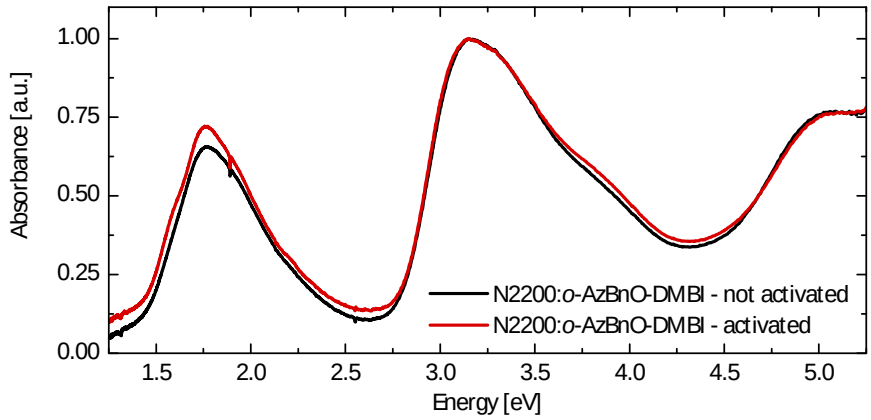

Figure A.10: Normalized UV-Vis absorbance measurements of N2200:*o*-AzBnO-DMBI after spin coating and after thermal activation at 130 °C for 10 min. The spectrum does not change significantly upon thermal activation.

Stability of Doped N2200

Figure A.11 displays conductivity measurements of N2200:*o*-BnO-DMBI and N2200:*o*-MeO-DMBI over a time period of roughly 20 days. The samples were stored and measured under intert N_2 atmosphere. It can be seen that the conductivity decreases strongly in this time period, which could be related to a degradation of the dopant molecules or the host matrix. A further explanation could be that host and dopants phase segregate [244], which would decrease the volume doping to a surface doping and hence significantly lower the overall conductivity.

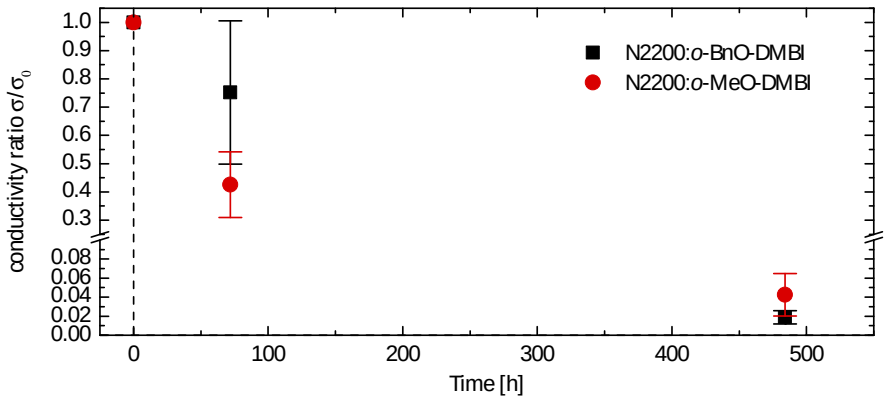

Figure A.11: Long-term conductivity measurements of N2200:*o*-BnO-DMBI and N2200:*o*-MeO-DMBI. The samples were stored and measured under inert N_2 atmosphere. The measurements were performed with the two-terminal sensing method.

BIBLIOGRAPHY

[1] Hideki Shirakawa, Edwin J. Louis, Alan G. MacDiarmid, Chwan K. Chiang, and Alan J. Heeger. "Synthesis of electrically conducting organic polymers: halogen derivatives of polyacetylene, (CH) x." en. In: *Journal of the Chemical Society, Chemical Communications* 16 (1977), p. 578.

[2] Ingo Salzmann and Georg Heimel. "Towards a comprehensive understanding of molecular doping organic semiconductors (Review)." In: *Journal of Electron Spectroscopy and Related Phenomena* 204 (2015), pp. 208–222.

[3] Nobel Media AB 2014. *The Nobel Prize in Chemistry 2000*.

[4] C. K. Chiang, C. R. Fincher, Y. W. Park, A. J. Heeger, H. Shirakawa, E. J. Louis, S. C. Gau, and Alan G. MacDiarmid. "Electrical Conductivity in Doped Polyacetylene." In: *Physical Review Letters* 39.17 (1977), pp. 1098–1101.

[5] Junji Kido and Toshio Matsumoto. "Bright organic electroluminescent devices having a metal-doped electron-injecting layer." In: *Applied Physics Letters* 73.20 (1998), pp. 2866–2868.

[6] G. Parthasarathy, C. Shen, A. Kahn, and S. R. Forrest. "Lithium doping of semiconducting organic charge transport materials." In: *Journal of Applied Physics* 89.9 (2001), p. 4986.

[7] S M Sze. *Physics of Semiconductor Devices*. John Wiley and Sons, 1981, pp. 812–816.

[8] C. W. Tang. "Two-layer organic photovoltaic cell." In: *Applied Physics Letters* 48.2 (1986), p. 183.

[9] C. W. Tang and S. A. VanSlyke. "Organic electroluminescent diodes." In: *Applied Physics Letters* 51.12 (1987), pp. 913–915.

[10] N S Sariciftci, L Smilowitz, A J Heeger, F Wudl, and A. J. Heeger. "Photoinduced electron transfer from a conducting polymer to buckminsterfullerene." In: *Science (New York, N.Y.)* 258.5087 (1992), pp. 1474–6.

[11] B. Maennig *et al.* "Organic p -i- n solar cells." In: *Applied Physics A: Materials Science & Processing* 79.1 (2004), pp. 1–14.

[12] J. Drechsel, B. Männig, F. Kozlowski, M. Pfeiffer, K. Leo, and H. Hoppe. "Efficient organic solar cells based on a double p-i-n architecture using doped wide-gap transport layers." In: *Applied Physics Letters* 86.24 (2005), p. 244102.

[13] Gufeng He, Martin Pfeiffer, Karl Leo, Michael Hofmann, Jan Birnstock, Robert Pudzich, and Josef Salbeck. "High-efficiency and low-voltage p-i-n electrophosphorescent organic light-emitting diodes with double-emission layers." In: *Applied Physics Letters* 85.17 (2004), pp. 3911–3913.

[14] K Walzer, B Maennig, M Pfeiffer, and K Leo. "Highly efficient organic devices based on electrically doped transport layers." In: *Chemical reviews* 107 (2007), pp. 1233–71.

[15] Björn Lüssem, Max L Tietze, Hans Kleemann, Christoph Hoßbach, Johann W Bartha, Alexander Zakhidov, and Karl Leo. "Doped organic transistors operating in the inversion and depletion regime." In: *Nature communications* 4 (2013), p. 2775.

[16] Qian Zhang, Yimeng Sun, Wei Xu, and Daoben Zhu. "Organic Thermoelectric Materials: Emerging Green Energy Materials Converting Heat to Electricity Directly and Efficiently." In: *Advanced Materials* 26.40 (2014), pp. 6829–6851.

[17] Renee Kroon, Desalegn Alemu Mengistie, David Kiefer, Jonna Hynynen, Jason D. Ryan, Liyang Yu, and Christian Müller. "Thermoelectric plastics: from design to synthesis, processing and structure–property relationships." In: *Chem. Soc. Rev.* 45.22 (2016), pp. 6147–6164.

[18] Sabine Ludwigs, ed. *P3HT Revisited – From Molecular Scale to Solar Cell Devices*. Vol. 265. Advances in Polymer Science. Berlin, Heidelberg: Springer, 2014.

[19] Ian E. Jacobs and Adam J. Moulé. "Controlling Molecular Doping in Organic Semiconductors." In: *Advanced Materials* 29.42 (2017), p. 1703063.

[20] Jian Gao, Edwards T. Niles, and John K. Grey. "Aggregates promote efficient charge transfer doping of Poly(3- hexylthiophene)." In: *Journal of Physical Chemistry Letters* 4.17 (2013), pp. 2953–2957.

[21] Jian Gao, Benjamin W. Stein, Alan K. Thomas, Jose Antonio Garcia-Galvez, Jing Yang, Martin L. Kirk, and John K. Grey. "Enhanced Charge Transfer Doping Efficiency in J-Aggregate Poly(3-hexylthiophene) Nanofibers." In: *The Journal of Physical Chemistry C* (2015), pp. 16396–16402.

[22] D. Tyler Scholes, Patrick Y. Yee, Jeffrey R. Lindemuth, Hyeyeon Kang, Jonathan Onorato, Raja Ghosh, Christine Luscombe, Frank C. Spano, and H Sarah. "The Effects of Crystallinity on Charge Transport and the Structure of Sequentially-Processed F 4 TCNQ-doped Conjugated Polymer Films." In: *Advanced Functional Materials* (2017), pp. 1–23.

[23] Jonna Hynynen, David Kiefer, Liyang Yu, Renee Kroon, Rahim Munir, Aram Amassian, Martijn Kemerink, and Christian Müller. "Enhanced Electrical Conductivity of Molecularly p-Doped Poly(3-hexylthiophene) through Understanding the Correlation with Solid-State Order." In: *Macromolecules* 50.20 (2017), pp. 8140–8148.

[24] D. Tyler Scholes, Steven A. Hawks, Patrick Y. Yee, Hao Wu, Jeffrey R. Lindemuth, Sarah H. Tolbert, and Benjamin J. Schwartz. "Overcoming Film Quality Issues for Conjugated Polymers Doped with F4TCNQ by Solution Sequential Processing: Hall Effect, Structural, and Optical Measurements." EN. In: *Journal of Physical Chemistry Letters* 6 (2015), pp. 4786–4793.

[25] Ian E Jacobs, Erik W. Aasen, Julia L. Oliveira, Tayane N. Fonseca, John D Roehling, Jun Li, Guangwu Zhang, Matthew P Augustine, Mark Mascal, and Adam Moule. "Comparison of solution-mixed and sequentially processed P3HT:F4TCNQ films: effect of doping-induced aggregation on film morphology." en. In: *J. Mater. Chem. C* 4 (2016), pp. 3454–3466.

[26] Priyanka Tyagi, Manas Kumar Dalai, C. K. Suman, Suneet Tuli, and Ritu Srivastava. "Study of 2,3,5,6-tetrafluoro-7,7′,8,8′-tetracyano quinodimethane diffusion in organic light emitting diodes using secondary ion mass spectroscopy." In: *RSC Advances* 3.46 (2013), p. 24553.

[27] Jun Li, Guangwu Zhang, Daniella M. Holm, Ian E. Jacobs, Bin Yin, Pieter Stroeve, Mark Mascal, and Adam J. Moulé. "Introducing Solubility Control for Improved Organic P-Type Dopants." In: *Chemistry of Materials* 27.16 (2015), pp. 5765–5774.

[28] Meghan P. Patankar, Kapil Joshi, and K. L. Narasimhan. "Study of F4TCNQ dopant diffusion using transport measurements in organic semiconductors." In: *arXiv preprint* (2013), p. 22.

[29] Elisa Leyva, Mary Jennifer, T. Young, and Matthew S. Platz. "High Yields of Formal CH Insertion Products in the Reactions of Polyfluorinated Aromatic Nitrenes." In: *Journal of the American Chemical Society* 108.26 (1986), pp. 8307–8309.

[30] Rui-Qi Png, Perq-Jon Chia, Jie-Cong Tang, Bo Liu, Sankaran Sivaramakrishnan, Mi Zhou, Siong-Hee Khong, Hardy S. O. Chan, Jeremy H. Burroughes, Lay-Lay Chua, Richard H. Friend, and Peter K. H. Ho. "High-performance polymer semiconducting heterostructure devices by nitrene-mediated photocrosslinking of alkyl side chains." In: *Nature Materials* 9.2 (2010), pp. 152–158.

[31] M. Brinkmann and P. Rannou. "Effect of Molecular Weight on the Structure and Morphology of Oriented Thin Films of Regioregular Poly(3-hexylthiophene) Grown by Directional Epitaxial Solidification." In: *Advanced Functional Materials* 17.1 (2007), pp. 101–108.

[32] Frank C. Spano. "Modeling disorder in polymer aggregates: The optical spectroscopy of regioregular poly(3-hexylthiophene) thin films." In: *Journal of Chemical Physics* 122 (2005), p. 234701.

[33] Jenny Clark, Carlos Silva, Richard H. Friend, and Frank C. Spano. "Role of Intermolecular Coupling in the Photophysics of Disordered Organic Semiconductors: Aggregate Emission in Regioregular Polythiophene." In: *Physical Review Letters* 98.20 (2007), p. 206406.

[34] M Schwoerer and H C Wolf. *Organic Molecular Solids*. John Wiley & Sons, Inc., 2008.

[35] Anna Köhler and Heinz Bässler. *Electronic Processes in Organic Semiconductors: An Introduction*. John Wiley & Sons, Inc., 2015.

[36] Martin Pope and Charles E. Swenberg. *Electronic processes in organic crystals and polymers*. Oxford University Press, 1999, p. 1328.

[37] Heinz Bässler and Anna Köhler. "Charge transport in organic semiconductors." In: *Topics in current chemistry* 312 (2012), pp. 1–65.

[38] I. Fishchuk, A. Kadashchuk, H. Bässler, and S. Nešpůrek. "Nondispersive polaron transport in disordered organic solids." In: *Physical Review B* 67.22 (2003), p. 224303.

[39] H. Bässler. "Charge Transport in Disordered Organic Photoconductors a Monte Carlo Simulation Study." In: *physica status solidi (b)* 175.1 (1993), pp. 15–56.

[40] S D Baranovskii, T Faber, F Hensel, and P Thomas. "The applicability of the transport-energy concept to various disordered materials." In: *Journal of Physics: Condensed Matter* 9.13 (1997), pp. 2699–2706.

[41] C. Tanase, E. J. Meijer, P. W. M. Blom, and D. M. de Leeuw. "Unification of the Hole Transport in Polymeric Field-Effect Transistors and Light-Emitting Diodes." In: *Physical Review Letters* 91.21 (2003), p. 216601.

[42] Guangzheng Zuo, Hassan Abdalla, and Martijn Kemerink. "Impact of doping on the density of states and the mobility in organic semiconductors." In: *Physical Review B* 93.23 (2016), p. 235203.

[43] Guangzheng Zuo, Zhaojun Li, Olof Andersson, Hassan Abdalla, Ergang Wang, and Martijn Kemerink. "Molecular Doping and Trap Filling in Organic Semiconductor Host-Guest Systems." In: *Journal of Physical Chemistry C* 121.14 (2017), pp. 7767–7775.

[44] Siegfried Hunklinger. *Festkörperphysik*. 2. Auflage. Oldenbourg Wissenschaftsverlag, 2009.

[45] Alexander Mityashin, Yoann Olivier, Tanguy Van Regemorter, Cedric Rolin, Stijn Verlaak, Nicolas G. Martinelli, David Beljonne, Jérôme Cornil, Jan Genoe, and Paul Heremans. "Unraveling the mechanism of molecular doping in organic semiconductors." In: *Advanced Materials* 24.12 (2012), pp. 1535–1539.

[46] Ingo Salzmann, Georg Heimel, Martin Oehzelt, Stefanie Winkler, and Norbert Koch. "Molecular Electrical Doping of Organic Semiconductors: Fundamental Mechanisms and Emerging Dopant Design Rules." In: *Accounts of Chemical Research* 49.3 (2016), pp. 370–378.

[47] Deepak Venkateshvaran *et al.* "Approaching disorder-free transport in high-mobility conjugated polymers." In: *Nature* 515.7527 (2014), pp. 384–388.

[48] Henry Méndez, Georg Heimel, Andreas Opitz, Katrein Sauer, Patrick Barkowski, Martin Oehzelt, Junshi Soeda, Toshihiro Okamoto, Jun Takeya, Jean-Baptiste Arlin, Jean-Yves Balandier, Yves Geerts, Norbert Koch, and Ingo Salzmann. "Doping of Organic Semiconductors: Impact of Dopant Strength and Electronic Coupling." In: *Angewandte Chemie International Edition* 52.30 (2013), pp. 7751–7755.

[49] Henry Méndez, Georg Heimel, Stefanie Winkler, Johannes Frisch, Andreas Opitz, Katrein Sauer, Berthold Wegner, Martin Oehzelt, Christian Röthel, Steffen Duhm, Daniel Többens, Norbert Koch, and Ingo Salzmann. "Charge-transfer crystallites as molecular electrical dopants." en. In: *Nature Communications* 6 (2015), p. 8560.

[50] Rodrigo Q. Albuquerque, Christiane C. Hofmann, Jurgen Kohler, and Anna Kohler. "Diffusion-Limited Energy Transfer in Blends of Oligofluorenes with an Anthracene Derivative." In: *The Journal of Physical Chemistry B* 115.25 (2011), pp. 8063–8070.

[51] Frank C. Spano and Carlos Silva. "H- and J-aggregate behavior in polymeric semiconductors." In: *Annual review of physical chemistry* 65.1 (2014), pp. 477–500.

[52] Stefanie Winkler, Patrick Amsalem, Johannes Frisch, Martin Oehzelt, Georg Heimel, and Norbert Koch. "Probing the energy levels in hole-doped molecular semiconductors." In: *Mater. Horiz.* 2.4 (2015), pp. 427–433.

[53] Georg Heimel. "The Optical Signature of Charges in Conjugated Polymers." In: *ACS central science* 2.5 (2016), pp. 309–315.

[54] R. Österbacka, C. P. An, X. M. Jiang, and Z. V. Vardeny. "Two-Dimensional Electronic Excitations in Self-Assembled Conjugated Polymer Nanocrystals." In: *Science* 287.5454 (2000), pp. 839–842.

[55] Annabel R. Chew and Alberto Salleo. "Spectroscopic studies of dopant-induced conformational changes in poly(3-hexylthiophene) thin films." In: *MRS Communications* 7.03 (2017), pp. 728–734.

[56] Simon Kahmann, Daniele Fazzi, Gebhard J. Matt, Walter Thiel, Maria A. Loi, and Christoph J. Brabec. "Polarons in Narrow Band Gap Polymers Probed over the Entire Infrared Range: A Joint Experimental and Theoretical Investigation." In: *Journal of Physical Chemistry Letters* 7.22 (2016), pp. 4438–4444.

[57] David B Williams and C Barry Carter. *Transmission Electron Microscopy: A Textbook for Materials Science*. Vol. V1-V4. Springer Science & Business Media, 2009.

[58] Ray Egerton. *Electron Energy-Loss Spectroscopy in the Electron Microscope*. Springer Science & Business Media, 2011.

[59] L. Reimer and H. Kohl. *Transmission Electron Microscopy - Physics of Image Formation*. Springer, 1997.

[60] Ray F. Egerton. *Physical Principles of Electron Microscopy*. Boston, MA: Springer US, 2005.

[61] Dmitri B. Strukov, Julien L. Borghetti, and R. Stanley Williams. "Coupled ionic and electronic transport model of thin-film semiconductor memristive behavior." In: *Small* 5.9 (2009), pp. 1058–1063.

[62] L. Chua. "Memristor-The missing circuit element." In: *IEEE Transactions on Circuit Theory* 18.5 (1971), pp. 507–519.

[63] Dmitri B. Strukov, Gregory S. Snider, Duncan R. Stewart, and R. Stanley Williams. "The missing memristor found." In: *Nature* 453.7191 (2008), pp. 80–3.

[64] Sascha Vongehr and Xiangkang Meng. "The Missing Memristor has Not been Found." In: *Scientific Reports* 5.1 (2015), p. 11657.

[65] L.O. Chua and Sung Mo Kang. "Memristive devices and systems." In: *Proceedings of the IEEE* 64.2 (1976), pp. 209–223.

[66] David Brandon and Wayne D. Kaplan. *Microstructural Characterization of Materials*. Chichester, UK: John Wiley & Sons, Ltd, 2008.

[67] Johannes Schindelin *et al.* "Fiji: an open-source platform for biological-image analysis." In: *Nature Methods* 9.7 (2012), pp. 676–682.

[68] Sebastian Beck. "Untersuchung des Ladungstransfers in organischen Halbleitern mit in-situ Infrarotspektroskopie." PhD thesis. Heidelberg University, 2014.

[69] Vipilan Sivanesan. "Infrarotspektroskopische Untersuchung der p-Dotierung von Poly(3-hexylthiophen)." MA thesis. Heidelberg University, 2016.

[70] Lukas Schmidt-Mende and Jonas Weickert. *Organic and Hybrid Solar Cells: an Introduction*. De Gruyter, 2016.

[71] Leo J. van der Pauw. "A Method of Measuring Specific Resistivity and Hall effect of Discs of Arbitrary Shape." In: *Philips Research Reports* 13.1 (1958), pp. 1–11.

[72] Sebastian Hietzschold. "Surface Functionalization of Nickel Oxide and Gallium Nitride for Hybrid Opto-Electronics." PhD thesis. Heidelberg University, 2017.

[73] Ze-Lei Guan, Jong Bok Kim, He Wang, Cherno Jaye, Daniel A. Fischer, Yueh-Lin Loo, and Antoine Kahn. "Direct determination of the electronic structure of the poly(3-hexylthiophene): phenyl-[6,6]-C61 butyric acid methyl ester blend." In: *Organic Electronics* 11.11 (2010), pp. 1779–1785.

[74] Sangwon Ko, Eric T. Hoke, Laxman Pandey, Sanghyun Hong, Rajib Mondal, Chad Risko, Yuanping Yi, Rodrigo Noriega, M. D. McGehee, Jean-Luc Brédas, Alberto Salleo, and Zhenan Bao. "Controlled Conjugated Backbone Twisting for an Increased Open-Circuit Voltage while Having a High Short-Circuit Current in Poly(hexylthiophene) Derivatives." In: *Journal of the American Chemical Society* 134.11 (2012), pp. 5222–5232.

[75] Kang Jun Baeg, Dongyoon Khim, Dong Yu Kim, Jae Bon Koo, In Kyu You, Won San Choi, and Yong Young Noh. "High mobility top-gated poly(3-hexylthiophene) field-effect transistors with high work-function Pt electrodes." In: *Thin Solid Films* 518.14 (2010), pp. 4024–4029.

[76] Zafer Hawash, Luis K. Ono, Sonia R. Raga, Michael V. Lee, and Yabing Qi. "Air-Exposure Induced Dopant Redistribution and Energy Level Shifts in Spin-Coated Spiro-MeOTAD Films." In: *Chemistry of Materials* 27.2 (2015), pp. 562–569.

[77] N. Thejo Kalyani and S. J. Dhoble. "Organic light emitting diodes: Energy saving lighting technology - A review." In: *Renewable and Sustainable Energy Reviews* 16.5 (2012), pp. 2696–2723.

[78] Alba Pellaroque, Nakita K. Noel, Severin N. Habisreutinger, Yadong Zhang, Stephen Barlow, Seth R. Marder, and Henry J. Snaith. "Efficient and Stable Perovskite Solar Cells Using Molybdenum Tris(dithiolene)s as p-Dopants for Spiro-OMeTAD." In: *ACS Energy Letters* 2.9 (2017), pp. 2044–2050.

[79] Dong-Yi Chen, Wei-Hsuan Tseng, Sheng-Ping Liang, Chih-I Wu, Che-Wei Hsu, Yun Chi, Wen-Yi Hung, and Pi-Tai Chou. "Application of F4TCNQ doped spiro-MeOTAD in high performance solid state dye sensitized solar cells." In: *Physical Chemistry Chemical Physics* 14.33 (2012), p. 11689.

[80] He Yan, Zhihua Chen, Yan Zheng, Christopher Newman, Jordan R. Quinn, Florian Dötz, Marcel Kastler, and Antonio Facchetti. "A high-mobility electron-transporting polymer for printed transistors." In: *Nature* 457.7230 (2009), pp. 679–686.

[81] Zhihua Chen, Yan Zheng, He Yan, and Antonio Facchetti. "Naphthalene-dicarboximide- vs Perylene-dicarboximide-Based Copolymers. Synthesis and Semiconducting Properties in Bottom-Gate N-Channel Organic Transistors." In: *Journal of the American Chemical Society* 131.1 (2009), pp. 8–9.

[82] Jin Young Kim, Kwanghee Lee, Nelson E Coates, Daniel Moses, Thuc-Quyen Nguyen, Mark Dante, and Alan J Heeger. "Efficient tandem polymer solar cells fabricated by all-solution processing." In: *Science (New York, N.Y.)* 317 (2007), pp. 222–5.

[83] Weiying Gao and Antoine Kahn. "Controlled p-doping of zinc phthalocyanine by coevaporation with tetrafluorotetracyanoquinodimethane: A direct and inverse photoemission study." In: *Applied Physics Letters* 79 (2001), pp. 4040–4042.

[84] An Dai, Yinhua Zhou, Andrew L. Shu, Swagat K. Mohapatra, He Wang, Canek Fuentes-Hernandez, Yadong Zhang, Stephen Barlow, Yueh Lin Loo, Seth R. Marder, Bernard Kippelen, and Antoine Kahn. "Enhanced charge-carrier injection and collection via lamination of doped polymer layers p-doped with a solution-processible molybdenum complex." In: *Advanced Functional Materials* 24.15 (2014), pp. 2197–2204.

[85] Benjamin D. Naab, Song Guo, Selina Olthof, Eric G. B. Evans, Peng Wei, Glenn L. Millhauser, Antoine Kahn, Stephen Barlow, Seth R. Marder, and Zhenan Bao. "Mechanistic Study on the Solution-Phase n-Doping of 1,3-Dimethyl-2-aryl-2,3-dihydro-1H-benzoimidazole Derivatives." In: *Journal of the American Chemical Society* 135.40 (2013), pp. 15018–25.

[86] Zhengyang Bin, Jiangwei Li, Liduo Wang, and Lian Duan. "Efficient n-type dopants with extremely low doping ratios for high performance inverted perovskite solar cells." In: *Energy Environ. Sci.* 9.11 (2016), pp. 3424–3428.

[87] Seiichiro Murase, Kenji Shibata, Hidemitsu Furukawa, Yoshiharu Miyashita, and Kazuyuki Horie. "Large photoinduced refractive index increase in polymer films containing phenylazide maintaining their transparency and thermal stability." In: *Polymer Journal* 35.2 (2003), pp. 203–208.

[88] Chenchen Wang, Duc T. Duong, Koen Vandewal, Jonathan Rivnay, and Alberto Salleo. "Optical measurement of doping efficiency in poly(3-hexylthiophene) solutions and thin films." In: *Physical Review B* 91 (2015), p. 085205.

[89] Lars Müller, Diana Nanova, Tobias Glaser, Sebastian Beck, Annemarie Pucci, Anne K. Kast, Rasmus R. Schröder, Eric Mankel, Patrick Pingel, Dieter Neher, Wolfgang Kowalsky, and Robert Lovrincic. "Charge-Transfer-Solvent Interaction Predefines Doping Efficiency in p-Doped P3HT Films." In: *Chemistry of Materials* 28.12 (2016), pp. 4432–4439.

[90] Zhenan Bao, Ananth Dodabalapur, and Andrew J. Lovinger. "Soluble and processable regioregular poly(3-hexylthiophene) for thin film field-effect transistor applications with high mobility." In: *Applied Physics Letters* 69.26 (1996), pp. 4108–4110.

[91] H. Sirringhaus, P. J. Brown, R. H. Friend, M. M. Nielsen, K. Bechgaard, B. M. W. Langeveld-Voss, A. J. H. Spiering, R. A. J. Janssen, E. W. Meijer, P. Herwig, and D. M. de Leeuw. "Two-dimensional charge transport in self-organized, high-mobility conjugated polymers." In: *Nature* 401.6754 (1999), pp. 685–688.

[92] R.J. Kline, M.D. McGehee, E.N. Kadnikova, J. Liu, and J.M.J. Fréchet. "Controlling the Field-Effect Mobility of Regioregular Polythiophene by Changing the Molecular Weight." In: *Advanced Materials* 15 (2003), pp. 1519–1522.

[93] Martin Brinkmann and Patrice Rannou. "Molecular Weight Dependence of Chain Packing and Semicrystalline Structure in Oriented Films of Regioregular Poly(3-hexylthiophene) Revealed by High-Resolution Transmission Electron Microscopy." In: *Macromolecules* 42.4 (2009), pp. 1125–1130.

[94] Maarten J M Wirix, Paul H H Bomans, Heiner Friedrich, Nico A J M Sommerdijk, and Gijsbertus de With. "Three-dimensional structure of P3HT assemblies in organic solvents revealed by cryo-TEM." In: *Nano letters* 14.4 (2014), pp. 2033–8.

[95] Diana Nanova. "Intermolecular Ordering in Organic Semiconductor Layers and its Correlation to Electronic Properties." PhD thesis. Heidelberg University, 2015.

[96] Jeffrey A. Merlo and C. Daniel Frisbie. "Field Effect Transport and Trapping in Regioregular Polythiophene Nanofibers." In: *The Journal of Physical Chemistry B* 108 (2004), pp. 19169–19179.

[97] Duc T. Duong, Chenchen Wang, Erin Antono, Michael F. Toney, and Alberto Salleo. "The chemical and structural origin of efficient p-type doping in P3HT." In: *Organic Electronics* 14 (2013), pp. 1330–1336.

[98] Kyo Jin Ihn, J. Moulton, and P. Smith. "Whiskers of poly (3-alkylthiophene)s." eng. In: *Journal of polymer science. Part B. Polymer physics* 31 (1993), pp. 735–742.

[99] Xiaobo Shen, Weiguo Hu, and Thomas P. Russell. "Measuring the degree of crystallinity in semicrystalline regioregular poly(3-hexylthiophene)." In: *Macromolecules* 49.12 (2016), pp. 4501–4509.

[100] Peter Brown, D. Thomas, Anna Köhler, Joanne Wilson, Ji-Seon Kim, Catherine Ramsdale, Henning Sirringhaus, and Richard Friend. "Effect of interchain interactions on the absorption and emission of poly(3-hexylthiophene)." In: *Physical Review B* 67.6 (2003), pp. 1–16.

[101] T. Thurn-Albrecht, R. Thomann, T. Heinzel, and S. Hugger. "Semi-crystalline morphology in thin films of poly(3-hexylthiophene)." In: *Colloid & Polymer Science* 282.8 (2004), pp. 932–938.

[102] Christina Scharsich, Ruth H. Lohwasser, Michael Sommer, Udom Asawapirom, Ullrich Scherf, Mukundan Thelakkat, Dieter Neher, and Anna Köhler. "Control of aggregate formation in poly(3-hexylthiophene) by solvent, molecular weight, and synthetic method." In: *Journal of Polymer Science, Part B: Polymer Physics* 50 (2012), pp. 442–453.

[103] Wing C Tsoi, David T James, Jong Soo Kim, Patrick G Nicholson, Craig E Murphy, Donal D C Bradley, Jenny Nelson, and Ji-Seon Kim. "The nature of in-plane skeleton Raman modes of P3HT and their correlation to the degree of molecular order in P3HT:PCBM blend thin films." In: *Journal of the American Chemical Society* 133 (2011), pp. 9834–43.

[104] Sebastian Wood, Jong Soo Kim, David T James, Wing C Tsoi, Craig E Murphy, and Ji-Seon Kim. "Understanding the relationship between molecular order and charge transport properties in conjugated polymer based organic blend photovoltaic devices." In: *The Journal of chemical physics* 139 (2013), p. 064901.

[105] Eric S. Manas and Frank C. Spano. "Absorption and spontaneous emission in aggregates of conjugated polymers." In: *The Journal of Chemical Physics* 109.18 (1998), p. 8087.

[106] D. Beljonne, J. Cornil, R. Silbey, P. Millie, and J. L. Bredas. "Interchain interactions in conjugated materials: The exciton model versus the supermolecular approach." In: *The Journal of Chemical Physics* 112.10 (2000), p. 4749.

[107] Jenny Clark, Jui Fen Chang, Frank C. Spano, Richard H. Friend, and Carlos Silva. "Determining exciton bandwidth and film microstructure in polythiophene films using linear absorption spectroscopy." In: *Applied Physics Letters* 94 (2009), pp. 2007–2010.

[108] Guy Louarn, Miroslaw Trznadel, J P Buisson, Jadwiga Laska, Adam Pron, Mieczyslaw Lapkowski, and Serge Lefrant. "Raman Spectroscopic Studies of Regioregular Poly (3-alkyl-thiophenes)." In: *Journal of Physical Chemistry* 100.30 (1996), pp. 12532–12539.

[109] John D. Roehling, Ilke Arslan, and Adam J. Moulé. "Controlling microstructure in poly(3-hexylthiophene) nanofibers." In: *Journal of Materials Chemistry* 22.6 (2012), p. 2498.

[110] Ralf Mauer, Marcel Kastler, and Frédéric Laquai. "The Impact of Polymer Regioregularity on Charge Transport and Efficiency of P3HT:PCBM Photovoltaic Devices." In: *Advanced Functional Materials* 20.13 (2010), pp. 2085–2092.

[111] Fatemeh Ghani, Andreas Opitz, Patrick Pingel, Georg Heimel, Ingo Salzmann, Johannes Frisch, Dieter Neher, Argiri Tsami, Ullrich Scherf, and Norbert Koch. "Charge transfer in and conductivity of molecularly doped thiophene-based copolymers." In: *Journal of Polymer Science Part B: Polymer Physics* 53 (2015), pp. 58–63.

[112] Rodrigo Noriega, Jonathan Rivnay, Koen Vandewal, Felix P V Koch, Natalie Stingelin, Paul Smith, Michael F Toney, and Alberto Salleo. "A general relationship between disorder, aggregation and charge transport in conjugated polymers." In: *Nature materials* 12 (2013), pp. 1038–44.

[113] P. Pingel and D. Neher. "Comprehensive picture of p-type doping of P3HT with the molecular acceptor F4TCNQ." In: *Physical Review B - Condensed Matter and Materials Physics* 87 (2013), pp. 1–9.

[114] Patrick Pingel, Malavika Arvind, Lisa Kölln, Robert Steyrleuthner, Felix Kraffert, Jan Behrends, Silvia Janietz, and Dieter Neher. "P-Type Doping of Poly(3-hexylthiophene) with the Strong Lewis Acid Tris(pentafluorophenyl)borane." In: *Advanced Electronic Materials* 2.10 (2016), pp. 1–7.

[115] David Kiefer, Liyang Yu, Erik Fransson, Andrés Gómez, Daniel Primetzhofer, Aram Amassian, Mariano Campoy-Quiles, and Christian Müller. "A Solution-Doped Polymer Semiconductor: Insulator Blend for Thermoelectrics." In: *Advanced Science* 4.1 (2017), p. 1600203.

[116] Y. Kim. "Photoexcitation and doping studies of poly(3-hexylthienylene)." In: *Physical Review B* 27.8 (1988), pp. 4804–5495.

[117] Tian An Chen, Xiaoming Wu, and Reuben D. Rieke. "Regiocontrolled Synthesis of Poly(3-alkylthiophenes) Mediated by Rieke Zinc: Their Characterization and Solid-State Properties." In: *Journal of the American Chemical Society* 117.1 (1995), pp. 233–244.

[118] Raja Ghosh, Christopher M. Pochas, and Frank C. Spano. "Polaron Delocalization in Conjugated Polymer Films." In: *The Journal of Physical Chemistry C* (2016), acs.jpcc.6b02917.

[119] Moreno Meneghetti and Cesare Pecile. "Charge–transfer organic crystals: Molecular vibrations and spectroscopic effects of electron–molecular vibration coupling of the strong electron acceptor TCNQF4." In: *The Journal of Chemical Physics* 84 (1986), pp. 4149–4162.

[120] Patrick Pingel, Lingyun Zhu, Kue Surk Park, Jörn Oliver Vogel, Silvia Janietz, Eung Gun Kim, Jürgen P. Rabe, Jean Luc Brédas, and Norbert Koch. "Charge-transfer localization in molecularly doped thiophene-based donor polymers." In: *Journal of Physical Chemistry Letters* 1 (2010), pp. 2037–2041.

[121] J. S. Chappell, A. N. Bloch, W. A. Bryden, M. Maxfield, T. O. Poehler, and D. O. Cowan. "Degree of charge transfer in organic conductors by infrared absorption spectroscopy." In: *Journal of the American Chemical Society* 103 (1981), pp. 2442–2443.

[122] A Salmeron-Valverde, J G Robles-Martinez, J Garcca-Serrano, R Gomez, R M Ridaura, M Quintana, and A Zehe. "A Study of the Degree of Charge Transfer in TTF Molecular Complexes with Nitro-Carboxylated Fluorene Derivatives." en. In: *Molecular Engineering* 8.4 (1999), pp. 419–426.

[123] John C Stires, Emily J McLaurin, and Clifford P Kubiak. "Infrared spectroscopic determination of the degree of charge transfer in complexes of TCNE with methyl-substituted benzenes." en. In: *Chemical communications (Cambridge, England)* (2005), pp. 3532–4.

[124] Lars Müller, Seon-Young Rhim, Vipilan Sivanesan, Dongxiang Wang, Sebastian Hietzschold, Patrick Reiser, Eric Mankel, Sebastian Beck, Stephen Barlow, Seth R. Marder, Annemarie Pucci, Wolfgang Kowalsky, and Robert Lovrincic. "Electric-Field-Controlled Dopant Distribution in Organic Semiconductors." In: *Advanced Materials* (2017), p. 1701466.

[125] Serap Günes, Helmut Neugebauer, and Niyazi Serdar Sariciftci. "Conjugated polymer-based organic solar cells." In: *Chemical Reviews* 107.4 (2007), pp. 1324–1338.

[126] M. C. Scharber and N. S. Sariciftci. "Efficiency of bulk-heterojunction organic solar cells." In: *Progress in Polymer Science* 38.12 (2013), pp. 1929–1940.

[127] Shin Sung Kim, Seunghwan Bae, and Won Ho Jo. "Performance enhancement of planar heterojunction perovskite solar cells by n-doping of the electron transporting layer." In: *Chem. Commun.* 51.98 (2015), pp. 17413–17416.

[128] Peng Wei, Nan Liu, Hye Ryoung Lee, Eric Adijanto, Lijie Ci, Benjamin D. Naab, Jian Qiang Zhong, Jinseong Park, Wei Chen, Yi Cui, and Zhenan Bao. "Tuning the dirac point in CVD-grown graphene through solution processed n-type doping with 2-(2-methoxyphenyl)-1,3-dimethyl-2,3-dihydro-1 H-benzoimidazole." In: *Nano Letters* 13.5 (2013), pp. 1890–1897.

[129] Zhengyang Bin, Lian Duan, and Yong Qiu. "Air stable organic salt as an n-type dopant for efficient and stable organic light-emitting diodes." In: *ACS Applied Materials and Interfaces* 7.12 (2015), pp. 6444–6450.

[130] Ruth A. Schlitz, Fulvio G. Brunetti, Anne M. Glaudell, P. Levi Miller, Michael A. Brady, Christopher J. Takacs, Craig J. Hawker, and Michael L. Chabinyc. "Solubility-limited extrinsic n-type doping of a high electron mobility polymer for thermoelectric applications." In: *Advanced Materials* 26.18 (2014), pp. 2825–2830.

[131] Jian Gao, John D. Roehling, Yongle Li, Hua Guo, Adam J. Moulé, and John K. Grey. "The effect of 2,3,5,6-tetrafluoro-7,7,8,8-tetra-cyano-quinodimethane charge transfer dopants on the conformation and aggregation of poly(3-hexylthiophene)." In: *Journal of Materials Chemistry C* 1 (2013), pp. 5638–5646.

[132] Rodrigo Noriega, Jonathan Rivnay, Koen Vandewal, Felix P V Koch, Natalie Stingelin, Paul Smith, Michael F Toney, and Alberto Salleo. "A general relationship between disorder, aggregation and charge transport in conjugated polymers." In: *Nature materials* 12 (2013), pp. 1038–44.

[133] Jean-Marie Verilhac, Gilles LeBlevennec, David Djurado, François Rieutord, Mustapha Chouiki, Jean-Pierre Travers, and Adam Pron. "Effect of macromolecular parameters and processing conditions on supramolecular organisation, morphology and electrical transport properties in thin layers of regioregular poly(3-hexylthiophene)." In: *Synthetic Metals* 156 (2006), pp. 815–823.

[134] Steffan Cook, Akihiro Furube, and Ryuzi Katoh. "Mixed solvents for morphology control of organic solar cell blend films." In: *Japanese Journal of Applied Physics* 47 (2008), pp. 1238–1241.

[135] Patrick Pingel, Achmad Zen, Ruben D. Abellón, Ferdinand C. Grozema, Laurens D.A. Siebbeles, and Dieter Neher. "Temperature-Resolved Local and Macroscopic Charge Carrier Transport in Thin P3HT Layers." In: *Advanced Functional Materials* 20 (2010), pp. 2286–2295.

[136] P. Pingel, R. Schwarzl, and D. Neher. "Effect of molecular p-doping on hole density and mobility in poly(3-hexylthiophene)." In: *Applied Physics Letters* 100 (2012), pp. 10–13.

[137] Duc T Duong, Hung Phan, David Hanifi, Pil Sung Jo, Thuc-Quyen Nguyen, and Alberto Salleo. "Direct observation of doping sites in temperature-controlled, p-doped P3HT thin films by conducting atomic force microscopy." In: *Advanced Materials* 26 (2014), pp. 6069–73.

[138] Thomas F. Harrelson, Yongqiang Q. Cheng, Jun Li, Ian E. Jacobs, Anibal J. Ramirez-Cuesta, Roland Faller, and Adam J. Moulé. "Identifying Atomic Scale Structure in Undoped/Doped Semicrystalline P3HT Using Inelastic Neutron Scattering." In: *Macromolecules* 50.6 (2017), pp. 2424–2435.

[139] Amer Hamidi-Sakr, Laure Biniek, Jean-Louis Bantignies, David Maurin, Laurent Herrmann, Nicolas Leclerc, Patrick Lévêque, Vishnu Vijayakumar, Nicolas Zimmermann, and Martin Brinkmann. "A Versatile Method to Fabricate Highly In-Plane Aligned Conducting Polymer Films with Anisotropic Charge Transport and Thermoelectric Properties: The Key Role of Alkyl Side Chain Layers on the Doping Mechanism." In: *Advanced Functional Materials* 1700173 (2017), p. 1700173.

[140] M. Wohlgenannt, X. M. Jiang, and Z. V. Vardeny. "Confined and delocalized polarons in π -conjugated oligomers and polymers: A study of the effective conjugation length." In: *Physical Review B* 69 (2004), p. 241204.

[141] Youngkyoo Kim, Steffan Cook, Sachetan M. Tuladhar, Stelios A. Choulis, Jenny Nelson, James R. Durrant, Donal D. C. Bradley, Mark Giles, Iain McCulloch, Chang-Sik Ha, and Moonhor Ree. "A strong regioregularity effect in self-organizing conjugated polymer films and high-efficiency polythiophene:fullerene solar cells." In: *Nature Materials* 5 (2006), pp. 197–203.

[142] N. Colaneri, M. Nowak, D. Spiegel, S. Hotta, and A. J. Heeger. "Bipolarons in poly(3-methylthiophene): Spectroscopic, magnetic, and electrochemical measurements." In: *Physical Review B* 36 (1987), pp. 7964–7968.

[143] Christian Reichardt. "Solvatochromic Dyes as Solvent Polarity Indicators." In: *Chemical Reviews* 94 (1994), pp. 2319–2358.

[144] Byung-Ryool Hyun, A. C. Bartnik, Jin-Kyun Lee, Hiroaki Imoto, Liangfeng Sun, Joshua J. Choi, Yoshiki Chujo, Tobias Hanrath, Christopher K. Ober, and F. W. Wise. "Role of Solvent Dielectric Properties on Charge Transfer from PbS Nanocrystals to Molecules." In: *Nano Letters* 10.1 (2010), pp. 318–323.

[145] Jun Li, Chris W. Rochester, Ian E. Jacobs, Stephan Friedrich, Pieter Stroeve, Moritz Riede, and Adam J. Moulé. "Measurement of Small Molecular Dopant F4TCNQ and C60F36 Diffusion in Organic Bilayer Architectures." In: *ACS Applied Materials and Interfaces* 7.51 (2015), pp. 28420–28428.

[146] An Dai, Alan Wan, Charles Magee, Yadong Zhang, Stephen Barlow, Seth R. Marder, and Antoine Kahn. "Investigation of p-dopant diffusion in polymer films and bulk heterojunctions: Stable spatially-confined doping for all-solution processed solar cells." In: *Organic Electronics* 23 (2015), pp. 151–157.

[147] Jacob L. Thelen, Shao-Ling Wu, Anna E. Javier, Venkat Srinivasan, Nitash P. Balsara, and Shrayesh N. Patel. "Relationship between Mobility and Lattice Strain in Electrochemically Doped Poly(3-hexylthiophene)." EN. In: *ACS Macro Letters* 4.12 (2015), pp. 1386–1391.

[148] Frederick M. McFarland, Clara M. Ellis, and Song Guo. "The Aggregation of Poly(3-hexylthiophene) into Nanowires: With and Without Chemical Doping." In: *The Journal of Physical Chemistry C* 121.8 (2017), acs.jpcc.7b00816.

[149] Jesus O. Guardado and Alberto Salleo. "Structural Effects of Gating Poly(3-hexylthiophene) through an Ionic Liquid." In: *Advanced Functional Materials* 1701791 (2017), p. 1701791.

[150] Scott Himmelberger, Duc T. Duong, John E. Northrup, Jonathan Rivnay, Felix P. V. Koch, Bryan S. Beckingham, Natalie Stingelin, Rachel A. Segalman, Stefan C. B. Mannsfeld, and Alberto Salleo. "Role of Side-Chain Branching on Thin-Film Structure and Electronic Properties of Polythiophenes." In: *Advanced Functional Materials* 25.17 (2015), pp. 2616–2624.

[151] Shrayesh Patel *et al.* "Morphology controls the thermoelectric power factor of a doped semiconducting polymer." In: *Science Advances* 3.6 (2017), e1700434.

[152] Dean M. DeLongchamp, R. Joseph Kline, Eric K. Lin, Daniel A. Fischer, Lee J. Richter, Leah A. Lucas, Martin Heeney, Iain McCulloch, and John E. Northrup. "High carrier mobility polythiophene thin films: Structure determination by experiment and theory." In: *Advanced Materials* 19.6 (2007), pp. 833–837.

[153] John P. Perdew, Kieron Burke, and Matthias Ernzerhof. "Generalized Gradient Approximation Made Simple." In: *Physical Review Letters* 77.18 (1996), pp. 3865–3868.

[154] P. E. Blöchl. "Projector augmented-wave method." In: *Physical Review B* 50.24 (1994), pp. 17953–17979.

[155] G. Kresse and D. Joubert. "From ultrasoft pseudopotentials to the projector augmented-wave method." In: *Physical Review B* 59.3 (1999), pp. 1758–1775.

[156] G. Kresse and J. Furthmüller. "Efficient iterative schemes for ab initio total-energy calculations using a plane-wave basis set." In: *Physical Review B* 54.16 (1996), pp. 11169–11186.

[157] G. Kresse and J. Furthmüller. "Efficiency of ab-initio total energy calculations for metals and semiconductors using a plane-wave basis set." In: *Computational Materials Science* 6.1 (1996), pp. 15–50.

[158] Axel D. Becke. "Density-functional thermochemistry. III. The role of exact exchange." In: *The Journal of Chemical Physics* 98.7 (1993), pp. 5648–5652.

[159] Chengteh Lee, Weitao Yang, and Robert G. Parr. "Development of the Colle-Salvetti correlation-energy formula into a functional of the electron density." In: *Physical Review B* 37.2 (1988), pp. 785–789.

[160] S. H. Vosko, L. Wilk, and M. Nusair. "Accurate spin-dependent electron liquid correlation energies for local spin density calculations: a critical analysis." In: *Canadian Journal of Physics* 58.8 (1980), pp. 1200–1211.

[161] P. J. Stephens, F. J. Devlin, C. F. Chabalowski, and M. J. Frisch. "Ab Initio Calculation of Vibrational Absorption and Circular Dichroism Spectra Using Density Functional Force Fields." In: *The Journal of Physical Chemistry* 98.45 (1994), pp. 11623–11627.

[162] Ansgar Schäfer, Christian Huber, and Reinhart Ahlrichs. "Fully optimized contracted Gaussian basis sets of triple zeta valence quality for atoms Li to Kr." In: *The Journal of Chemical Physics* 100.8 (1994), pp. 5829–5835.

[163] Turbomole GmbH. *TURBOMOLE V 7.1-2016*.

[164] János Pipek and Paul G. Mezey. "A fast intrinsic localization procedure applicable for ab initio and semiempirical linear combination of atomic orbital wave functions." In: *The Journal of Chemical Physics* 90.9 (1989), pp. 4916–4926.

[165] Wenlan Liu, Bernd Lunkenheimer, Volker Settels, Bernd Engels, Reinhold F. Fink, and Andreas Köhn. "A general ansatz for constructing quasi-diabatic states in electronically excited aggregated systems." In: *Journal of Chemical Physics* 143.8 (2015), p. 084106.

[166] A. Zen, J. Pflaum, S. Hirschmann, W. Zhuang, F. Jaiser, U. Asawapirom, J. P. Rabe, U. Scherf, and D. Neher. "Effect of Molecular Weight and Annealing of Poly(3-hexylthiophene)s on the Performance of Organic Field-Effect Transistors." In: *Advanced Functional Materials* 14.8 (2004), pp. 757–764.

[167] Jacob L. Thelen, Shao Ling Wu, Anna E. Javier, Venkat Srinivasan, Nitash P. Balsara, and Shrayesh N. Patel. "Relationship between Mobility and Lattice Strain in Electrochemically Doped Poly(3-hexylthiophene)." In: *ACS Macro Letters* 4.12 (2015), pp. 1386–1391.

[168] Carl Poelking and Denis Andrienko. "Effect of polymorphism, regioregularity and paracrystallinity on charge transport in poly(3-hexylthiophene) [P3HT] nanofibers." In: *Macromolecules* 46.22 (2013), pp. 8941–8956.

[169] Liang Sheng Liao, Wojciech K. Slusarek, Tukaram K. Hatwar, Michele L. Ricks, and Dustin L. Comfort. "Tandem organic light-emitting diode using hexaazatriphenylene hexacarbonitrile in the intermediate connector." In: *Advanced Materials* 20.2 (2008), pp. 324–329.

[170] Björn Lüssem, Chang Min Keum, Daniel Kasemann, Ben Naab, Zhenan Bao, and Karl Leo. "Doped Organic Transistors." In: *Chemical Reviews* 116.22 (2016), pp. 13714–13751.

[171] V. I. Arkhipov, E. V. Emelianova, and H. Bässler. "Quenching of excitons in doped disordered organic semiconductors." In: *Physical Review B - Condensed Matter and Materials Physics* 70.20 (2004), p. 205205.

[172] Brian W. D'Andrade, Stephen R. Forrest, and Anna B. Chwang. "Operational stability of electrophosphorescent devices containing p and n doped transport layers." In: *Applied Physics Letters* 83.19 (2003), pp. 3858–3860.

[173] Priyanka Tyagi, Suneet Tuli, and Ritu Srivastava. "Study of fluorescence quenching due to 2, 3, 5, 6-tetrafluoro-7, 7', 8, 8'-tetracyano quinodimethane and its solid state diffusion analysis using photoluminescence spectroscopy." In: *Journal of Chemical Physics* 142.5 (2015), p. 054707.

[174] W Lin, Wei-Ben Wang, Yu-Chin Lin, Bang-Ying Yu, Ying-Yu Chen, Mao-Feng Hsu, Jwo-Huei Jou, and Jing-Jong Shyue. "Migration of small molecules during the degradation of organic light-emitting diodes." In: *Organic Electronics* 10.4 (2009), pp. 581–586.

[175] Rico Meerheim, Selina Olthof, Martin Hermenau, Sebastian Scholz, Annette Petrich, Nir Tessler, Olga Solomeshch, Bjrn Lssem, Moritz Riede, and Karl Leo. "Investigation of C60F36 as low-volatility p-dopant in organic optoelectronic devices."

In: *Journal of Applied Physics*. Vol. 109. 10. American Institute of Physics, 2011, p. 103102.

[176] Weiying Gao and Antoine Kahn. "Controlled p doping of the hole-transport molecular material N,N'-diphenyl-N,N'-bis(1-naphthyl)-1,1'-biphenyl-4,4'-di amine with tetra-fluoro-tetra-cyano-quinodimethane." In: *Journal of Applied Physics* 94.1 (2003), pp. 359–366.

[177] Steffen Duhm, Ingo Salzmann, Benjamin Broker, Hendrik Glowatzki, Robert L. Johnson, and Norbert Koch. "Interdiffusion of molecular acceptors through organic layers to metal substrates mimics doping-related energy level shifts." In: *Applied Physics Letters* 95.9 (2009), p. 093305.

[178] Min Cherl Jung and Yabing Qi. "Dopant interdiffusion effects in n-i-p structured spiro-OMeTAD hole transport layer of organo-metal halide perovskite solar cells." In: *Organic Electronics: physics, materials, applications* 31 (2016), pp. 71–76.

[179] Lei Zhang, Feng-Shuo Zu, Ya-Li Deng, Femi Igbari, Zhao-Kui Wang, and Liang-Sheng Liao. "Origin of Enhanced Hole Injection in Organic Light-Emitting Diodes with an Electron-Acceptor Doping Layer: p-Type Doping or Interfacial Diffusion?" In: *ACS Applied Materials & Interfaces* 7.22 (2015), pp. 11965–11971.

[180] Keehoon Kang, Shun Watanabe, Katharina Broch, Alessandro Sepe, Adam Brown, Iyad Nasrallah, Mark Nikolka, Zhuping Fei, Martin Heeney, Daisuke Matsumoto, Kazuhiro Marumoto, Hisaaki Tanaka, Shin-ichi Kuroda, and Henning Sirringhaus. "2D coherent charge transport in highly ordered conducting polymers doped by solid state diffusion." In: *Nature Materials* May (2016), pp. 1–8.

[181] Jun Li, Correy Koshnick, Souleymane O. Diallo, Sophia Ackling, David M. Huang, Ian E. Jacobs, Thomas F. Harrelson, Kunlun Hong, Guangwu Zhang, Joseph Beckett, Mark Mascal, and Adam J. Moulé. "Quantitative Measurements of the Temperature-Dependent Microscopic and Macroscopic Dynamics of a Molecular Dopant in a Conjugated Polymer." In: *Macromolecules* 50.14 (2017), pp. 5476–5489.

[182] Neil D. Treat, Michael A. Brady, Gordon Smith, Michael F. Toney, Edward J. Kramer, Craig J. Hawker, and Michael L. Chabinyc. "Interdiffusion of PCBM and P3HT reveals miscibility in a photovoltaically active blend." In: *Advanced Energy Materials* 1.1 (2011), pp. 82–89.

[183] Jun Li, Christopher W. Rochester, Ian E. Jacobs, Erik W. Aasen, Stephan Friedrich, Pieter Stroeve, and Adam J. Moulé. "The effect of thermal annealing on dopant site choice in conjugated

polymers." In: *Organic Electronics: physics, materials, applications* 33 (2016), pp. 23–31.

[184] Renee Kroon, David Kiefer, Dominik Stegerer, Liyang Yu, Michael Sommer, and Christian Müller. "Polar Side Chains Enhance Processability, Electrical Conductivity, and Thermal Stability of a Molecularly p-Doped Polythiophene." In: *Advanced Materials* 29.24 (2017), p. 1700930.

[185] Jordan C. Aguirre, Steven A. Hawks, Amy S. Ferreira, Patrick Yee, Selvam Subramaniyan, Samson A. Jenekhe, Sarah H. Tolbert, and Benjamin J. Schwartz. "Sequential processing for organic photovoltaics: Design rules for morphology control by tailored semi-orthogonal solvent blends." In: *Advanced Energy Materials* 5.11 (2015), p. 1402020.

[186] M. Hedenqvist, A. Angelstok, L. Edsberg, P. T. Larssont, and U. W. Gedde. "Diffusion of small-molecule penetrants in polyethylene: Free volume and morphology." In: *Polymer* 37.14 (1996), pp. 2887–2902.

[187] Cameron S. Lee and Mark D. Dadmun. "Important thermodynamic characteristics of poly(3-hexyl thiophene)." In: *Polymer (United Kingdom)* 55.1 (2014), pp. 4–7.

[188] D.B.A. Rep, A. F. Morpurgo, W. G. Sloof, and T. M. Klapwijk. "Mobile ionic impurities in organic semiconductors." In: *Journal of Applied Physics* 93.4 (2003), p. 2082.

[189] S Arumugam, J Shi, D P Tunstall, and C A Vincent. "Cation and anion diffusion coefficients in a solid polymer electrolyte measured by pulsed-field-gradient nuclear magnetic resonance." In: *Journal of Physics: Condensed Matter* 5.2 (1993), pp. 153–160.

[190] I. M. Ward, N. Boden, J. Cruickshank, and S. A. Leng. "NMR studies of ionic mobility and molecular mobility in polymer electrolytes." In: *Electrochimica Acta* 40.13-14 (1995), pp. 2071–2076.

[191] Mahati Chintapalli, Ksenia Timachova, Kevin R. Olson, Sue J. Mecham, Didier Devaux, Joseph M. Desimone, and Nitash P. Balsara. "Relationship between Conductivity, Ion Diffusion, and Transference Number in Perfluoropolyether Electrolytes." In: *Macromolecules* 49.9 (2016), pp. 3508–3515.

[192] Chimed Ganzorig and Masamichi Fujihira. "Improved drive voltages of organic electroluminescent devices with an efficient p-type aromatic diamine hole-injection layer." In: *Applied Physics Letters* 77.25 (2000), pp. 4211–4213.

[193] X. Zhou, M. Pfeiffer, J. Blochwitz, A. Werner, A. Nollau, T. Fritz, and K. Leo. "Very-low-operating-voltage organic light-emitting diodes using a p-doped amorphous hole injection layer." In: *Applied Physics Letters* 78.4 (2001), pp. 410–412.

[194] Yulong Shen, Ahmad R. Hosseini, Man Hoi Wong, and George G. Malliaras. "How to make ohmic contacts to organic semiconductors." In: *ChemPhysChem* 5.1 (2004), pp. 16–25.

[195] M. R. Mahani, A. Mirsakiyeva, and Anna Delin. "Breakdown of Polarons in Conducting Polymers at Device Field Strengths." In: *Journal of Physical Chemistry C* 121.19 (2017), pp. 10317–10324.

[196] Weiying Gao and Antoine Kahn. "Electronic structure and current injection in zinc phthalocyanine doped with tetrafluorotetracyanoquinodimethane: Interface versus bulk effects." In: *Organic Electronics: physics, materials, applications* 3.2 (2002), pp. 53–63.

[197] J. Salbeck, N. Yu, J. Bauer, F. Weissörtel, and H. Bestgen. "Low molecular organic glasses for blue electroluminescence." In: *Synthetic Metals* 91.1-3 (1997), pp. 209–215.

[198] Seon-Young Rhim. "Untersuchungen des Verhaltens und der Anwendungsmöglichkeit des Dotandendrifts in Poly(3-hexylthiophen-2,5-diyl)." MA thesis. Heidelberg University, 2017.

[199] V. I. Arkhipov, P. Heremans, E. V. Emelianova, and H. Bässler. "Effect of doping on the density-of-states distribution and carrier hopping in disordered organic semiconductors." In: *Physical Review B - Condensed Matter and Materials Physics* 71.4 (2005), p. 045214.

[200] Selina Olthof, Shafigh Mehraeen, Swagat K. Mohapatra, Stephen Barlow, Veaceslav Coropceanu, Jean-Luc Brédas, Seth R. Marder, and Antoine Kahn. "Ultralow Doping in Organic Semiconductors: Evidence of Trap Filling." In: *Physical Review Letters* 109.17 (2012), p. 176601.

[201] Rico Meerheim, Selina Olthof, Martin Hermenau, Sebastian Scholz, Annette Petrich, Nir Tessler, Olga Solomeshch, Bjrn Lssem, Moritz Riede, and Karl Leo. "Investigation of C60F36 as low-volatility p-dopant in organic optoelectronic devices." In: *Journal of Applied Physics* 109.10 (2011).

[202] Vladimir A. Kolesov, Canek Fuentes-Hernandez, Wen-Fang Chou, Naoya Aizawa, Felipe A. Larrain, Ming Wang, Alberto Perrotta, Sangmoo Choi, Samuel Graham, Guillermo C. Bazan, Thuc-Quyen Nguyen, Seth R. Marder, and Bernard Kippelen. "Solution-based electrical doping of semiconducting polymer films over a limited depth." In: *Nature Materials* 16.4 (2016), pp. 474–480.

[203] Jonathan Rivnay, Michael F. Toney, Yan Zheng, Isaac V. Kauvar, Zhihua Chen, Veit Wagner, Antonio Facchetti, and Alberto Salleo. "Unconventional face-on texture and exceptional in-

plane order of a high mobility n-type polymer." In: *Advanced Materials* 22.39 (2010), pp. 4359–4363.

[204] Torben Schuettfort, Sven Huettner, Samuele Lilliu, J. Emyr MacDonald, Lars Thomsen, and Christopher R. McNeill. "Surface and bulk structural characterization of a high-mobility electron-transporting polymer." In: *Macromolecules* 44.6 (2011), pp. 1530–1539.

[205] Jonathan Rivnay, Robert Steyrleuthner, Leslie H. Jimison, Alberto Casadei, Zhihua Chen, Michael F. Toney, Antonio Facchetti, Dieter Neher, and Alberto Salleo. "Drastic control of texture in a high performance n-type polymeric semiconductor and implications for charge transport." In: *Macromolecules* 44.13 (2011), pp. 5246–5255.

[206] Jakob Bernhardt. "Infrarotspektroskopische Untersuchung organischer Halbleiter." MA thesis. Heidelberg University, 2017.

[207] Mary J.T. Young and Matthew S. Platz. "Mechanistic Analysis of the Reactions of (Pentafluorophenyl)nitrene in Alkanes." In: *Journal of Organic Chemistry* 56.22 (1991), pp. 6403–6406.

[208] Elisa Leyva, Matthew S. Matz, Gabriele Persy, and Jakob Wirz'. "Photochemistry of Phenyl Azide: The Role of Singlet and Triplet Phenylnitrene as Transient Intermediates." In: *Journal of the American Chemical Society* 108.13 (1986), pp. 3783–3790.

[209] Roberto Marani, Gennaro Gelao, and Anna Gina Perri. "A review on memristor applications." In: *arXiv preprint* 6.5 (2015), pp. 1–17.

[210] F. Pan, S. Gao, C. Chen, C. Song, and F. Zeng. "Recent progress in resistive random access memories: Materials, switching mechanisms, and performance." In: *Materials Science and Engineering R: Reports* 83.1 (2014), pp. 1–59.

[211] Leon Chua. "Resistance switching memories are memristors." In: *Applied Physics A: Materials Science and Processing* 102.4 (2011), pp. 765–783.

[212] Ritu Chaudhary. "Review on Memristors – The Forth Fundamental Circuit Element." In: *International Journal of Electronics, Electrical and Computational System* 6.3 (2017), pp. 130–135.

[213] Shizuo Tokito, Koji Noda, and Yasunori Taga. "Metal oxides as a hole-injecting layer for an organic electroluminescent device." In: *Journal of Physics D: Applied Physics* 29.11 (1996), pp. 2750–2753.

[214] Jaap H. A. Smits, Stefan C. J. Meskers, René A. J. Janssen, Albert W. Marsman, and Dago M. De Leeuw. "Electrically rewritable memory cells from poly(3-hexylthiophene) Schottky diodes." In: *Advanced Materials* 17.9 (2005), pp. 1169–1173.

[215] Sreetosh Goswami *et al.* "Robust resistive memory devices using solution-processable metal-coordinated azo aromatics." In: *Nature Materials* (2017), nmat5009.

[216] Qi Dan Ling, Der Jang Liaw, Chunxiang Zhu, Daniel Siu Hung Chan, En Tang Kang, and Koon Gee Neoh. *Polymer electronic memories: Materials, devices and mechanisms*. 2008.

[217] Wen Peng Lin, Shu Juan Liu, Tao Gong, Qiang Zhao, and Wei Huang. "Polymer-based resistive memory materials and devices." In: *Advanced Materials* 26.4 (2014), pp. 570–606.

[218] Byungjin Cho, Sunghun Song, Yongsung Ji, Tae Wook Kim, and Takhee Lee. "Organic resistive memory devices: Performance enhancement, integration, and advanced architectures." In: *Advanced Functional Materials* 21.15 (2011), pp. 2806–2829.

[219] Qianxi Lai, Zuhua Zhu, Yong Chen, Satish Patil, and Fred Wudl. "Organic nonvolatile memory by dopant-configurable polymer." In: *Applied Physics Letters* 88.13 (2006), p. 133515.

[220] Frank Verbakel, S. C J Meskers, and René A. J. Janssen. "Electronic memory effects in a sexithiophene-poly(ethylene oxide) block copolymer doped with NaCl. Combined diode and resistive switching behavior." In: *Chemistry of Materials* 18.11 (2006), pp. 2707–2712.

[221] Unnat S. Bhansali, Mohd A. Khan, Dongkyu Cha, Mahmoud N. Almadhoun, Ruipeng Li, Long Chen, Aram Amassian, Ihab N. Odeh, and Husam N. Alshareef. "Metal-free, single-polymer device exhibits resistive memory effect." In: *ACS Nano* 7.12 (2013), pp. 10518–10524.

[222] Yongbian Kuang, Ru Huang, Yu Tang, Wei Ding, Lijie Zhang, and Yangyuan Wang. "Flexible single-component-polymer resistive memory for ultrafast and highly compatible nonvolatile memory applications." In: *IEEE Electron Device Letters* 31.7 (2010), pp. 758–760.

[223] Wen-Ya Lee, Hung-Chin Wu, Chien Lu, Benjamin D. Naab, Wen-Chang Chen, and Zhenan Bao. "n-Type Doped Conjugated Polymer for Nonvolatile Memory." In: *Advanced Materials* (2017), p. 1605166.

[224] Yoeri van de Burgt, Ewout Lubberman, Elliot J. Fuller, Scott T. Keene, Grégorio C. Faria, Sapan Agarwal, Matthew J. Marinella, A. Alec Talin, and Alberto Salleo. "A non-volatile organic electrochemical device as a low-voltage artificial synapse for neuromorphic computing." In: *Nature Materials* (2017).

[225] Albert Y. Zomaya. *Handbook of Nature-Inspired and Innovative Computing Integrating Classical Models with Emerging Technologies*. May. Springer Science & Business Media, 2006.

[226] Eugene M Izhikevich and Gerald M Edelman. "Large-scale model of mammalian thalamocortical systems." In: *Proceedings of the National Academy of Sciences of the United States of America* 105.9 (2008), pp. 3593–8.

[227] Rajagopal Ananthanarayanan, Steven K. Esser, Horst D. Simon, and Dharmendra S. Modha. "The cat is out of the bag." In: *Proceedings of the Conference on High Performance Computing Networking, Storage and Analysis - SC '09*. New York, New York, USA: ACM Press, 2009, p. 1.

[228] Sung Hyun Jo, Ting Chang, Idongesit Ebong, Bhavitavya B. Bhadviya, Pinaki Mazumder, and Wei Lu. "Nanoscale memristor device as synapse in neuromorphic systems." In: *Nano Letters* 10.4 (2010), pp. 1297–1301.

[229] Bente Pakkenberg, Dorte Pelvig, Lisbeth Marner, Mads J. Bundgaard, Hans Jørgen G Gundersen, Jens R. Nyengaard, and Lisbeth Regeur. "Aging and the human neocortex." In: *Experimental Gerontology*. Vol. 38. 1-2. Pergamon, 2003, pp. 95–99.

[230] Yong Tang, Jens R. Nyengaard, Didima M.G. De Groot, and Hans Jørgen G. Gundersen. "Total regional and global number of synapses in the human brain neocortex." In: *Synapse* 41.3 (2001), pp. 258–273.

[231] Kyungah Seo, Insung Kim, Seungjae Jung, Minseok Jo, Sangsu Park, Jubong Park, Jungho Shin, Kuyyadi P Biju, Jaemin Kong, Kwanghee Lee, Byounghun Lee, and Hyunsang Hwang. "Analog memory and spike-timing-dependent plasticity characteristics of a nanoscale titanium oxide bilayer resistive switching device." In: *Nanotechnology* 22.25 (2011), p. 254023.

[232] Geoffrey W. Burr, Robert M. Shelby, Severin Sidler, Carmelo Di Nolfo, Junwoo Jang, Irem Boybat, Rohit S. Shenoy, Pritish Narayanan, Kumar Virwani, Emanuele U. Giacometti, Bulent N. Kurdi, and Hyunsang Hwang. "Experimental Demonstration and Tolerancing of a Large-Scale Neural Network (165 000 Synapses) Using Phase-Change Memory as the Synaptic Weight Element." In: *IEEE Transactions on Electron Devices* 62.11 (2015), pp. 3498–3507.

[233] M. Prezioso, F. Merrikh-Bayat, B. D. Hoskins, G. C. Adam, K. K. Likharev, and D. B. Strukov. "Training and operation of an integrated neuromorphic network based on metal-oxide memristors." In: *Nature* 521.7550 (2015), pp. 61–64.

[234] Web of Science (accessed on 2017-10-12). *https://webofknowledge.com*.

[235] Mohamad H. Hassoun. *Fundamentals of artificial neural networks*. MIT Press, 1995.

[236] Sungho Kim, Chao Du, Patrick Sheridan, Wen Ma, ShinHyun Choi, and Wei D. Lu. "Experimental demonstration of a second-order memristor and its ability to biorealistically implement synaptic plasticity." In: *Nano Letters* 15.3 (2015), pp. 2203–2211.

[237] Paschalis Gkoupidenis, Nathan Schaefer, Benjamin Garlan, and George G. Malliaras. "Neuromorphic Functions in PEDOT:PSS Organic Electrochemical Transistors." In: *Advanced Materials* 27.44 (2015), pp. 7176–7180.

[238] W. Xu, S.-Y. Min, H. Hwang, and T.-W. Lee. "Organic core-sheath nanowire artificial synapses with femtojoule energy consumption." In: *Science Advances* 2.6 (2016), e1501326–e1501326.

[239] Amanda Jonsson, Sahika Inal, Llke Uguz, Adam J Williamson, Loïg Kergoat, Jonathan Rivnay, Dion Khodagholy, Magnus Berggren, Christophe Bernard, George G Malliaras, and Daniel T Simon. "Bioelectronic neural pixel: Chemical stimulation and electrical sensing at the same site." In: *Proceedings of the National Academy of Sciences* 113.34 (2016), pp. 9440–9445.

[240] Karin C. Larsson, Peter Kjäll, and Agneta Richter-Dahlfors. "Organic bioelectronics for electronic-to-chemical translation in modulation of neuronal signaling and machine-to-brain interfacing." In: *Biochimica et Biophysica Acta - General Subjects* 1830.9 (2013), pp. 4334–4344.

[241] Daniel T. Simon, Karin C. Larsson, David Nilsson, Gustav Burström, Dagmar Galter, Magnus Berggren, and Agneta Richter-Dahlfors. "An organic electronic biomimetic neuron enables auto-regulated neuromodulation." In: *Biosensors and Bioelectronics* 71 (2015), pp. 359–364.

[242] Max L. Tietze, Paul Pahner, Kathleen Schmidt, Karl Leo, and Björn Lüssem. "Doped organic semiconductors: Trap-filling, impurity saturation, and reserve regimes." In: *Advanced Functional Materials* 25.18 (2015), pp. 2701–2707.

[243] S. Nicht, H. Kleemann, A. Fischer, K. Leo, and B. Lüssem. "Functionalized p-dopants as self-assembled monolayers for enhanced charge carrier injection in organic electronic devices." In: *Organic Electronics: physics, materials, applications* 15.3 (2014), pp. 654–660.

[244] Jian Liu, Li Qiu, Giuseppe Portale, Marten Koopmans, Gert ten Brink, Jan C. Hummelen, and L. Jan Anton Koster. "N-Type Organic Thermoelectrics: Improved Power Factor by Tailoring Host-Dopant Miscibility." In: *Advanced Materials* 1701641 (2017), p. 1701641.

LIST OF FIGURES

PUBLICATIONS, PRESENTATIONS, THESES

JOURNAL PUBLICATIONS

1. **Lars Müller**, Diana Nanova, Tobias Glaser, Sebastian Beck, Annemarie Pucci, Anne K. Kast, Rasmus R. Schröder, Eric Mankel, Patrick Pingel, Dieter Neher, Wolfgang Kowalsky, and Robert Lovrincic. *Charge-Transfer-Solvent Interaction Predefines Doping Efficiency in p-Doped P3HT Films.* In: Chemistry of Materials 28.12 (2016), pp. 4432-4439

2. **Lars Müller**, Seon-Young Rhim, Vipilan Sivanesan, Dongxiang Wang, Sebastian Hietzschold, Patrick Reiser, Eric Mankel, Sebastian Beck, Stephen Barlow, Seth R. Marder, Annemarie Pucci, Wolfgang Kowalsky, and Robert Lovrincic. *Electric-Field-Controlled Dopant Distribution in Organic Semiconductors.* In: Advanced Materials (2017), p. 1701466.

3. Patrick Reiser, **Lars Müller**, Vipilan Sivanesan, Robert Lovrincic, Stephen Barlow, Seth R. Marder, Annemarie Pucci, Wolfgang Kowalsky, Wolfram Jaegermann, Eric Mankel, and Sebastian Beck. *Diffusion Properties of Molecular Dopants in Sequentially Doped Semiconducting Polymers.* In preparation.

SELECTION OF CONFERENCE PRESENTATIONS

1. Lars Müller, Diana Nanova, Tobias Glaser, Sebastian Beck, Annemarie Pucci, Anne K. Kast, Rasmus R. Schröder, Eric Mankel, Patrick Pingel, Dieter Neher, Wolfgang Kowalsky, and Robert Lovrincic. *Charge-Transfer - Solvent Interaction Predefines Doping Efficiency in p-Doped P3HT-Films.* Talk, DPG Spring Meeting 2016, Regensburg, Germany.

2. Lars Müller, Diana Nanova, Tobias Glaser, Sebastian Beck, Annemarie Pucci, Anne K. Kast, Rasmus R. Schröder, Eric Mankel, Robert Lovrincic, and Wolfgang Kowalsky. *The Role of Structural Order in p-Type Doping of P3HT.* Poster, MRS Spring Meeting 2016, Phoenix, USA.

3. Lars Müller, Sebastian Beck, Annemarie Pucci, Wolfgang Kowalsky, and Robert Lovrincic. *Charge-Transfer – Solvent Interaction Predefines Doping Efficiency in p-Doped P3HT-Films.* Poster, International Conference on Organic Electronics 2016, Moscow, Russia.

4. Lars Müller, Vipilan Sivanesan, Seon-Young Rhim, Dongxiang Wang, Sebastian Beck, Annemarie Pucci, Wolfgang Kowalsky, and Robert Lovrincic. *Dynamics of Polymer-Dopant Interactions: From Solution to Thin Films.* Talk, MRS Fall Meeting 2016, Boston, USA.

5. Lars Müller, Seon-Young Rhim, Vipilan Sivanesan, Dongxiang Wang, Sebastian Beck, Annemarie Pucci, Wolfgang Kowalsky, and Robert Lovrincic. *Drift of Dopants in Organic Semiconductors.* Talk, DPG Spring Meeting 2017, Dresden, Germany.

6. Lars Müller, Seon-Young Rhim, Vipilan Sivanesan, Jakob Bernhardt, Dongxiang Wang, Sebastian Beck, Annemarie Pucci, Wolfgang Kowalsky, and Robert Lovrincic. *Controlled Drift of Small Molecule Dopants in Organic Semiconductors.* Poster, International Conference on Organic Electronics 2017, St. Petersburg, Russia.

CO-SUPERVISED THESES

- Christian Willig, Heidelberg University: *Herstellung und Charakterisierung organischer Dünnschichtsolarzellen basierend auf kleinen Molekülen*, bachelor's thesis.
- Dongxiang Wang, Karlsruhe Institute of Technology: *The Drift of p-type Dopants in Organic Semiconductors*, master's thesis.
- Martin Gebhardt, TU Braunschweig: *Ionentransistoren*, master's thesis.
- Seon-Young Rhim, Heidelberg University: *Untersuchungen des Verhaltens und der Anwendungsmöglichkeit des Dotandendrifts in Poly(3-hexylthiophen-2,5-diyl)*, master's thesis.
- Yaoxin Liu, Karlsruhe Institute of Technology: *Doped P3HT-based Photodiodes*, research internship.

DANKSAGUNG

Ich möchte mich bei zahlreichen Personen für die vielfältige Unterstützung während meiner gesamten Promotion bedanken. Mein Dank gilt insbesondere:

Prof. Wolfgang Kowalsky für die Möglichkeit, in seiner Arbeitsgruppe am InnovationLab zu promovieren. Weiterhin für das Schaffen von Rahmenbedingungen, die mit hervorragend ausgestatteten Laboren und vielfältigen Konferenzbesuchen nicht besser hätten sein können.

Prof. Albrecht Winnacker für die bereitwillige Übernahme des Zweitgutachtens.

Dr. Robert Lovrincic für die exzellente Betreuung meiner Promotion und die andauernde Bereitschaft, mir bei Problemen zu helfen und meine Promotion voranzubringen. Einen besonderen Dank auch für das Korrekturlesen dieser Arbeit.

Der Carl-Zeiss-Stiftung für die großzügige Unterstützung durch das Stipendium und die sehr interessanten Stipendiaten-Treffen.

Allen Kollegen, die mit Messungen und Diskussionen unmittelbar an dieser Arbeit beteiligt waren für die äußerst ertragreiche Kollaboration: Sebastian Beck, Vipilan Sivanesan, Tobias Glaser, Jakob Bernhardt, Sebastian Hietzschold, Patrick Reiser, Wenlan Liu, Simon Benneckendorf und Anne Kast.

Yaoxin, Seon-Young, Dongxiang, Martin und Christian, die ich während meiner Promotion betreuen durfte, für die hervorragende Arbeit im Labor und die auch außerhalb des Labors angenehme Zeit.

Allen Analytik-Gruppenmitgliedern, iL-Mitarbeitern und Kollegen aus anderen Arbeitsgruppen für die außerordentlich gute Zusammenarbeit und Arbeitsatmosphäre. Allen voran möchte ich meinen Büro-Kollegen danken, die jeden Tag abwechslungsreich gemacht haben und immer für eine tolle Atmosphäre gesorgt haben. Danke auch an Jean-Nicolas für das Korrekturlesen.

Meiner Familie und Nicole für die bedingungslose Unterstützung in jeglicher Hinsicht. DANKE!

COLOPHON

This document was typeset using the typographical look-and-feel `classicthesis` developed by André Miede and Ivo Pletikosić. The style was inspired by Robert Bringhurst's seminal book on typography "*The Elements of Typographic Style*". `classicthesis` is available for both LaTeX and LyX:

`https://bitbucket.org/amiede/classicthesis/`

Final Version as of December 14, 2017 (`classicthesis` version 4.4).